

nature

CLIMATE PLEDGES

Fully realizing current promises could limit warming to just below 2 °C, but 1.5 °C is still out of reach

Protein predictions
How AlphaFold is changing the shape of biology

Industrial evolution
Lessons learnt from commercializing methane capture

DNA degradation
Anti-plasmid defence systems in bacterium that causes cholera

Nature.2022.04.17

[Sun, 17 Apr 2022]

- [This Week](#)
- [News in Focus](#)
- [Books & Arts](#)
- [Opinion](#)
- [Work](#)
- [Research](#)
- [Amendments & Corrections](#)

This Week

- **The war in Ukraine is exposing gaps in the world's food-systems research** [12 April 2022]
Editorial • Russia's invasion is the latest threat to the stability of world food supplies. Researchers must act now to halt the cycle of repeated food crises.
- **Global science must stand up for Iran's imprisoned scholars** [13 April 2022]
Editorial • Iranian researchers are at risk as never before. Governments are urging quiet diplomacy. But a new book shows why public campaigns matter.
- **University culture wars over race theory recall 1920s fight to teach evolution** [12 April 2022]
World View • Arguments for quality work better than quibbles over facts.

- EDITORIAL
- 12 April 2022

The war in Ukraine is exposing gaps in the world's food-systems research

Russia's invasion is the latest threat to the stability of world food supplies. Researchers must act now to halt the cycle of repeated food crises.



Ukraine is a major exporter of wheat, but the Russian invasion is threatening this year's crop. Credit: Vincent Mundy/Bloomberg/Getty

An invasion. A war. A pandemic. A financial crisis. All have conspired to put unprecedented stress on global food systems. Ukraine and Russia produce a combined total of 14% of the world's wheat and 30% of the world's wheat exports, as well as 60% of the world's sunflower oil. These supplies are under threat, with Russia suspending food and fertilizer exports, and Ukraine's farmers under extreme stress, fighting an invading army while tending to this year's crop.

And Russia is not alone in limiting its exports. According to Rob Vos at the International Food Policy Research Institute, based in Washington DC, by 12 April, a total of 16 countries had banned or restricted food exports. This marked reduction in supply is fuelling inflation. Taken together, the impacts could be catastrophic for some of the world's poorest and most vulnerable people. At least 26 countries, including Somalia, Senegal and Egypt, rely on one or both of Russia and Ukraine for between 50% and 100% of their wheat. If the war continues, many countries already saddled with pandemic debt could be forced to borrow more to subsidize staple foods, creating more hardship.

Clearly, action must be taken now. Priorities must include preventing and rolling back export bans, and funding the World Food Programme's emergency-relief efforts. The agency said last month that, because of inflation, it needs to find an extra US\$60 million to \$75 million a month.

Schools of thought

The diagnosis might be clear, but there's less consensus on what needs to be done in the medium-to-long term to increase nations' resilience to the hunger that follows pandemics, wars and extreme weather. Food-systems science is complex, with many perspectives, and there are gaps in the research. There is also no intergovernmental mechanism through which governments, having been informed by research advice, are bound to act on food systems.

According to one school of thought, every policy lever must be applied to reduce countries' dependence on food imports — even if that means choosing options that might not be the most environmentally sound. It could

mean, for example, felling forests so that more cereal and oil crops can be grown closer to home markets.

A second school of thought argues that the crisis presents a chance to speed up moves towards a more environmentally conscious future. Intensive agriculture is the leading cause of biodiversity loss and, globally, farming contributes 30% of all greenhouse-gas emissions. At least four policies could minimize these impacts, while at the same time securing food supplies, say proponents.

First, around one-third of global croplands produce animal feed, according to the World Resources Institute, an environmental think tank based in Washington DC. Humans could meet their energy needs using a lot less land if they ate fewer animal products. Second, one-third of all food produced globally never reaches the plate — it is lost in the production chain or wasted once it reaches households. Improvements in harvesting and storage methods could potentially reduce losses, as might efforts to nudge consumers to make more responsible choices.

Third, most land under cultivation is occupied by a small number of food crops, such as wheat, rice, maize (corn), soya and potatoes. This contributes to biodiversity loss. Diversifying agriculture to include more legumes, nuts and vegetables would benefit both the planet and people, because these crops provide important nutrients.

Finally, croplands that are currently being used to grow biofuels could be converted back to growing food crops. In the United States, some 40% of maize is used to make ethanol. Research shows that biofuels grown on croplands are not as useful in climate mitigation as once thought¹.

The research challenge

Each of these measures will have associated costs, and the trade-offs must be assessed, which is why research is crucial. Some areas of this research are patchy. An analysis of published agricultural science (a project called Ceres2030) found that less than 5% was relevant to the needs of smallholder farmers (see go.nature.com/3rjkwiw). Moreover, the major funders of

agricultural research overwhelmingly finance research into the staple cereal crops². Esther Turnhout, chair of science, technology and society at the University of Twente in the Netherlands, says: “Something is going wrong here in how we understand food systems, and part of the problem lies in how we do research into food systems.”

At a key United Nations summit last year, delegates discussed the idea of establishing a body akin to the Intergovernmental Panel on Climate Change (IPCC) for food systems. It would respond to questions from policymakers and produce advice based on a synthesis of the available evidence. Its reports would also remind funders of gaps in the science that need addressing.

But the idea has its detractors, who rightly point out that the food-systems field does not lack high-level panels of scientists producing research evidence. At least 11 such panels³ have a remit that covers this; these include the high-level panel of experts of the Committee on World Food Security, which provides ongoing science advice to the UN system.

What food systems lacks is an intergovernmental mechanism by which policymakers are given independent assessments of the literature and commit to acting on these findings, in the way that the IPCC’s reports inform the work of governments meeting at UN climate conventions.

The feasibility of the IPCC-style panel for food systems is being researched by an expert group reporting to the European Commission in Brussels. Its recommendations, due to be published this summer, are expected to confirm that existing organizations are not delivering what is needed. But the solution, says one group member, environmental scientist Jacqueline McGlade, is not necessarily a new IPCC-style body. Instead, the group is expected to recommend a greater effort to gather knowledge and evidence from under-represented groups. In addition, a UN ‘clearing house’ could extract what governments need from existing science-advice panels and embed these recommendations in global commitments such as those on climate change, biodiversity and the UN Sustainable Development Goals.

Whether the expert group persuades enough people and organizations to come together to improve the breadth and clout of food-systems science

advice remains to be seen. But the analysis and soul-searching along the way will be productive. The latest crisis should be seen as the moment when the world came together to renovate the food system and the research agenda behind it. As Sheryl Hendriks, a food-policy researcher at the University of Pretoria, says: “The geopolitics are more clear than we’ve ever, ever imagined.”

Nature **604**, 217-218 (2022)

doi: <https://doi.org/10.1038/d41586-022-00994-8>

References

1. Jeswani, H. K., Chilvers, A. & Azapagic, A. *Proc. R. Soc. A* **476**, 20200351 (2020).
2. Pingali, P. *Food Sec.* **7**, 583–591 (2015).
3. Singh, B. K. *et al.* *Nature Food* **2**, 838–842 (2021).

This article was downloaded by **calibre** from <https://www.nature.com/articles/d41586-022-00994-8>

| [Section menu](#) | [Main menu](#) |

- EDITORIAL
- 13 April 2022

Global science must stand up for Iran's imprisoned scholars

Iranian researchers are at risk as never before. Governments are urging quiet diplomacy. But a new book shows why public campaigns matter.



Niloufar Bayani, a conservation researcher, has been in prison since 2018. Credit: Niloufar Bayani

For an all-too-brief period last month, it seemed that Morad Tahbaz, co-founder of conservation charity the Persian Wildlife Heritage Foundation in

Tehran, might be free to go home after four years as a prisoner in Iran. Tahbaz's charity had been monitoring the critically endangered Asiatic cheetah (*Acinonyx jubatus venaticus*) by laying camera traps. Iran's judicial system decreed that this was spying — and Tahbaz, with seven colleagues, is serving a ten-year jail sentence. The charity's other co-founder, sociologist Kavous Seyed Emami, died in prison just weeks after his arrest.

Tahbaz has Iranian, UK and US citizenship. He was initially freed as part of a deal involving two UK–Iranian citizens, charity worker Nazanin Zaghari-Ratcliffe and engineer Anoosheh Ashoori. The latter two were swiftly put on aeroplanes to the United Kingdom, but Tahbaz was returned to prison. His family is in shock and disbelief.

Tahbaz is one in a lengthening list of people involved in scientific activities who are being jailed in Iran for spying. Their plight is all the more precarious because there's little publicity about the charges against them or the horrendous conditions in which they're kept. Those arrested include dual nationals, such as Swedish–Iranian Ahmadreza Djalali, who studies how to make hospitals disaster-proof and is facing a death sentence; and Fariba Adelkhah, a French–Iranian anthropologist working at Sciences Po in Paris, who was arrested and imprisoned in 2019.

One reason dual nationals are arrested is to be used as hostages to extract concessions from Western governments. But the majority of scholars in prison are Iranian nationals and their stories are not well known. They include Niloufar Bayani, a wildlife conservationist formerly with the United Nations. Younger people have been caught up, too, such as Ali Younesi, an award-winning computer-science student at Sharif University of Technology in Tehran.



Fariba Adelkhah, an anthropologist, was arrested and jailed in 2019. Credit: Thomas Coex/AFP/Getty

A new book, *The Uncaged Sky*, by anthropologist Kylie Moore-Gilbert lays bare the severe mental and physical punishments they are enduring — especially women. Moore-Gilbert, who has dual UK and Australian citizenship, is uniquely placed to write this account. Formerly at the University of Melbourne in Australia, she travelled to Iran in 2018 to attend a conference and was arrested at the airport as she was preparing to return to Australia. She was imprisoned for two years on spying charges before being released last year as part of a prisoner swap.

Moore-Gilbert spent time with both Bayani and Adelkhah at the notorious Evin Prison in Tehran. She describes in vivid detail how women undergo interrogation and torture, how they are sexually harassed, forced to spend periods in solitary confinement and denied basic medical care. It's a means of breaking them so they will confess to things they did not do.

The importance of publicity is an overriding message. Moore-Gilbert's family in Australia was advised by its government not to go public about her case, because this could complicate negotiations for her release. But those who avoid publicity become a lower priority for their governments. Moore-Gilbert recalls a phone call with her father in which he said the government was advising staying quiet. In response, she said, "Dad, listen to me — I don't have much time. You need to go to the media. Tell them what's happening to me. Tell them I've been arrested and that I'm being kept in solitary and denied visits from the embassy."

Hostage taking can be countered if governments speak with one voice, instead of each dealing bilaterally with Iran. And constant publicity is one of the best ways to put pressure on all sides to act.

The scientific community must do more to raise its voice in support of jailed scholars. International scientists should speak out for Iranian colleagues who don't benefit from the freedom of speech that they do. Statements, letters — and even mentioning Iran's imprisoned researchers at conferences and events — are ways to tell Iranian scholars that global science stands with them. Iranian science will not flourish until its scholars feel safe.

Nature **604**, 218 (2022)

doi: <https://doi.org/10.1038/d41586-022-00995-7>

This article was downloaded by **calibre** from <https://www.nature.com/articles/d41586-022-00995-7>

- WORLD VIEW
- 12 April 2022

University culture wars over race theory recall 1920s fight to teach evolution



Arguments for quality work better than quibbles over facts.

- [Adam Laats](#) 0

When Texas lieutenant governor Dan Patrick declared earlier this year that he would remove tenure protections so that a “handful of professors” can no longer “indoctrinate students with critical race theory”, he was unwittingly repeating rhetoric from the unsuccessful side of a 100-year-old culture war. Across the United States, there at least 49 active bills that would crush the freedom to learn and teach on university campuses — 25 of the 50 states have at least one.

As a historian, I've studied the battles over education in the United States. Although fights for control of universities are waged on the fields of science, literature and history, they are won with different sorts of argument.

Critical race theory (CRT) emerged in the 1970s as a legal analysis of racism deeply embedded in society. Warnings against CRT are new, but the arguments mirror a 1920s-era assault on teaching evolution in US universities. Conservatives then, as now, sought to ban teaching of an accepted theory that threatened their world view.

In May 1921, the University of Wisconsin in Madison hosted an anti-evolution lecture by popular pundit William Jennings Bryan — who later became famous for arguing in the Scopes monkey trial in Tennessee, about teaching evolution to schoolchildren. University president Edward Birge, a prominent zoologist, criticized Bryan's speech and drew national conservative fury.

Bryan demanded that Wisconsin's instructors stop teaching evolution, and that Birge personally affirm a belief in creation as described in the biblical Book of Genesis. Otherwise, Bryan said, a sign should be posted at the entrance to campus describing its classrooms as "an arena in which a brutish doctrine tears to pieces the religious faith of young men and young women".

Meanwhile, another campaign took aim at Howard Odum, a professor at the University of North Carolina in Chapel Hill and editor of a peer-reviewed journal, which had published two articles critical of the historical truth of Christian miracles. Conservatives called for Odum to be fired or reprimanded and for the university to support only research that affirmed Christian doctrine. In Greensboro, North Carolina, another instructor, Albert Keister, described evolutionary theory as a powerful scientific tool and accounts of six-day creation as "a form of mythology." This fuelled calls for a state-wide law to ban teaching of evolutionary theory at public colleges and universities. Harry Chase, the president of the University of North Carolina, managed to defeat the proposed legislation.

How? He did not engage in debates about evolutionary theory. He did not rebut (absurd) charges that only atheists could embrace modern science, nor address distinctions between religion and mythology. Instead, he argued that a law banning the teaching of evolution would spell the death of any “real university”, and that attacking the “quality of faculty” would undermine high-quality education. Faculty members, students and administrators were able to organize and mobilize a broad mass of popular support that had been relatively quiescent. Support for the restrictive bill turned out to be a paper tiger.

In Wisconsin, Birge took a similar stance. Instead of taking on Bryan’s arguments that evolutionary theory was weak or that learning science turned people into atheists, Birge argued in favour of academic prestige. If Wisconsin wanted a high-quality university, it must accept academic freedom. He recruited prominent faculty members across disciplines to back him. He publicized the demands of tax-paying Wisconsinites who decried an “expurgated education” and successfully defended his university.

Today’s push for conservative control of universities is just as ambitious. Moreover, today’s scholars are more vulnerable: higher-education budgets are depleted, and some university departments and programmes are simply being eliminated, not just criticized. The situation in the United States is exacerbated because higher education is decentralized and so more vulnerable to pressure from local zealots. Yet that broad support remains powerful. However, just like in the 1920s, tapping into it requires clear-sighted leadership by professors and administrators.

Jay Hartzell, the current president of the University of Texas at Austin, repeated the 1920s defence almost verbatim, saying that the proposed legislation would “cripple Texas’s ability to recruit and retain great faculty members”.

The fact that this tack worked before is no reason to be complacent. Just like in the 1920s, today’s threats to academic freedom are severe and will require staunch activism to defeat. Yet even politicians who campaign against what can be taught in children’s schools still want universities that attract prestige and research funds. The support comes from influential big-

business organizations as well as tech leaders, university-attending families, and even state pride.

It might be tempting for scholars and university presidents to enter into point-by-point refutations of conservative charges or make technical arguments about whether lectures on history or science are actually critical race theory (or other conservative bogies).

Those attempts have never worked. Facts alone — no matter how well-grounded — have never been able to defeat determined assaults on intellectual freedom at research universities. Instead, made forcefully, broadly and fully, arguments about quality have prevailed.

Nature **604**, 219 (2022)

doi: <https://doi.org/10.1038/d41586-022-00922-w>

This article was downloaded by **calibre** from <https://www.nature.com/articles/d41586-022-00922-w>

| [Section menu](#) | [Main menu](#) |

News in Focus

- **[Funny paper titles, COVID immunity and carbon storage](#)** [13 April 2022]
News Round-Up • The latest science news, in brief.
- **[Particle's surprise mass threatens to upend the standard model](#)** [07 April 2022]
News • Data from an old experiment find that the mass of the W boson is higher than theory predicts, hinting at future breakthroughs.
- **[The countries maintaining research ties with Russia despite Ukraine](#)** [06 April 2022]
News • Many Western nations are severing scientific links — but it's a different story in China, India and South Africa.
- **[Will Russia use chemical weapons in Ukraine? Researchers evaluate the risks](#)** [05 April 2022]
News Explainer • Analysts explain why some fear that the Russian military will use chemical weapons — and how the world would know if it did.
- **[Your brain expands and shrinks over time — these charts show how](#)** [06 April 2022]
News • Based on more than 120,000 brain scans, the charts are still preliminary. But researchers hope they could one day be used as a routine clinical tool by physicians.
- **[What triggers severe COVID? Infected immune cells hold clues](#)** [06 April 2022]
News • Studies have revealed that infected immune cells prompt a massive inflammatory response.
- **[What the war in Ukraine means for energy, climate and food](#)** [05 April 2022]
News Feature • Russia's invasion has caused a short-term spike in prices, but could prompt a long-term shift towards sustainability.
- **[What's next for AlphaFold and the AI protein-folding revolution](#)** [13 April 2022]

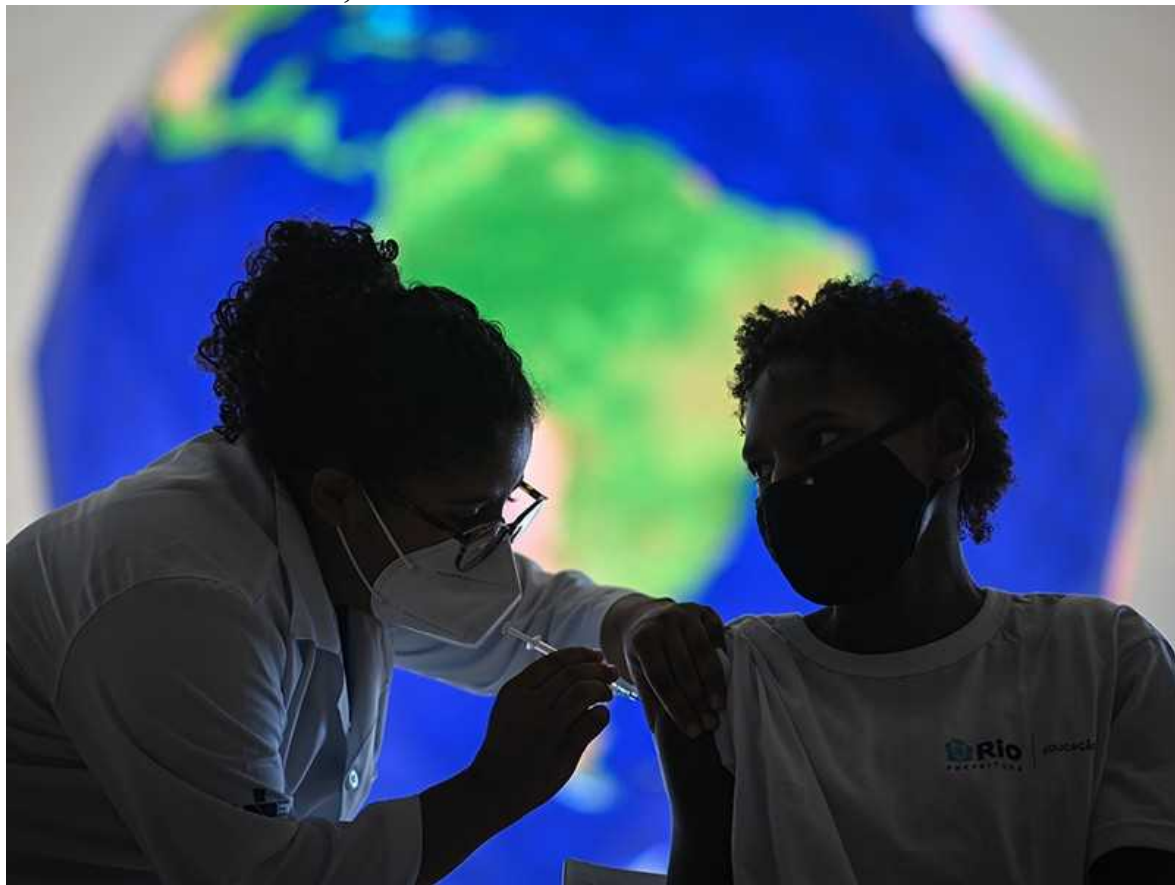
News Feature • DeepMind software that can predict the 3D shape of proteins is already changing biology.

| [Next section](#) | [Main menu](#) | [Previous section](#) |

- NEWS ROUND-UP
- 13 April 2022

Funny paper titles, COVID immunity and carbon storage

The latest science news, in brief.



A health-care worker administers a COVID-19 vaccine in Rio de Janeiro, Brazil. Credit: Andres Borges/Bloomberg/Getty

Pairing COVID with a vaccine leads to long-lasting immunity

Even people who have had COVID-19 [receive long-lasting benefits](#) from a full course of vaccination, according to three studies. The data were collected before the Omicron variant emerged, casting some doubt on their relevance today. But if the findings hold up, they could inform vaccine passports, which some countries require for entry to places such as restaurants.

One study examined data from people in Brazil who had been infected with SARS-CoV-2 before vaccination ([T. Cerqueira-Silva et al. Lancet Inf. Dis. https://doi.org/hpqm; 2022](#)). Participants who had received one dose of vaccine avoided as many as 45% of COVID-19 cases that would have been expected without vaccination. A study in Sweden also found that vaccination increased protection on top of that provided by infection ([P. Nordström et al. Lancet Inf. Dis. https://doi.org/hpqn; 2022](#)).

The third study, of UK health workers, confirmed the benefits of the ‘hybrid’ immunity conferred by infection plus vaccination ([V. Hall et al. N. Engl. J. Med. 386, 1207–1220; 2022](#)). The authors also showed that those who had been infected with the coronavirus and then received two doses of vaccine had nearly 100% protection from symptomatic COVID-19 for at least six to eight months.

Funny paper titles might lead to more citations

Including a joke in the title of a scholarly paper [could pay off in terms of citations](#), according to a study. The finding — which was posted as a preprint and has not been peer reviewed — suggests that researchers could gain citations by giving their papers funnier titles ([S. B. Heard et al. https://doi.org/hpsf; 2022](#)).

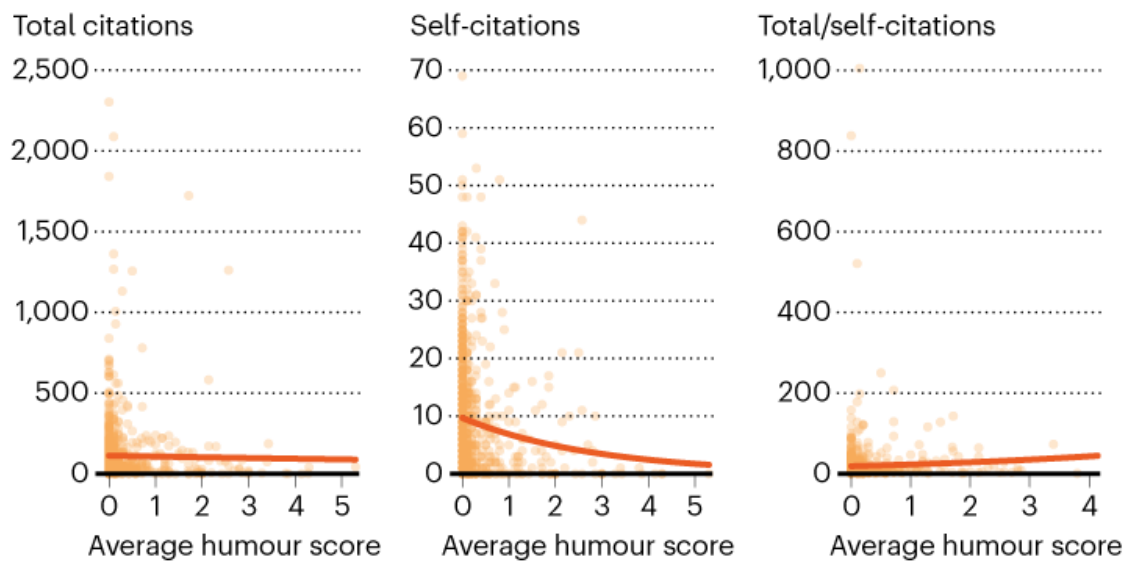
Researchers looked at 2,439 papers published in 2000 and 2001 in 9 ecology and evolution journals, scoring how humorous their titles were on a 7-point scale. They then looked for a link between papers’ humour scores and the number of citations they had received.

Papers with funny titles were cited slightly less often than their more serious counterparts. However, papers with more amusing titles also tended to have

fewer self-citations from their own authors, which led the team to speculate that scientists might give funnier titles to less important papers.

AMUSING ARTICLES

When papers' importance (indicated by self-citations) is controlled for, those with funnier titles are cited more often.



2,439 papers published during 2000 and 2001 in 9 ecology and evolution journals.

©nature

Source: S. B. Heard *et al.* Preprint at bioRxiv <https://doi.org/hpsf> (2022)

After controlling for self-citations as a measure of a paper's importance, the team found that articles with funny titles are in fact cited more than those with serious titles (see 'Amusing articles').

Some researchers question the study's conclusions, pointing out that self-citations might not be a good proxy for a paper's importance.



Tropical forests create cloud cover that reflects sunlight and cools the air.Credit: Thomas Marent/Minden Pictures

Carbon storage is just part of how forests cool the planet

Tropical forests have a crucial role in cooling Earth's surface by extracting carbon dioxide from the air. But only two-thirds of their cooling power comes from this ability, according to a study. The other one-third comes from their ability to create clouds, humidify the air and release cooling chemicals.

This is a larger contribution than expected for these 'biophysical effects' says Bronson Griscom, a forest climate scientist at the non-profit environmental organization Conservation International, headquartered in Arlington, Virginia.

The analysis (D. Lawrence *et al. Front. For. Glob. Change* <https://doi.org/hpqt>; 2022) could enable scientists to improve their climate models, while helping governments to devise better conservation and climate strategies.

A team including Deborah Lawrence, an environmental scientist at the University of Virginia in Charlottesville, compared how the effects of forests around the world feed into the climate system, breaking down their contributions in bands of ten degrees of latitude. Tropical forests, they found, can cool Earth by a whole 1 °C — and biophysical effects contribute significantly.

Nature **604**, 223 (2022)

doi: <https://doi.org/10.1038/d41586-022-00996-6>

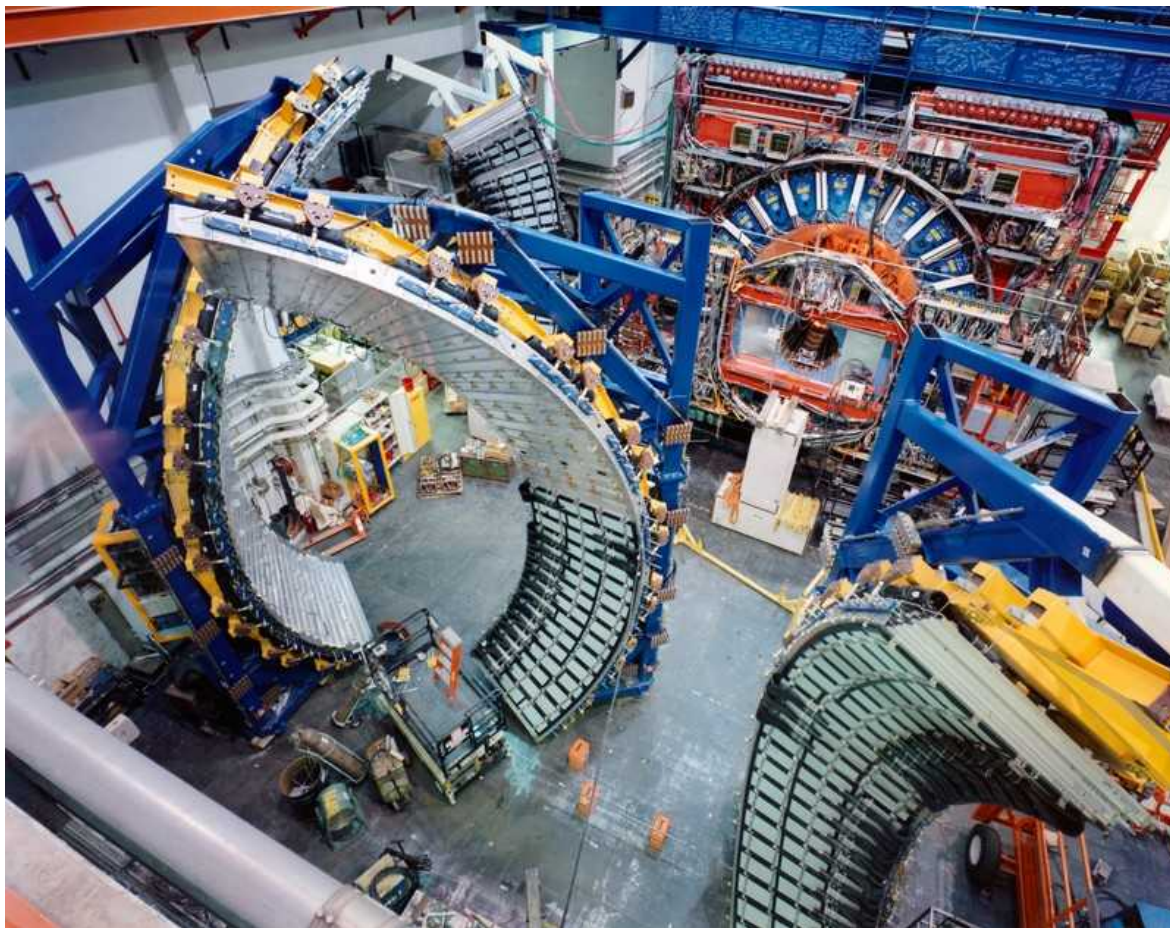
This article was downloaded by **calibre** from <https://www.nature.com/articles/d41586-022-00996-6>

- NEWS
- 07 April 2022

Particle's surprise mass threatens to upend the standard model

Data from an old experiment find that the mass of the W boson is higher than theory predicts, hinting at future breakthroughs.

- [Davide Castelvecchi &](#)
- [Elizabeth Gibney](#)



The Tevatron particle collider at Fermilab in Batavia, Illinois, was once the world's most powerful accelerator. Credit: Granger/Alamy

From its resting place outside Chicago, Illinois, a long-defunct experiment is threatening to throw the field of elementary particles off balance. Physicists have toiled for ten years to squeeze a crucial new measurement out of the experiment's old data, and the results are now in. The team has found that the W boson — a fundamental particle that carries the weak nuclear force — is significantly heavier than theory predicts.

Although the difference between the theoretical prediction and the experimental value is only 0.09%, it is significantly larger than the result's error margins, which are around 0.01%. The finding also disagrees with some other measurements of the mass. The collaboration that ran the latest experiment, called CDF at the Fermi National Accelerator Laboratory (Fermilab), reported the findings in *Science*¹ on 7 April.

The measurement “is extremely exciting and a truly monumental result in our field”, says Florencia Canelli, an experimental particle physicist at the University of Zurich in Switzerland. If it is confirmed by other experiments, it could be the first major breach in the standard model of particle physics, a theory that has been spectacularly successful since it was introduced in the 1970s. The standard model is known to be incomplete, however, and any hint of how it might fail could point the way to its replacement, and to the existence of new elementary particles. “We believe there is a strong clue in this particular measurement about what nature might have in store for us,” says Ashutosh Kotwal, an experimental particle physicist at Duke University in Durham, North Carolina, who led the CDF study.

Some physicists strike a note of caution. Generating a W boson mass measurement from experimental data is famously complex. Although the work is impressive, “I would be cautious to interpret the significant difference to the standard model as a sign of new physics,” says Matthias Schott, a physicist at the Johannes Gutenberg University of Mainz in Germany, who works on the ATLAS experiment at CERN, Europe’s particle-physics lab near Geneva, Switzerland. Physicists should prioritize working out why the value differs from the other recent results, he says.

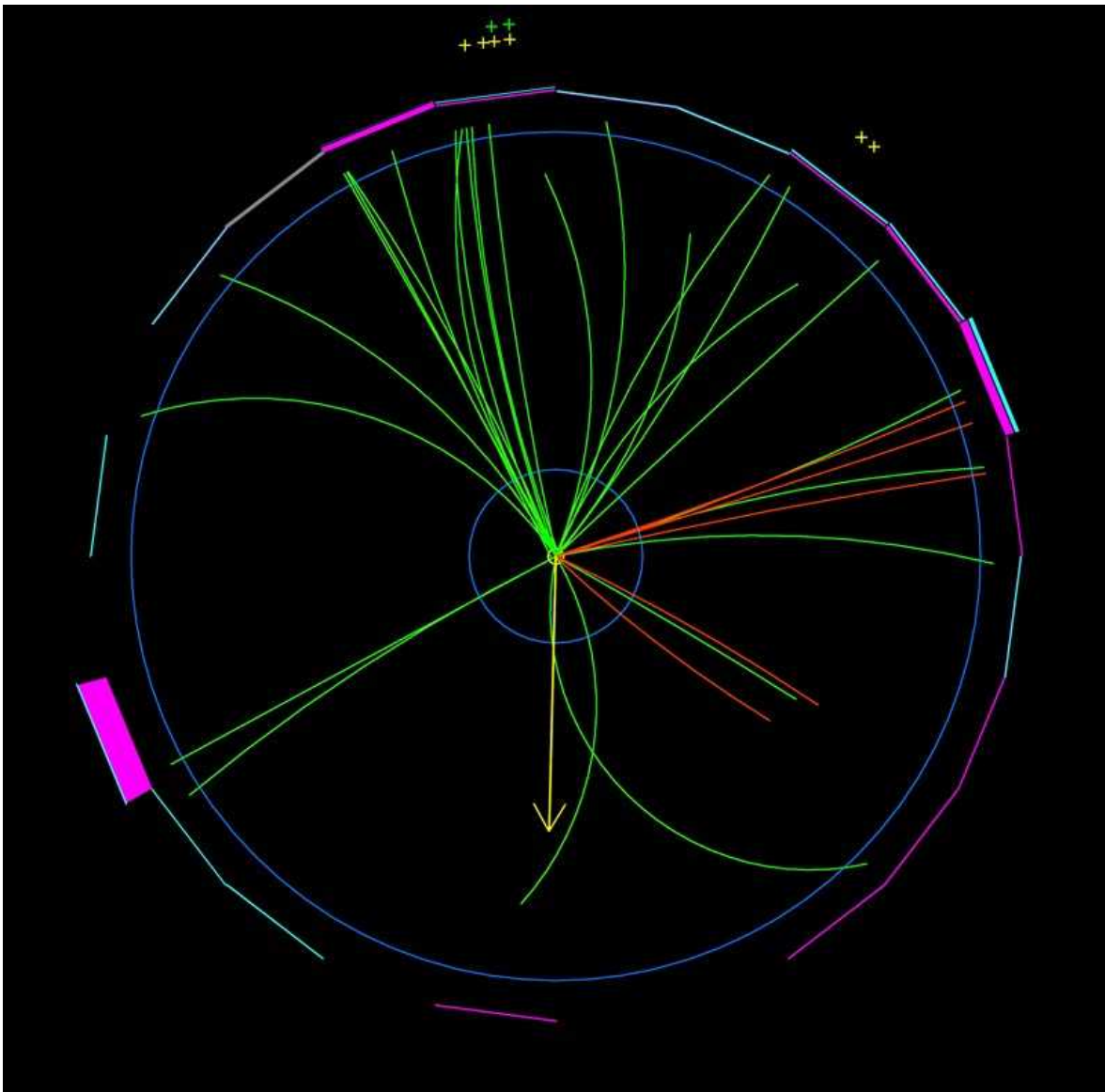
Overweight particle

Since the W boson was discovered at CERN in 1983, experiments have calculated that it weighs around the same as 85 protons. But its exact mass has been challenging to quantify: the first experimental estimate had error margins of 5% or more. “The measurement of the W boson mass is arguably the single most challenging parameter to measure in our field,” says Mika Vesterinen, a particle physicist at the University of Warwick, UK, who works on this measurement at CERN’s LHCb experiment.

With its cousin, the Z boson, the W is involved in most types of nuclear reaction, including the [fusion that powers the Sun](#). The W and Z bosons carry the weak nuclear force — one of the four fundamental forces of nature — in a similar way to how every electromagnetic interaction involves the exchange of photons.

Colliders produce W bosons by smashing particles together at high energies. Experiments typically detect the bosons when they decay into a neutrino plus either a type of electron or its heavier cousin, the muon. The neutrino escapes the detector without a trace, whereas the electron or muon leaves conspicuous tracks.

In the decay, most of the W’s original mass transforms into the energy of the new particles. If physicists could measure that energy and the path of all the decay particles, they could immediately calculate the mass of the W that produced them. But without being able to track the neutrino, they can’t say for sure which portion of the electron or muon’s energy comes from the W’s mass and which comes from its momentum. This makes the measurement “notoriously difficult”, Vesterinen says. “You try to construct the mass when you only see half of the decay.”



A computer image of a particle collision in Fermilab's CDF detector shows a W boson decaying into a positron (magenta block, lower left) and an unseen neutrino (yellow arrow). Credit: Fermilab/Science Photo Library

Old experiment, new tricks

In the latest work, Kotwal and his collaborators aimed to take the most precise measurement ever of the W's mass. The data had all been collected by 2011, when [Fermilab's Tevatron](#) — a 6-kilometre-long circular machine that collided protons with antiprotons and was once the world's most powerful accelerator — shut down. But the latest measurement would not

have been possible back then, says Kotwal. Instead, it is the result of a steady improvement of techniques in data analysis, as well as the particle-physics community's improved understanding of how protons and antiprotons behave in collisions. "Many of the techniques to achieve that kind of precision we had not even learned about by 2012."

The team looked at roughly four million W bosons produced inside the CDF detector between 2002 and 2011 — a data set four times larger than the group used in an early measurement in 2012². The researchers calculated the energy of each decay electron by measuring how its trajectory bent in a magnetic field. One painstaking advance over the past decade improved the resolution of the trajectories from roughly 150 micrometres to less than 30 micrometres, says Kotwal.

After mapping the distribution of the electrons' energies, the team calculated the boson mass that best fit the data. That was 80,433.5 megaelectronvolts (MeV), with an error margin of just 9.4 MeV.

The results join a clutch of W mass measurements produced by leading particle colliders worldwide; the precision has improved since the particle's discovery. Researchers working on CDF and DZero, the other major detector at the Tevatron, published earlier, less-precise measurements of the W mass^{2,3}. The ATLAS and LHCb experiments at CERN's Large Hadron Collider, the world's most powerful accelerator, have also published their own values^{4,5}.

The latest CDF result claims to double the precision of the previous record holder, the ATLAS measurement of 80,370 MeV with a margin of ± 19 MeV. But it disagrees with several previous measurements that were all compatible with the best theoretical prediction of 80,357 MeV. ATLAS and LHCb are updating their W boson measurement. Within a few years, they should be able to reach the precision of the CDF result, says Vesterinen, and could confirm or challenge it.

One difference between the experiments lies in how the teams model the production of the W boson, which affects calculations of its mass. LHC physicists have previously highlighted faults with the computer program used by CDF, called Resbos; an improved iteration exists. But Kotwal says

that CDF researchers picked the original technique long in advance, and it would have been wrong to change techniques to make the result converge with theory.

Harbinger of theory woes

If the mass result stands, theorists will have a field day. Theoretical physicists have produced a plethora of hypothetical extensions or reforms of the standard model, and many of those also predict a mass of the W boson different from that in the vanilla theory. “The mass of the W is the perfect place to look for new physics and deviations from the standard model,” says Sven Heinemeyer, a theoretician at the Physics Institute of Cantabria in Santander, Spain.

Heinemeyer’s favourite explanation for the discrepancy is supersymmetry, a model that predicts the existence of a heavier partner for each standard-model particle. Such particles could continually pop in and out of the vacuum surrounding a W particle, making it heftier.

Other possible explanations relate to the Higgs particle, another boson, which was discovered by the LHC in 2012. If the Higgs’s properties differ from those currently theorized — for example, if it is a composite particle rather than an elementary one, or if multiple versions of it exist — that would affect the W mass.

Another major LHC experiment, called CMS, is working on its own measurement of the W boson’s mass, says Canelli, a leading researcher in the CMS collaboration (Canelli is also a member of the CDF collaboration, but she was not involved in generating the latest result, to avoid conflicts of interest). “It is one of the most important measurements from our physics programme.”

Nature **604**, 225-226 (2022)

doi: <https://doi.org/10.1038/d41586-022-01014-5>

References

1. Aaltonen, T. *et al.* *Science* **376**, 170–176 (2022).
2. Aaltonen, T. *et al.* *Phys. Rev. Lett.* **108**, 151803 (2012).
3. Abazov, V. M. *et al.* *Phys. Rev. Lett.* **108**, 151804 (2012).
4. Aaboud, M. *et al.* *Europ. Phys. J. C* **78**, 110 (2018).
5. Aaij, R. *et al.* *J. High Energy Phys.* **2022**, 36 (2022).

This article was downloaded by **calibre** from <https://www.nature.com/articles/d41586-022-01014-5>

| [Section menu](#) | [Main menu](#) |

- NEWS
- 06 April 2022

The countries maintaining research ties with Russia despite Ukraine

Many Western nations are severing scientific links — but it's a different story in China, India and South Africa.

- [Smriti Mallapaty](#)⁰,
- [T. V. Padma](#)¹,
- [Emiliano Rodríguez Mega](#)²,
- [Richard Van Noorden](#) &
- [Ehsan Masood](#)



A research reactor at Russia's Konstantinov Institute of Nuclear Physics near St Petersburg.Credit: Peter Kovalev/ITAR-TASS/Alamy

Is Russia's invasion of Ukraine redrawing the map of international scientific cooperation? Whereas Europe and the United States are swiftly moving to cut long-standing ties, the governments of China, India and South Africa are maintaining links.

They are members of the BRICS, a group of five countries — including Brazil and Russia — that work together to promote trade and economic development, and have an active programme of scientific cooperation. Last year, researchers from the 5 nations organized some 100 meetings under the BRICS umbrella in a spectrum of fields including astronomy, climate and energy, health and medicine.

Vaccines are an important focus. India and South Africa are leading a campaign for intellectual-property relief on COVID-19 vaccines during the pandemic. Last month, all five governments announced a new partnership on vaccines research and development at a launch event on 22 March attended by science and health ministers. In a statement, Russia's health minister, Mikhail Murashko, said the initiative would build on the first COVID-19 vaccines, which were developed and tested in BRICS countries. Russia approved its first coronavirus vaccine in August 2020.

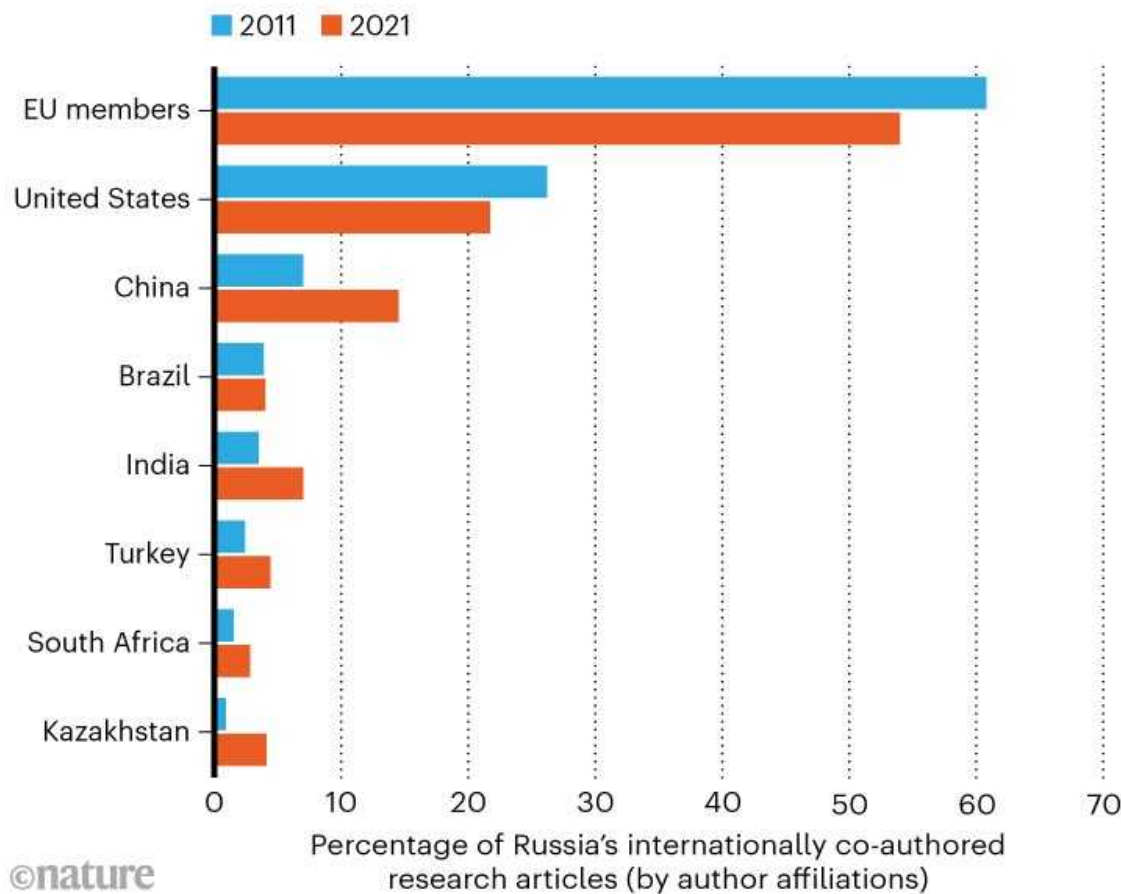
And on 26–27 April, the five countries' national science academies will host a meeting aimed at sharing data on biodiversity, climate and food security as a means to achieving the United Nations Sustainable Development Goals.

Brazil's research leaders have openly said they are against the invasion. They have also set up a fund for scientists fleeing Ukraine, Russia and other conflict zones to come to Brazil. There is also opposition from researchers in South Africa, but it's harder to determine what scientists in China and India think. Of those approached, none agreed to comment for this article. Some researchers in India and South Africa have published open letters condemning the invasion. South Africa's government is advising research institutions — although not scientists — not to speak on what it calls the war's "political aspects".

China, India and South Africa are not alone in keeping ties to Russia. Comstech, an Islamabad-based organization representing science ministers from countries that are part of the 57-member Organisation of Islamic Cooperation (OIC), is discussing a long-term science-cooperation agreement with Russia, which is an observer state to the OIC.

TREND IN RUSSIA'S SCIENCE COLLABORATIONS

Brazil, India and China's shares of papers co-authored with researchers from Russia have increased (as a fraction of Russia's internationally collaborative papers).



Source: Scopus.

China's East–West balancing act

The Chinese government says it maintains a “neutral stance” on Russia’s invasion of Ukraine. Universities, research organizations and funding

agencies are not making public statements, but there are no signs that collaborations will be affected.

The past decade has seen a steady increase in research publications with authors from the two countries (see ‘Trend in Russia’s science collaborations’), although this is in line with China’s research growth with many more countries. Physical sciences stand out as popular fields for researchers from China and Russia — especially physics and astronomy, as well as materials science and engineering.

China and Russia designated 2020–21 a year of scientific and technological innovation, with plans for collaborations in nuclear energy, COVID-19 studies and mathematics, among other areas. Alexander Sergeev, president of the Russian Academy of Sciences in Moscow, is also one of the vice-presidents of the Alliance of International Science Organizations (ANSO), a 67-member network of research organizations around the world established by China in 2018.

“Economic sanctions on Russia will have little or no impact on ANSO’s activities,” predicts Qasim Jan, a geologist at Peshawar University in Pakistan and a former ANSO vice-president. That’s because, he says, “China provides most of ANSO’s funding”. Five institutions are involved in an ANSO project to study green economic opportunities involving China, Mongolia and Russia.

Space policy could be ripe for more cooperation, researchers are predicting, if Russia splits permanently from US- and European-led international space collaborations. In 2021, Russia and China’s space agencies agreed to work together to build a base on the Moon. This could now be “accelerated and potentially expanded”, says Malcolm Davis, who studies space policy at the Australian Strategic Policy Institute in Canberra.

And because selected Russian banks are now barred from the international financial-transactions platform SWIFT, payments between Russia and China are likely to use the countries’ respective currencies. Murad Ali, head of political science at the University of Malakand in Chakdara, Pakistan, who studies China’s international finance, says more than 20 countries have similar currency-swap arrangements with China.

In 2015, China also launched an alternative to SWIFT called the Cross-Border Interbank Payment System (CIPS). Before the invasion of Ukraine, the system was used for around US\$49 billion in daily transactions, says Łukasz Kobierski, who studies international relations at the Institute of New Europe, a think tank in Warsaw. This compares with \$5 trillion that goes through SWIFT daily, according to the US treasury. However, ongoing sanctions on Russia could see CIPS usage increase.

Some China–Russia science ties date from at least the 1950s, explains Isak Froumin, a higher-education researcher at the Higher School of Economics in Moscow, currently on sabbatical in Boston, Massachusetts. This is when newly communist China adopted the Soviet Union’s model of concentrating research in state-funded and state-directed academies of sciences. Relations between the two have been through turbulent times and China began to look west for scientific cooperation after the fall of the Soviet Union, Froumin adds.

Some observers are cautioning that China will not want to jeopardize its many existing scientific partnerships with Europe and the United States. China’s scientific community does not want to be isolated from the West, says Futaoh Huang, a higher-education researcher at Hiroshima University in Japan.



Vladimir Putin, Narendra Modi and Xi Jinping at the 2019 G20 summit in Osaka, Japan. Credit: Mikhail Svetlov/Getty

Modi–Putin science plan

Over the past few decades, India has had less scientific cooperation with Russia than with Europe and the United States. But in December 2021, Indian Prime Minister Narendra Modi and Russian President Vladimir Putin agreed to strengthen scientific links between the two countries.

The leaders agreed on a lengthy list of topics on which they want to see more cooperation. These include: agriculture and food science and technology, the ocean economy, climate, data science, energy, health and medicine, polar research, quantum technologies and water.

This would be in addition to existing ties in nuclear energy and space. Russia has supplied India with nuclear reactors and fuel, and the countries' space cooperation dates from the 1970s. In 1984, Rakesh Sharma, an Indian

air-force pilot, joined the Soviet Union's Soyuz T-11 expedition, becoming the first person from India to travel to space.

The new Modi–Putin science plan will not be affected by the invasion of Ukraine, says Jagannath Panda, head of the Stockholm Centre for South Asian and Indo-Pacific Affairs in Sweden. “New Delhi has a vested interest in ensuring such cooperation with the long-standing partner [Russia] continues despite disruptions.”

The last time the two countries scaled up their joint projects was 1987–90, when they established eight collaborative centres, including some in materials science, advanced computing and ayurvedic medicine.

India's largest research partners (as measured by joint publications) are in Europe and the United States. Researchers with knowledge of how the Indian government organizes science told *Nature* that they do not anticipate these research relationships changing.

However, D. Raghunandan, president of the Delhi Science Forum, a non-profit science-policy organization, predicts that international sanctions will eventually have a more serious impact on India's research collaborations across the board. Trade sanctions against Russia, he says, mean researchers in India and Russia might be unable to transfer research material between the countries. Moreover, banking sanctions are likely to prevent funds being transferred using international banks.

To get around this, India and Russia are reported to be discussing trading with each other using the rupee and the rouble instead of US dollars. However, Raghunandan warns there's a risk that sanctions might extend to a ban on technologies that can be used for both military and civilian purposes.

“Monetary sanctions can be taken care of,” Raghunandan says, but he predicts trouble for India's scientists if Europe and the United States decide to extend sanctions to apply to countries that have relations with Russia. “International collaborations in science will depend on how far the US and Europe are willing to take the sanctions. We do not know how the future will unfold.”

Brazil warns of ‘serious consequences’ for collaborations

Unlike China and India, Brazil is expected to experience serious consequences for its joint projects as a result of international economic sanctions against Russia, some of Brazil’s researchers have told *Nature*. At the same time, scientists and funding agencies are organizing to support colleagues who need to flee either Ukraine or Russia.

Before the invasion, Ricardo Galvão, a fusion-energy physicist at the University of São Paulo, was expecting to start a collaboration with two of Russia’s largest physics institutes, the Ioffe Institute in St Petersburg and the Kurchatov Institute in Moscow. The project aimed to measure energy and rotation in the plasma inside tokamaks — doughnut-shaped fusion reactors with powerful magnets.

“Those plans were also destroyed by the missiles of this war,” Galvão says. At the very least, there will be delays and increased costs, he adds. In the first weeks after the war started on 24 February, the rouble lost 20% of its value against the Brazilian real.

Brazil’s research leaders are “obviously against war”, says Jerson Silva, a biochemist at the Federal University of Rio de Janeiro and director of the state’s science funding agency, FAPERJ. FAPERJ has launched a funding call for researchers in Rio de Janeiro who wish to host scientists fleeing Ukraine, Russia and other conflict zones.

The US\$2-million programme, which started on 24 March, will provide aeroplane tickets to Rio, travel insurance and a monthly stipend of 9,000 reais (around US\$1,900) for up to a year. Some of Brazil’s 25 other science funding agencies, including FAPESP in São Paulo, are launching similar calls.

The goal, says biochemist Vânia Paschoalin, FAPERJ’s coordinator of international relations, is to allow Ukrainian and Russian researchers to continue their work. “The conflict ends,” she says. “Science doesn’t. Science is always alive.”

Some also disagree with the pressure to cut scientific links with Russia. Paulo Artaxo, an atmospheric physicist at the University of São Paulo, says: “You cannot exclude Israeli, South African or Russian scientists, because they are not responsible for [their] government’s actions.”

Brazilian Physics Society president Débora Peres Menezes also opposes a boycott. Peres Menezes, a nuclear physicist at the Federal University of Santa Catarina in Florianópolis, says physics is a collaborative science and some of her students have benefited from visiting research institutions in Russia. “Scientists should not individually pay the price of war.”

Nature **604**, 227-228 (2022)

doi: <https://doi.org/10.1038/d41586-022-00945-3>

This article was downloaded by **calibre** from <https://www.nature.com/articles/d41586-022-00945-3>

| [Section menu](#) | [Main menu](#) |

- NEWS EXPLAINER
- 05 April 2022

Will Russia use chemical weapons in Ukraine? Researchers evaluate the risks

Analysts explain why some fear that the Russian military will use chemical weapons — and how the world would know if it did.

- [Davide Castelvecchi](#)



Ukrainians walk past a building in Mariupol that was destroyed during the Russian military's invasion of their country.Credit: Alexander

Ermochenko/Reuters

As Russia's invasion of Ukraine nears its 7th week, Western governments and independent observers continue to warn that Russia's military could escalate from [indiscriminately bombing cities](#) to using non-conventional warfare, in particular chemical weapons.

The Kremlin has denied any intention to use chemical weapons. But the Russian government has been linked over the past two decades with this type of attack. And concern over President Vladimir Putin's intentions spiked on 28 March, [when The Wall Street Journal reported](#) that envoys and mediators in Russia–Ukraine peace talks earlier in the month had been poisoned — although at least one Ukrainian government source [has reportedly denied the story](#).

Nature spoke to several analysts to explore the chances of chemical weapons being deployed in the war.

Why do Western leaders think Russia might use chemical weapons in Ukraine?

Even though the world has outlawed the use of chemical weapons, the Russian government has been linked to them on several occasions, some recent.

In 2018, [the UK government accused Russia](#) of using a Novichok chemical — a nerve agent developed by the Soviet Union decades ago — to poison Sergei Skripal, a Russian former double agent living in the United Kingdom. In another high-profile incident, [Russian opposition leader Alexei Navalny was poisoned](#) with a different type of Novichok agent in 2020. The Kremlin denied involvement in either event.



In 2018, UK military personnel intensely investigated the poisoning of former spy Sergei Skripal with a nerve agent. The UK government accused the Kremlin of being involved. Credit: Chris J Ratcliffe/Getty

“These two incidents raise question marks on whether elements of the former Soviet programme have not been eliminated,” says Ralf Trapp, a disarmament consultant based in Chessenaz, France.

Furthermore, Russian troops have fought alongside the regular Syrian army during that country’s civil war, which began in 2011. The Organisation for the Prohibition of Chemical Weapons (OPCW), based in The Hague, the Netherlands, confirmed that [the Syrian army deployed chemical weapons](#) against its own people. The Russian government denied involvement in any of these attacks.

When it comes to Ukraine, the Russian government has accused the country of preparing to use chemical weapons. But Western governments say this could be a ‘false flag’ tactic, which the Kremlin has used in the past. “Russia has a long track record of accusing others of what they are either already

doing or about to do,” said US President Joe Biden on 22 March, [according to news outlet CNBC](#).

Trapp, who is a former OPCW officer and was involved in verifying adherence to the 1997 Chemical Weapons Convention (CWC) in several countries, including Ukraine, says there is no evidence that Ukraine has chemical weapons. “It doesn’t make any sense for the Ukrainians to think of using them,” he adds.

Russia and Ukraine are signatories to the CWC, which outlaws the use of chemicals in warfare. This includes substances with legitimate applications such as chlorine, which is used, for instance, to sanitize water. The OPCW, which monitors compliance to the treaty, [verified in 2017](#) that Russia had destroyed all its declared stockpiles of chemical weapons.

If Russia or any other signatory uses chemical weapons, it’s a breach of the convention, says Leiv Sydnes, a chemist at the University of Bergen in Norway, who has chaired a task group for the OPCW and helped to draft previous reviews of the treaty.

The [Russian Foreign Ministry has called accusations](#) that the country’s military plans to use chemical weapons in Ukraine a “smear campaign” by Western nations.

Why would Russia use chemical weapons in Ukraine?

Analysts say that chemical weapons have limited usefulness in the battleground, especially against armies, such as Ukraine’s, that are equipped with protective gear. “If you are using them against a military target, it is relatively straightforward for the defenders to have CBW [chemical- and biological-weapon] protection kits,” says Paul Rogers, a peace-studies researcher at the University of Bradford, UK.

Instead, chemical weapons are primarily a tool for terrorizing populations and breaking their will to resist, Rogers and other researchers say. “The main

purpose to use chemical weapons is to terrify people and to generate panic,” Sydnes says.

Observers fear that the Russian military could launch chemical attacks on Ukrainian cities to cause panic amongst civilians. Chlorine gas, in particular, is denser than air and could settle into the underground shelters used by the populations of cities during bombardments, causing people to suffocate.

The Russian military could also use nerve agents such as sarin, which is extremely deadly but dissipates quickly, enabling the attacking army to subsequently occupy the targeted site. Chemicals such as Novichok agents, though, would be less practical for Russian troops because these substances are persistent and would require extensive decontamination before the army could occupy the site.

Recent developments on the ground, with the Russian military seemingly refocusing its efforts on eastern regions of Ukraine, could make a chemical attack less likely, Rogers says. “I think the risk is less than two or three weeks ago.”

Is there any way to prevent the use of chemical weapons in Ukraine?

If the Kremlin is serious about its accusation that Ukraine is preparing to use chemical weapons, it could pursue its allegations through the proper channels. “They can demand from the OPCW what is called a challenge inspection,” Sydnes says. “If this is a real issue for Putin, and he doesn’t want to use chemical weapons, that is what he should do.”

But if the Russian government is claiming that Ukraine has chemical weapons as a pretext to use such weapons itself, then any country — even Ukraine — could trigger OPCW inspections of Ukraine to challenge the assertion. “The Ukrainians could say, ‘Come and have a look, we have nothing to hide’,” says Alastair Hay, an environmental toxicologist at the University of Leeds, UK. “That would clearly wrong-foot the Russians.”

In either scenario, international inspectors would need guarantees for their safety, such as a ceasefire in the areas they are visiting.

The OPCW told *Nature* that it has not received any requests for a challenge inspection.

Can science help to verify a suspected attack?

The OPCW would be called on to verify any allegations of a chemical weapons attack. Even without direct access to the war zone, the organization can gather evidence, in particular from satellite imagery and medical reports, Trapp says. “If there are victims, you will see victims being treated in medical facilities.” And their symptoms and medical records would give clues.

Chemical weapons vary greatly in how they work and the types of evidence they leave behind. If inspectors have direct access in the immediate aftermath of an attack, they could collect samples — such as the by-products that nerve agents leave in the blood, or trace residues in the environment. In some situations, evidence collection could be more difficult; for instance, a chlorine attack might be hard to prove, because the gas can dissipate without leaving any trace.

There is precedent for this type of inspection, Trapp says: during the Syrian civil war, OPCW inspectors collected evidence in a war zone for the first time and reported that both chlorine and nerve agents had been used — something the Syrian government has denied. The inspectors did so at considerable risk, and came under fire [in at least one incident](#).

More recently, the organization has tested methods for remotely gathering evidence from the site of a chemical attack. Researchers are exploring the use of a land or aerial drone to collect samples or even analyse them on site.

Nature **604**, 228-229 (2022)

doi: <https://doi.org/10.1038/d41586-022-00948-0>

This article was downloaded by **calibre** from <https://www.nature.com/articles/d41586-022-00948-0>

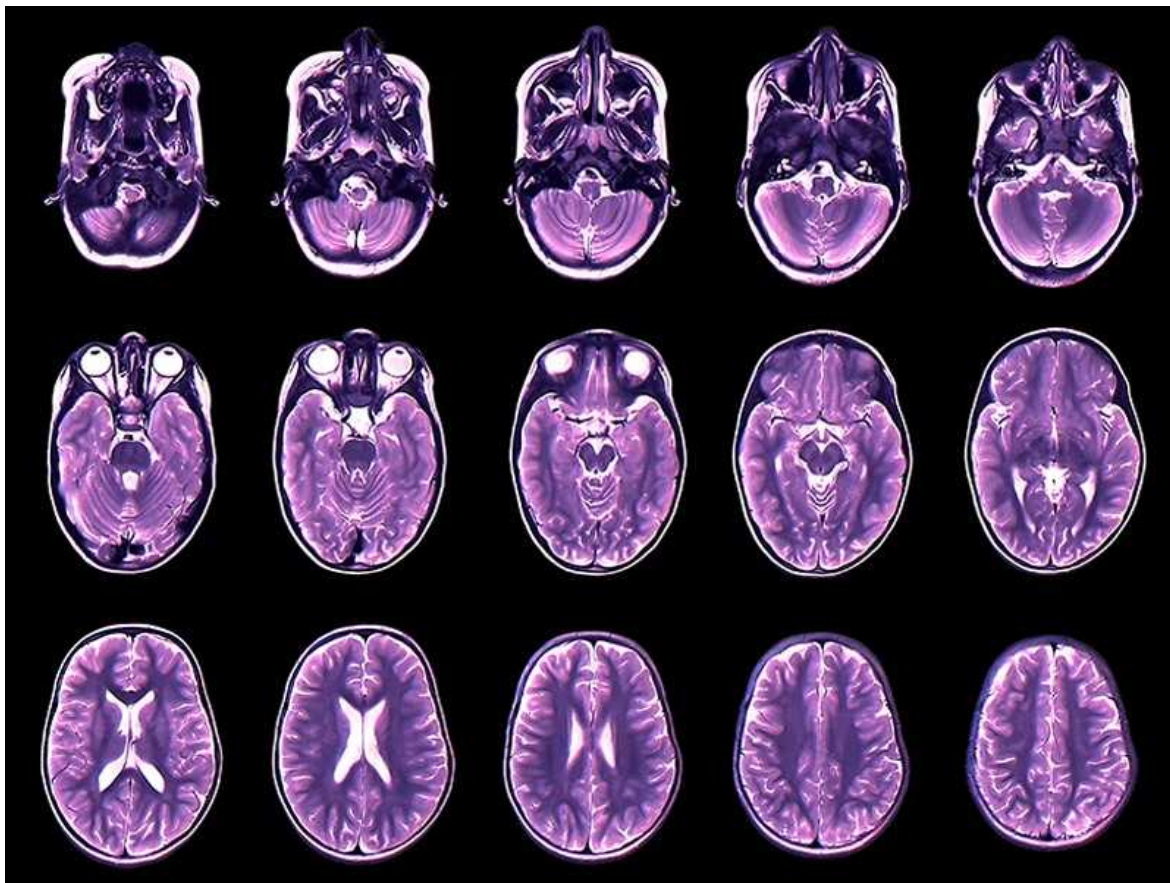
| [Section menu](#) | [Main menu](#) |

- NEWS
- 06 April 2022

Your brain expands and shrinks over time — these charts show how

Based on more than 120,000 brain scans, the charts are still preliminary. But researchers hope they could one day be used as a routine clinical tool by physicians.

- [Max Kozlov](#)



Researchers have created brain growth charts that cover the human lifespan by aggregating more than 120,000 scans.Credit: Zephyr/SPL

When neuroscientist Jakob Seidlitz took his 15-month-old son to the paediatrician for a check-up last week, he left feeling unsatisfied. There wasn't anything wrong with his son — the youngster seemed to be developing at a typical pace, according to the height and weight charts the physician used. What Seidlitz felt was missing was an equivalent metric to gauge how his son's brain was growing. "It is shocking how little biological information doctors have about this critical organ," says Seidlitz, who is based at the University of Pennsylvania in Philadelphia.

Soon, he might be able to change that. Working with colleagues, Seidlitz has amassed more than 120,000 brain scans — the largest collection of its kind — to create the first comprehensive growth charts for brain development. The charts show visually how human brains expand quickly early in life and then shrink slowly with age. The sheer magnitude of the study, published in *Nature* on 6 April¹, has stunned neuroscientists, who have [long had to contend with reproducibility issues](#) in their research, in part because of small sample sizes. Magnetic resonance imaging (MRI) is expensive, meaning that scientists are often limited in the number of participants they can enrol in experiments.

"The massive data set they assembled is extremely impressive and really sets a new standard for the field," says Angela Laird, a cognitive neuroscientist at Florida International University in Miami.

Even so, the authors caution that their database isn't completely inclusive — they struggled to gather brain scans from all regions of the globe. The resulting charts, they say, are therefore just a first draft, and further tweaks would be needed to deploy them in clinical settings.

If the charts are eventually rolled out to paediatricians, great care will be needed to ensure that they are not misinterpreted, says Hannah Tully, a paediatric neurologist at the University of Washington in Seattle. "A big brain is not necessarily a well-functioning brain," she says.

No easy task

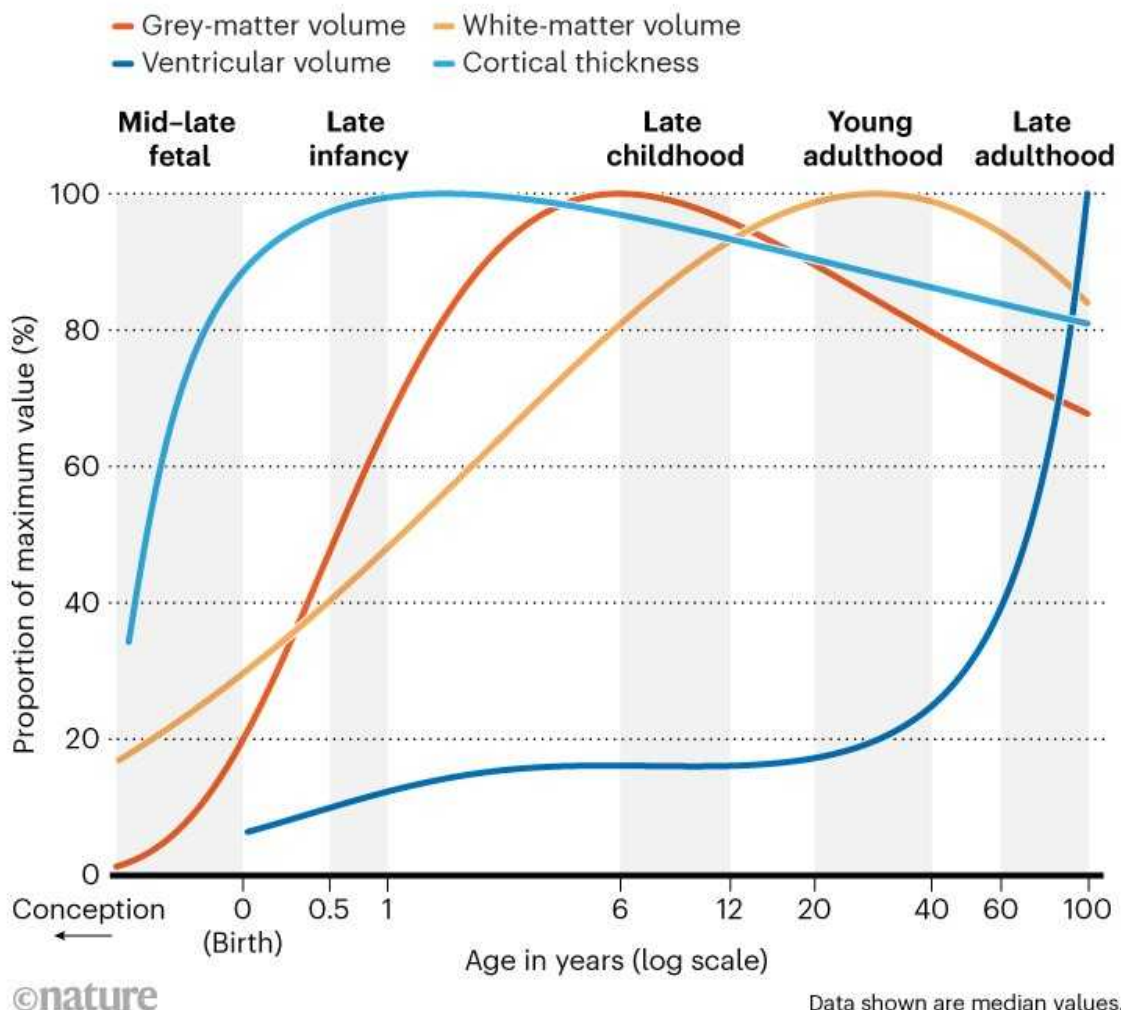
Because brain structure varies significantly from person to person, the researchers had to aggregate a huge number of scans to create an authoritative set of growth charts with statistical significance. That's no easy task, says Richard Bethlehem, a neuroscientist at the University of Cambridge, UK, and a co-author of the study. Instead of running thousands of scans themselves, which would take decades and be prohibitively costly, the researchers turned to already-completed neuroimaging studies.

Bethlehem and Seidlitz sent e-mails to researchers all over the world asking if they would share their neuroimaging data for the project. The duo was amazed by the number of replies, which they attribute to the COVID-19 pandemic giving researchers less time in their laboratories and more time than usual with their e-mail inboxes.

In total, the team aggregated 123,894 MRI scans from 101,457 people, who ran the gamut from fetuses 16 weeks after conception to 100-year-old adults. The scans included brains from neurotypical people, as well as people with a variety of medical conditions, such as Alzheimer's disease, and neurocognitive differences, including autism spectrum disorder. The researchers used statistical models to extract information from the images, and ensure that the scans were directly comparable, no matter what type of MRI machine had been used.

BRAIN CHANGE

Researchers analysed more than 120,000 brain scans to assemble the most comprehensive growth chart of the brain so far. White- and grey-matter volume and mean cortical thickness (the width of the grey matter) increase rapidly early in development, whereas ventricular volume (the amount of cerebrospinal fluid in the brain) increases rapidly later in life.



Source: Ref. 1

The end result is a set of charts plotting several key brain metrics by age. Some metrics, such as grey-matter volume and mean cortical thickness (the width of the grey matter) peak early in a person's development, whereas the volume of white matter (found deeper in the brain) tends to peak by around age 30 (see 'Brain change'). The data on ventricular volume (the amount of cerebrospinal fluid in the brain), in particular, surprised Bethlehem.

Scientists knew that this volume increases with age, because it is typically associated with brain atrophy, but Bethlehem was shocked by how rapidly it tends to grow in late adulthood.

A first draft

The study comes on the heels of a bombshell paper published in *Nature* on 16 March² showing that most brain-imaging experiments [contain too few scans](#) to reliably detect links between brain function and behaviour, meaning that their conclusions might be incorrect. Given this finding, Laird expects the field to move towards adopting a framework similar to the one used by Seidlitz and Bethlehem, to increase statistical power.

To amass so many data sets is akin to a “diplomatic masterpiece”, says Nico Dosenbach, a neuroscientist at Washington University in St. Louis, Missouri, who co-authored the 16 March study. He says this is the scale on which researchers should operate when aggregating brain images.

Despite the size of the data set, Seidlitz, Bethlehem and their colleagues acknowledge that their study suffers from a problem endemic to neuroimaging studies — a remarkable lack of diversity. The brain scans they collected come mainly from North America and Europe, and disproportionately reflect populations that are white, university-aged, urban and affluent. This limits the generalizability of the findings, says Sarah-Jayne Blakemore, a cognitive neuroscientist at the University of Cambridge. The study includes only three data sets from South America and one from Africa — accounting for around 1% of all the brain scans used in the study.

Billions of people worldwide lack access to MRI machines, making diverse brain-imaging data difficult to come by, Laird says. But the authors haven’t stopped trying. They have launched [a website where they intend to update their growth charts](#) in real time as they receive more brain scans.

With big data sets, big responsibility

Another challenge was determining how to give proper credit to the owners of the brain scans used to construct the charts. Some of the scans came from

open-access data sets, but others were closed to researchers. Most of the closed-data scans hadn't yet been processed in a way that would allow them to be incorporated into the growth charts, so their owners did extra work to share them. These scientists were then named as authors of the paper.

Meanwhile, the owners of the open data sets received only a citation in the paper — which doesn't hold as much prestige for researchers seeking funding, collaborations and promotions. Seidlitz, Bethlehem and their colleagues processed these data. In most cases, Bethlehem says that there was essentially no direct contact with the owners of these data sets. The paper lists about 200 authors and cites the work of hundreds of others who contributed brain scans.

There are a number of reasons that data sets might be closed: for instance, to protect the privacy of health data, or because researchers don't have the resources to make them public. But this doesn't make it fair that the researchers who opened their data sets didn't get authorship, the authors say. In their paper's Supplementary Information, they argue that the situation "perversely disincentivises open science, since the people who do most to make their data openly available could be least likely to merit recognition". Bethlehem and Seidlitz contend that authorship guidelines from journals, including *Nature* — which say that each author is expected to have made "substantial contributions" to, for example, the analysis or interpretation of data — are an obstacle. (*Nature*'s news team is editorially independent of its publisher.)

A *Nature* spokesperson responds that the issue was "considered carefully by the editors and authors according to our authorship policies" and that "all datasets were appropriately credited per our data citation policy".

Ultimately, these concerns can be traced back to how researchers are evaluated by the scientific enterprise, says Kaja LeWinn, a social epidemiologist at the University of California, San Francisco, who studies neurodevelopment. She says that it's incumbent on all of the relevant stakeholders — including funders, journals and research institutions — to re-evaluate how brain science can be properly recognized and rewarded, especially as these types of large-scale study become more common.

Nature **604**, 230-231 (2022)

doi: <https://doi.org/10.1038/d41586-022-00971-1>

References

1. Bethlehem, R. A. I. *et al.* *Nature* <https://doi.org/10.1038/s41586-022-04554-y> (2022).
2. Marek, S. *et al.* *Nature* **603**, 654–660 (2022).

This article was downloaded by **calibre** from <https://www.nature.com/articles/d41586-022-00971-1>

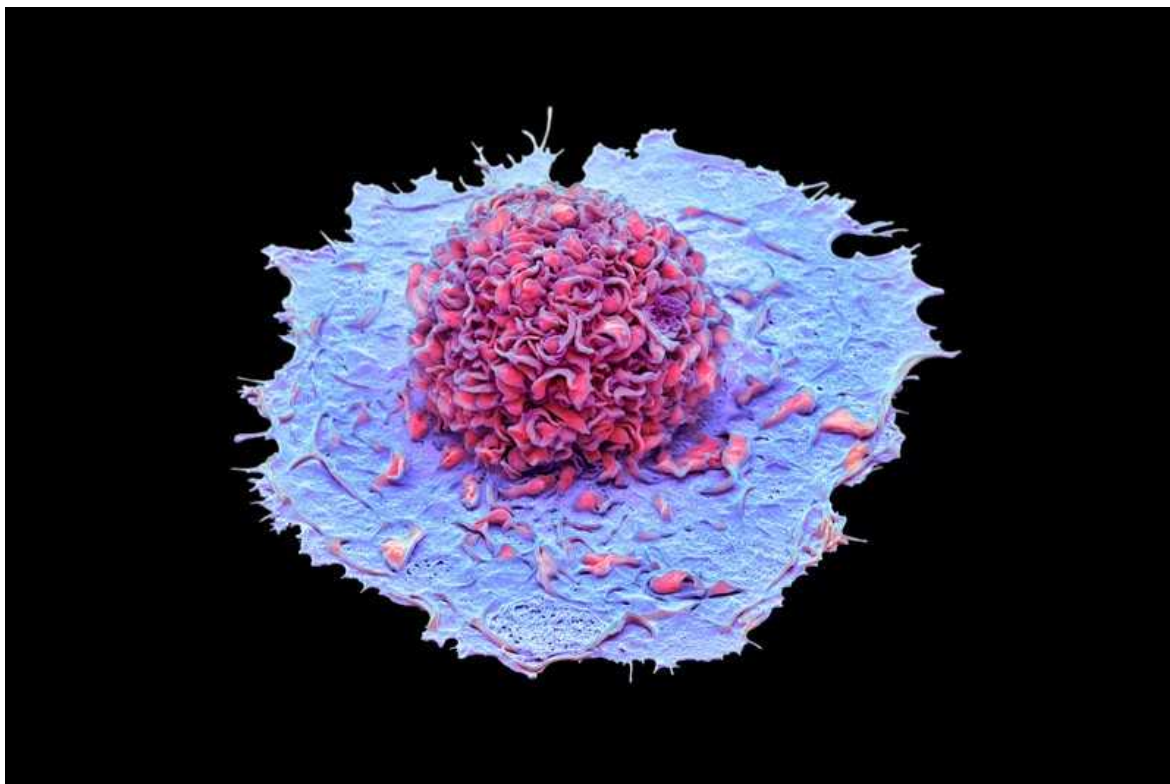
| [Section menu](#) | [Main menu](#) |

- NEWS
- 06 April 2022

What triggers severe COVID? Infected immune cells hold clues

Studies have revealed that infected immune cells prompt a massive inflammatory response.

- [Smriti Mallapaty](#)



SARS-CoV-2 can enter immune cells, macrophages (pictured), in the lungs, triggering a massive inflammatory response. Credit: Steve Gschmeissner/Science Photo Library

Immune cells infected with SARS-CoV-2 can trigger a massive inflammatory response that contributes to severe COVID-19, suggest two papers — one published today in *Nature*, and a preprint posted online on 1 April.

Since the early days of the pandemic, research has suggested that inflammation leads to significant respiratory distress and other organ damage, hallmarks of severe COVID-19. But scientists have struggled to pinpoint what triggers the inflammation.

The latest studies implicate two types of white blood cells — macrophages in the lungs, and monocytes in the blood — which, once infected with the virus, trigger the inflammation. The studies also provide conclusive evidence that the virus can infect and replicate in immune cells — and reveal how it enters those cells. Evidence of such infections has been mixed until now.

The studies offer a plausible explanation for how severe COVID-19 progresses, says Malik Peiris, a virologist at the University of Hong Kong. “I don’t think it is the only or most important pathway, but it is certainly interesting.”

Still, infected immune cells could offer a potential target for drug development, says Jian Zheng, an immunologist at the University of Iowa in Iowa City.

Overactive response

In the *Nature* paper¹, Judy Lieberman, an immunologist at the Boston Children’s Hospital in Massachusetts, and her colleagues looked at blood samples from people with COVID-19. They found that about 6% of monocytes — ‘early responder’ immune cells that patrol the body for foreign invaders — were undergoing a type of cell death associated with inflammation, known as pyroptosis. To see that many cells dying is unusual, she says, because the body typically gets rid of dead cells quickly.

When the researchers looked at the dying cells, they found they were infected with SARS-CoV-2. They suggest the virus was probably activating inflammasomes, large molecules that trigger a cascade of inflammatory responses that ended in cell death.

The researchers also looked at another type of immune cell, macrophages, in the lungs of people who had died of COVID-19. Because macrophages collect cellular garbage, including viral debris, it has been difficult to show whether macrophages were infected with SARS-CoV-2 or just sopping up this debris. The team found that about a quarter of macrophages had activated inflammasomes, and a fraction of those had indeed been infected with the virus. Other infected lung cells, epithelium, did not display the same response.

The results align with those of the second study, posted on bioRxiv² and yet to be peer reviewed, by Esen Sefik, an immunologist at the Yale University School of Medicine, New Haven, and her colleagues. They also found that the virus could infect and replicate in macrophages in human lung cells and in a mouse model of the human immune system. The macrophages displayed the same inflammatory response described by Lieberman, and eventually died.

The team also found that giving the mice drugs that blocked inflammasomes prevented severe respiratory distress. The drugs “rescued the mice so they were not as sick”, says Sefik. This suggests that infected macrophages have a role in the pneumonia observed in people with severe COVID-19.

The macrophages’ inflammatory response could be their way of stopping SARS-CoV-2 from replicating, says study co-author Richard Flavell, an immunologist, also at Yale, and the Howard Hughes Medical Institute. When inflammasomes were activated, the virus stopped replicating in the cells. But when the researchers blocked inflammasomes, the macrophages started producing infectious virus particles.

That is a “startling” finding, says Peiris, because it shows that macrophages can assist infection.

But Stanley Perlman, a virologist also at the University of Iowa, says follow-up studies will be needed to work out how important infected immune cells are in inducing severe COVID-19 compared with other possible mechanisms.

Viral entry

Both teams were also able to show how SARS-CoV-2 can enter immune cells. Researchers have been puzzled over this because the cells don't carry many ACE2 receptors, the virus's main entry point.

In experiments with human and mouse cells, Sefik and Flavell found that SARS-CoV-2 could get into lung macrophages through the limited number of ACE2 receptors present. But the virus was also sneaking in through another surface protein, known as the Fc γ receptor, with the help of antibodies. When the virus encountered antibodies attached to the Fc γ receptor, instead of the virus being disabled, it got scooped up into the cell.

Lieberman says this is also how the virus enters monocytes, which do not have ACE2 receptors. Only monocytes with the Fc γ receptor could be infected.

But Lieberman says that not all antibodies facilitate viral entry. The team found that antibodies produced by people who received the mRNA vaccine developed by Pfizer and BioNTech did not allow monocytes to take up the virus.

That finding is reassuring, given that many people have been vaccinated with mRNA vaccines, says Peiris. But more studies are needed to understand which types of antibodies are facilitating viral uptake by monocytes, and whether vaccines that use other technologies might induce a different response.

Nature **604**, 231 (2022)

doi: <https://doi.org/10.1038/d41586-022-00965-z>

References

1. Junqueira, C. *et al.* *Nature* <https://doi.org/10.1038/s41586-022-04702-4> (2022).
2. Sefik, E. *et al.* Preprint at bioRxiv
<https://doi.org/10.1101/2021.09.27.461948> (2022).

This article was downloaded by **calibre** from <https://www.nature.com/articles/d41586-022-00965-z>

| [Section menu](#) | [Main menu](#) |

- NEWS FEATURE
- 05 April 2022

What the war in Ukraine means for energy, climate and food

Russia's invasion has caused a short-term spike in prices, but could prompt a long-term shift towards sustainability.

- [Jeff Tollefson](#)



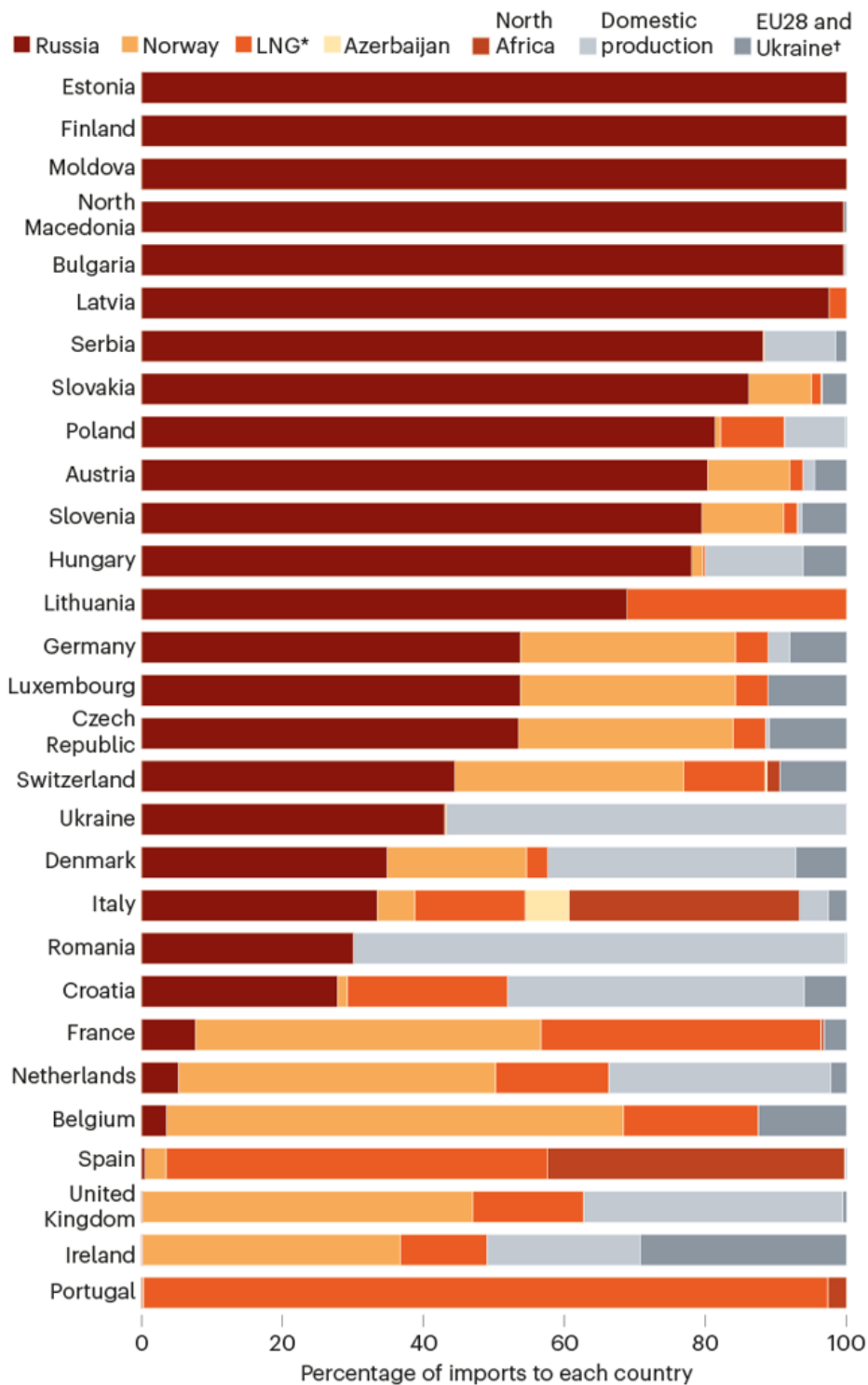
The Russian end of the Nord Stream 2 gas pipeline to Europe. Germany halted its approval of the pipeline after Russia's invasion of Ukraine. Credit: Andrey Rudakov/Bloomberg via Getty

On 22 February, Germany scuttled its approval of a newly built gas pipeline from Russia, and is now planning to import liquefied natural gas from countries such as Qatar and the United States. Belgium is reconsidering its exit from nuclear power, while Italy, the Netherlands and the United Kingdom are all accelerating efforts to install wind power. Fertilizer plants across Europe have announced they will scale back production, and 31 countries around the world have agreed to release oil from their strategic reserves.

Russia's [unprovoked invasion of Ukraine](#) has roiled the markets and geopolitics of energy, driving oil and gas prices to their highest levels in nearly a decade and forcing many countries to reconsider [their energy supplies](#). According to the International Energy Agency, Russia is the world's largest oil exporter to global markets, and its natural gas fuels the European economy. The United States, the European Union and others have imposed economic sanctions on Russia, and have announced plans to wean themselves off that country's fossil fuels. But even as Russia's bombs rain down on Ukraine, [its oil and gas continues to flow to Western nations that have condemned the invasion](#) (see 'Where Europe gets its gas').

WHERE EUROPE GETS ITS GAS

Russia supplies about 40% of the natural gas to the European Union overall, but many individual countries receive a much higher proportion.



*LNG, liquefied natural gas imports.

†Does not include nation's own production. The UK left the EU28 in January 2020.

Sources: Bruegel/European Network of Transmission System Operators for Gas/Eurostat/UK Government/Government of Ukraine

This isn't the first time that Russian military aggression has prompted world leaders to fret about energy security. Similar concerns arose when Russia invaded Georgia in 2008, and in 2014 when it invaded and then annexed the Ukrainian territory of Crimea. The allure of cheap Russian energy proved too strong in the past, but this time might be different, says Veronika Grimm, an economist at the Friedrich Alexander University of Erlangen–Nuremberg in Erlangen, Germany. "We have a war at our back door," she says. "It's hard to avoid taking action."

The war has prompted political leaders to rethink their energy plans, which could have profound impacts on a range of issues, from a burgeoning food crisis to global efforts to [curb greenhouse-gas emissions](#). Here, *Nature* takes a look at some of the choices the world faces, as well as potential repercussions that could play out over the course of years or even decades.

Energy crunch

For now, the biggest question facing world leaders is how to sever their energy dependence on Russia. The United States and the United Kingdom were the first major countries to ban Russian oil, but neither depends heavily on these imports. Moreover, the impact of such actions is minimal because Russia can simply redirect that oil elsewhere on the global market. An embargo would only work if the EU took part, economists say, because it would be difficult for Russia to quickly find new customers for the oil and gas it sends to Europe.



Coal wagons await export at the Russian port of Murmansk. Credit: Andrey Rudakov/Bloomberg via Getty

The EU imported around 40% of its natural gas, more than one-quarter of its oil and about half of its coal from Russia in 2019. And despite bold promises about cutting ties with Russia, European nations have thus far opted for easy energy: the amount of Russian oil and gas entering Europe has actually increased since the war in Ukraine began. Europe sent Russia around €22 billion (US\$24 billion) for oil and gas in March alone, according to Bruegel, a think tank based in Brussels. But that could change in the coming months, as countries implement plans to diversify their energy sources and reduce the flow of Russian oil and gas. Poland, for example, has announced it will ban all imports of Russian oil, gas and coal by the end of this year, and Germany and Austria are laying the groundwork for rationing natural gas.

The European Commission has released plans to curb imports of Russian gas by around two-thirds by the end of the year. That strategy relies largely on increasing imports of natural gas from abroad, and is it not clear whether individual nations in Europe will follow this plan. On 25 March, US

President Joe Biden pledged to send more liquefied natural gas to Europe, and Germany has already signed a deal to import the product from Qatar. European officials have also been in talks with Japan and South Korea about redirecting liquefied natural gas that would otherwise go to those two countries.

The commission's plan seeks to replace 101.5 billion cubic metres of Russian gas by the end of the year. Boosting imports to Europe from other countries could account for nearly 60% of that reduction, and another 33% would come from new renewable-energy generation and conservation measures, the plan suggests.

"We need a portfolio of options to replace Russian gas and safeguard energy security in the short term," says Simone Tagliapietra, an economist at Bruegel. That portfolio includes ramping up natural-gas imports to Europe, as well as increasing the use of coal-fired power plants to ensure that the lights stay on and houses remain warm next winter, he says. "And then we need to really double down on the clean energy transition."

The energy crisis is particularly acute in Germany, which relies on Russia for roughly half of its natural gas and coal and for more than one-third of its oil. Germany's immediate challenge is to reduce reliance on natural gas in the power-generation sector, which is further complicated by the country's exit from nuclear power: its last three nuclear stations are scheduled to close down this year.

A report last month by Leopoldina, the German National Academy of Sciences, found that Germany could survive the next winter without Russian energy (see go.nature.com/3jdtes1; in German), but only with extreme efforts to replace Russian gas with imports while ramping up coal-fired power plants and promoting large-scale conservation and energy efficiency. It also depends on higher prices causing a slowdown in heavy industry in the country.

Although the next few years could be tough, the long-term impact on energy policy and greenhouse-gas emissions in Europe could be beneficial, according to Grimm, a co-author of the Leopoldina report. The power sector is covered by the European trading system, which caps cumulative carbon

emissions, so a temporary increase in coal power, for instance, should drive up the price of carbon credits and force emissions reductions elsewhere.

In the longer term, Grimm says, the German government is proposing to increase the share of renewable energy sources in the power sector from around 40% today to 100% by 2035, 5 years earlier than planned. “That’s quite ambitious,” Grimm says. A sustained period of high energy prices could also drive significant investments in energy efficiency, an area that has enormous potential but has attracted less attention than renewables. “This will speed up a lot of work that we needed to do anyway.”

Longer-term outlook

The energy picture is less clear at the global level. When prices for oil and gas have surged in the past, it has spurred a series of changes in opposite directions: consumers tended to drive vehicles less and purchase more fuel-efficient versions, whereas companies and nations invested in oil and gas infrastructure around the globe to ramp up production. But the current crisis might not trigger the same response.

On the consumer side, growing gaps between the richest and poorest people in many countries are changing patterns of car buying. Although consumption is likely to drop in the short term as drivers respond to rising prices, that doesn’t mean we should expect a massive shift towards smaller or electric vehicles, says John DeCicco, an engineer at the University of Michigan in Ann Arbor who tracks the vehicle industry. That’s because the people who tend to buy new vehicles are wealthier than they were in decades past, meaning they won’t react to the economic pressure of higher petrol prices as much as before.

“Compared to previous oil shocks,” DeCicco says, “this is a different world.”

By contrast, economists have yet to see major oil and gas companies ramp up their investments in fossil-fuel production. Global leaders have been emphasizing the need for decarbonization in the past few years, and companies are now more wary of sinking their own capital into assets that

could be stranded as climate policies are ratcheted up in the future, says Ricardo Hausmann, an economist at Harvard University in Cambridge, Massachusetts.

“The market is scared,” Hausmann says, but so far, global supply and demand haven’t changed much — a dynamic that could change if prices remain high for a sustained period.

Although the war in Ukraine will probably speed up Europe’s move away from fossil fuels, it could slow the clean energy transition — and boost greenhouse-gas emissions — in other parts of the world, fears Nikos Tsafos, who tracks global energy and geopolitics at the Center For Strategic and International Studies, a think tank in Washington DC. Southeast Asia, in particular, could turn back towards coal if Europe effectively corners the international market for liquefied natural gas, according to Tsafos. And then there’s Russia itself, which accounted for nearly 5% of global emissions in 2020 and is unlikely to move forward with decarbonization in the absence of international political and economic engagement.

Food prices

Another key question, some economists say, is how rising energy prices and the potential loss of grain supplies from Ukraine and Russia could reinforce inflationary effects and drive up prices for food and other commodities.

“The potential reverberations on food prices and therefore on conflict and politics around the world are vast,” says Nathaniel Keohane, president of the Center For Climate and Energy Solutions, an environmental think tank in Arlington, Virginia.

In the short term, prices have increased owing to hoarding and bidding wars. But global food stocks are sufficient to cover the loss of wheat and other grains from Ukraine as a result of the war itself, and losses from Russia owing to economic sanctions, says Christopher Barrett, an economist at Cornell University in Ithaca, New York. There could be disruptions to fertilizer markets because fossil fuels are a major feed stock, but Barrett says farmers around the world should be able to negotiate these changes by using substitutes.

Still, the cost of rising petrol and electricity prices to the larger food-supply system could be substantial, says Barrett. “One of the big casualties of the Russian invasion will be people who are already teetering on the edge in other places,” he says. “It’s not just Ukrainians. It’s Yemenis, and Syrians and Nigerians.”

Nature **604**, 232-233 (2022)

doi: <https://doi.org/10.1038/d41586-022-00969-9>

This article was downloaded by **calibre** from <https://www.nature.com/articles/d41586-022-00969-9>

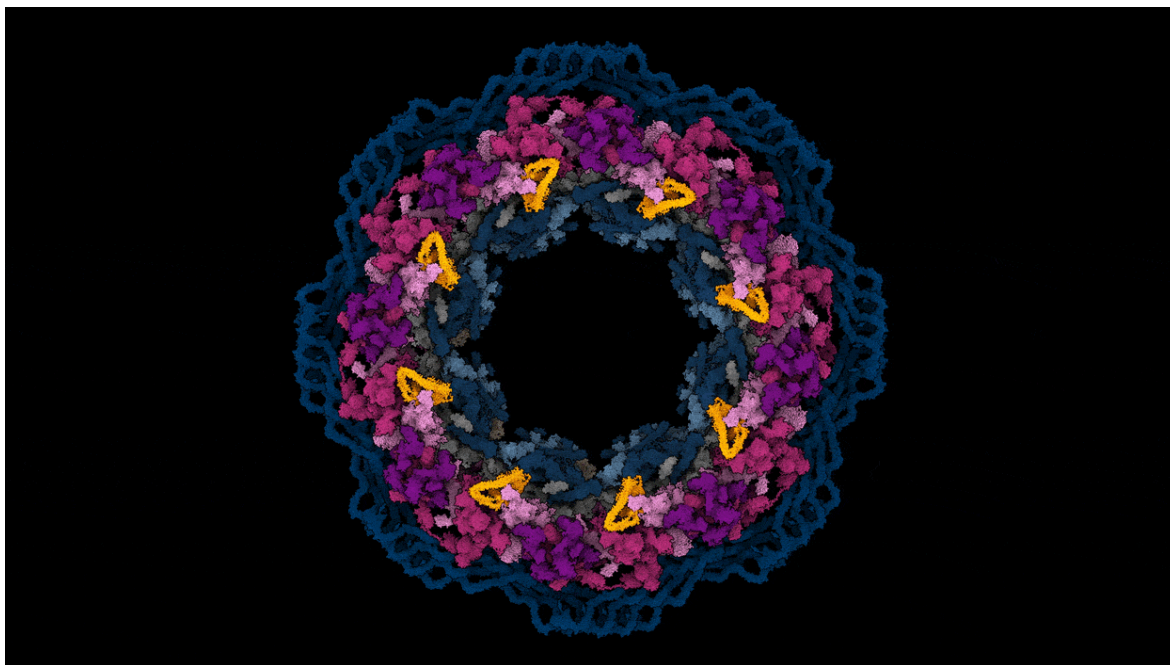
| [Section menu](#) | [Main menu](#) |

- NEWS FEATURE
- 13 April 2022

What's next for AlphaFold and the AI protein-folding revolution

DeepMind software that can predict the 3D shape of proteins is already changing biology.

- [Ewen Callaway](#)



A top-down view of the human nuclear pore complex, the largest molecular machine in human cells. Credit: Agnieszka Obarska-Kosinska

For more than a decade, molecular biologist Martin Beck and his colleagues have been trying to piece together one of the world's hardest jigsaw puzzles: a detailed model of the largest molecular machine in human cells.

This behemoth, called the nuclear pore complex, controls the flow of molecules in and out of the nucleus of the cell, where the genome sits. Hundreds of these complexes exist in every cell. Each is made up of more than 1,000 proteins that together form rings around a hole through the nuclear membrane.

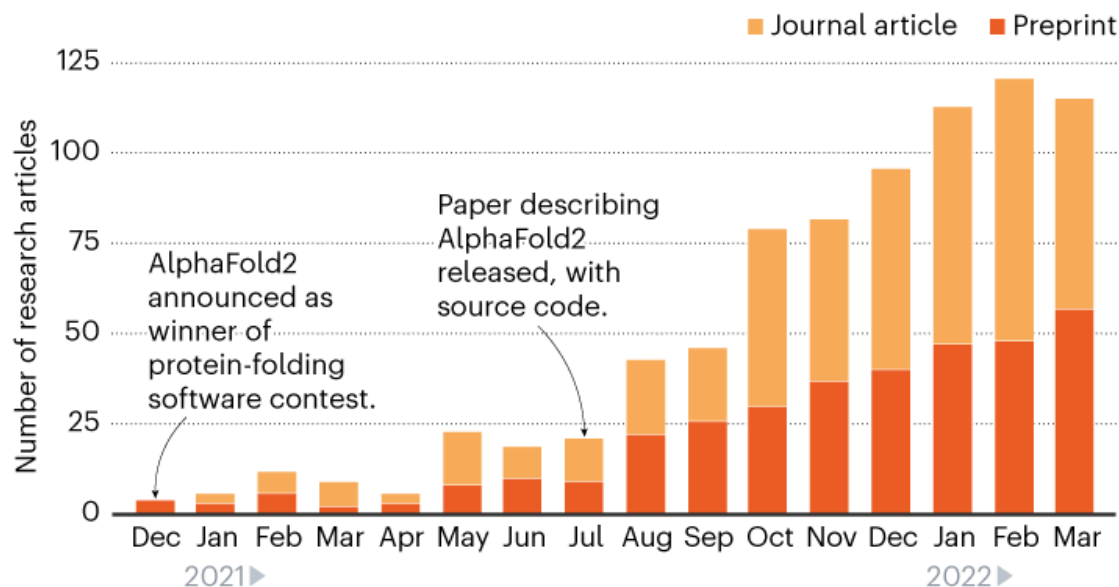
These 1,000 puzzle pieces are drawn from more than 30 protein building blocks that interlace in myriad ways. Making the puzzle even harder, the experimentally determined 3D shapes of these building blocks are a potpourri of structures gathered from many species, so don't always mesh together well. And the picture on the puzzle's box — a low-resolution 3D view of the nuclear pore complex — lacks sufficient detail to know how many of the pieces precisely fit together.

In 2016, a team led by Beck, who is based at the Max Planck Institute of Biophysics (MPIB) in Frankfurt, Germany, reported a model¹ that covered about 30% of the nuclear pore complex and around half of the 30 building blocks, called Nup proteins.

Then, last July, London-based firm DeepMind, part of Alphabet — Google's parent company — made public an artificial intelligence (AI) tool called AlphaFold². The software could predict the 3D shape of proteins from their genetic sequence with, for the most part, pinpoint accuracy. This transformed Beck's task, and the studies of thousands of other biologists (see 'AlphaFold mania').

ALPHAFOLD MANIA

The number of research papers and preprints citing the AlphaFold2 AI software has shot up since its source code was released in July 2021*.



*Nature analysis using Dimensions database; removing duplicate preprints and papers/R. Van Noorden, E. Callaway.

©nature

“AlphaFold changes the game,” says Beck. “This is like an earthquake. You can see it everywhere,” says Ora Schueler-Furman, a computational structural biologist at the Hebrew University of Jerusalem in Israel, who is using AlphaFold to model protein interactions. “There is before July and after.”

Using AlphaFold, Beck and others at the MPIB — molecular biologist Agnieszka Obarska-Kosinska and a group led by biochemist Gerhard Hummer — as well as a team led by structural modeller Jan Kosinski, at the European Molecular Biology Laboratory (EMBL) in Hamburg in Germany, could predict shapes for human versions of the Nup proteins more accurately. And by taking advantage of a tweak that helped AlphaFold to model how proteins interact, they managed to publish a model last October that covered 60% of the complex³. It reveals how the complex stabilizes holes in the nucleus, as well as hinting at how the complex controls what gets in and out.

In the past half-year, AlphaFold mania has gripped the life sciences. “Every meeting I’m in, people are saying ‘why not use AlphaFold?’,” says Christine

Orengo, a computational biologist at University College London.

In some cases, the AI has saved scientists time; in others it has made possible research that was previously inconceivable or wildly impractical. It has limitations, and some scientists are finding its predictions to be too unreliable for their work. But the pace of experimentation is frenetic.

Even those who developed the software are struggling to keep up with its use in areas ranging from drug discovery and protein design to the origins of complex life. “I wake up and type AlphaFold into Twitter,” says John Jumper, who leads the AlphaFold team at DeepMind. “It’s quite the experience to see everything.”

A startling success

[AlphaFold caused a sensation in December 2020](#), when it dominated a contest called the Critical Assessment of Protein Structure Prediction, or CASP. The competition, held every two years, measures progress in one of biology’s grandest challenges: determining the 3D shapes of proteins from their amino-acid sequence alone. Computer-software entries are judged against structures of the same proteins determined using experimental methods such as X-ray crystallography or cryo-electron microscopy (cryo-EM), which fire X-rays or electron beams at proteins to build up a picture of their shape.

The 2020 version of AlphaFold was the software’s second edition. [It had also won the 2018 CASP](#), but its earlier efforts mostly weren’t good enough to stand in for experimentally determined structures, says Jumper. However, AlphaFold2’s predictions were, on average, on par with the empirical structures.

It wasn’t clear when DeepMind would make the software or its predictions widely available, so researchers used information from a public talk by Jumper, and their own insights, to develop their own AI tool, called [RoseTTAFold](#).

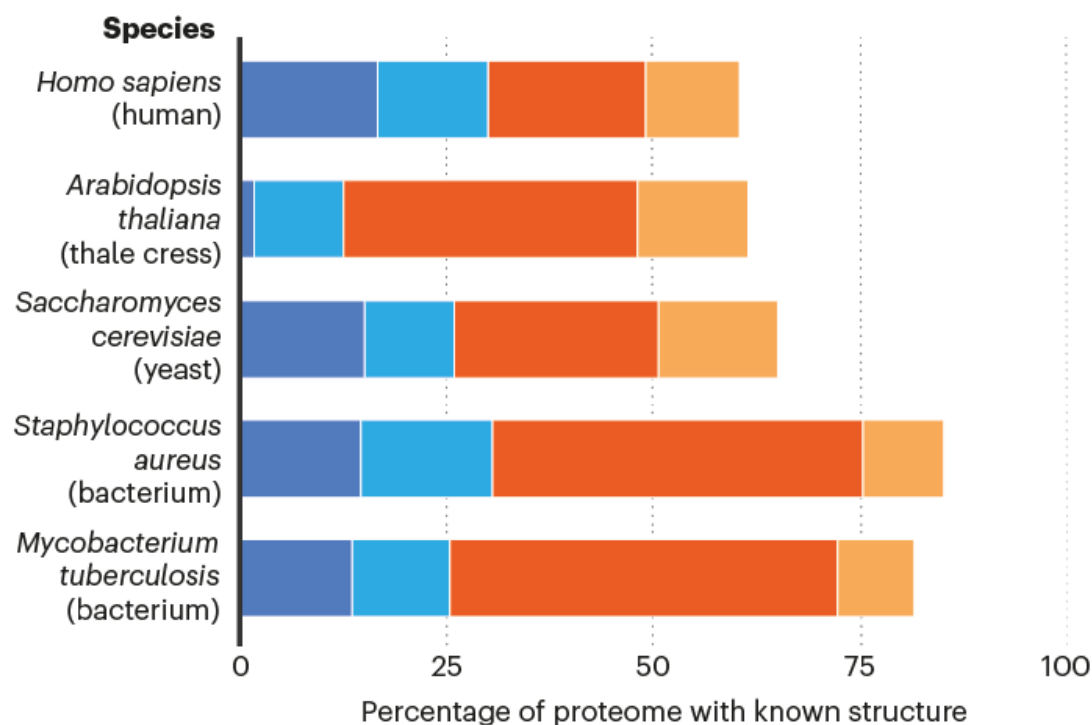
Then on 15 July 2021, papers describing RoseTTAFold and AlphaFold2 appeared^{2,4}, along with freely available, open-source code and other information needed for specialists to run their own versions of the tools. A week later, DeepMind announced that it had used AlphaFold to predict the structure of nearly every protein made by humans, as well as the entire ‘proteomes’ of 20 other widely studied organisms, such as mice and the bacterium *Escherichia coli* — more than 365,000 structures in total (see ‘What’s known about proteomes’). DeepMind also publicly released these to a database maintained by the EMBL’s European Bioinformatics Institute (EMBL–EBI), in Hinxton, UK. That database has since swelled to almost one million structures.

WHAT'S KNOWN ABOUT PROTEOMES

AlphaFold's predictions have greatly increased the proportion of confidently known structures in the human proteome — the collection of all human proteins. The software is even more useful for other species.

Source of knowledge about proteome

- High-quality experimental structures in the PDB*
- Structural knowledge derived from related proteins in the PDB*
- Knowledge from AlphaFold models only (high confidence)
- Knowledge from AlphaFold models only (intermediate confidence)



*PDB: Protein Data Bank. AlphaFold can also be used to calculate these structures — but doesn't add significantly to what's already known.

©nature

Source: E. Porta-Pardo *et al.* *PLoS Comput. Biol.* **18**, e1009818 (2022).

This year, DeepMind plans to release a total of more than 100 million structure predictions. That is nearly half of all known proteins — and hundreds of times more than the number of experimentally determined proteins in the Protein Data Bank (PDB) structure repository.

AlphaFold deploys deep-learning neural networks: computational architectures inspired by the brain’s neural wiring to discern patterns in data. It has been trained on hundreds of thousands of experimentally determined protein structures and sequences in the PDB and other databases. Faced with a new sequence, it first looks for related sequences in databases, which can identify amino acids that have tended to evolve together, suggesting they’re close in 3D space. The structure of existing related proteins provides another way to estimate distances between amino-acid pairs in the new sequence.

AlphaFold iterates clues from these parallel tracks back and forth as it tries to model the 3D positions of amino acids, continually updating its estimate. Specialists say the software’s application of new ideas in machine learning research seems to be what makes AlphaFold so good — in particular, its use of an AI mechanism termed ‘attention’ to determine which amino-acid connections are most salient for its task at any moment.

The network’s reliance on information about related protein sequences means that AlphaFold has some limitations. It is not designed to predict the effect of mutations, such as those that cause disease, on a protein’s shape. Nor was it trained to determine how proteins change shape in the presence of other interacting proteins, or molecules such as drugs. But its models come with scores that gauge the network’s confidence in its prediction for each amino-acid unit of a protein — and researchers are tweaking AlphaFold’s code to expand its capabilities.

By now, more than 400,000 people have used the EMBL-EBI’s AlphaFold database, according to DeepMind. There are also AlphaFold ‘power users’: researchers who’ve set up the software on their own servers or turned to cloud-based versions of AlphaFold to predict structures not in the EMBL-EBI database, or to dream up new uses for the tool.

Solving structures

Biologists are already impressed with AlphaFold’s ability to solve structures. “Based on what I’ve seen so far, I trust AlphaFold quite a lot,” says Thomas Boesen, a structural biologist at Aarhus University in Denmark. The software has successfully predicted the shapes of proteins that Boesen’s

centre has determined but not yet published. “That’s a big validation from my side,” he says. He and Aarhus microbial ecologist Tina Šantl-Temkiv are using AlphaFold to model the structure of bacterial proteins that promote the formation of ice — and which could contribute to the cooling effects of ice in clouds — because biologists haven’t been able to fully determine the structures experimentally⁵.

As long as a protein curls up into a single well-defined 3D shape — and not all do — AlphaFold’s prediction can be hard to beat, says Arne Elofsson, a protein bioinformatician at Stockholm University. “It’s a one-click solution to get probably the best model you’re going to get.”

Where AlphaFold is less confident, “it’s very good at telling you when it doesn’t work”, Elofsson says. In such cases, predicted structures can resemble floating spaghetti strands (see ‘The good, the bad and the ugly’). This often corresponds to regions of proteins that lack a defined shape, at least in isolation. Such intrinsically disordered regions — which make up around one-third of the human proteome — might become well defined only when another molecule, such as a signalling partner, is present.

THE GOOD, THE BAD AND THE UGLY

AlphaFold's predictions of a folded protein's structure come with confidence estimates. Superimposing each model on the experimentally determined structure (if available) shows the accuracy of the prediction.

Protein Data Bank
(PDB) structure



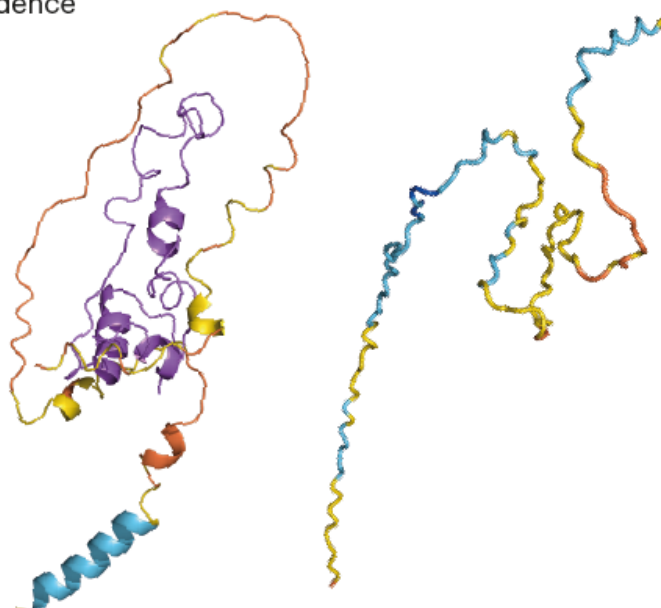
AlphaFold structure, with confidence estimates for each section.

■ Very high ■ High ■ Low ■ Very low



Good

AlphaFold model of phosphohistidine phosphatase overlaps closely with PDB structure.



Bad

AlphaFold model of human insulin bears no relation to the PDB structure.

Ugly

AlphaFold has little confidence across much of its prediction for this human ubiquitin-protein ligase. There is no PDB structure to compare it with.

©nature

Images: J. M. Thornton *et al.* *Nature Med.* **27**, 1666–1669 (2021).

Norman Davey, a computational biologist at the Institute of Cancer Research in London, says AlphaFold's ability to identify disorder has been a game-changer for his work studying the properties of these regions. “Instantly there was a huge increase in the quality of the predictions we had, without any effort on our part,” he says.

AlphaFold's dump of protein structures into the EMBL-EBI database is also immediately being put to use. Orengo's team is searching it to identify fresh

kinds of proteins (without experimentally verifying them) and has turned up hundreds, perhaps thousands, of potentially new protein families, expanding scientists' knowledge of what proteins look like and can do. In another effort, the team is scouring databases of DNA sequences harvested from the ocean and waste water, to try to identify new plastic-eating enzymes. Using AlphaFold to quickly approximate the structures of thousands of proteins, the researchers hope to better understand how enzymes evolved to break down plastic, and potentially to improve them.

The ability to transform any protein-coding gene sequence into a reliable structure should be especially powerful for evolution studies, says Sergey Ovchinnikov, an evolutionary biologist at Harvard University in Cambridge, Massachusetts. Researchers compare genetic sequences to determine how organisms and their genes are related across species. For distantly related genes, comparisons might fail to turn up evolutionary relatives because the sequences have changed so much. But by comparing protein structures — which tend to change less rapidly than genetic sequences — researchers might be able to uncover overlooked ancient relationships. "This opens up an amazing opportunity to study the evolution of proteins and the origins of life," says Pedro Beltrao, a computational biologist at the Swiss Federal Institute of Technology in Zurich.

To test this idea, a team led by Martin Steinegger, a computational biologist at Seoul National University, and his colleagues used a tool they developed, called Foldseek, to look for relatives of the RNA-copying enzyme of SARS-CoV-2 — the virus that causes COVID-19 — in the EMBL-EBI's AlphaFold database⁶. This search turned up previously unidentified possible ancient relatives: proteins across eukaryotes — including slime moulds — that resemble, in their 3D structure, enzymes called reverse transcriptases that viruses such as HIV use to copy RNA into DNA, despite very little similarity at the genetic-sequence level.

Experimental assistant

For scientists who want to determine the detailed structure of a specific protein, an AlphaFold prediction isn't necessarily an immediate solution. Rather, it provides an initial approximation that can be validated or refined

by experiment — and which itself helps to make sense of experimental data. Raw data from X-ray crystallography, for instance, appear as patterns of diffracted X-rays. Typically, scientists need a starting guess at a protein’s structure to interpret these patterns. Previously, they’d often cobble together information from related proteins in the PDB or use experimental approaches, says Randy Read, a structural biologist at the University of Cambridge, UK, whose lab specialized in some of these methods. Now, AlphaFold’s predictions have rendered such approaches unnecessary for most X-ray patterns, Read says, and his lab is working to make better use of AlphaFold in experimental models. “We’ve totally refocused our research.”

He and other researchers have used AlphaFold to determine crystal structures from X-ray data that were uninterpretable without an adequate starting model. “People are solving structures that, for years, had not been solved,” says Claudia Millán Nebot, a former postdoc in Read’s lab who now works at the analytics firm SciBite in Cambridge. She expects to see a glut of new protein structures submitted to the PDB, in large part as a result of AlphaFold.

The same is true for labs specializing in cryo-EM, which captures pictures of flash-frozen proteins. In some instances, AlphaFold’s models have accurately predicted unique features of proteins called G-protein-coupled receptors (GPCRs) — which are important drug targets — that other computational tools got wrong, says Bryan Roth, a structural biologist and pharmacologist at the University of North Carolina at Chapel Hill. “It seems to be really good for generating first models, which we then refine with some experimental data,” he says. “That saves us some time.”

But Roth adds that AlphaFold isn’t always that accurate. Of the several dozen GPCR structures his lab has solved, but not yet published, he says, “about half the time, the AlphaFold structures are fairly good, and half the time they’re more or less useless for our purposes”. In some instances, he says, AlphaFold labels predictions with high confidence, but experimental structures show that it is wrong. Even when the software gets it right, it cannot model how a protein would look when bound to a drug or other small molecule (ligand), which can substantially alter the structure. Such caveats make Roth wonder [how useful AlphaFold will be for drug discovery](#).

It's increasingly common in drug-discovery efforts to use computational-docking software that screens billions of small molecules to find some that might bind to proteins — one indication that they could make useful drugs. Roth is now working with Brian Shoichet, a medicinal chemist at the University of California, San Francisco, to see how AlphaFold's predictions compare with experimentally determined structures in this exercise.

Shoichet says they are limiting their work to proteins for which AlphaFold's prediction chimes with experimental structures. But even in these instances, the docking software is turning up different drug hits for the experimental structure and AlphaFold's take, suggesting that small discrepancies could matter. "That doesn't mean we won't find new ligands, we'll just find different ones," says Shoichet. His team is now synthesizing potential drugs identified using AlphaFold structures, and testing their activity in the lab.

Critical optimism

Researchers at pharmaceutical companies and biotechnology firms are excited about AlphaFold's potential to help with drug discovery, says Shoichet. "Critical optimism is how I'd describe it." In November 2021, DeepMind [launched its own spin-off, IsoMorphic Labs](#), which aims to apply AlphaFold and other AI tools to drug discovery. But the company has said little else about its plans.

Karen Akinsanya, who leads therapeutics development at Schrödinger, a drug-discovery firm headquartered in New York City that also publishes chemical-simulations software, says she and her colleagues are already having some success using AlphaFold structures, including for GPCRs, in virtual screens and compound design for drug candidates. She finds that, just as with experimental structures, extra software is needed to get at the fine details of amino-acid side chains or locations where individual hydrogen atoms might sit. Once this is done, AlphaFold structures have proved good enough to guide drug discovery — in some cases.

"It's hard to say 'this is a panacea'; that because you can do it very well for one structure — surprisingly and excitingly well — that it is eminently applicable to all structures. It clearly isn't," Akinsanya says. And she and her

colleagues have found that AlphaFold's accuracy predictions don't show whether a structure will be useful for later drug screening. AlphaFold structures will never fully replace experimental ones in drug discovery, she says. But they might speed up the process by complementing experimental methods.

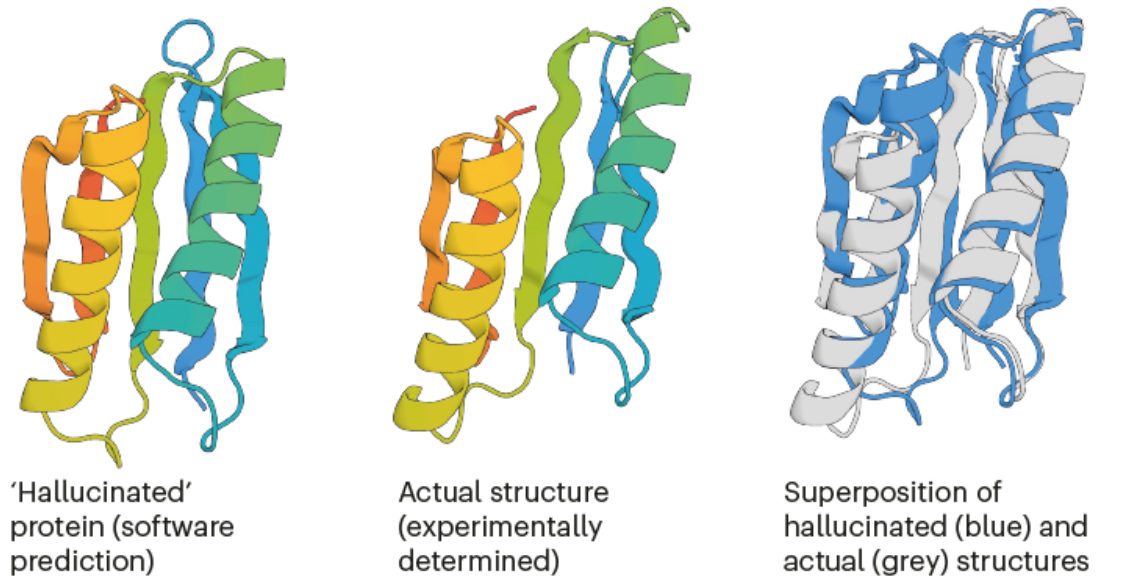
Drug developers curious about AlphaFold received good news in January, [when DeepMind lifted a key restriction on its use for commercial applications](#). When the company released AlphaFold's code in July 2021, it had stipulated that the parameters, or weights, needed to run the AlphaFold neural network — the end result of training the network on hundreds of thousands of protein structures and sequences — were for non-commercial use only. Akinsanya says this was a bottleneck for some in industry, and there was a “wave of excitement” when DeepMind changed tack. (RoseTTAFold came with similar restrictions, says Ovchinnikov, one of its developers. But the next version will be fully open-source.)

AI tools are not just changing how scientists determine what proteins look like. Some researchers are using them to make entirely new proteins. “Deep learning is completely transforming the way that protein design is being done in my group,” says David Baker, a biochemist at the University of Washington in Seattle and a leader in the field of designing proteins, as well as predicting their structures. His team, with computational chemist Minkyung Baek, led the work to develop RoseTTAFold.

Baker’s team gets AlphaFold and RoseTTAFold to “hallucinate” new proteins. The researchers have altered the AI code so that, given random sequences of amino acids, the software will optimize them until they resemble something that the neural networks recognize as a protein (see ‘Dreaming up proteins’).

DREAMING UP PROTEINS

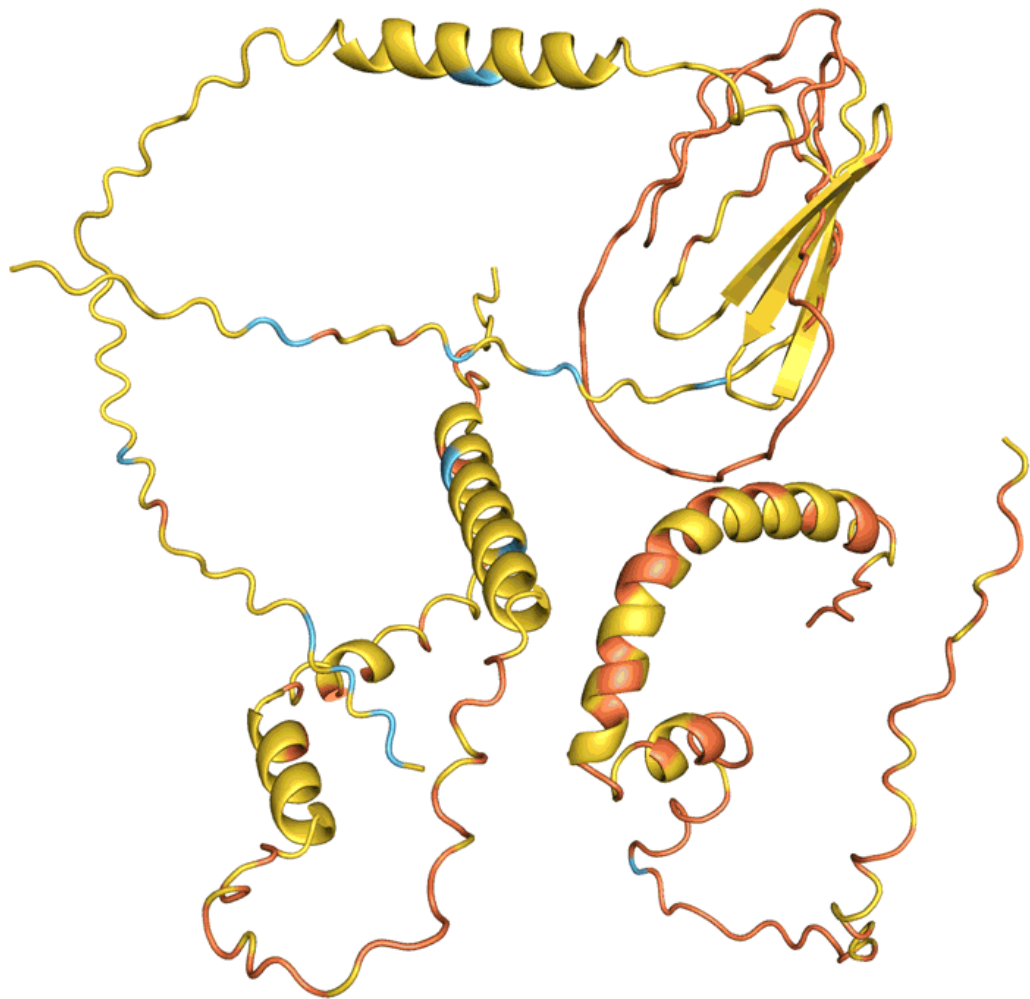
Researchers used deep neural networks to invent, or ‘hallucinate’, sequences of amino acids that could fold into proteins; in some cases they have synthesized these proteins to compare their actual structures with predictions.



©nature

Images: Ref. 7

In December 2021, Baker and his colleagues reported expressing 129 of these hallucinated proteins in bacteria, and found that about one-fifth of them folded into something resembling their predicted shape⁷. “That’s really the first demonstration that you can design proteins using these networks,” Baker says. His team is now using this approach to design proteins that do useful things, such as catalyse a particular chemical reaction, by specifying the amino acids responsible for the desired function and letting the AI dream up the rest.



Four examples of protein ‘hallucination’. In each case, AlphaFold is presented with a random amino-acid sequence, predicts the structure, and changes the sequence until the software confidently predicts that it will fold into a protein with a well-defined 3D shape. Colours show prediction confidence (from red for very low confidence, through yellow and light blue to dark blue for very high confidence). Initial frames have been slowed down for clarity.Credit: Sergey Ovchinnikov

Hacking AlphaFold

When DeepMind released its AlphaFold code, Ovchinnikov wanted to better understand how the tool worked. Within days, he and computational-biology colleagues, including Steinegger, [set up a website called ColabFold](#) that allowed anyone to submit a protein sequence to AlphaFold or RoseTTAFold and get a structure prediction. Ovchinnikov imagined that he and other scientists would use ColabFold to try and ‘break’ AlphaFold, for instance, by supplying false information about a target protein sequence’s evolutionary relatives. By doing this, Ovchinnikov hoped he could determine how the network had learnt to predict structures so well.

As it turned out, most researchers who used ColabFold just wanted to get a protein structure. But others used it as a platform to modify the inputs to AlphaFold to tackle new applications. “I didn’t expect the number of hacks of various types,” says Jumper.

By far the most popular hack has been to wield the tool on protein complexes comprised of multiple, interacting — and often intertwined — chains of peptides. Just as with the nuclear pore complex, many proteins in cells gain their function when they form complexes with multiple protein subunits.

AlphaFold was designed to predict the shape of single peptide chains, and its training consisted entirely of such proteins. But the network seems to have learnt something about how complexes fold together. Several days after AlphaFold’s code was released, Yoshitaka Moriwaki, a protein bioinformatician at the University of Tokyo, [tweeted that it could accurately predict interactions](#) between two protein sequences if they were stitched together with a long linker sequence. Baek soon shared another hack to predict complexes, gleaned from developing RoseTTAFold.

ColabFold later incorporated the ability to predict complexes. And in October 2021, DeepMind released an update called AlphaFold-Multimer⁸ that was specifically trained on protein complexes, unlike its predecessor. Jumper’s team applied it to thousands of complexes in the PDB, and found that it predicted around 70% of the known protein–protein interactions.

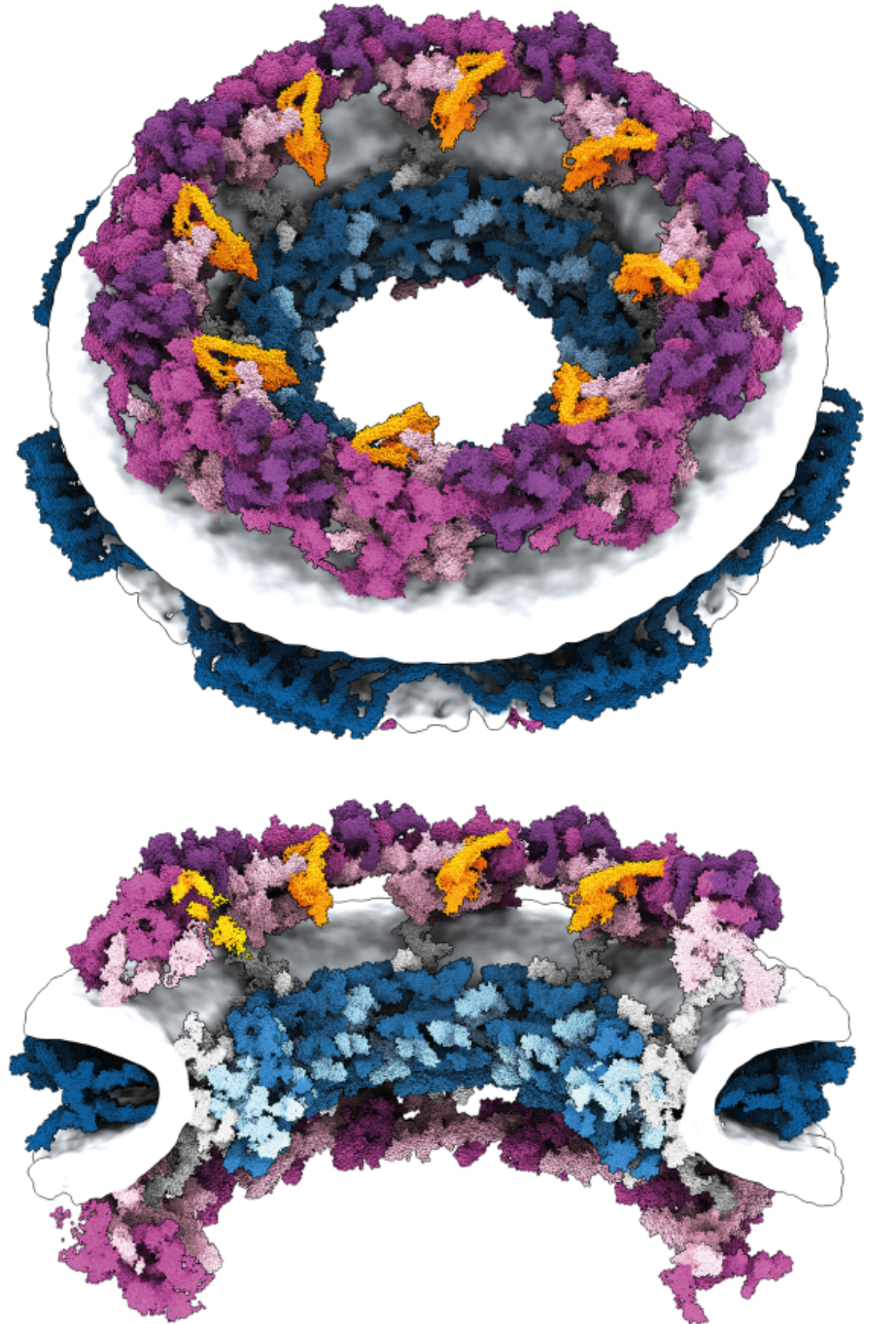
These tools are already helping researchers to spot potential new protein partners. Elofsson’s team used AlphaFold to predict the structures of 65,000

human protein pairs that were suspected to interact on the basis of experimental data⁹. And a team led by Baker used AlphaFold and RoseTTAFold to model interactions between nearly every pair of proteins encoded by yeast, identifying more than 100 previously unknown complexes¹⁰. Such screens are just starting points, says Elofsson. They do a good job of predicting some protein pairings, particularly those that are stable, but struggle to identify more transient interactions. “Because it looks nice doesn’t mean it is correct,” says Elofsson. “You need some experimental data that show you’re right.”

The nuclear pore complex work is a good example of how predictions and experimental data can work together, says Kosinski (see ‘Genome gateway’). “It’s not like we take all the 30 proteins, throw them into AlphaFold and get the structure out.” To put the predicted protein structures together, the team used 3D images of the nuclear pore complex, captured using a form of cryo-EM called cryo-electron tomography. In one instance, experiments that can determine the proximity of proteins turned up a surprising interaction between two components of the complex, which AlphaFold’s models then confirmed.

GENOME GATEWAY

Two views of the human nuclear pore complex show how this massive assembly embeds into the nuclear membrane (white).



©nature

Images adapted from ref. 3/Agnieszka Obarska-Kosinska

Kosinski sees the team's current map of the nuclear pore complex as a starting point for experiments and simulations that examine how the pore complex functions — and how it malfunctions in disease.

AlphaFold's limits

For all the progress made with AlphaFold, scientists say that it is important to be clear about its limitations — particularly because researchers who don't specialize in predicting protein structures use it.

Attempts to apply AlphaFold to various mutations that disrupt a protein's natural structure, including one linked to early breast cancer, have confirmed that the software is not equipped to predict the consequences of new mutations in proteins, since there are no evolutionarily-related sequences to examine¹¹.

The AlphaFold team is now thinking about how a neural network could be designed to deal with new mutations. Jumper expects this would require the network to better predict how a protein goes from its unfolded to its folded state. That would probably need software that relies only on what it has learnt about protein physics to predict structures, says Mohammed AlQuraishi, a computational biologist at Columbia University in New York City. “One thing we are interested in is making predictions from single sequences without using evolutionary information,” he says. “That’s a key problem that does remain open.”

AlphaFold is also designed to predict a single structure, although it has been hacked to spit out more than one. But many proteins take on multiple conformations, which can be important to their function. “AlphaFold can’t really deal with proteins that can adopt different structures in different conformations,” says Schueler-Furman. And the predictions are for structures in isolation, whereas many proteins function alongside ligands such as DNA and RNA, fat molecules and minerals such as iron. “We are still missing ligands, we are missing everything else about proteins,” says Elofsson.

Developing these next-generation neural networks will be a huge challenge, says AlQuraishi. AlphaFold relied on decades of research which generated experimental structures of proteins that the network could learn from. That volume of data is currently not available to capture protein dynamics, or the shapes of the trillions of smaller molecules that proteins could interact with. The PDB includes structures of proteins as they interact with other molecules, but this captures just a sliver of chemical diversity, Jumper adds.

Researchers think that it will take time for them to determine how best to wield AlphaFold and related AI tools. AlQuraishi sees parallels with the early days of television, when some programmes consisted of radio broadcasters simply reading the news. “I think we’re going to find new applications of structure that we haven’t conceived of yet.”

Where the AlphaFold revolution is ends up is anybody’s guess. “Things are just changing so fast,” says Baker. “Even in the next year, we’re going to see really major breakthroughs made using these tools.” Janet Thornton, a computational biologist at the EMBL-EBI, thinks one of AlphaFold’s biggest impacts might be simply to convince biologists to be more open to insights from computational and theoretical approaches. “To me, the revolution is the mindset change,” she says.

The AlphaFold revolution has inspired Kosinski to dream big. He imagines that AlphaFold-inspired tools could be used to model not just individual proteins and complexes, but entire organelles or even cells down to the level of individual protein molecules. “This is the dream we will follow for the next decades.”

Nature **604**, 234–238 (2022)

doi: <https://doi.org/10.1038/d41586-022-00997-5>

References

1. Kosinski, J. *et al.* *Science* **5**, 363–365 (2016).
2. Jumper, J. *et al.* *Nature* **596**, 583–589 (2021).

3. Mosalaganti, S. *et al.* Preprint at bioRxiv
<https://doi.org/10.1101/2021.10.26.465776> (2021).
4. Baek, M. *et al.* *Science* **373**, 871–876 (2021).
5. Hartmann, S. *et al.* Preprint at bioRxiv
<https://doi.org/10.1101/2022.01.21.477219> (2022).
6. van Kempen, M. *et al.* Preprint at bioRxiv
<https://doi.org/10.1101/2022.02.07.479398> (2022).
7. Anishchenko, I. *et al.* *Nature* **600**, 547–552 (2021).
8. Evans, R. *et al.* Preprint at bioRxiv
<https://doi.org/10.1101/2021.10.04.463034> (2021).
9. Bryant, P., Pozzati, G. & Elofsson, A. *Nature Commun.* **13**, 1265 (2022).
10. Humphreys, I. R. *et al.* *Science* **374**, eabm4805 (2021).
11. Buel, G. R. & Walters, K. J. *Nature Struct. Mol. Biol.* **29**, 1–2 (2022).

This article was downloaded by **calibre** from <https://www.nature.com/articles/d41586-022-00997-5>

Books & Arts

- **Climate change — four decades of missed opportunities**
[11 April 2022]
Book Review • The United States should learn from its mistakes on decarbonization.
 - **Maize under threat, and morality for cars: Books in brief**
[30 March 2022]
Book Review • Andrew Robinson reviews five of the week's best science picks.
-

- BOOK REVIEW
- 11 April 2022

Climate change — four decades of missed opportunities

The United States should learn from its mistakes on decarbonization.

- [Alexandra Witze](#)



In 1979, US president Jimmy Carter installed solar panels on the White House roof. Credit: Bettmann/Getty

Fire and Flood: A People's History of Climate Change, from 1979 to the Present Eugene Linden Penguin (2022)

Russia's violent invasion of Ukraine has sent shock waves through the world's energy markets, causing oil prices to swing wildly and nations to redraw allegiances over gas supplies. The war could drive the world towards a more decarbonized economy — or further entrench dependence on fossil fuels.

Given the global nature of the current events, it seems an odd time to explore a US-centric perspective on the failure to confront climate change. But journalist Eugene Linden's *Fire and Flood* could hold lessons for the energy emergency. Although the book veers at times into parochialism in its US focus, it reminds us of the many forces that have held society back from developing effective solutions to the climate crisis. It describes missed opportunities in the past and highlights strategies, particularly in business and finance, for the future.

Having covered environmental affairs for *Time* magazine for many years, Linden is efficient at summarizing scientific knowledge. His tale begins in 1979, when meteorologist Jule Charney chaired a US National Academy of Sciences committee that explored the effects of carbon dioxide on the climate. The background is well known: in the 1850s, with the industrial revolution under way, scientists such as Eunice Newton Foote and John Tyndall observed that CO₂ gas heated up faster than air did. In the 1890s, physical chemist Svante Arrhenius calculated how extra CO₂ could warm the planet. By the 1950s, the oceanographer Roger Revelle was tracking how much human-produced CO₂ must be going into the atmosphere and Charles David Keeling was beginning his iconic measurements of CO₂ levels above Mauna Loa, Hawaii.

By 1979, Charney and his colleagues were well aware that humanity was pouring CO₂ into the atmosphere, with potentially huge societal consequences. Linden introduces a useful framework for thinking about what came next: four clocks. The first tracks climate change in real time; the clock's hands advance with every climate-driven storm, drought, flood and other extreme event. Each of the three other clocks lags behind the first at different speeds. One represents research, which tries to explain climate change as quickly as possible but is slowed by the pace of investigation and

publication. Another is public awareness, which lags behind discovery. The final clock, the slowest, is the business world.

Linden steps through the years after 1979 in terms of opportunities missed. In the 1980s, the business clock was set back in the United States, when president Ronald Reagan slashed federal support for developing renewable energies, especially solar power. The country ceded technological leadership in these fields to Germany, Japan and others. Meanwhile, fossil-fuel companies such as Exxon began developing their highly effective tactics in the United States for delaying action to curb emissions, by sowing doubt about the facts of global warming. The public-awareness clock slowed.

In the 1990s, the scientific clock was doing pretty well. Researchers extracted long cores of ice from the Greenland ice sheet, solidifying their understanding of how abruptly the climate has changed in the past. Sadly society did not keep pace. After the collapse of the Soviet Union in 1991, the former Soviet states missed the opportunity to decarbonize rapidly. Emerging nations, too, failed to leapfrog dirty energy supplies and go straight to cleaner sources of power. China began its coal-fuelled rise.

This era, which lasted into the 2000s, was also the heyday of climate denialism, particularly in the United States and Australia, where the rhetoric of individual freedom and battling regulation has deep roots. Doubt-mERCHANTS fuelled fights over the ‘hockey stick’ graph (showing an abrupt rise in temperatures over time) and whether global warming had ‘stalled’ after the powerful 1997–98 El Niño event, and they stoked the 2009 Climategate scandal over scientists’ internal discussions. The public-awareness clock fell further behind.

Linden aims a fire hose of cynicism at international policymakers. He derides many reports by the Intergovernmental Panel on Climate Change as timid, and the United Nations agreements to limit greenhouse-gas emissions as toothless. His greatest ire, however, is directed at businesses that mortgaged a liveable future for today’s profits. Researchers proposed integrated tools for reducing carbon emissions, such as the 2000s concept of ‘stabilization wedges’: multiple strategies across transport, heating and so on, to collectively reduce emissions. Yet even insurance companies — which, more than any other business, should want to eliminate the risk of

climate change sooner rather than later — failed to adequately incorporate such strategies.

Throughout the 2000s and 2010s, as global temperatures rose and extreme weather events became more common, insurance companies continued to underwrite policies in the communities most at risk. Here are the fires and the floods of the title, many affecting the most vulnerable communities. Urban heat, exacerbated by climate change, hits hardest along racial and ethnic lines. Sea-level rise drowns not only beach homes of the affluent but also poorer neighbourhoods with little coastal protection. Like so many areas of environmental justice, the impacts of climate change ultimately come down to issues of inequity.

In this, Linden falls well short of other recent histories such as Alice Bell's *Our Biggest Experiment* (2021), which explores the intersection of race, class and climate in a much more sophisticated fashion. Linden's subtitle of a 'people's history' is odd: there are very few in his narrative who are not scientists, politicians and business leaders. He spends little time exploring how to address the outsized climate impacts on, for instance, low-lying island nations that will soon be submerged by sea-level rise or Indigenous peoples living in the fast-warming Arctic.

Linden argues that extreme weather events, such as prolonged droughts in Australia and hurricanes in the Caribbean and North America, are now so pronounced and obvious that they might force political change when previous discussions could not. Yet the path forward is not so clear. The clocks of public awareness and of business interests, especially, continue to lag behind the reality of what's transpiring.

The outlook becomes even more bleak towards the end. Linden concludes that the global response to COVID-19 shows that the world is ill-equipped to deal with any complex, far-reaching problem. Tribalism, autocracy and misinformation are on the rise, and even the promise of jobs in a decarbonized economy is not enough to trump those forces. Will the collapsing Russian economy drive many nations back to a reliance on fossil fuels, or will the fuel shock caused by Russia's invasion of Ukraine accelerate the transition to renewable energies?

That, like so many other things in these uncertain times, remains to be seen.

Nature **604**, 239-240 (2022)

doi: <https://doi.org/10.1038/d41586-022-00998-4>

This article was downloaded by **calibre** from <https://www.nature.com/articles/d41586-022-00998-4>

| [Section menu](#) | [Main menu](#) |

- BOOK REVIEW
- 30 March 2022

Maize under threat, and morality for cars: Books in brief

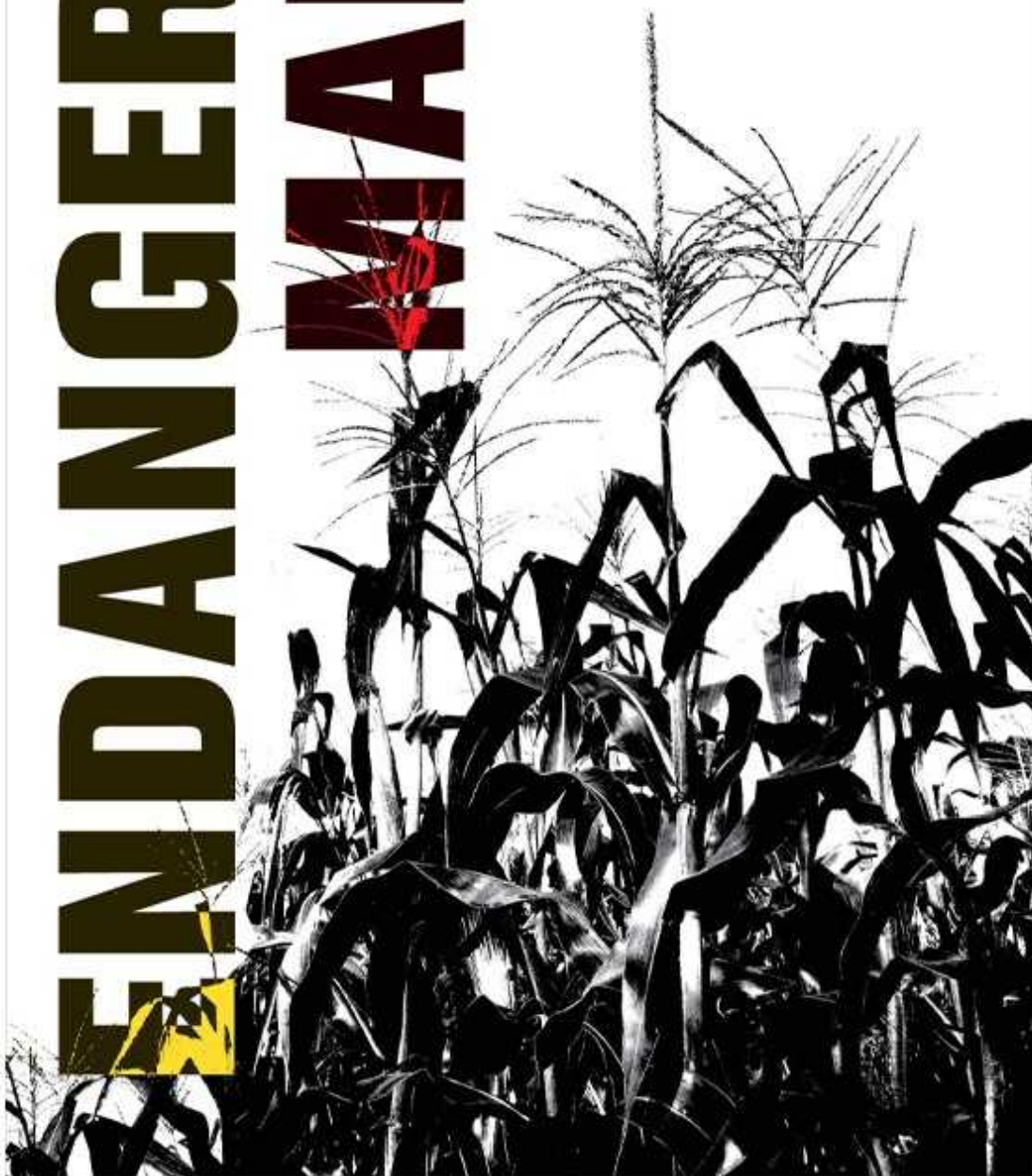
Andrew Robinson reviews five of the week's best science picks.

- [Andrew Robinson](#) 0

ENDANGERED MAIZE

INDUSTRIAL AGRICULTURE
AND THE CRISIS OF
EXTINCTION

HELEN ANNE CURRY

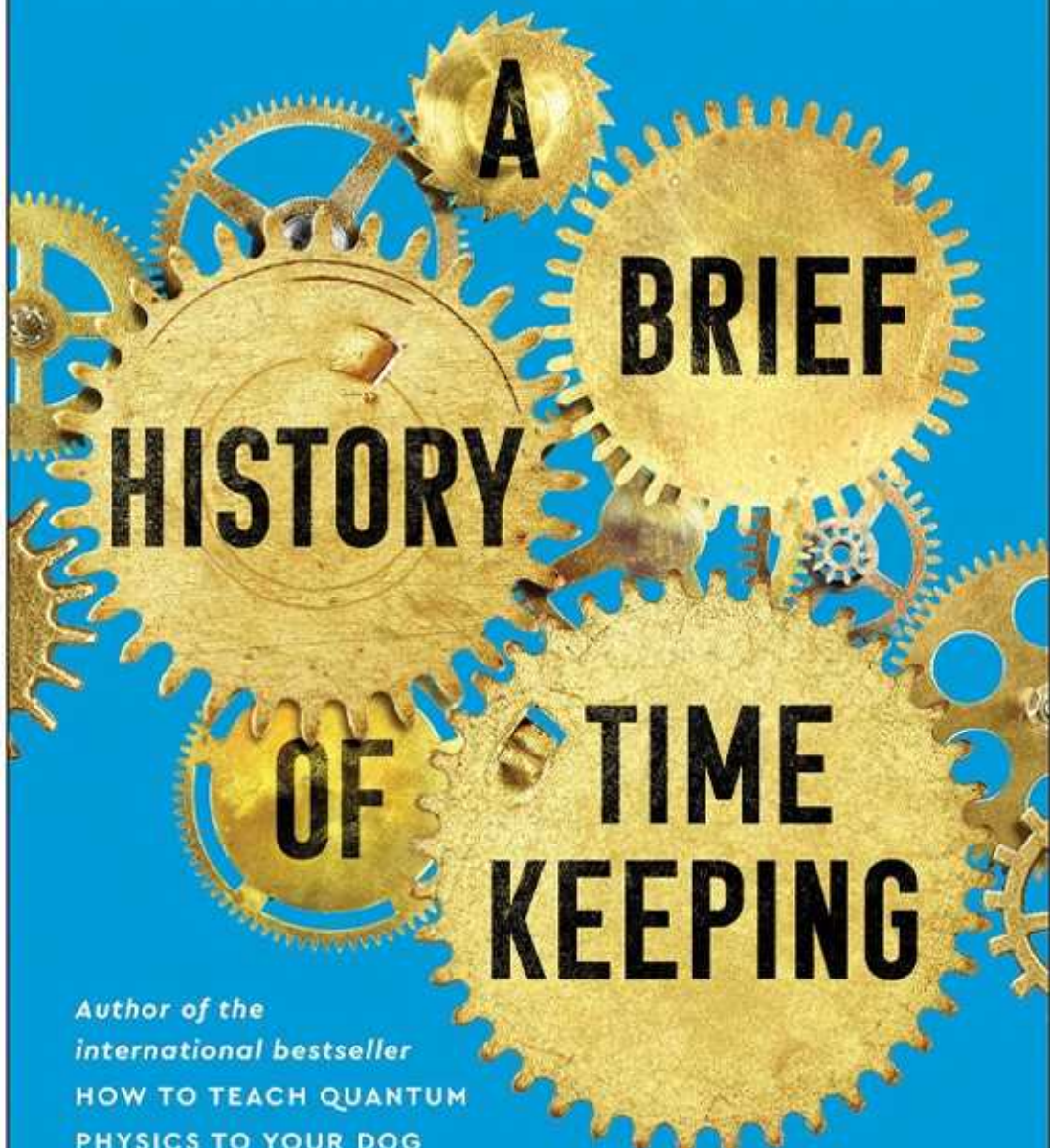


Endangered Maize

Helen Anne Curry *Univ. California Press* (2022)

Maize (corn; *Zea mays*) originated in Mexico 6,000–10,000 years ago, when the grass teosinte was domesticated. By Christopher Columbus's time, it had more than 200 sub-populations. Now, annual global production of the crop exceeds one billion tonnes, providing 20% of human calorie intake. But maize diversity is threatened by many factors, as science historian Helen Curry expertly discusses with specialists. She sees hope in the variety Glass Gem, inspired by Native American cultivation techniques.

The Science of Marking Time,
from Stonehenge to Atomic Clocks



CHAD ORZEL

A Brief History of Timekeeping

Chad Orzel *BenBella* (2022)

“Timekeeping has always been as much about the future as the past,” writes physicist Chad Orzel — whether for ancient societies tracking when to plant crops, medieval astrologers forecasting with the stars or modern astronomers predicting celestial transits. It also involves the quest for a regular, countable tick, such as the transition between the hyperfine levels of the caesium-133 atom’s ground state, now used to define the second. Full of history, physics and physicists, this varied book oddly omits Stephen Hawking’s 1988 *A Brief History of Time*.

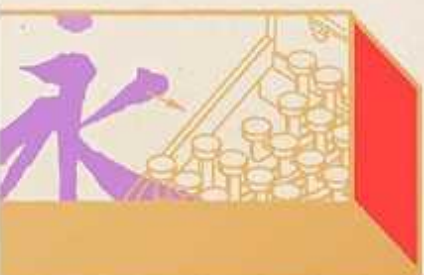
KINGDOM OF CHARACTERS



THE LANGUAGE REVOLUTION
THAT MADE CHINA MODERN



JING TSU



Kingdom of Characters

Jing Tsu *Riverhead* (2022)

Chinese characters have always unified China but isolated it from most of the rest of the world, because of their complexity. Yet, notes US-based sinologist Jing Tsu, “Every technology that has ever confronted the Chinese script, or challenged it, also had to bow before it.” Her stimulating book discusses the typewriter, telegraph, librarian’s catalogue and computer. Human stories include that of physicist Zhi Bingyi, who invented a way to input the characters into computers while imprisoned in a ‘cowshed’ during the Cultural Revolution.

THE END OF GENETICS



Designing
Humanity's
DNA

David B. Goldstein

The End of Genetics

David B. Goldstein *Yale Univ. Press* (2022)

Geneticist David Goldstein thinks that advances in human genomic sequencing and editing signal the end of present-day genetics. But “our technological ability to design the genomes of our children” — possible in 10–30 years, he estimates in this intriguing and disturbing book — “is set to far exceed our knowledge of the consequences.” His informal survey of geneticists revealed little agreement, even in broad outline, on what a common-variant human, created by removing rare, potentially harmful, variants, would look like.



THE CAR THAT KNEW TOO MUCH

Can a Machine Be Moral?

JEAN-FRANÇOIS BONNEFON

The Car That Knew Too Much

Jean-François Bonnefon *MIT Press* (2021)

Will a passenger in a self-driving car involved in an accident accept artificially programmed injury or death to save others? Such dilemmas were explored by the Moral Machine, an online platform devised by psychologist Jean-François Bonnefon and others, which collected 40 million decisions in 10 languages from millions of people in 233 countries and territories ([E. Awad et al. *Nature* 563, 59–64; 2018](#)). Participants preferred to save “the most lives possible, and the lives of the youngest”, notes this intriguing memoir.

Nature **604**, 240 (2022)

doi: <https://doi.org/10.1038/d41586-022-00907-9>

This article was downloaded by **calibre** from <https://www.nature.com/articles/d41586-022-00907-9>

| [Section menu](#) | [Main menu](#) |

Opinion

- **We commercialized a methane capture technology in ten years — here's how** [12 April 2022]

Comment • Lessons from launching a spin-off company: invest in collaborations and engineering, and protect intellectual property to speed up tech development.

- COMMENT
- 12 April 2022

We commercialized a methane capture technology in ten years — here's how

Lessons from launching a spin-off company: invest in collaborations and engineering, and protect intellectual property to speed up tech development.

- [Guoping Hu](#) ⁰,
- [Eric F. May](#) ¹ &
- [Kevin Gang Li](#) ²



A natural-gas flare at a refinery in Corpus Christi, Texas. Credit: Eddie Seal/Bloomberg via Getty

Methane accounts for 16–20% of global greenhouse-gas emissions, and is more potent at trapping heat in the atmosphere than carbon dioxide (see [*Nature* 596, 461; 2021](#)). More than half of methane emissions come from human activities, including leaks from refineries, coal mines and landfill sites. We developed a material that removes methane from streams of mixed waste gases (see, for example, ref. 1).

Commercializing our material took ten years: from developing it in a chemistry laboratory (2011–18), to proving its effectiveness in a coal-mine gas plant (2018–21), to manufacturing and beginning to sell it (2019–21).

That sounds like a long time, but it's actually fast. In our field of industrial chemistry, it often takes up to 20 years to get a product out of the lab and on to the market. Most prototypes fail at the first hurdle — getting industry backing. Patents last for only 20 years, making it a race against time.

The world needs new technologies urgently to avert climate change. Unfortunately, there's little guidance to help academics on the commercialization journey and through unfamiliar territory in the corporate and legal worlds, while juggling university career requirements along the way.

To spur others on, we share here our lessons for speeding up technology translation. Beyond an exciting product, it needs time, money, business management and collaboration across many sectors. Clear identification of the market position of the product, strategic collaboration with key partners, and access to excellent manufacturing and engineering capabilities make a new technology more likely to cross the finish line.

Identify the product

Start with the ‘5W’ questions: what is the product, who are the customers, what are the competing technologies, what is the product’s economic value and what are its social and environmental impacts. The answers will direct

you to the right industries, sources of finance and marketing messages. Address any problems raised in parallel.

Our product is a new type of adsorbent material (ionic liquidic zeolites; ILZs)¹ that captures methane efficiently. It gets around a problem that has challenged chemists for decades — separating methane from nitrogen in the air. The two gases have similar molecule sizes, boiling points and reactive characteristics².

On discovery, it wasn't obvious how our material would be used. Serendipity played a part. K.G.L. moved jobs in 2012 to study natural-gas processing (with E.F.M.) at the University of Western Australia in Perth. We worked on a project to reduce methane emissions from the vent streams of liquefied natural gas plants. ILZ materials seemed a good fit. And the target customers became clear: liquefied natural gas refineries, coal-gas enrichment plants and landfill sites, as well as renewable-biogas production facilities.

We focused first on customers that would reap the most benefits of trialling our technology for the least cost. Large liquefied natural gas plants were too complex. Chinese coal mines fitted the bill. In 2014, natural gas was cheap and abundant in the West but in great demand in China. And China supplies most of the raw materials for adsorbents. Researchers who commercialized porous catalyst materials called metal–organic frameworks³ also started by targeting small-scale research institutions rather than large chemical plants.

Next, we needed to face the competition. Methane treatment is a fast-moving field. There are many options for treating low-grade methane mixtures. Each has pros and cons. Lean-burn gas-to-power generators are portable and simple, but have low yields. Catalytic and thermal oxidizers work well on dilute streams of gases but waste heat energy. Activated carbons are cheap but struggle to separate methane and nitrogen. Our ILZs are more selective but we still had to maximize their performance — by controlling particle shape and size to maximize how much ILZ material could fit inside the industrial vessels used to capture the methane.



Excess methane gas is burnt off at a landfill site.Credit: Robert Brook/Science Photo Library

Pricing is challenging for any new technology. Ultimately, a price is set by estimating the marginal value a technology can deliver to a customer, relative to conventional options, offset by the risk to the customer of doing something new. Cost of production might be high at the outset when there's an immature supply chain. Direct costs (labour, materials, storage, transport and utilities) and indirect expenses (sales, marketing, financing, tax, depreciation and patenting) must be factored in.

At each step, it's important to listen to what customers, partners and other stakeholders say. The product might not be what the market needs right now; the business model might not be profitable. In our case, we sold advanced engineering solutions alongside the materials as a package to add profit — similar to how printer manufacturers make extra money by selling ink cartridges.

Environmental impacts must be considered, such as material toxicity, waste management and carbon footprints. Our materials can be used for 8–20 years, after which they are heated and recycled or buried. This disposal cost is then weighed against the environmental benefits of using the material. One tonne of ILZ can capture about 40 million tonnes of CO₂-equivalent greenhouse gases over its lifetime.

Answers to the ‘5W’ questions might change during the journey, as the technology and supply chain develop. Gather data to define the answers more precisely. Keep an eye on global shifts, in technology, economies and policy.

Protect intellectual property

A patent confers a legal right to make, use and sell a technology for a period of time, often 20 years (as, for example, in the United States, China and Europe). It excludes others from doing so for that time. Trade secrets are an alternative to patents for protecting intellectual property. That requires you to avoid publicizing key manufacturing steps so that they are hard for others to follow. In practice, a mixture of approaches could be used. We started off relying on trade secrets but deployed multiple patents as we proceeded.

First, narrow down which aspect to patent. It could be a material, its use, a device or a concept. Second, talk to an institutional intellectual property (IP) officer and a patent attorney early on. They will know, for example, whether a product has commercial value, whether it is practical to enforce protection, and whether there are sufficient data to support your claims.

We lodged our first provisional patent application in Australia in 2015. That stage requires only a solid proof-of-concept. Accurate wording is crucial.

Start with broad claims, provide specifics to prove inventiveness and disclose as little as possible on specific techniques.

A patent is important for setting up a spin-off company. Albeit intangible, it is the company's initial asset and it attracts collaborators and investors. The security offered by our patent enabled us to disclose our recipe to collaborators, which was crucial for scaling up our product's manufacture.

However, the patent process is lengthy and expensive. It took us between four and seven years from applying for the international patent in Australia (2015), to the award of the first full patents in national territories, in the United States (2019), China and Australia (2021). We invested more than Aus\$20, 000 (roughly US\$15,000) to secure the US patent alone and each patent has an annual fee, as well as the continuing costs for a patent attorney. That's a lot of money for a spin-off. We targeted the countries most likely to provide big markets. And we lodged more patents as the product developed and as other candidates emerged.

That's a long time for any researcher to spend working on a project in the shadows. Most academics, including us, feel conflicted about limiting access to their work. Openness is key for scientific progress. And researchers need publications to get jobs, grants and promotions. For us, that meant walking a narrow line. We chose to publish journal articles on advanced uses of our material⁴, rather than disclose sensitive information about its manufacture. Later on, we were able to say more by citing patents⁵.

Secure funding and partnerships

It takes millions of dollars to move a technology such as ours through the three stages of research and development: laboratory research, industrial demonstration and commercial-plant trials.

The first step, research, is familiar. To develop the material in the lab, we initially received grants totalling a few million dollars from the Australian Research Council (ARC), Western Australia's state government and global energy companies. Cross-collaboration with E.F.M.'s group opened up lines of funding for industrial transformation from the ARC. These enabled us to

scale up the production of our material to kilograms, build apparatus and test the performances of adsorbents and cycles for methane capture.

This stage is where most projects stall. Once the research funding was depleted, we too almost wrapped up the work. Fortunately, the promise of our material urged us on.



The methane-capture plant at Qinshui Basin in Shanxi, China, uses the technology developed by Guoping Hu, Eric May and Kevin Gang Li.Credit: Yongqiang Wang

Accessing funds beyond research grants requires building partnerships with industry and other specialist groups. These might range from chemical, mechanical and electrical engineers to business managers, economists, legal consultants and accountants. It's these interconnections that eventually allow efforts to snowball. Here are some tips.

First, seek strategic partnerships as soon as the product is identified. These might not necessarily be with the big players. We had little luck when we approached large adsorbent and gas-separation companies. But we did get attention when we reached out to small-to-medium enterprises, which were more willing to take risks.

Second, forge international links. These open up funding channels, areas of expertise and markets. Conferences and exhibitions are good places to connect. For example, during a meeting on methane abatement from coal beds, we initiated a collaboration with a Chinese gas-separation company. We agreed to conduct tests while the terms and conditions were being negotiated. We protected our IP through a non-disclosure agreement and by keeping trade secrets while building mutual trust. Such careful steps avoid future business disputes.

Third, access grants for boosting collaborations. In 2017, we were fortunate to receive Aus\$2 million (in direct and in-kind support) through the Australian government's Global Innovation Linkages Program. Those links brought three organizations together to establish a start-up company called Gas Capture Technologies.

Finally, find collaborators wherever conditions are most favourable. For example, we benefited from working with partners in Australia for IP generation, a German manufacturer who supplied specialized raw materials, and gas companies in China for processing and commercial demonstration.

Engage engineers

Good engineering is crucial. Working closely with production engineers can speed things up. For example, working alongside the Chinese manufacturer, it took us two years and many iterations to find a commercially viable recipe for our material (see go.nature.com/3j3tatb). Along the way, we developed a engineering cycle⁶ that allowed us to double our methane-capture efficiency and cut capital costs. Using established facilities, engineers and supporting teams is also faster and cheaper than starting from scratch.

The next step, commercial-plant trials, required us to find an organization that stood to gain from and that was willing to test the technology. After many site visits, workshops and feasibility studies, one of the leading coal-bed methane-gas companies agreed to support us to build our first commercial methane-recovery plant at the Qinshui Basin in Shanxi province, China. It was a small plant in one of the world's largest regions of coal-bed methane reserves. Our team spent five months on site to install, commission and test the plant.

Success won sales orders from customers in North America and Europe, on the basis of information on our website and published papers. We were able to use the Chinese partner's plant to manufacture materials at scale and treat waste. Using others' facilities reduced the time for upscaling by two to three years.

Communicate effectively

Miscommunication is probably the biggest cause of commercialization delays. Misunderstandings waste time and money and cause tensions and delays. Good communication builds trust. Broad teams (accountants, engineers, scientists and sales people) are necessary to be successful but are not all on the same page. A balance needs to be found to engage the whole team, to keep everyone in harmony and to split up specialized work to sub-groups for efficiency. Language and cultural barriers can be an issue in international collaborations, and appointing personnel able to work across different cultural backgrounds was a crucial step.

Communications across disciplines was also key. For example, before constructing a demonstration plant, we ran through every piece of equipment in our piping and instrumentation diagram at least 20 times with the design, mechanical and electrical engineers involved. And we continued to speak to them through the entire process. When the local rainy season interrupted progress, they helped us to get back on course swiftly, for example by improving the instrumentation's water resistance.

What next

More hard work lies ahead — increasing productivity, securing capital and building a robust supply chain. We need to diversify products and revenue streams and hire talented people, who can work full time. For us, it's been a second job alongside academia. Had we known what lay ahead, we might have reached commercial scale even faster by working full time.

If we had the same opportunity again, we'd establish our spin-off sooner, engage with industry more frequently, get more feedback at industry sessions in conferences or exhibitions and put our technology into a commercial environment earlier. We might have applied for patents separately in different countries rather than go through the slow international process.

We call on IP authorities to speed up the patent examination process, communicate more effectively with other jurisdictions, and avoid duplicating patent searches and queries.

Government and institutional support for commercialization is crucial. Long-term support for innovation hubs or parks needs to be sustained. And funding and training should be more systematic and widely available. Training in IP protection and commercialization should be readily available to researchers, from tutors with experiences in the business world and entrepreneurs who are involved in commercialization themselves. Directors' courses, and training in governance and business would also help.

Lastly, we encourage lab researchers who are feeling entrepreneurial to embrace the journey, with patience, perseverance and a proactive approach.

Nature **604**, 242-245 (2022)

doi: <https://doi.org/10.1038/d41586-022-00999-3>

References

1. Li, G., May, E. F., Webley, P. A., Huang, S. H. & Chan, K. I. Method for gas separation. US Patent US20170348670A1 (2015).
2. Rufford, T. E. *et al. J. Pet. Sci. Eng.* **94–95**, 123–154 (2012).

3. Peters, A. W., Howarth, A. J. & Farha, O. K. *Nature* **551**, 433–434 (2017).
4. May, E. F. *et al.* *Sep. Purif. Technol.* **177**, 161–175 (2017).
5. Hu, G. *et al.* *Chem. Eng. J.* **427**, 130810 (2022).
6. Hu, G., Manning, M., Li, G., Xiao, Y. & Webley, P. A. A method for increasing concentration of easily adsorbed gas by pressure swing adsorption. China patent CN110354637B (2021; in Chinese).

This article was downloaded by **calibre** from <https://www.nature.com/articles/d41586-022-00999-3>

| [Section menu](#) | [Main menu](#) |

Work

- **[The marine biologist whose photography pastime became a profession](#)** [25 March 2022]

Career Column • Alexander Semenov's foray into science communication began with amateur photography at a remote research station. His career change has brought him to unvisited dive sites and in direct contact with the public and press.

- **[A grass-roots science movement to rebuild Lebanon](#)** [11 April 2022]

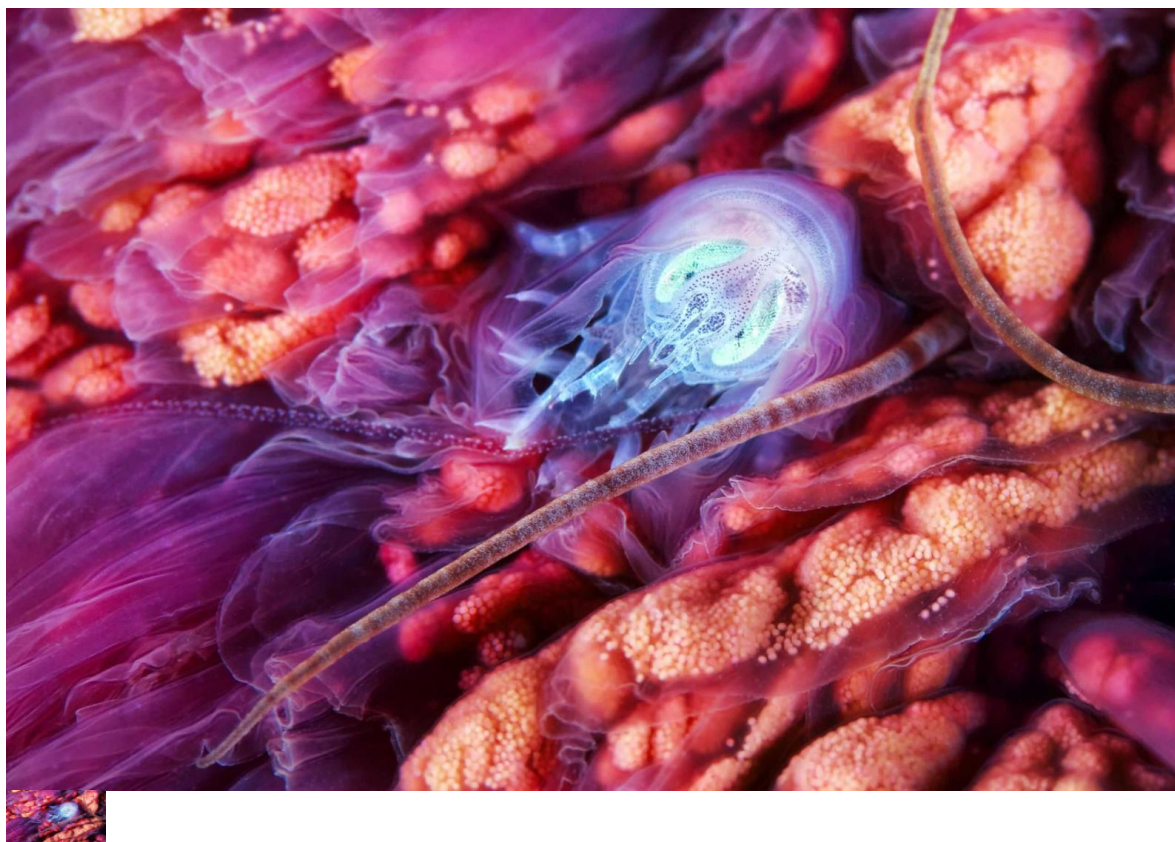
Where I Work • Najat Saliba is pairing researchers around the world with local communities in Lebanon.

The marine biologist whose photography pastime became a profession

By Alexander Semenov

All photos courtesy of Alexander Semenov

25 March 2022



The parasitic amphipod *Hyperia galba* inside the jellyfish *Cyanea capillata*.

The parasitic amphipod *Hyperia galba* inside the jellyfish *Cyanea capillata*.

After graduating with a master's degree in marine biology from Lomonosov Moscow State University in 2007, I joined the White Sea Biological Station in Primorskiy, Russia, as a diver assistant — effectively working as a kind of undersea technician.

The station, a research centre based on the Karelian coast of the White Sea, at the edge of the polar circle, is part of Moscow State University. In my first year, I was so impressed by the beauty of the cold, underwater world and the strangeness of the animals living there that I became obsessed with photographing them.



Alexander Semenov during a field expedition in March 2017.

Alexander Semenov during a field expedition in March 2017.

At first, I pulled invertebrates out of the water and took pictures of them in the laboratory without special lighting or much understanding of the buttons on the camera. I learnt on the fly, just by gut feeling — there was no Internet at the station to help me, so I experimented and tried set-ups, settings and

lighting that came to my mind. Today, I could complete a full-fledged photography course on YouTube in just a few days.

Eventually, the station director asked me for detailed photos of around 300 invertebrate species for an illustrated atlas of the flora and fauna of the White Sea. I was soon able to capture images of any critter larger than 3 millimetres in less than 5 minutes.

Early photography work from Semenov's blog. Species names are (going clockwise): *C. capillata*, *C. limacina*, *Flabellina verrucosa* and its prey *Ectopleyra larynx* (in foreground), *Stomphia coccinea* and sea spider *Nymphon* sp..

Early photography work from Semenov's blog. Species names are (going clockwise): *C. capillata*, *C. limacina*, *Flabellina verrucosa* and its prey *Ectopleyra larynx* (in foreground), *Stomphia coccinea* and sea spider *Nymphon* sp..

I now have a unique collection of images of cold-water invertebrates, some of the least-photographed creatures in the world. I had attempted to get some of those pictures for years, such as one of the sea angel (*Clione limacina*) catching sea butterfly (*Limacina helicina*). The mollusc splits its head in half in an instant and throws out six huge tentacles to trap its prey. The process is lightning-quick: it was impossible for me to get my camera up in time to focus on the tiny 3-centimetre creature furiously waving its wings. After mastering some tricky techniques to feed the angels underwater, I now have more than 50 amazing photos of them hunting.



Thanks to his patience underwater, Semenov captured this photograph of a sea angel trapping a sea butterfly.

Thanks to his patience underwater, Semenov captured this photograph of a sea angel trapping a sea butterfly.

My [blog posts](#) rapidly gained views and great feedback as I uploaded more images, and then I started getting media attention. In 2011, for example, the *BBC Science Focus* magazine paid me for a double-page spread of sea-angel photographs. My fee was equal to two months' salary. I realized that

underwater photography was not only useful for science and science communication, but could also be a source of income.

Semenov learnt to feed sea angels from pipettes, which led to a series of successful photographs.

Semenov learnt to feed sea angels from pipettes, which led to a series of successful photographs.

I am now a professional photographer and lead the scientific diving team at the station. I've won photo contests and, in 2012, *Nature* published one of my images in its compilation of the best scientific photos of the year. *The Magical World of the Cold Seas*, my book about the creatures I photograph, was published in 2016. But for me, the highlights of my career have been the work visits to places no one has ever been diving before. These include the Novaya Zemlya archipelago and some incredible spots on the Kuril Islands, both off Russia's coast.

When I started my career 14 years ago, the university provided underwater equipment and cool cameras. I now provide my own, and show students what can be done with them.

My experience of communicating science through photography has convinced me that someone who is genuinely passionate about what they do is best placed to capture the public's imagination and interest.

Impressive visual content — which includes hand-drawn illustrations, 3D graphics and videos — grabs people's attention in a way that few other methods can. A photograph of a jellyfish ingesting litter can be understood both by a child with no biological training and a policymaker who has data but no emotional understanding of pollution's effects on our oceans. Visual representation of research is the art of finding ways to make implicit knowledge become explicit by providing a pictorial foundation for an understanding of complex issues.



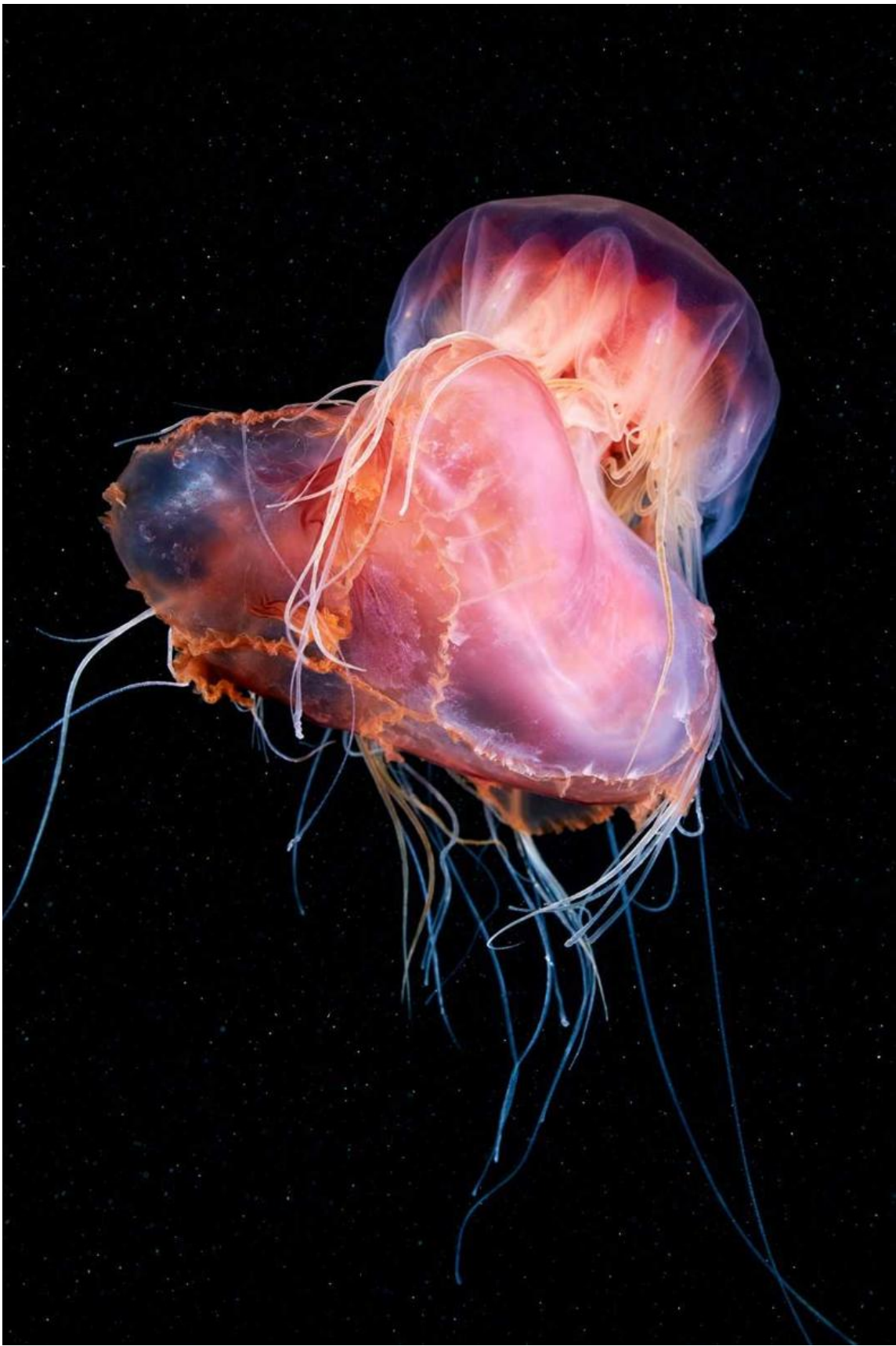
H. galba inside the *C. capillata* jellyfish. Photographed in August 2016.

H. galba inside the *C. capillata* jellyfish. Photographed in August 2016.



A king ragworm (*Alitta virens*), photographed in July 2012.

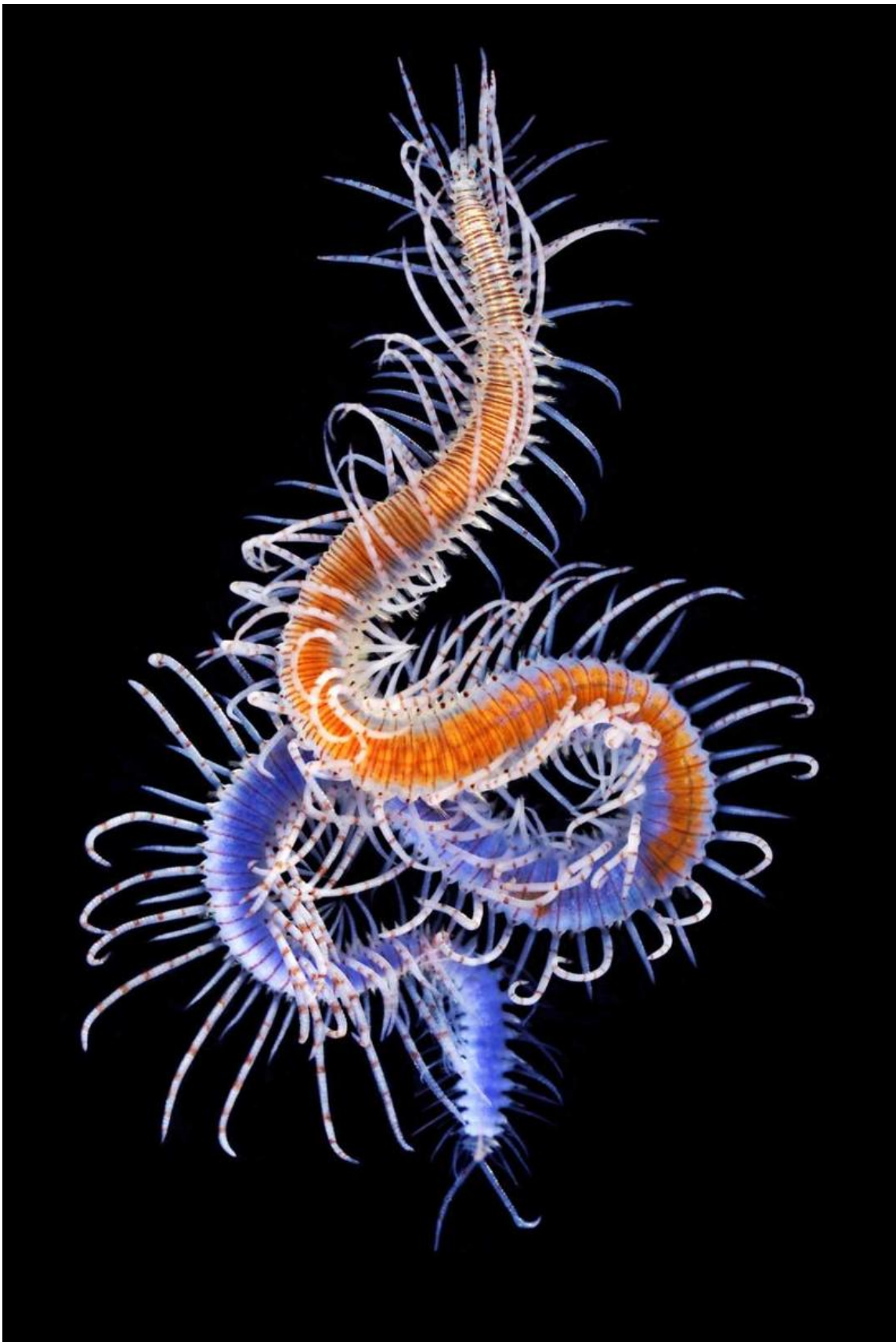
A king ragworm (*Alitta virens*), photographed in July 2012.



A *C. capillata* jellyfish eating an *Aurelia* jellyfish, photographed in June 2018.

If you are a scientist hoping to photograph and share your own research:

- Don't underestimate the power of modern media and social-media platforms. Content is changing the world and people's lives, and it can easily change your life. Stay at the forefront of media technology, or at least be aware of developments. It's a never-ending race, but it's easy to get into.
- If you plan to share your work with others, imagine what will be of interest to them. If you can excitingly describe your work to a 5-year-old, you won't have any trouble getting anyone interested. Beautiful pictures help, but the story always comes first.



Syllis maganda — a new species discovered and photographed at the Lizard Island Research Station in the Coral Sea in July 2012.

- You will stand out much more if you have a niche and unique story. It could be your rare field of science or a special angle that you use to tell the story of your work. Being different is awesome.
- Set the bar very high. You can find dozens of examples of truly high-quality content on the Internet. And you can almost always find resources that can help you to learn how to create work of the same calibre. With practice, your skills will inevitably rise — but at any given time, it's important to know the level you should aim for.
- Find people who are cooler than you. Don't hesitate to ask them for advice or to shadow them. Have them share their experiences, stand behind them and observe their work if they'll let you. Few things are more useful than real work experience, both your own and that of others.
- Take on a project. This could be a an illustrated workbook for colleagues or students, a guide book, a lecture for schoolchildren with compelling visuals, a course for students or a documentary on your topic.
- If you work in a team, you can raise the bar even higher. Use each other's strengths, share experiences, make plans, apply for grants and take on challenging science-communication projects together. This multiplies the fun and the results.

A *C. capillata* jellyfish eating an *Aurelia* jellyfish, photographed in June 2018.

A *C. capillata* jellyfish eating an *Aurelia* jellyfish, photographed in June 2018.

Syllis maganda — a new species discovered and photographed at the Lizard Island Research Station in the Coral Sea in July 2012.

Syllis maganda — a new species discovered and photographed at the Lizard Island Research Station in the Coral Sea in July 2012.

Alexander Semenov is a marine biologist and head of the scientific diving team at the White Sea Biological Station of Moscow State University.

Correction 30 March 2022: A picture caption in an earlier version of this story erroneously stated that *Hyperia galba* was caught by a jellyfish. In fact, it is a parasite of jellyfish.

SPRINGER NATURE

Springer Nature

- [Privacy Policy](#)
- [Use of cookies](#)
- [Legal notice](#)
- [Terms & Conditions](#)
- [Accessibility statement](#)

© 2021 Springer Nature Limited. All rights reserved.

[Top](#)[Built with Shorthand](#)

This article was downloaded by **calibre** from <https://www.nature.com/articles/d41586-022-00757-5>

| [Section menu](#) | [Main menu](#) |

- WHERE I WORK
- 11 April 2022

A grass-roots science movement to rebuild Lebanon

Najat Saliba is pairing researchers around the world with local communities in Lebanon.

- [Benjamin Plackett](#)



Najat Saliba is an associate professor of analytical chemistry at the American University of Beirut in Lebanon and co-founder of the Environment Academy. Credit: Diego Ibarra Sánchez for *Nature*

I'm standing among the pine trees of Ras El Metn, about a 40-minute drive from Beirut. There's still snow on the hill crests and it makes for an imposing outlook.

We have a picturesque country, but it's threatened by air and water pollution, poor urban planning and negligence. Lebanon is deeply troubled. We've contended with COVID-19 like everyone else, but we're also experiencing economic collapse and political turmoil. And there was the 2020 explosion at the Port of Beirut — caused by incorrectly stored chemicals — that was the world's largest non-nuclear blast.

I've been studying air pollution in Lebanon for many years, collecting data to try to convince the government to act, but with no real results. The level of particulate pollution in Beirut, for example, is 3.8 times what the World Health Organization considers safe.

Surrounded by these disasters, I realized that I needed to get off the university campus and work with local communities to make a difference. In 2019, I co-founded the Environment Academy. It's a collective of researchers — experts in disciplines from wastewater management and engineering to soil biophysics — united by a desire to use their expertise to assist people living in Lebanon. Communities apply to the academy for help with various projects, and we match them with a relevant expert.

Here, I'm standing in one of these projects. The community in and around Ras El Metn wanted advice about how to protect the forest from fires — probably made worse by climate change — and regenerate what's been lost to flames. The Environment Academy paired them with the Lebanese Reforestation Initiative, a non-governmental organization. It is advising on the most important species to replant, and building paths so that firefighters can access forest fires.

Through direct action like this, bringing the scientific process into the community, researchers can feel their work has an impact.

Nature **604**, 394 (2022)

doi: <https://doi.org/10.1038/d41586-022-01000-x>

This article was downloaded by **calibre** from <https://www.nature.com/articles/d41586-022-01000-x>

| [Section menu](#) | [Main menu](#) |

Research

- [**Brain-inspired computing needs a master plan**](#) [13 April 2022]
Perspective • The benefits and future prospects of neuromorphic, or bio-inspired, computing technologies are discussed, as is the need for a global, coordinated approach to funding, research and collaboration.
- [**A joint NCBI and EMBL-EBI transcript set for clinical genomics and research**](#) [06 April 2022]
Analysis • Matched Annotation from NCBI and EMBL-EBI (MANE) delivers joint transcript sets from Ensembl/Gencode and RefSeq for standardizing variant reporting in clinical genomics and research.
- [**Thermophotovoltaic efficiency of 40%**](#) [13 April 2022]
Article • Two-junction TPV cells with efficiencies of more than 40% are reported, using an emitter with a temperature between 1,900 and 2,400 °C, for integration into a TPV system for thermal energy grid storage.
- [**Synthesis of chiral sulfinate esters by asymmetric condensation**](#) [14 February 2022]
Article • A synthetic strategy for the stereoselective preparation of sulfinate esters and related sulfur stereogenic centres via asymmetric condensation expands the drug discovery toolbox for these compounds.
- [**Bat coronaviruses related to SARS-CoV-2 and infectious for human cells**](#) [16 February 2022]
Article • A study reports the detection and characterization of SARS-CoV-2-like viruses in Laotian cave-dwelling bats that are also demonstrated to infect human cells through the ACE2 pathway.
- [**Compartmentalized metabolism supports midgestation mammalian development**](#) [06 April 2022]
Article • Metabolomics analysis of the mouse embryo shows a metabolic shift towards the tricarboxylic acid cycle between gestational days 10.5 and 11.5, leading to the subsequent development of organ-specific metabolic programmes.
- [**Capturing a rhodopsin receptor signalling cascade across a native membrane**](#) [06 April 2022]
Article • The rhodopsin signalling cascade, initiated by light, is captured using mass spectrometry of a native membrane.

| [Next section](#) | [Main menu](#) | [Previous section](#) |

[Download PDF](#)

- Perspective
- [Published: 13 April 2022](#)

Brain-inspired computing needs a master plan

- [A. Mehonic](#) [ORCID: orcid.org/0000-0002-2476-5038¹](#) &
- [A. J. Kenyon](#) [ORCID: orcid.org/0000-0003-2249-2184¹](#)

Nature volume **604**, pages 255–260 (2022)

- 8573 Accesses
- 86 Altmetric
- [Metrics details](#)

Subjects

- [Electrical and electronic engineering](#)
- [Information technology](#)

Abstract

New computing technologies inspired by the brain promise fundamentally different ways to process information with extreme energy efficiency and the ability to handle the avalanche of unstructured and noisy data that we are generating at an ever-increasing rate. To realize this promise requires a brave and coordinated plan to bring together disparate research communities and to provide them with the funding, focus and support needed. We have done

this in the past with digital technologies; we are in the process of doing it with quantum technologies; can we now do it for brain-inspired computing?

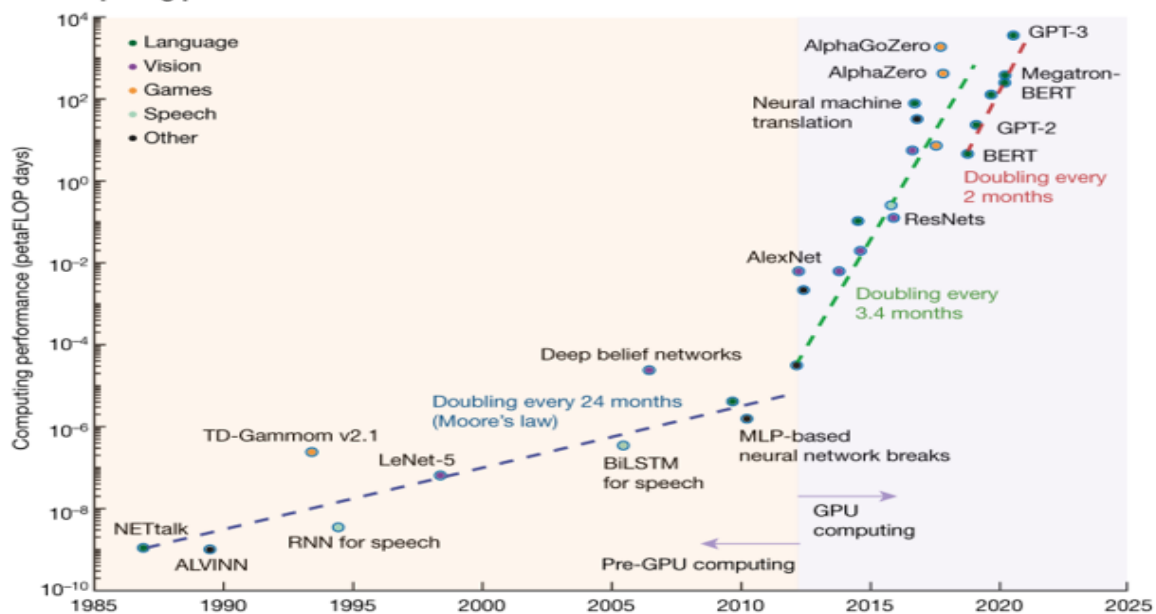
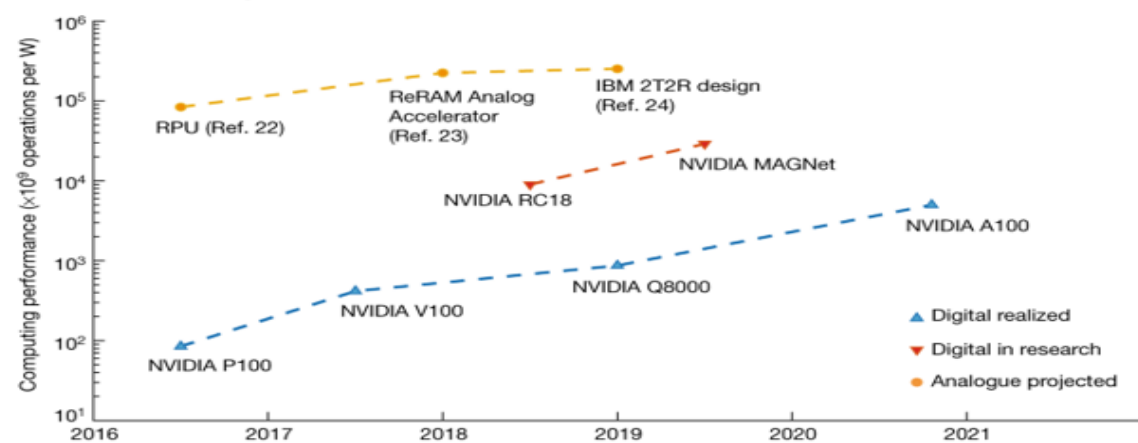
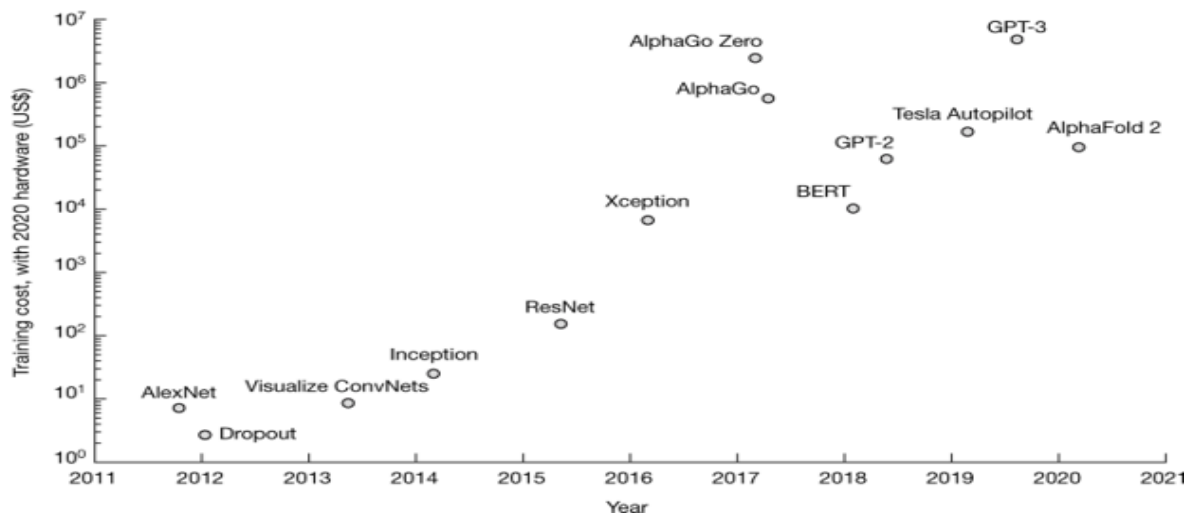
Main

Modern computing systems consume far too much energy. They are not sustainable platforms for the complex artificial intelligence (AI) applications that are increasingly a part of our lives. We usually do not see this, particularly in the case of cloud-based systems, as we focus on functionality —how fast are they; how accurate; how many parallel operations per second? We are so accustomed to accessing information near-instantaneously that we neglect the energy—and therefore environmental—consequences of the computing systems giving us this access. Nevertheless, each Google search has a cost: data centres currently use around 200 terawatt hours of energy per year, forecast to grow by around an order of magnitude by 2030¹. Similarly, the astonishing achievements of high-end AI systems such as DeepMind’s AlphaGo and AlphaZero, which can beat human experts at complex strategy games, require thousands of parallel processing units, each of which can consume around 200 watts (ref. ²).

Although not all data-intensive computing requires AI or deep learning, deep learning is deployed so widely that we must worry about its environmental cost. We should also consider applications including the Internet of Things (IoT) and autonomous robotic agents that may not need always to be operated by computationally intense deep learning algorithms but must still reduce their energy consumption. The vision of the IoT cannot be achieved if the energy requirements of the myriad connected devices are too high. Recent analysis shows that increasing demand for computing power vastly outpaces improvements made through Moore’s law scaling³. Computing power demands now double every two months (Fig. [1a](#)). Remarkable improvements have been made through a combination of smart architecture and software–hardware co-design. For example, the performance of NVIDIA GPUs (graphics processing units) has improved by the factor of 317 since 2012: far beyond what would be expected from Moore’s law alone (Fig. [1b](#))—although the power consumption of units has increased from approximately 25 W to around 320 W in the same period. Further impressive performance improvements have been demonstrated at

the research and development stage (Fig. [1b](#), red) and it is likely that we can achieve more^{[4,5](#)}. Unfortunately, it is unlikely that conventional computing solutions alone will cope with demand over an extended period. This is especially apparent when we consider the shockingly high cost of training required for the most complex deep learning models (Fig. [1c](#)). We need alternative approaches.

Fig. 1 : Computational demands are increasing rapidly.

a Computing power demands**b Hardware development****c Cost**

a, The increase in computing power demands over the past four decades expressed in petaFLOPS days. Until 2012, computing power demand doubled every 24 months; recently this has shortened to approximately every 2 months. The colour legend indicates different application domains. Data are from ref. [3](#). **b**, Improvements in AI hardware efficiency over the past five years. State-of-the-art solutions have driven increases in computing efficiency of more than 300 times. Solutions in research and development promise further improvements [22,23,24](#). **c**, Increase since 2011 of the costs of training AI models. Such an exponential increase is clearly unsustainable. Data are from ref. [25](#).

The energy problem is largely a consequence of digital computing systems storing data separately from where they are processed. This is the classical von Neumann architecture underpinning digital computing systems. Processors spend most of their time and energy moving data. Fortunately, we can improve the situation by taking inspiration from biology, which takes a different approach entirely—co-locating memory and processing, encoding information in a wholly different way or operating directly on signals, and employing massive parallelism, for example (Box 1). There is a system that achieves both energy efficiency and advanced functionality remarkably well: the brain. Recognizing that we still have much to learn about how the brain operates and that our aim is not simply to emulate biological systems, we can nevertheless learn from the substantial progress in neuroscience and computational neuroscience in the last few decades. We know just enough about the brain to use it as an inspiration.

Box 1 ■ What do we mean by ‘neuromorphic’ systems?

Taking inspiration from the brain allows us to approach information processing fundamentally differently to the way existing conventional computing systems work. Different brain-inspired ('neuromorphic') platforms use combinations of different approaches: analogue data processing, asynchronous communication, massively parallel information processing or spiking-based information representation. These properties distinguish them from von Neumann computers.

The term neuromorphic encompasses at least three broad communities of researchers, distinguished by whether their aim is to emulate neural function (reverse-engineer the brain), simulate neural networks (develop new computational approaches), or engineer new classes of electronic device.

‘Neuromorphic engineering’ looks at how the brain uses the physics of biological synapses and neurons to ‘compute’. Neuromorphic engineers work to emulate the functions of biological neurons and synapses by harnessing the physics of analogue electronics—such as carrier tunnelling, charge retention on silicon floating gates, and the exponential dependence of various device or material properties on field—to define elementary operations to underpin audio or video processing or smart sensors, for example. Transistors are used as analogue circuit elements with rich dynamic behaviour rather than binary switches. More details can be found in ref. [41](#) and related work.

‘Neuromorphic computing’ looks to biology to inspire new ways to process data. This could be considered as the computing science of neuromorphic systems. Research looks to simulate the structure and/or operation of biological neural networks, which may mean co-locating storage and computing, as the brain does; or perhaps adopting wholly different ways of computing based on voltage spikes modelling the action potentials of biological systems.

Underpinning everything are the devices and materials needed to implement bio-inspired functions. Here, recent developments promise new electronic and photonic devices, the properties of which we can tailor to mimic biological elements such as synapses and neurons. These ‘neuromorphic devices’ could provide exciting new technologies to expand the capabilities of neuromorphic engineering and computing.

Foremost amongst these new devices are memristors: electronic devices the resistance of which is a function of their history. Their complex dynamic electrical response means they can be used as digital memory elements, as variable weights in artificial synapses, as cognitive processing elements, optical sensors, and devices that mimic biological neurons^{[42](#)}. They may embody some of the functionality of biological dendrites^{[43](#)} and their dynamic response can generate oscillatory behaviour similar to that of the

brain—controversially, operating on the ‘edge of chaos’^{44,45}. They may also be linked with biological neurons in a single system⁴⁶. They do all of this while expending very little energy.

Biological inspiration

In biology, data storage is not separate from processing. The same elements—principally neurons and synapses—perform both functions in massively parallel and adaptable structures. The 10^{11} neurons and 10^{15} synapses contained in the typical human brain expend approximately 20 W of power, whereas a digital simulation of an artificial neural network of approximately the same size consumes 7.9 MW (ref. [6](#)). That six-order-of-magnitude gap poses us a challenge. The brain directly processes with extreme efficiency signals that are noisy. This contrasts with the signal-to-data conversion and high-precision computing in our conventional computer system that produces huge costs in energy and time for even the most powerful digital supercomputers. Brain-inspired, or ‘neuromorphic’, computing systems could therefore transform the way we process signals and data, both in terms of energy efficiency and of their capacity to handle real-world uncertainty.

This is not a new idea. The term neuromorphic, describing devices and systems that mimic some functions of biological neural systems, was coined in the late 1980s by Carver Mead at the California Institute of Technology^{7,8}. The inspiration came from work undertaken over previous decades to model the nervous system as equivalent electrical circuits⁹ and to build analogue electronic devices and systems to provide similar functionality (Box 1).

A word about ‘data’. We use the term to describe information encoded in, say, an analogue signal or the physical response of a sensor, as well as the more standard computing-focused sense of digital data. When we refer to the brain “processing data” we describe an integrated set of signal-processing tasks that do not rely on digitization of signals in any conventional sense. We can think of brain-inspired systems operating at different levels: from analogue signal processing to working with large digital datasets. In the former case, we can avoid generating large datasets in the first place; in the latter we can greatly increase the efficiency of processing by moving away from the von Neumann model. Of course, there are good reasons why we

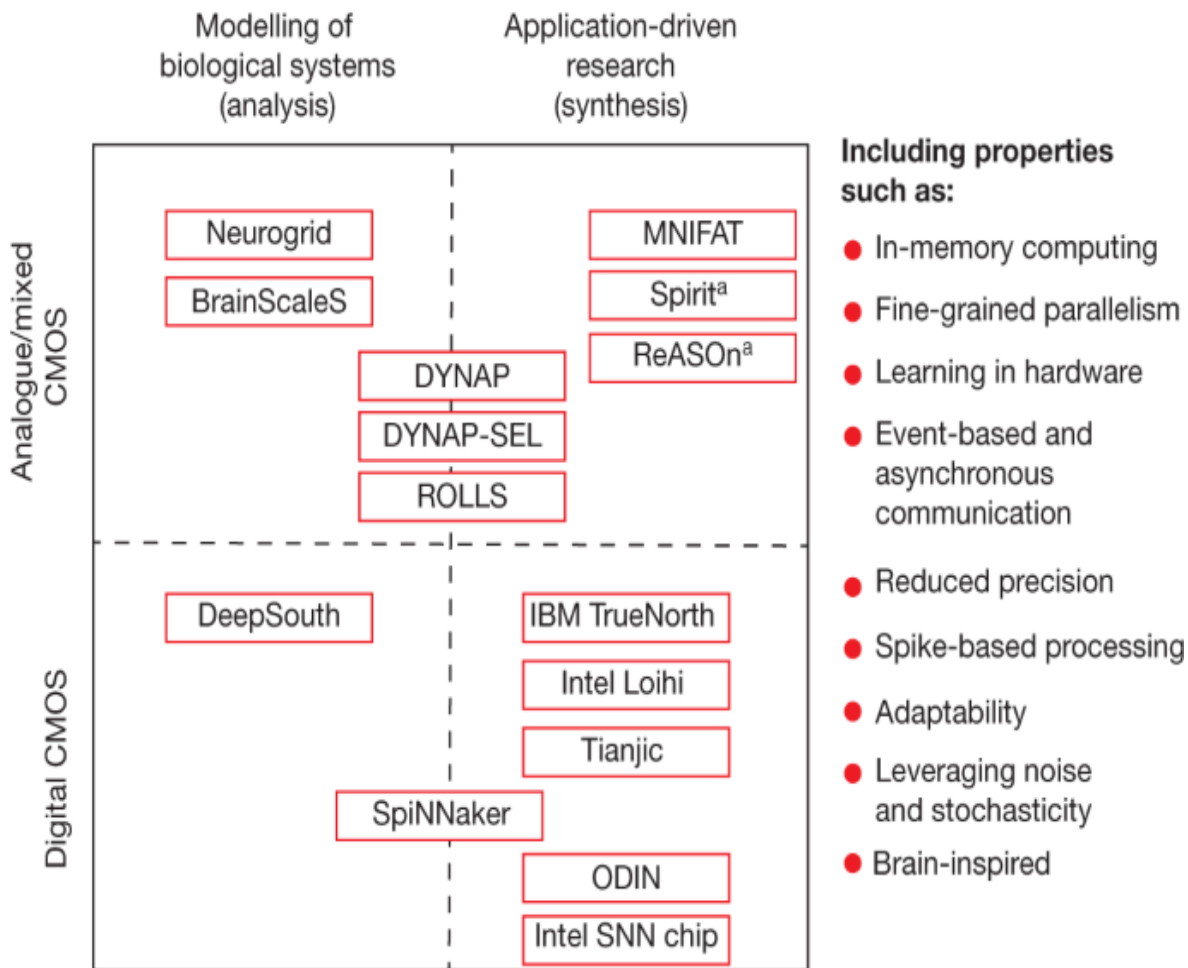
represent data digitally for many applications: we want high precision, reliability and determinacy. However, digital abstraction discards massive amounts of information, found in the physics of transistors, for the minimum information quantum: a single bit. And we pay a considerable energy cost by trading efficiency for reliability. AI applications are often probabilistic at heart, and so we must consider if this trade-off makes sense. The computational tasks underpinning AI applications are very compute-intensive (and therefore energy-hungry) when performed by conventional von Neumann computers. However, we might perform similar tasks much more energy-efficiently on analogue or mixed systems that use a spike-based representation of information. There has therefore been a recent resurgence in interest in neuromorphic computing, driven by the growth in AI systems and by the emergence of new devices that offer new and exciting ways to mimic some of the capabilities of biological neural systems (Box 1).

Definitions of ‘neuromorphic’ vary considerably. Loosely speaking, the story is a hardware one: neuromorphic chips aim to integrate and utilize various useful features of the brain, including in-memory computing, spike-based information processing, fine-grained parallelism, signal processing resilient to noise and stochasticity, adaptability, learning in hardware, asynchronous communication, and analogue processing. Although it is debatable how many of these need to be implemented for something to be classified as neuromorphic, this is clearly a different approach from AI implemented on mainstream computing systems. Nevertheless, we should not be lost in terminology; the main question is whether this approach is useful.

Approaches to neuromorphic technologies lie on a spectrum between reverse-engineering the structure and function of the brain (analysis) and living with our current lack of knowledge of the brain but taking inspiration from what we do know (synthesis). Perhaps foremost among the former approaches is the Human Brain Project, a high-profile and hugely ambitious ten-year programme funded by the European Union from 2013. The programme supported the adoption and further development of two existing neuromorphic hardware platforms—SpiNNaker (at The University of Manchester) and BrainScaleS (at Heidelberg University)—as openly accessible neuromorphic platforms. Both systems implement highly complex silicon models of brain architectures to better understand the

operation of the biological brain. At the other end of the spectrum, numerous groups augment the performance of digital or analogue electronics using selected biologically inspired methods. Figure 2 summarizes the range of existing neuromorphic chips, divided into four categories depending on their position on the analysis–synthesis spectrum and their technology platform. It is important to remember that neuromorphic engineering is not just about high-level cognitive systems, but also offering energy, speed and security gains (at least by removing the need for constant communication to the cloud) in small-scale edge devices with limited cognitive abilities.

Fig. 2: The landscape of neuromorphic systems.
Neuromorphic chips



Neuromorphic chips can be classified as either modelling biological systems or applying brain-inspired principles to novel computing applications. They may be further subdivided into those based on digital CMOS with novel

architecture (for example, spikes may be simulated in the digital domain rather than implemented as analogue voltages) and those implemented using some degree of analogue circuitry. In all cases, however, they share at least some of the properties listed on the right-hand side, which distinguish them from conventional CMOS chips. Here we classify examples of recently developed neuromorphic chips. Further details of each can be found in the relevant reference: Neurogrid²⁶, BrainSclaseS²⁷, MNIFAT²⁸, DYNAP²⁹, DYNAP-SEL³⁰, ROLLS³¹, Spirit³², ReASON³³, DeepSouth³⁴, SpiNNaker³⁵, IBM TrueNorth³⁶, Intel Loihi³⁷, Tianjic³⁸, ODIN³⁹ and the Intel SNN chip⁴⁰. ^aImplemented with memristors.

Prospects

We do not propose that neuromorphic systems will, or should, replace conventional computing platforms. Instead, precision calculations should remain the preserve of digital computation, whereas neuromorphic systems can process unstructured data, perform image recognition, classification of noisy and uncertain datasets, and underpin novel learning and inference systems. In autonomous and IoT-connected systems, they can provide huge energy savings over their conventional counterparts. Quantum computing is also part of this vision. A practical quantum computer, although still several years away by any estimation, would certainly revolutionize many computing tasks. However, it is unlikely that IoT-connected smart sensors, edge computing devices, or autonomous robotic systems will adopt quantum computing without depending on cloud computing. There will remain a need for low-power computing elements capable of dealing with uncertain and noisy data. We can imagine a three-way synergy between digital, neuromorphic and quantum systems.

Just as the development of semiconductor microelectronics relied on many different disciplines, including solid-state physics, electronic engineering, computer science and materials science, neuromorphic computing is profoundly cross- and inter-disciplinary. Physicists, chemists, engineers, computer scientists, biologists and neuroscientists all have key roles. Simply getting researchers from such a diverse set of disciplines to speak a common language is challenging. In our own work we spend considerable time and effort ensuring that everyone in the room understands terminology and

concepts in the same way. A case for bridging the communities of computer science (specifically AI) and neuroscience (initially computational neuroscience) is clear. After all, many concepts found in today's state-of-the-art AI systems arose in the 1970s and 80s in neuroscience, although, of course, AI systems need not be completely bio-realistic. We must include other disciplines, recognizing that many of the strides we have made in AI or neuroscience have been enabled by different communities—for example, innovations in material science, nanotechnology or electronic engineering. Further, conventional CMOS (complementary metal–oxide–semiconductor) technology may not be the best fabric with which to efficiently implement new brain-inspired algorithms; innovations across the board are needed. Engaging these communities early reduces the risk of wasting effort on directions that have already been explored and failed, or of reinventing the wheel.

Further, we should not neglect the challenges of integrating new neuromorphic technologies at the system level. Beyond the development of brain-inspired devices and algorithms there are pressing questions around how existing, mainstream, AI systems can be replaced with functionally equivalent neuromorphic alternatives. This further emphasizes the need for a fully integrated approach to brain-inspired computation.

We should point out that, despite the potential outlined above, there is as yet no compelling demonstration of a commercial neuromorphic technology. Existing systems and platforms are primarily research tools. However, this is equally true of quantum computing, which remains a longer-term prospect. We should not let this delay the development of brain-inspired computing; the need for lower-power computing systems is pressing and we are tantalizingly close to achieving this with all the added functionality that comes from a radically different approach to computation. Commercial systems will surely emerge.

Seizing the opportunity

If neuromorphic computing is needed, how can it be achieved? First, the technical requirements. Bringing together diverse research communities is necessary but not sufficient. Incentives, opportunities and infrastructure are

needed. The neuromorphic community is a disparate one lacking the focus of quantum computing, or the clear roadmap of the semiconductor industry. Initiatives around the globe are starting to gather the required expertise, and early-stage momentum is building. To foster this, funding is key. Investment in neuromorphic research is nowhere near the scale of that in digital AI or quantum technologies (Box 2). Although that is not surprising given the maturity of digital semiconductor technology, it is a missed opportunity. There are a few examples of medium-scale investment in neuromorphic research and development, such as the IBM AI Hardware Centre’s range of brain-inspired projects (including the TrueNorth chip), Intel’s development of the Loihi processor, and the US Brain Initiative project, but the sums committed are well below what they should be given the promise of the technology to disrupt digital AI.

The neuromorphic community is a large and growing one, but one that lacks a focus. Although there are numerous conferences, symposia and journals emerging in this space there remains much work to be done to bring the disparate communities together and to corral their efforts to persuade funding bodies and governments of the importance of this field.

The time is ripe for bold initiatives. At a national level, governments need to work with academic researchers and industry to create mission-oriented research centres to accelerate the development of neuromorphic technologies. This has worked well in areas such as quantum technologies and nanotechnology—the US National Nanotechnology Initiative demonstrates this very well¹⁰, and provides focus and stimulus. Such centres may be physical or virtual but must bring together the best researchers across diverse fields. Their approach must be different from that of conventional electronic technologies in which every level of abstraction (materials, devices, circuits, systems, algorithms and applications) belongs to a different community. We need holistic and concurrent design across the whole stack. It is not enough for circuit designers to consult computational neuroscientists before designing systems; engineers and neuroscientists must work together throughout the process to ensure as full an integration of bio-inspired principles into hardware as possible. Interdisciplinary co-creation must be at the heart of our approach. Research centres must house a broad constituency of researchers.

Alongside the required physical and financial infrastructure, we need a trained workforce. Electronic engineers are rarely exposed to ideas from neuroscience, and vice versa. Circuit designers and physicists may have a passing knowledge of neurons and synapses but are unlikely to be familiar with cutting-edge computational neuroscience. There is a strong case to set up Masters courses and doctoral training programmes to develop neuromorphic engineers. UK research councils sponsor Centres for Doctoral Training (CDTs), which are focused programmes supporting areas with an identified need for trained researchers. CDTs can be single- or multi-institution; there are substantial benefits to institutions collaborating on these programmes by creating complementary teams across institutional boundaries. Programmes generally work closely with industry and build cohorts of highly skilled researchers in ways that more traditional doctoral programmes often do not. There is a good case to be made to develop something similar, to stimulate interaction between nascent neuromorphic engineering communities and provide the next generation of researchers and research leaders. Pioneering examples include the Groningen Cognitive Systems and Materials research programme, which aims to train tens of doctoral students specifically in materials for cognitive (AI) systems^{[11](#)}, the Masters programme in neuroengineering at the Technical University of Munich^{[12](#)}; ETH Zurich courses on analogue circuit design for neuromorphic engineering^{[13](#)}; large-scale neural modelling at Stanford University^{[14](#)}; and development of visual neuromorphic systems at the Instituto de Microelectrónica de Sevilla^{[15](#)}. There is scope to do much more.

Similar approaches could work at the trans-national level. As always in research, collaboration is most successful when it is the best working with the best, irrespective of borders. In such an interdisciplinary endeavour as neuromorphic computing this is critical, so international research networks and projects undoubtedly have a part to play. Early examples include the European Neurotech consortium^{[16](#)}, focusing on neuromorphic computing technologies, as well as the Chua Memristor Centre at the University of Dresden^{[17](#)}, which brings together many of the leading memristor researchers across materials, devices and algorithms. Again, much more can and must be done.

How can this be made attractive to governments? Government commitment to more energy-efficient bio-inspired computing can be part of a broader large-scale decarbonization push. This will not only address climate change but also will accelerate the emergence of new, low-carbon, industries around big data, IoT, healthcare analytics, modelling for drug and vaccine discovery, and robotics, amongst others. If existing industries rely on ever more large-scale conventional digital data analysis, they increase their energy cost while offering sub-optimal performance. We can instead create a virtuous circle in which we greatly reduce the carbon footprint of the knowledge technologies that will drive the next generation of disruptive industries and, in doing so, seed a host of new neuromorphic industries.

If this sounds a tall order, consider quantum technologies. In the UK the government has so far committed around £1 billion to a range of quantum initiatives, largely under the umbrella of the National Quantum Technologies Programme. A series of research hubs, bringing together industry and academia, translate quantum science into technologies targeted at sensors and metrology, imaging, communications and computing. A separate National Quantum Computing Centre builds on the work of the hubs and other researchers to deliver demonstrator hardware and software to develop a general-purpose quantum computer. China has established a multi-billion (US) dollar Chinese National Laboratory for Quantum Information Sciences, and the USA in 2018 commissioned a National Strategic Overview for Quantum Information Science¹⁸, which resulted in a five-year US\$1.2 billion investment, on top of supporting a range of national quantum research centres¹⁹. Thanks to this research work there has been a global rush to start up quantum technology companies. One analysis found that in 2017 and 2018 funding for private companies reached \$450 million²⁰. No such joined-up support exists for neuromorphic computing, despite the technology being more established than quantum, and despite its potential to disrupt existing AI technologies on a much shorter time horizon. Of the three strands of future computing in our vision, neuromorphic is woefully under-invested.

Finally, some words about what bearing the COVID-19 pandemic might have on our arguments. There is a growing consensus that the crisis has accelerated many developments already under way: for example, the move

to more homeworking. Although reducing commuting and travel has direct benefits—some estimates put the reduction in global CO₂ as a result of the crisis at up to 17%²¹—new ways of working have a cost. To what extent will carbon savings from reduced travel be offset by increased data centre emissions? If anything, the COVID pandemic further emphasizes the need to develop low-carbon computing technologies such as neuromorphic systems.

Our message about how to realize the potential of neuromorphic systems is clear: provide targeted support for collaborative research through the establishment of research centres of excellence; provide agile funding mechanisms to enable rapid progress; provide mechanisms for close collaboration with industry to bring in commercial funding and generate new spin-outs and start-ups, similar to schemes already in place for quantum technology; develop training programmes for the next generation of neuromorphic researchers and entrepreneurs; and do all of this quickly and at scale.

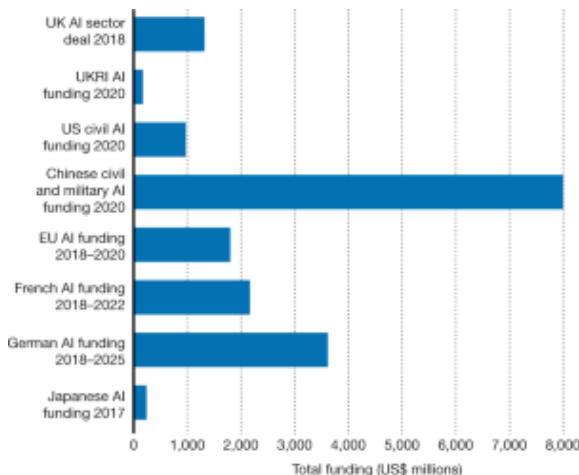
Neuromorphic computing has the potential to transform our approach to AI. Thanks to the conjunction of new technologies and a massive, growing demand for efficient AI we have a timely opportunity. Bold thinking is needed, and bold initiatives to support this thinking. Will we seize the opportunity?

Box 2 The AI funding landscape

Investment in ‘conventional’ digital AI is booming, fuelled by the need to process ever-increasing volumes of data, and the development of hardware to support existing compute- and memory-intensive algorithms. The UK government announced in April 2018 a £950 million ‘sector deal’ in digital AI, in addition to existing research council support. France announced a €1.8 billion government investment in AI from 2018 to 2022⁴⁷, Germany committed €3 billion from 2018 to 2025, and Japan spent ¥26 trillion in 2017. US government funding of civil AI technologies was US\$973 million in 2020⁴⁸; figures are harder to come by for US military AI funding, as non-AI projects are often included in published analysis. China is estimated to be investing up to US\$8 billion in both civil and military AI and is constructing a US\$2.1 billion AI research park near Beijing⁴⁹, and the European

Commission committed €1.5 billion in the period 2018–2020⁵⁰. Commercial investment dwarfs this. In the USA one estimate puts the total investment in AI companies in 2019 at \$19.5 billion⁵¹, and global investment is predicted to be around \$98 billion by 2023⁵². Such sums must be considered at risk if our current hardware systems cannot support potentially disruptive neuromorphic algorithms and architectures. If neuromorphic technologies offer anything like the efficiency savings and enhanced performance they promise, smart money will hedge its bets on novel technologies and architectures alongside digital systems.

Comparable figures are not available for neuromorphic technologies, as they currently lack focus and government-level visibility. Research funding is therefore piecemeal and at project, rather than strategic, level. Although there have been various estimates published—for example, that the global neuromorphic chip market will grow from US\$22.7 million in 2021 to \$550.6 million in 2026⁵³, the safest conclusion to draw is that funding of neuromorphic systems lags way behind that of digital AI or of quantum.



Box 2 Figure | A comparison of recent global public research funding of digital AI technologies.

Figures are in US dollar equivalent (2021 exchange rate) and are expressed as millions of dollars.

Whereas some are in-year snapshots (for example, UKRI funding committed for 2020), some have no

specified period (the UK AI sector deal, for example), and others are for multi-year programmes, the figure illustrates the scale of public funding in digital technologies. Disruption of the AI ecosystem by the development of efficient neuromorphic technologies would put much of this investment at risk.

References

1. Jones, N. How to stop data centres from gobbling up the world's electricity. *Nature* <https://doi.org/10.1038/d41586-018-06610-y> (12 September 2018).
2. Wu, K. J. Google's new AI is a master of games, but how does it compare to the human mind? *Smithsonian* <https://www.smithsonianmag.com/innovation/google-ai-deepminds-alphazero-games-chess-and-go-180970981/> (10 December 2018).
3. Amodei, D. & Hernandez, D. AI and compute. *OpenAI Blog* <https://openai.com/blog/ai-and-compute/> (16 May 2018).
4. Venkatesan, R. et al. in *2019 IEEE Hot Chips 31 Symp. (HCS)* <https://doi.org/10.1109/HOTCHIPS.2019.8875657> (IEEE, 2019).
5. Venkatesan, R. et al. in *2019 IEEE/ACM Intl Conf. Computer-Aided Design (ICCAD)* <https://doi.org/10.1109/ICCAD45719.2019.8942127> (IEEE, 2019).
6. Wong, T. M. et al. 10^{14} . Report no. RJ10502 (ALM1211-004) (IBM, 2012). **The power consumption of this simulation of the brain puts that of conventional digital systems into context.**
7. Mead, C. *Analog VLSI and Neural Systems* (Addison-Wesley, 1989).

8. Mead, C. A. Author Correction: How we created neuromorphic engineering. *Nat. Electron.* **3**, 579–579 (2020).
9. Hodgkin, A. L. & Huxley, A. F. A quantitative description of membrane current and its application to conduction and excitation in nerve. *J. Physiol.* **117**, 500–544 (1952). **More complex models followed, but this seminal work remains the clearest and an excellent starting point, developing equivalent electrical circuits and circuit models for the neural membrane.**
10. National Nanotechnology Initiative. *US National Nanotechnology Initiative* <https://www.nano.gov> (National Nanotechnology Coordination Office, accessed 18 August 2021).
11. About Groningen Cognitive Systems and Materials. *University of Groningen* <https://www.rug.nl/research/fse/cognitive-systems-and-materials/about/> (accessed 9 November 2020).
12. Degree programs: Neuroengineering. *Technical University of Munich* <https://www.tum.de/en/studies/degree-programs/detail/detail/StudyCourse/neuroengineering-master-of-science-msc/> (accessed 18 August 2021).
13. Course catalogue: 227-1033-00L Neuromorphic Engineering I. *ETH Zürich* <http://www.vvz.ethz.ch/Vorlesungsverzeichnis/lerneinheit.view?lerneinheitId=132789&semkez=2019W&ansicht=KATALOGDATEN&lang=en> (accessed 9 November 2020).
14. Brains in Silicon. <http://web.stanford.edu/group/brainsinsilicon/> (accessed 16 March 2022).
15. Neuromorphs. *Instituto de Microelectrónica de Sevilla* <http://www2.imse-cnm.csic.es/neuromorphs> (accessed 9 November 2020).
16. Neurotech. <https://neurotechai.eu> (accessed 18 August 2021).
17. Chua Memristor Center: Members. *Technische Universität Dresden* <https://cmc-dresden.org/members> (accessed 9 November 2020).

18. Subcommittee on Quantum Information Science. National Strategic Overview for Quantum Information Science.
<https://web.archive.org/web/20201109201659/https://www.whitehouse.gov/wp-content/uploads/2018/09/National-Strategic-Overview-for-Quantum-Information-Science.pdf> (US Government, 2018; accessed 17 March 2022).
19. Smith-Goodson, P. Quantum USA vs. quantum China: the world's most important technology race. *Forbes* <https://www.forbes.com/sites/moorinsights/2019/10/10/quantum-usa-vs-quantum-china-the-worlds-most-important-technology-race/#371aad5172de> (10 October 2019).
20. Gibney, E. Quantum gold rush: the private funding pouring into quantum start-ups. *Nature* <https://doi.org/10.1038/d41586-019-02935-4> (2 October 2019).
21. Le Quéré, C. et al. Temporary reduction in daily global CO₂ emissions during the COVID-19 forced confinement. *Nat. Clim. Change* **10**, 647–653 (2020).
22. Gokmen, T. & Vlasov, Y. Acceleration of deep neural network training with resistive cross-point devices: design considerations. *Front. Neurosci.* 1010.3389/fnins.2016.00333 (2016).
23. Marinella, M. J. et al. Multiscale co-design analysis of energy latency area and accuracy of a ReRAM analog neural training accelerator. *IEEE J. Emerg. Selected Topics Circuits Systems* **8**, 86–101 (2018).
24. Chang, H.-Y. et al. AI hardware acceleration with analog memory: microarchitectures for low energy at high speed. *IBM J. Res. Dev.* **63**, 8:1–8:14 (2019).
25. ARK Invest. *Big Ideas 2021* https://research.ark-invest.com/hubfs/1_Download_Files_ARK-Invest/White_Papers/ARK-Invest_BigIdeas_2021.pdf (ARK Investment Management, 2021; accessed 27 April 2021).

26. Benjamin, B. V. et al. Neurogrid: a mixed-analog–digital multichip system for large-scale neural simulations. *Proc. IEEE* **102**, 699–716 (2014).
27. Schmitt, S. et al. Neuromorphic hardware in the loop: training a deep spiking network on the BrainScaleS wafer-scale system. In *2017 Intl Joint Conf. Neural Networks (IJCNN)* <https://doi.org/10.1109/ijcnn.2017.7966125> (IEEE, 2017).
28. Lichtsteiner, P., Posch, C. & Delbrück, T. A 128×128 120 dB 15 μ s latency asynchronous temporal contrast vision sensor. *IEEE J. Solid-State Circuits* **43**, 566–576 (2008).
29. Moradi, S., Qiao, N., Stefanini, F. & Indiveri, G. A scalable multicore architecture with heterogeneous memory structures for dynamic neuromorphic asynchronous processors (DYNAPs). *IEEE Trans. Biomed. Circuits Syst.* **12**, 106–122 (2018).
30. Thakur, C. S. et al. Large-scale neuromorphic spiking array processors: a quest to mimic the brain. *Front. Neurosci.* **12**, 891 (2018).
31. Qiao, N. et al. A reconfigurable on-line learning spiking neuromorphic processor comprising 256 neurons and 128K synapses. *Front. Neurosci.* **9**, 141 (2015).
32. Valentian, A. et al. in *2019 IEEE Intl Electron Devices Meeting (IEDM)* 14.3.1–14.3.4 <https://doi.org/10.1109/IEDM19573.2019.8993431> (IEEE, 2019).
33. Resistive Array of Synapses with ONline Learning (ReASON)
Developed by NeuRAM3 Project
<https://cordis.europa.eu/project/id/687299/reporting> (2021).
34. Wang, R. et al. Neuromorphic hardware architecture using the neural engineering framework for pattern recognition. *IEEE Trans. Biomed. Circuits Syst.* **11**, 574–584 (2017).
35. Furber, S. B., Galluppi, F., Temple, S. & Plana, L. A. The SpiNNaker Project. *Proc. IEEE* **102**, 652–665 (2014). **An example of a large-scale**

neuromorphic system as a model for the brain.

36. Merolla, P. A. et al. A million spiking-neuron integrated circuit with a scalable communication network and interface. *Science* **345**, 668–673 (2014).
37. Davies, M. et al. Loihi: a neuromorphic manycore processor with on-chip learning. *IEEE Micro* **38**, 82–99 (2018).
38. Pei, J. et al. Towards artificial general intelligence with hybrid Tianjic chip architecture. *Nature* **572**, 106–111 (2019).
39. Frenkel, C., Lefebvre, M., Legat, J.-D. & Bol, D. A 0.086-mm² 12.7-pJ/SOP 64k-synapse 256-neuron online-learning digital spiking neuromorphic processor in 28-nm CMOS. *IEEE Trans. Biomed. Circuits Syst.* **13**, 145–158 (2018).
40. Chen, G. K., Kumar, R., Sumbul, H. E., Knag, P. C. & Krishnamurthy, R. K. A 4096-neuron 1M-synapse 3.8-pJ/SOP spiking neural network with on-chip STDP learning and sparse weights in 10-nm FinFET CMOS. *IEEE J. Solid-State Circuits* **54**, 992–1002 (2019).
41. Indiveri, G. et al. Neuromorphic silicon neuron circuits. *Front. Neurosci.* **5**, 73 (2011).
42. Mehonic, A. et al. Memristors—from in-memory computing, deep learning acceleration, and spiking neural networks to the future of neuromorphic and bio-inspired computing. *Adv. Intell. Syst.* **2**, 2000085 (2020). **A review of the promise of memristors across a range of applications, including spike-based neuromorphic systems.**
43. Li, X. et al. Power-efficient neural network with artificial dendrites. *Nat. Nanotechnol.* **15**, 776–782 (2020).
44. Chua, L. Memristor, Hodgkin–Huxley, and edge of chaos. *Nanotechnology* **24**, 383001 (2013).

45. Kumar, S., Strachan, J. P. & Williams, R. S. Chaotic dynamics in nanoscale NbO₂ Mott memristors for analogue computing. *Nature* **548**, 318–321 (2017).
46. Serb, A. et al. Memristive synapses connect brain and silicon spiking neurons. *Sci Rep.* **10**, 2590 (2020).
47. Rosemain, M. & Rose, M. France to spend \$1.8 billion on AI to compete with U.S., China. *Reuters* <https://www.reuters.com/article/us-france-tech-idUSKBN1H51XP> (29 March 2018).
48. Castellanos, S. Executives say \$1 billion for AI research isn't enough. *Wall Street J.* <https://www.wsj.com/articles/executives-say-1-billion-for-ai-research-isnt-enough-11568153863> (10 September 2019).
49. Larson, C. China's AI imperative. *Science* **359**, 628–630 (2018).
50. European Commission. A European approach to artificial intelligence. <https://ec.europa.eu/digital-single-market/en/artificial-intelligence> (accessed 9 November 2020).
51. Artificial intelligence (AI) funding investment in the United States from 2011 to 2019. *Statista* <https://www.statista.com/statistics/672712/ai-funding-united-states> (accessed 9 November 2020).
52. Worldwide artificial intelligence spending guide. *IDC Trackers* https://www.idc.com/getdoc.jsp?containerId=IDC_P33198 (accessed 9 November 2020).
53. Markets and Markets.com. *Neuromorphic Computing Market* https://www.marketsandmarkets.com/Market-Reports/neuromorphic-chip-market-227703024.html?gclid=CjwKCAjwlcaRBhBYEiwAK341jS3mzHf9nSIOEcj3MxSj27HVewqXDR2v4TlsZYaH1RWC4qdM0fKdlxoC3NYQAvD_BwE. (accessed 17 March 2022).

Acknowledgements

A.J.K. thanks the Engineering and Physical Sciences for financial support from grants EP/K01739X/1 and EP/P013503/1. A.M. acknowledges financial support from the Royal Academy of Engineering in the form of a Research Fellowship (RF201617\16\9).

Author information

Affiliations

1. Department of Electronic and Electrical Engineering, UCL, London, UK

A. Mehonic & A. J. Kenyon

Contributions

Both authors contributed equally to the manuscript and revisions.

Corresponding authors

Correspondence to [A. Mehonic](#) or [A. J. Kenyon](#).

Ethics declarations

Competing interests

The authors are founders and directors of Intrinsic Semiconductor Technologies Ltd (www.intrinsicst.com), a spin-out company commercializing silicon oxide RRAM.

Peer review

Peer review information

Nature thanks Steve Furber and Yulia Sandamirskaya for their contribution to the peer review of this work.

Additional information

Publisher's note Springer Nature remains neutral with regard to jurisdictional claims in published maps and institutional affiliations.

Rights and permissions

[Reprints and Permissions](#)

About this article

Cite this article

Mehonic, A., Kenyon, A.J. Brain-inspired computing needs a master plan. *Nature* **604**, 255–260 (2022). <https://doi.org/10.1038/s41586-021-04362-w>

- Received: 29 April 2021
- Accepted: 10 December 2021
- Published: 13 April 2022
- Issue Date: 14 April 2022
- DOI: <https://doi.org/10.1038/s41586-021-04362-w>

Share this article

Anyone you share the following link with will be able to read this content:

[Get shareable link](#)

Sorry, a shareable link is not currently available for this article.

[Copy to clipboard](#)

Provided by the Springer Nature SharedIt content-sharing initiative

This article was downloaded by **calibre** from <https://www.nature.com/articles/s41586-021-04362-w>

| [Section menu](#) | [Main menu](#) |

[Download PDF](#)

- Analysis
- Open Access
- [Published: 06 April 2022](#)

A joint NCBI and EMBL-EBI transcript set for clinical genomics and research

- [Joannella Morales](#)¹ na1,
- [Shashikant Pujar](#)² na1,
- [Jane E. Loveland](#)¹,
- [Alex Astashyn](#)²,
- [Ruth Bennett](#)¹,
- [Andrew Berry](#)¹,
- [Eric Cox](#) [ORCID: orcid.org/0000-0001-7691-4835](#)²,
- [Claire Davidson](#)¹,
- [Olga Ermolaeva](#)²,
- [Catherine M. Farrell](#)²,
- [Reham Fatima](#)¹,
- [Laurent Gil](#)¹,
- [Tamara Goldfarb](#)²,
- [Jose M. Gonzalez](#) [ORCID: orcid.org/0000-0001-5569-0705](#)¹,
- [Diana Haddad](#)²,
- [Matthew Hardy](#) [ORCID: orcid.org/0000-0001-6420-1715](#)¹,
- [Toby Hunt](#)¹,
- [John Jackson](#)²,
- [Vinita S. Joardar](#)²,
- [Michael Kay](#)¹,
- [Vamsi K. Kodali](#)²,

- [Kelly M. McGarvey²](#),
- [Aoife McMahon¹](#),
- [Jonathan M. Mudge¹](#),
- [Daniel N. Murphy¹](#),
- [Michael R. Murphy²](#),
- [Bhanu Rajput²](#),
- [Sanjida H. Rangwala²](#),
- [Lillian D. Riddick²](#),
- [Françoise Thibaud-Nissen](#) [ORCID: orcid.org/0000-0003-4957-7807²](#),
- [Glen Threadgold¹](#),
- [Anjana R. Vatsan²](#),
- [Craig Wallin²](#),
- [David Webb²](#),
- [Paul Flicek](#) [ORCID: orcid.org/0000-0002-3897-7955¹](#),
- [Ewan Birney](#) [ORCID: orcid.org/0000-0001-8314-8497¹](#),
- [Kim D. Pruitt²](#),
- [Adam Frankish¹](#),
- [Fiona Cunningham](#) [ORCID: orcid.org/0000-0002-7445-2419¹](#) &
- [Terence D. Murphy](#) [ORCID: orcid.org/0000-0001-9311-9745²](#)

Nature volume **604**, pages 310–315 (2022)

- 10k Accesses
- 133 Altmetric
- [Metrics details](#)

Subjects

- [Clinical genetics](#)
- [Databases](#)
- [Genome informatics](#)
- [Sequence annotation](#)
- [Standards](#)

Abstract

Comprehensive genome annotation is essential to understand the impact of clinically relevant variants. However, the absence of a standard for clinical reporting and browser display complicates the process of consistent interpretation and reporting. To address these challenges, Ensembl/Gencode¹ and RefSeq² launched a joint initiative, the Matched Annotation from NCBI and EMBL-EBI (MANE) collaboration, to converge on human gene and transcript annotation and to jointly define a high-value set of transcripts and corresponding proteins. Here, we describe the MANE transcript sets for use as universal standards for variant reporting and browser display. The MANE Select set identifies a representative transcript for each human protein-coding gene, whereas the MANE Plus Clinical set provides additional transcripts at loci where the Select transcripts alone are not sufficient to report all currently known clinical variants. Each MANE transcript represents an exact match between the exonic sequences of an Ensembl/Gencode transcript and its counterpart in RefSeq such that the identifiers can be used synonymously. We have now released MANE Select transcripts for 97% of human protein-coding genes, including all American College of Medical Genetics and Genomics Secondary Findings list v3.0 (ref. ³) genes. MANE transcripts are accessible from major genome browsers and key resources. Widespread adoption of these transcript sets will increase the consistency of reporting, facilitate the exchange of data regardless of the annotation source and help to streamline clinical interpretation.

Main

For more than 20 years, the RefSeq and Ensembl/Gencode teams, the two major sources of human genome annotation, have provided high-quality reference gene and transcript sets. These resources are used widely for biological research and discovery, with the choice of set depending on the use case. For instance, RefSeq transcripts are typically used for variant submissions to ClinVar⁴ or for variant descriptions in publications. Conversely, large-scale research projects such as ENCODE⁵, gnomAD⁶, DECIPHER⁷ and GTEx⁸ use the Ensembl/Gencode set. Although both

sets are supported by abundant evidence, the two are not identical owing to differences in curation timing, methodology and interpretation of evidence in data-poor genomic regions. Moreover, sequence differences are present because a few RefSeq transcripts do not perfectly match the reference genome sequence. No simple method has been developed thus far to determine end-to-end equivalence between entire transcripts from the two sources, and navigating these differences can therefore be challenging.

In the clinical context, no accepted standard reference sequence is available for reporting variants. Therefore, individuals or laboratories choose their own transcript, typically according to criteria such as transcript length or creation date. Additionally, resources and tools that are routinely consulted for clinical genomics often differ in their choice of preferred transcript. This can confound data interpretation and may cause errors in variant classification, potentially leading to real clinical harm. These challenges call for a transcript set that can be universally adopted across the clinical and research communities as a biologically informed standard reference for variant reporting to provide consistency across browser displays, resources and tools. Indeed, a 2018 survey⁹ conducted by Ensembl highlighted this need, with the majority of respondents expressing the desire for Ensembl/Gencode and RefSeq to agree on a primary transcript for each gene. The respondents included approximately 800 individuals, of whom around 35% were healthcare professionals or were working in clinical diagnostics.

MANE collaboration

To meet community needs, we established the Matched Annotation from NCBI and EMBL-EBI (MANE) collaboration. The initial results of this effort are (1) the MANE Select transcript set, designed to include a single representative transcript for every protein-coding gene for clinical reporting and other applications, and (2) the MANE Plus Clinical set for genes at which the MANE Select transcript alone is inadequate for describing all publicly available pathogenic (P) variants. Key features of the MANE transcripts include end-to-end matching between the exons of Ensembl/Gencode and RefSeq transcript sequences, perfect alignment to the GRCh38 reference genome assembly¹⁰ (Discussion) and the use of

biologically relevant criteria for transcript selection, such as transcript expression levels and conservation of the coding regions. Together, the two sets eliminate the need to choose between annotations when selecting a default transcript or when reporting variants. Access to the MANE data and detailed documentation on the MANE collaboration is available on the NCBI (<https://www.ncbi.nlm.nih.gov/refseq/MANE/>) and EMBL-EBI Transcript Archive (Tark; http://tark.ensembl.org/web/mane_project/) websites.

MANE Select

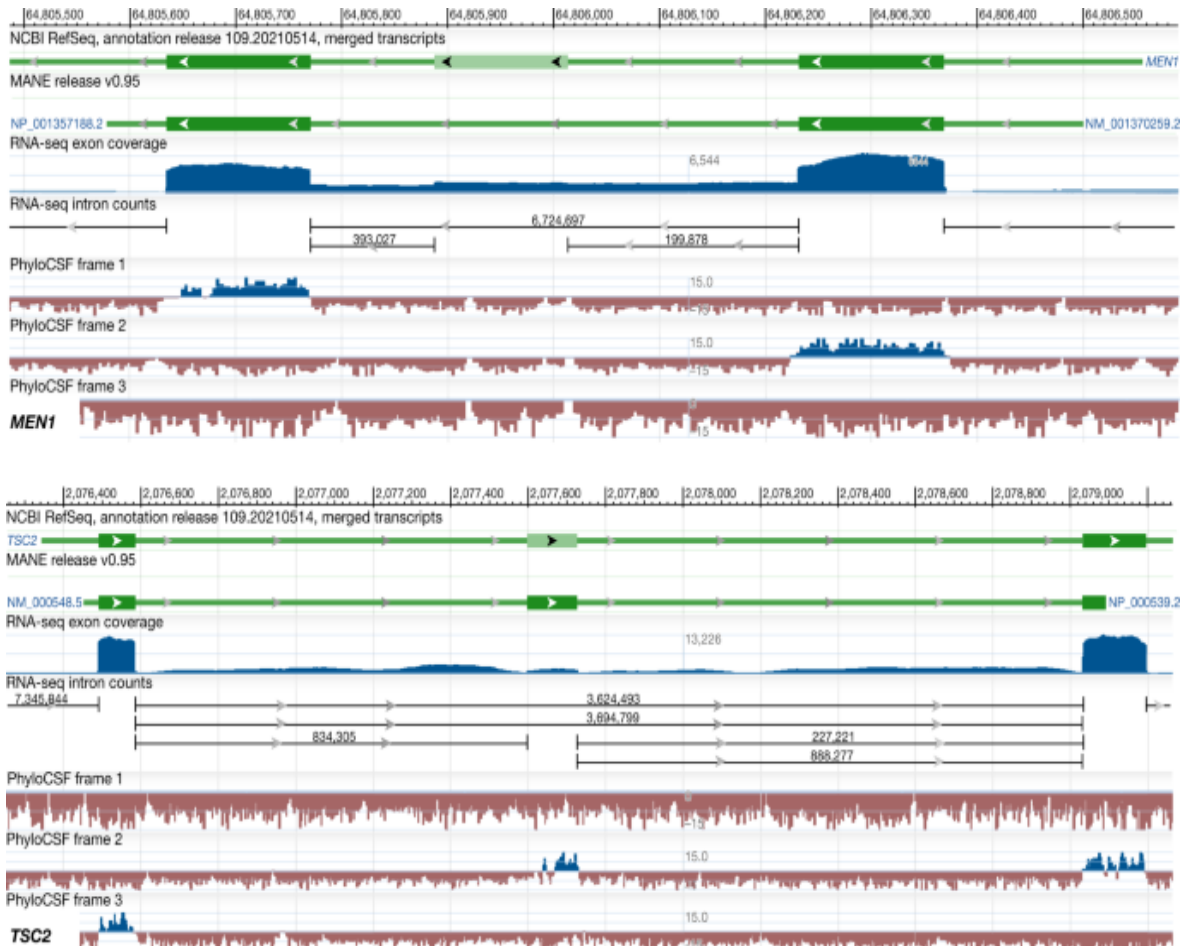
To build the MANE Select set, our joint approach involved designing independent pipelines that would each identify representative transcripts for protein-coding genes (Supplementary Methods 1 and Extended Data Fig. 1). We aimed to include all coding exons that are well expressed and show evidence of evolutionary conservation. We then developed a workflow to iteratively compare the pipeline outputs, identify transcript pairs with the same coding sequence (CDS) and exon structure, and standardize the transcript ends.

When using transcripts on GRCh38 available as of May 2018 in our initial comparison of the pipeline outputs, we determined that the Ensembl/GENCODE and RefSeq selections were identical for only 14% of protein-coding genes. In particular, 73% had differences only in the untranslated regions (UTRs), either in the extent of the 5' or 3' end or in the choice of UTR exons, and 11% differed in the CDS. For the remaining 2% of genes, we observed other scenarios, such as a missing corresponding transcript in one source. For choices that differed in CDS or UTR exons, we iteratively resolved these differences through pipeline improvements, additional automated data analyses and manual curation following consensus curation guidelines (Supplementary Methods 2). Manual review was aided by quality assurance metrics that flagged discrepancies (Supplementary Table 2).

Owing to strong interest from the clinical community, we focused our manual curation efforts on a subset of clinically relevant genes ($n = 3,803$). The clinical relevance of these genes was validated by key clinical partners,

including the Transforming Genomic Medicine Initiative (TGMI; <http://www.thetgmi.org>) and the Clinical Genome Resource (ClinGen)¹¹; alternatively, inclusion in repositories such as Genomics England (PanelApp¹²), Gene2Phenotype¹³, OMIM¹⁴ and ClinVar was used for validation. For genes in the American College of Medical Genetics and Genomics Secondary Findings list (ACMG SF v2.0; ref. ¹⁵), we reviewed the suitability of the pipeline choice and discussed challenging genes with our clinical partners. Figure 1 illustrates the application of our key criteria, conservation and expression, when choosing a MANE Select transcript for two high-value clinical genes. As mentioned above, our goal was to select transcripts that include well-conserved and well-expressed protein-coding exons. When a coding exon did not meet either criterion (for example, in *MEN1*), a transcript excluding that exon was chosen as the MANE Select transcript. However, a coding exon displaying a signal of conservation was considered for inclusion if it passed our minimum expression threshold, even if this exon was expressed at lower levels than neighbouring exons (for example, in *TSC2*).

Fig. 1: Conservation versus expression when manually curating two high-value clinical genes.



Top, gene *MEN1* (HGNC:7010) tracks from NCBI GDV, as described below from top to bottom. Track 1, magnified region of the gene showing a portion of the CDS including an alternatively spliced exon (NCBI annotation release 109.20210514). Track 2, MANE v0.95 track showing the corresponding region of the MANE Select transcript ([NM_001370259.2](#)) lacking the alternatively spliced exon. Track 3, RNA-seq exon coverage (aggregate, filtered), with the numbers indicating the peak heights of the graph on a linear scale. Track 4, RNA-seq intron-spanning data from recount3, with horizontal lines depicting introns and numbers above the line indicating the number of reads. Track 5, PhyloCSF tracks. A transcript excluding the alternatively spliced exon was chosen as the MANE Select transcript owing to low expression (tracks 3 and 4) and lack of evolutionary constraint (no positive PhyloCSF signal, as indicated by blue colour) for the alternatively spliced exon. Bottom, gene *TSC2* (HGNC:12363) tracks from GDV, as described below from top to bottom. Track 1, NCBI annotation release 109.20210514 track showing a portion of the coding region. Track 2, MANE

v0.95 track showing the corresponding region of the MANE Select transcript ([NM_000548.5](#)). Track 3, RNA-seq exon coverage (aggregate, filtered). Track 4, portion of RNA-seq intron-spanning data from recount3. Track 5, PhyloCSF tracks. The MANE Select transcript includes the alternatively spliced protein-coding exon, which, despite its lower expression compared with neighbouring exons, shows evolutionary constraint of the CDS (presence of positive signal in the PhyloCSF track, as indicated by blue colour).

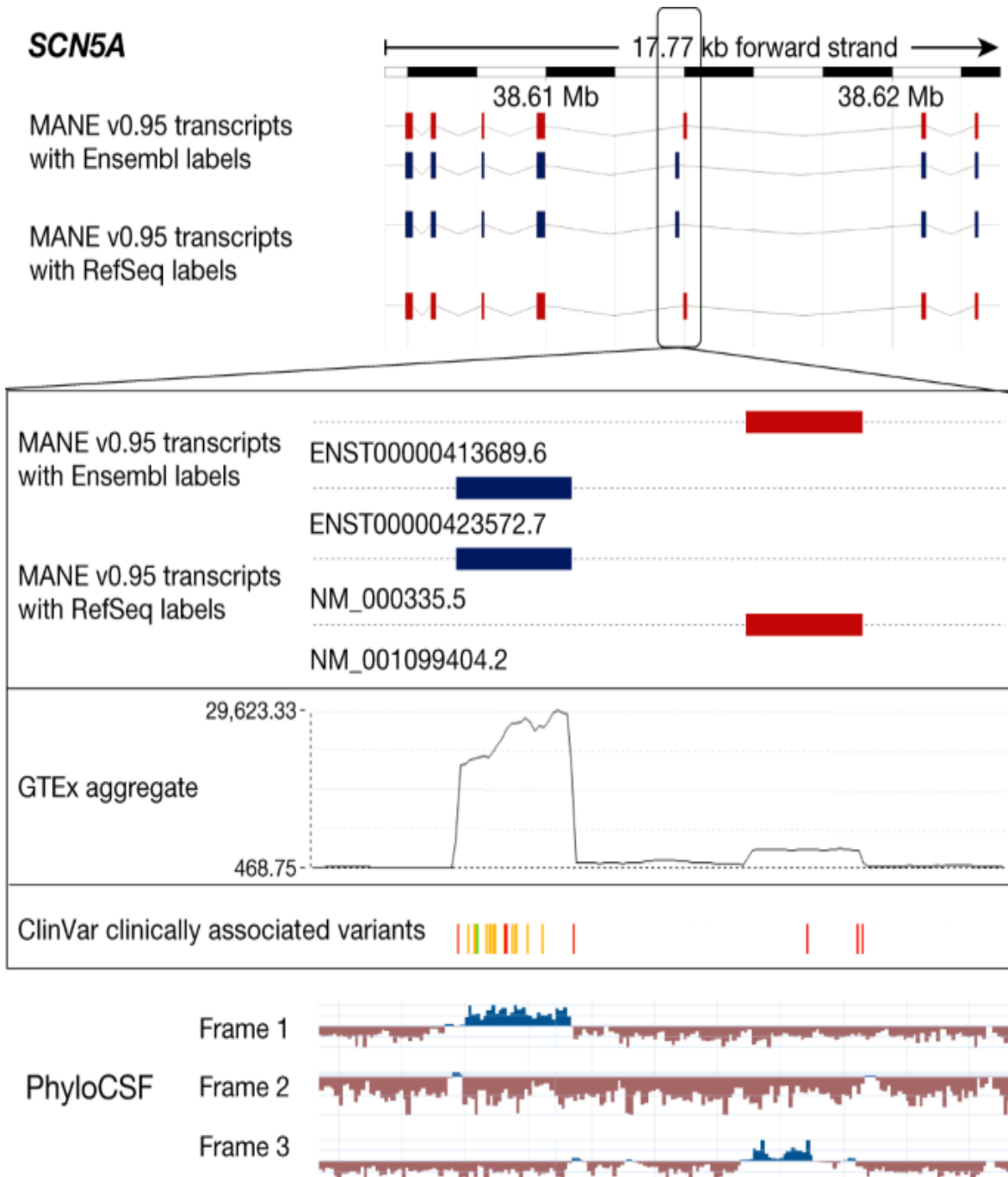
After selecting transcript pairs, with one transcript from each source, we determined the optimal 5' and 3' ends on the basis of the supporting evidence. We incorporated high-throughput datasets (described in [Methods](#)) to programmatically determine and automatically update the 5' and 3' ends of both the RefSeq and Ensembl/Gencode transcripts, even for some of the pairs that were initially found to be identical. Once updates were completed and perfect identity was achieved, both transcripts in the pair were tagged as MANE Select. Extended Data Fig. [2](#) illustrates our method to determine the transcription start site (TSS) for the MANE Select transcript of the gene *PTPRC* (HGNC:9666). Similar logic was used to compute poly(A) clusters to determine the 3' ends of transcripts. Additional details are provided in Supplementary Methods [3](#). The 5'-end updates of the transcripts resulted in an enrichment for motifs characteristic of eukaryotic transcription initiation^{[16](#)}, including initiation at purines and the presence of properly positioned TATA box or initiator motifs for a subset of transcripts (Extended Data Fig. [3](#)).

By June 2021 (MANE release v0.95), we had defined a MANE Select transcript for 97% (18,584) of protein-coding genes across the genome. This includes all ACMG SF v3.0 genes and more than 99% (3,793 of 3,803) of the subset of disease-associated genes (Extended Data Fig. [4](#)). The outstanding clinical genes include those to be added in the next release (*KLK4*, *TOMT*) or those affected by errors in the GRCh38 chromosome sequences (*ABO*, *FUT3*, *MUC1*, *ORAI1*, *POLR2A*, *SHANK3*) or atypically complex annotation (*PEG10*). We aim to complete the set in early 2022. The vast majority of MANE Select transcripts will be stable. However, we will allow updates on the rare occasion that new data demonstrate, without ambiguity, that the MANE Select transcript requires an update or needs to be replaced with a better transcript.

MANE Plus Clinical

Although the MANE Select set serves as a variant reporting standard for the majority of genes, some clinically relevant genes require more than one transcript to report all known P or likely pathogenic (LP) variants if these variants map to alternatively spliced exons. For cases in which the MANE Select transcript alone is not sufficient to report all known variants, we defined an additional transcript: the MANE Plus Clinical transcript. After consultation with our clinical partners, we have released MANE Plus Clinical transcripts for 55 genes. Figure 2 illustrates the need for a second transcript to report the P and LP variants that map to mutually exclusive exons in the *SCN5A* (HGNC:10593) gene.

Fig. 2: The need for a MANE Plus Clinical transcript for the *SCN5A* (HGNC:10593) gene.



Top, Ensembl browser display of the *SCN5A* gene showing MANE Select (blue) and MANE Plus Clinical (red) transcripts (Ensembl/GENCODE on top and RefSeq below) from MANE release v0.95. Bottom, magnified view of the portion of the gene that includes two mutually exclusive exons. The tracks are as described below, from top to bottom. Track 1, MANE v0.95 track showing the upstream MANE Select exon and downstream MANE

Plus Clinical exon, shown in blue and red, respectively. Track 2, GTEx aggregate exon coverage (black wiggle plot). Track 3, ClinVar variants described as P or LP, coloured to indicate the type of variant (green, synonymous; yellow, missense; red, stop gained). Track 4, PhyloCSF tracks (one row for each frame) from NCBI GDV, with positive signal shown in blue.

Updates to original transcript datasets

A crucial aspect of the MANE set is the fact that the Ensembl/GENCODE and RefSeq transcripts (and, therefore, proteins) in a MANE pair are identical, and the identifiers can be used interchangeably. To achieve the perfect match, the vast majority of transcripts selected by both pipelines (94% for RefSeq and 94.1% for Ensembl/GENCODE) underwent updates, resulting in version increments (Table 1). This includes some of the transcripts that were identical at the beginning of the project but did not conform to the UTR rules mentioned above. Most of the updates (86% for RefSeq and 88% for Ensembl/GENCODE) were in the UTR. However, a small percentage of transcripts required changes to the CDS (1.8% for RefSeq and 1.5% for Ensembl/GENCODE), which typically involved a change to the location of the start codon. In addition to these updates, new transcripts were created for existing annotations that were incomplete or inconsistent with the MANE criteria (2.4% for RefSeq and 1.6% for Ensembl/GENCODE).

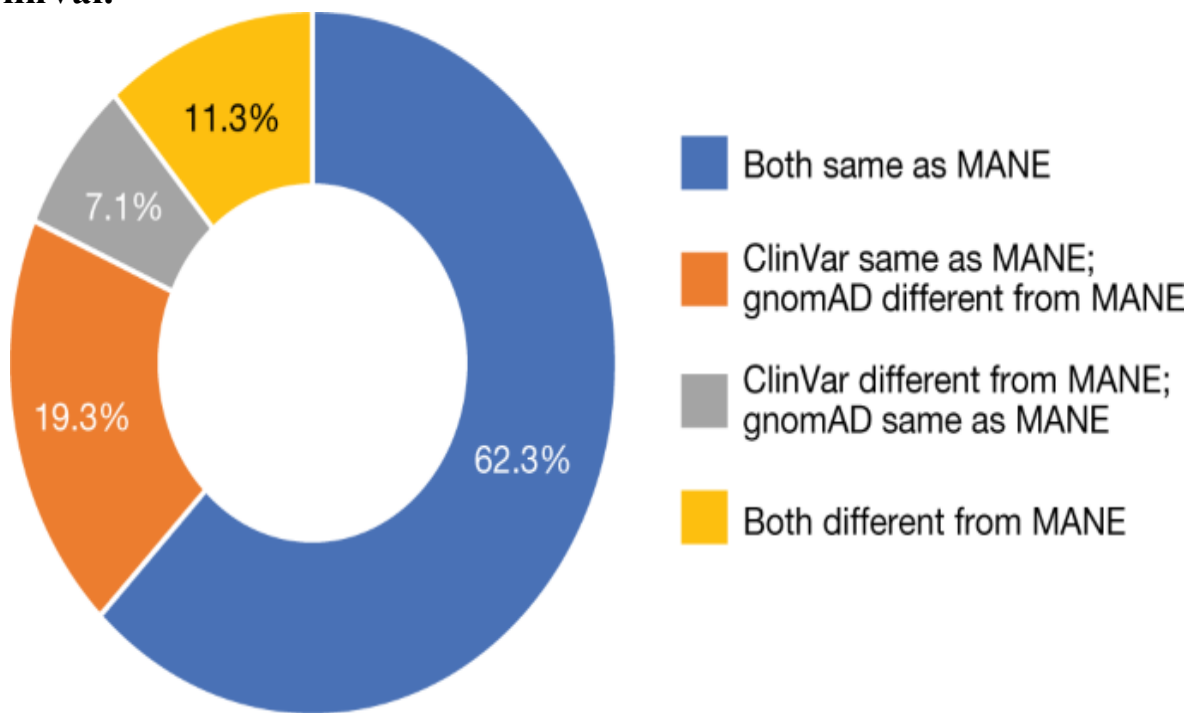
Table 1 Updates to RefSeq and Ensembl/GENCODE transcripts.

Comparison with alternative datasets

A goal of the MANE collaboration is to deliver a transcript set that can be widely adopted as a standard for reporting and for display across resources commonly used by the clinical and research communities. To assess the impact of our work, we aimed to quantify the overlap between the MANE Select set and two representative resources, gnomAD and ClinVar, which use Ensembl/GENCODE and RefSeq annotations, respectively. We chose to analyse disease-associated genes and these two resources because they reflect data used in the clinical community, represent orthogonal views of

what users are exposed to or are using, and were available with sufficiently broad gene coverage to make the analysis informative. gnomAD shows Ensembl transcripts and could be perceived by users as a recommendation of a particular canonical transcript. The ClinVar submission data indicate which RefSeq transcripts are being used by submitters on the basis of unknown and likely varied criteria. The choice of datasets informed the set of genes included in the analysis. For the subset of manually curated disease-associated genes, we determined whether the canonical transcript in gnomAD (v3.1.1) and the transcript most commonly used for variant submission to ClinVar matched the MANE Select transcript accession. As shown in Fig. 3, the same accession as that for MANE Select was used for 62.3% ($n = 2,945$) of the genes we reviewed. However, different accessions were used in one or both resources for the remaining 37.7% ($n = 1,779$) of genes (7.1% and 19.3% in ClinVar and gnomAD, respectively). This divergence demonstrates the consequence of having no standard transcript set and affirms the aims of our collaboration.

Fig. 3: Comparison of the MANE Select dataset with gnomAD and ClinVar.



Doughnut chart showing a comparison of MANE Select transcripts with the most frequently used RefSeq transcript accession for variant submission in

ClinVar and Ensembl canonical transcripts used for display in the gnomAD v3.1.1 resource.

Source data

We collaborated with resources such as ExAC/gnomAD, ClinGen, ClinVar, DECIPHER and the Ensembl Variant Effect Predictor (VEP)¹⁷, all of which had different preferred transcripts, to encourage adoption of the MANE Select set, achieve standardization and ensure consistency. The interfaces of these resources now display the MANE Select transcript (Extended Data Fig. 5). In addition, UniProt is expected to update its browser in the near future to include flagged MANE Select proteins.

Access and display of MANE data

All data produced by the MANE collaboration are freely accessible in genome browsers, by bulk download and programmatically (see links in Extended Data Table 1). A complete list of MANE transcripts with RefSeq and Ensembl identifiers in the latest MANE release (v0.95) is available in the MANE.GRCh38.v0.95.summary.txt.gz file on the FTP site (https://ftp.ncbi.nlm.nih.gov/refseq/MANE/MANE_human/release_0.95/) and Tark (<http://tark.ensembl.org/web/manelist>). As shown in Extended Data Fig. 6, the Ensembl browser displays MANE data using a custom-made track hub and labels the MANE transcripts in the transcript table within the gene-specific pages. The NCBI Genome Data Viewer (GDV)¹⁸ allows display of tracks for each MANE release and includes MANE tags in the RefSeq annotation (Extended Data Fig. 7). In addition, the University of California, Santa Cruz (UCSC) Genome Browser¹⁹ allows selection of a MANE data track in the Genes and Gene Predictions section and exploration of the data in the Table Browser tool (Extended Data Fig. 8).

Discussion

RefSeq and Ensembl/GENCODE have collaborated in the past to converge on annotation and provide joint, high-quality, evidence-based reference sets. We initiated the Consensus Coding Sequence (CCDS)²⁰ project in 2005 to

provide transcript coding regions consistently annotated by the two groups. In 2008, we established the Locus Reference Genomic (LRG)²¹ project to provide stable reference sequences to report clinical variants. The MANE project goes beyond these collaborations in scope and content. It is not limited to coding regions, as in CCDS, but provides end-to-end matches between transcripts from the two sources. MANE is an improvement over LRG because, in addition to covering all protein-coding genes rather than a limited set of clinical genes, it provides transcript annotations that perfectly match the reference assembly. This is vital to reduce errors, considering that diagnostic pipelines now use whole-exome sequencing or whole-genome sequencing or will implement these methods in the near future. Therefore, NCBI and EMBL-EBI leaders of the LRG project decided to keep the LRG webpage and existing data available but have stopped expanding the LRG set. We recommend using the MANE transcript sets over those of LRG as a reference standard for clinical reporting. Existing LRG accessions now incorporate MANE transcript annotation (Extended Data Fig. 9) and will continue to be supported. Moreover, the Human Genome Variant Society (HGVS)²² now includes a recommendation to use MANE transcripts in its general and reference sequence guidelines.

Caveats and limitations

Selection of one transcript does not imply that the rich biology of the human genome can be reduced to one transcript at each locus, nor does it mean that transcripts not included in the MANE set are inferior or can be ignored. Even though the MANE set drives standardization for browser display and clinical reporting, we are not suggesting that only MANE transcripts be considered when analysing variants of potential clinical significance. For example, some disease mechanisms involve regulating expression in a tissue-specific manner or during a particular stage of development. This level of specificity and transcript diversity is not within the scope of the MANE Select set. Furthermore, when generating the MANE Plus Clinical set, we considered only P or LP exonic variants reported in ClinVar or other public resources. Given that not all laboratories make their variants freely accessible, our Plus Clinical set is a work in progress. We expect the set to increase as new variants are discovered and reported in public archives. Although this work has been driven by our annotation expertise, feedback

from the community is encouraged. We will consider additional transcripts of clinical interest after consulting clinical experts. Enquiries about existing MANE transcripts and addition of new transcripts may be sent to mane-help@ncbi.nlm.nih.gov or mane-help@ebi.ac.uk.

The MANE sets are currently limited to protein-coding genes. We anticipate including well-supported non-coding genes in the future, particularly those with clinical relevance. In addition, a small percentage of protein-coding genes cannot currently be matched between RefSeq and Ensembl owing to errors in the GRCh38 primary reference assembly. We are collaborating with the Genome Reference Consortium (GRC) to generate patch sequences that correct errors or improve the assembly. GRC has indefinitely postponed the release of GRCh39; therefore, some protein-coding genes in MANE will have annotation on a patch. Additionally, mitochondrial genes and genes that undergo ribosomal slippage, such as *PEG10*, are presently not included in the MANE sets. However, we intend to include them in the future.

The MANE transcript sets are based on GRCh38 by design; thus, we plan to keep MANE matched only to GRCh38 for the foreseeable future to provide a unified stable clinical reporting standard. Most users are well served by a single reference genome assembly used uniformly across different resources. The most recent research data, analysis and annotation are available exclusively on GRCh38, which is supported in key clinical resources and tools such as gnomAD, ClinVar and DECIPHER. Accordingly, RefSeq and GENCODE will continue using GRCh38 as the primary annotation reference for years to come. However, we recognize that many clinical laboratories will continue to use GRCh37 and that there is interest in new complete or nearly complete genome assemblies representing additional population diversity²³. Thus, RefSeq and Ensembl/GENCODE will develop further resources and tools to enable future pan-genomes and variation in other assemblies to be interpreted relative to MANE transcripts. For example, the RefSeq annotation of GRCh37, updated in March 2022, is available with markup for RefSeq Select transcripts, including those mapped to GRCh37 from MANE v0.95. A comparison of MANE transcripts to Ensembl/GENCODE annotation on GRCh37 is available at http://tark.ensembl.org/web/mane_GRCh37_list/. Mappings of MANE annotation from GRCh38 will be available on additional human assemblies in the future from both RefSeq and Ensembl/GENCODE. However, because

MANE transcripts are planned to be generated only on GRCh38, those mapped to other assemblies may have sequence differences (for example, for 5% of genes in GRCh37), which need to be accounted for when generating HGVS expressions. We therefore recommend broad adoption of GRCh38 in the clinical community to take full advantage of MANE, improve consistency in variant identification and promote the exchange of clinical variant data. Failure to transition could cause discordance in variant identification²⁴, making variant interpretation vulnerable to outdated or incomplete genome annotation and severely limiting the exchange of clinical variant reports.

Future plans

We expect to finalize the MANE Select set in early 2022 (or finish as close to 100% of genes as possible given the limitations mentioned above) and to iteratively extend the MANE Plus Clinical set as new P variants are discovered. We are working with UniProt to align its set with MANE Select to provide access to a wealth of protein-based annotation in a consistent manner. Genes not currently in the MANE set include those for which the annotation differs between Ensembl/GENCODE and RefSeq owing to locus complexity and lack of evidence. In addition, genes needing genome patches and those annotated in only one of the two sets will be manually reviewed.

In the long term, we aim to produce a new set to include additional high-value transcripts, including those for the non-coding genome, such as transcripts that carry exclusive, well-conserved exons that utilize alternative promoters or that have different termini. We will work on this set once we have mature workflows to integrate long transcriptomic data and data arising from rapid technical advances in the wider transcriptomics and proteomics fields. We are also considering the development of a set to label genes and transcripts relevant for human diseases. As a starting point, we plan to use the sets of genes defined by groups that are actively assessing gene–disease validity, such as the global Gene Curation Coalition (<https://thegencc.org/>).

In summary, as a result of our efforts to converge on the annotation of human protein-coding genes, our collaboration initiative between RefSeq and Ensembl/GENCODE delivers a joint transcript set to standardize

clinical genomics and research. This set of one transcript per gene can be used as a default for tools and resources and as a reference set for clinical reporting and research. Universal adoption of this high-value set will promote consistency in reporting, limit clinical harm caused by errors in interpretation, increase the bidirectional exchange of data and help drive improvements in human health and diagnostics.

Methods

MANE Select workflow

To produce the MANE Select set, (1) both annotation groups developed pipelines to choose a representative transcript; (2) the two pipeline choices were compared; (3) the matched choices were updated to adjust the ends; and (4) when the two pipeline choices did not match, they were binned into multiple categories (Supplementary Table 1) to be resolved by pipeline refinements or manual review (Supplementary Methods 2). Although the two pipelines are described in detail in Supplementary Methods 1 and Extended Data Fig. 1, the key features are outlined here. The Ensembl pipeline takes into account evidence of functional potential, including transcript expression levels (Intropolis²⁵ and recount3; ref. 26) and evolutionary constraint of the coding region (Phylogenetic Codon Substitution Frequencies, PhyloCSF²⁷). Other factors are CDS length and concordance with the APPRIS²⁸ principal isoform and the UniProt/Swiss-Prot²⁹ canonical isoform. The pipeline assigns a score for each component from which a composite score is derived. The transcript with the highest composite score is selected as the Ensembl choice, although some length exceptions apply. The RefSeq Select pipeline uses a hierarchical list of parameters, with prior use in clinical reporting and conservation of the coding region (PhyloCSF) at the top. Each parameter is assigned a binary score, and the RefSeq Select transcript is chosen on the basis of a composite score reflecting the ranked choice of the individual parameters.

Defining UTRs

To standardize the 5' and 3' ends of the transcripts, we used high-throughput cap analysis of gene expression (CAGE) data from the FANTOM consortium³⁰ and poly(A)-seq data from multiple studies^{31,32,33,34,35,36,37}, respectively. For the 5' ends, we imported the CTSS TotalCounts data included for 2,006 runs of CAGE sequence data on the HelicoScope platform from 1,829 distinct samples mapped to the GRCh38 assembly (BioProject, [PRJDB1099](#)). The FANTOM data were reprocessed to combine CAGE clusters found in close proximity (within 50 nucleotides of each other) on the same strand and to re-analyse the TotalCounts data in the region of each merged cluster to find the maximum peak. The TSS was then recalculated to be the 5'-most peak in the merged cluster with a signal of at least 50% of the maximum peak. This criterion is referred to as the ‘longest strong’ rule. The goal of the reprocessing is to determine a frequently used TSS that is representative of the overall data rather than that with the absolute maximum tag counts. In this way, we maximize the coverage of commonly observed 5'-UTR bases (and any sequence- or structure-based features they contain). The reprocessed CAGE tracks are available from NCBI GDV as RefSeq-processed FANTOM CAGE peaks tracks. To update the transcripts to the calculated longest strong TSS, we used an automated process that identified CAGE clusters overlapping the first exons of transcripts or those within 500 nucleotides of the first nucleotide. Alternatively, we updated them manually when the genes required additional review. We followed a similar logic for the 3' end and poly(A)-seq clusters (Supplementary Methods 3).

Comparison of transcript ends with genomic TSS signatures

We scanned the genomic sequence for the following TSS signatures: (1) enrichment of purines (A or G), which is characteristic of RNA polymerase II transcription initiation, and (2) TATA box motifs at about -30 and initiator³⁸ motifs at -1 relative to the TSS. We performed a comparison with two datasets, transcripts at the beginning of this project as well as predating bulk CAGE-based transcripts and those in the current MANE set. We used HOMER³⁹ to analyse nucleotide frequencies, the FIMO⁴⁰ tool from the MEME suite to scan for motifs using a position weight matrix (PWM) from JASPAR⁴¹ for analysis of TATA boxes and a PWM from ref. ³⁸ for analysis of the initiator motif. The 200-nucleotide sequence centred on each TSS was

scanned using FIMO, and the position of the highest scoring match to the PWM was recorded using a *P*-value threshold of 0.01. Additional details are provided in Supplementary Methods 3 and Extended Data Fig. 3.

MANE Plus Clinical workflow

The starting point for the MANE Plus Clinical set was the list of known P and LP variants available in the ClinVar 20200513 release. All P and LP variants were considered, regardless of their review status ('star' designation). We identified transcripts that contained conserved coding exons not represented in the MANE Select set and that overlapped these P or LP variants. This set of additional transcripts was manually reviewed to ensure the same high degree of quality as for the transcripts in the MANE Select set.

RefSeq and Ensembl/GENCODE transcript updates

The annotation comparison logic used for the MANE workflow (Supplementary Methods 4) was adapted to compare transcripts from the early RefSeq and Ensembl/GENCODE annotation sets with those of the most recent MANE release. The first comparison was carried out using the human RefSeq 109 and Ensembl 92 annotation sets. For each MANE Select transcript, the comparison dataset was checked for transcript and CDS annotations that were completely identical; differed only in the extent of the 5' and 3' UTRs; differed in the CDS but had the same transcript splice pattern, indicating a change in start codon; or cases in which a transcript lacked an equivalent splice pattern. The comparisons were performed independently of transcript identifiers; in some cases, a transcript was indicated as 'new' when it was an update of an existing transcript but exons were added or removed. The comparisons did not consider sequence changes or the removal of poly(A) tails from some RefSeq transcripts, which resulted in additional updates.

Reporting summary

Further information on research design is available in the [Nature Research Reporting Summary](#) linked to this paper.

Data availability

The datasets generated during the current study are available on the NCBI FTP site (https://ftp.ncbi.nlm.nih.gov/refseq/MANE/MANE_human/) and the Tark webpage (http://tark.ensembl.org/web/mane_project/). Source data are provided with this paper. The datasets analysed during the current study can be accessed using the following resources. All Ensembl/GENCODE annotation builds used in the comparison of RefSeq and Ensembl/GENCODE transcripts for determination of transcript matches in the MANE analysis are available in the release 96–105 directories on the Ensembl FTP site (http://ftp.ensembl.org/pub/release-105/gtf/homo_sapiens/Homo_sapiens.GRCh38.105.gtf.gz). All RefSeq annotation builds used in the comparison of RefSeq and Ensembl/GENCODE transcripts for determination of transcript matches in the MANE analysis are available at https://ftp.ncbi.nlm.nih.gov/genomes/refseq/vertebrate_mammalian/Homo_sapiens/annotation_releases/. The Ensembl canonical transcripts used for the comparison of gnomAD versus ClinVar versus MANE were from Ensembl release 103. These can be accessed using the Ensembl Perl API for release 103 with the following call on the gene:
http://www.ensembl.org/info/docs/Doxygen/core-api/classBio_1_1EnsEMBL_1_1Gene.html. Alternatively, the same data are available through the Ensembl REST API by using the following lookup endpoint: <https://jan2020.rest.ensembl.org/documentation/info/lookup>. The aggregated CTSS TotalCounts CAGE data and the CAGE clusters as computed by the FANTOM consortium were imported from http://fantom.gsc.riken.jp/5/datafiles/reprocessed/hg38_latest/extra/CAGE_peaks/hg38_fair+new_CAGE_peaks_phase1and2.bed.gz and <https://fantom.gsc.riken.jp/5/datahub/hg38/reads/>. The poly(A)-seq data used to generate the poly(A) clusters and to determine the poly(A) sites were from multiple studies listed in refs. [31,32,33,34,35,36,37](#). The data are available in study accessions [SRP041182](#), [SRP003483](#), [SRP007359](#) and [SRP133500](#) in the NCBI Sequence Read Archive (SRA; <https://www.ncbi.nlm.nih.gov/sra>) and at PolyASite 2.0 (<https://www.polyasite.unibas.ch/>). APPRIS data are available at <https://appris.bioinfo.cnio.es/#/downloads>, which is updated for every Ensembl/GENCODE release. These data are based on Ensembl releases 95–

104. The PhyloCSF data used to identify conserved sequences were imported from <https://data.broadinstitute.org/compbio1/PhyloCSFtracks/>. Intron support data from Snaptron/recount3 were imported from <http://snaptron.cs.jhu.edu/data/>. Source data are provided with this paper.

Code availability

The analysis code used for this study is largely integral to the RefSeq and Ensembl/GENCODE curation databases and was not designed for use in isolation or with other annotation datasets. The most critical aspect of the analysis was the tens of thousands of working hours spent in curator review to produce the final dataset. HOMER v4.11 is available at <http://homer.ucsd.edu/homer/>. FIMO v5.3.2 is available at https://meme-suite.org/meme/meme_5.3.2/doc/fimo.html. HISAT 2.2.1 is available at <http://daehwankimlab.github.io/hisat2/>.

References

1. Frankish, A. et al. GENCODE 2021. *Nucleic Acids Res.* **49**, D916–D923 (2021).
2. O’Leary, N. A. et al. Reference sequence (RefSeq) database at NCBI: current status, taxonomic expansion, and functional annotation. *Nucleic Acids Res.* **44**, D733–D745 (2016).
3. Miller, D. T. et al. ACMG SF v3.0 list for reporting of secondary findings in clinical exome and genome sequencing: a policy statement of the American College of Medical Genetics and Genomics (ACMG). *Genet. Med.* **23**, 1381–1390 (2021).
4. Landrum, M. J. et al. ClinVar: improvements to accessing data. *Nucleic Acids Res.* **48**, D835–D844 (2020).
5. ENCODE Project Consortium. Expanded encyclopaedias of DNA elements in the human and mouse genomes. *Nature* **583**, 699–710 (2020).

6. Karczewski, K. J. et al. The mutational constraint spectrum quantified from variation in 141,456 humans. *Nature* **581**, 434–443 (2020).
7. Firth, H. V. et al. DECIPHER: Database of Chromosomal Imbalance and Phenotype in Humans Using Ensembl Resources. *Am. J. Hum. Genet.* **84**, 524–533 (2009).
8. GTEx Consortium. The GTEx Consortium atlas of genetic regulatory effects across human tissues. *Science* **369**, 1318–1330 (2020).
9. Morales, J. et al. The value of primary transcripts to the clinical and non-clinical genomics community: survey results and roadmap for improvements. *Mol. Genet. Genomic Med.* **9**, e1786 (2021).
10. Schneider, V. A. et al. Evaluation of GRCh38 and de novo haploid genome assemblies demonstrates the enduring quality of the reference assembly. *Genome Res.* **27**, 849–864 (2017).
11. Rehm, H. L. et al. ClinGen—the clinical genome resource. *N. Engl. J. Med.* **372**, 2235–2242 (2015).
12. Martin, A. R. et al. PanelApp crowdsources expert knowledge to establish consensus diagnostic gene panels. *Nat. Genet.* **51**, 1560–1565 (2019).
13. Thormann, A. et al. Flexible and scalable diagnostic filtering of genomic variants using G2P with Ensembl VEP. *Nat. Commun.* **10**, 2373 (2019).
14. Amberger, J. S. & Hamosh, A. Searching Online Mendelian Inheritance in Man (OMIM): a knowledgebase of human genes and genetic phenotypes. *Curr. Protoc. Bioinformatics* **58**, 1.2.1–1.2.12 (2017).
15. Kalia, S. S. et al. Recommendations for reporting of secondary findings in clinical exome and genome sequencing, 2016 update (ACMG SF v2.0): a policy statement of the American College of Medical Genetics and Genomics. *Genet. Med.* **19**, 249–255 (2017).

16. Haberle, V. & Stark, A. Eukaryotic core promoters and the functional basis of transcription initiation. *Nat. Rev. Mol. Cell Biol.* **19**, 621–637 (2018).
17. McLaren, W. et al. The Ensembl variant effect predictor. *Genome Biol.* **17**, 122 (2016).
18. Rangwala, S. H. et al. Accessing NCBI data using the NCBI Sequence Viewer and Genome Data Viewer (GDV). *Genome Res.* **31**, 159–169 (2021).
19. Lee, C. M. et al. UCSC Genome Browser enters 20th year. *Nucleic Acids Res.* **48**, D756–D761 (2020).
20. Pujar, S. et al. Consensus coding sequence (CCDS) database: a standardized set of human and mouse protein-coding regions supported by expert curation. *Nucleic Acids Res.* **46**, D221–D228 (2018).
21. MacArthur, J. A. L. et al. Locus Reference Genomic: reference sequences for the reporting of clinically relevant sequence variants. *Nucleic Acids Res.* **42**, D873–D878 (2014).
22. den Dunnen, J. T. Describing sequence variants using HGVS nomenclature. *Methods Mol. Biol.* **1492**, 243–251 (2017).
23. Miga, K. H. & Wang, T. The need for a human pangenome reference sequence. *Annu. Rev. Genomics Hum. Genet.* **22**, 81–102 (2021).
24. Li, H. et al. Exome variant discrepancies due to reference genome differences. *Am. J. Hum. Genet.* **108**, 1239–1250 (2021).
25. Nellore, A. et al. Human splicing diversity and the extent of unannotated splice junctions across human RNA-seq samples on the Sequence Read Archive. *Genome Biol.* **17**, 266 (2016).
26. Wilks, C. et al. Recount3: summaries and queries for large-scale RNA-seq expression and splicing. *Genome Biol.* **22**, 323 (2021).

27. Lin, M. F., Jungreis, I. & Kellis, M. PhyloCSF: a comparative genomics method to distinguish protein coding and non-coding regions. *Bioinformatics* **27**, i275–i282 (2011).
28. Rodriguez, J. M. et al. APPRIS 2017: principal isoforms for multiple gene sets. *Nucleic Acids Res.* **46**, D213–D217 (2018).
29. UniProt Consortium. UniProt: the universal protein knowledgebase in 2021. *Nucleic Acids Res.* **49**, D480–D489 (2021).
30. Noguchi, S. et al. FANTOM5 CAGE profiles of human and mouse samples. *Sci. Data* **4**, 170112 (2017).
31. Wang, R., Zheng, D., Yehia, G. & Tian, B. A compendium of conserved cleavage and polyadenylation events in mammalian genes. *Genome Res.* **28**, 1427–1441 (2018).
32. Zheng, D. et al. Cellular stress alters 3'UTR landscape through alternative polyadenylation and isoform-specific degradation. *Nat. Commun.* **9**, 2268 (2018).
33. Fontes, M. M. et al. Activity-dependent regulation of alternative cleavage and polyadenylation during hippocampal long-term potentiation. *Sci. Rep.* **7**, 17377 (2017).
34. Li, W. et al. Alternative cleavage and polyadenylation in spermatogenesis connects chromatin regulation with post-transcriptional control. *BMC Biol.* **14**, 6 (2016).
35. Yang, Y. et al. PAF complex plays novel subunit-specific roles in alternative cleavage and polyadenylation. *PLoS Genet.* **12**, e1005794 (2016).
36. Li, W. et al. Systematic profiling of poly(A)⁺ transcripts modulated by core 3' end processing and splicing factors reveals regulatory rules of alternative cleavage and polyadenylation. *PLoS Genet.* **11**, e1005166 (2015).

37. Derti, A. et al. A quantitative atlas of polyadenylation in five mammals. *Genome Res.* **22**, 1173–1183 (2012).
38. Vo Ngoc, L., Cassidy, C. J., Huang, C. Y., Duttke, S. H. C. & Kadonaga, J. T. The human initiator is a distinct and abundant element that is precisely positioned in focused core promoters. *Genes Dev.* **31**, 6–11 (2017).
39. Heinz, S. et al. Simple combinations of lineage-determining transcription factors prime *cis*-regulatory elements required for macrophage and B cell identities. *Mol. Cell* **38**, 576–589 (2010).
40. Grant, C. E., Bailey, T. L. & Noble, W. S. FIMO: scanning for occurrences of a given motif. *Bioinformatics* **27**, 1017–1018 (2011).
41. Fornes, O. et al. JASPAR 2020: update of the open-access database of transcription factor binding profiles. *Nucleic Acids Res.* **48**, D87–D92 (2020).

Acknowledgements

We would like to thank B. Aken, the Transforming Genomic Medicine Initiative Consortium (G. Black, S. Ellard, H. Firth, D. Fitzpatrick, M. Hurles, H. Rehm, J. Ware and C. Wright), the Clinical Genome Resource (H. Rehm and S. Harrison), DECIPHER (H. Firth and J. Foreman), the FANTOM Consortium (K. Hideya), PanelApp (E. McDonaugh), ClinVar (M. Landrum), OMIM (A. Hamosh), the CRUCS team within Ensembl (B. Flint, S. Hunt, E. Perry, S. Trevanion, A. Winterbottom and A. Yates), I. Armean, S. Boddu and F. Martin. Ensembl and Ensembl VEP are registered trademarks of EMBL. The work performed by the authors at EMBL-EBI was supported by the Wellcome Trust (WT200990/Z/16/Z, WT200990/A/16/Z, WT108749/Z/15/Z), the National Human Genome Research Institute of the National Institutes of Health under award number 2U41HG007234 and EMBL. The work performed by the authors at NCBI is supported by the Intramural Research Program of the National Library of Medicine, National Institutes of Health. The content is solely the

responsibility of the authors and does not necessarily represent the official views of the National Institutes of Health.

Author information

Author notes

1. These authors contributed equally: Joannella Morales, Shashikant Pujar

Affiliations

1. European Molecular Biology Laboratory, European Bioinformatics Institute, Wellcome Genome Campus, Hinxton, UK

Joannella Morales, Jane E. Loveland, Ruth Bennett, Andrew Berry, Claire Davidson, Reham Fatima, Laurent Gil, Jose M. Gonzalez, Matthew Hardy, Toby Hunt, Michael Kay, Aoife McMahon, Jonathan M. Mudge, Daniel N. Murphy, Glen Threadgold, Paul Flicek, Ewan Birney, Adam Frankish & Fiona Cunningham

2. National Center for Biotechnology Information, National Library of Medicine, National Institutes of Health, Bethesda, MD, USA

Shashikant Pujar, Alex Astashyn, Eric Cox, Olga Ermolaeva, Catherine M. Farrell, Tamara Goldfarb, Diana Haddad, John Jackson, Vinita S. Joardar, Vamsi K. Kodali, Kelly M. McGarvey, Michael R. Murphy, Bhanu Rajput, Sanjida H. Rangwala, Lillian D. Riddick, Françoise Thibaud-Nissen, Anjana R. Vatsan, Craig Wallin, David Webb, Kim D. Pruitt & Terence D. Murphy

Contributions

F.C. and T.D.M. served as joint last authors. F.C., A.F., T.D.M., J.M., S.P. and J.E.L. provided research design, management and leadership. E.B., F.C., K.D.P. and P.F. provided management support and secured funding. R.B., A.B., E.C., C.D., C.M.F., T.G., D.H., M.H., T.H., J.J., V.S.J., M.K.,

J.E.L., K.M.M., A.M., J.M., J.M.M., M.R.M., T.D.M., S.P., S.H.R., L.D.R., F.T.N., G.T., A.R.V. and D.W. performed manual curation and annotation updates. R.F., J.M.G., D.N.M., L.G., A.A., C.W., O.E. and V.K.K. developed the Select pipelines and processed outputs. J.M., S.P., J.E.L., R.B., C.D., M.K., A.M., G.T., A.A., V.K.K., O.E., C.W. and T.D.M. engaged in data analysis, data interpretation and pipeline quality control. J.M., S.P. and T.D.M. created the figures. J.M. and S.P. drafted the manuscript with significant review from F.C., T.D.M., A.F. and J.E.L. All authors reviewed the manuscript before submission.

Corresponding author

Correspondence to [Terence D. Murphy](#).

Ethics declarations

Competing interests

E.B. is a paid consultant for Oxford Nanopore Technologies and Dovetail, Inc. P.F. is a member of the scientific advisory boards of Fabric Genomics, Inc., and Eagle Genomics, Ltd. All other authors declare no competing interests.

Peer review

Peer review information

Nature thanks Marina DiStefano, Sharon Plon and the other, anonymous, reviewer(s) for their contribution to the peer review of this work.

Additional information

Publisher's note Springer Nature remains neutral with regard to jurisdictional claims in published maps and institutional affiliations.

Extended data figures and tables

Extended Data Fig. 1 The Select pipelines.

a, The RefSeq Pipeline picks the Select transcript based on a set of hierarchically scored criteria described in the Methods section and in more detail in Supplementary Method 1. **b**, The Ensembl pipeline assigns Ensembl Canonical to the transcript with the highest score, which is a sum of the component scores for each criteria (e.g. conservation, expression, APPRIS choice, UniProt choice, length). Details are listed in Supplementary Method 1.

Extended Data Fig. 2 MANE collaboration UTR definition.

Graphic display of the 5' terminal UTR exon of the gene *PTPRC* (HGNC:9666) in NCBI GDV to illustrate how we defined the 5' end of the transcript. Annotation tracks (top to bottom) show transcripts in RefSeq Annotation Release 109_20210514, transcripts in Ensembl Release 104 and the MANE Select (v0.95) track. The longest 5' UTR among the RefSeq and Ensembl/GENCODE annotation sets is flagged at the first base with a blue vertical box. The “FANTOM Total CTSS Counts” track displays histograms representing CAGE tag counts at each base position. The strongest CAGE peak (the most abundant start site or the base position with the absolute maximum CAGE tag count) is highlighted with a yellow vertical box. The “RefSeq Processed CAGE” track at the bottom displays the start site (highlighted with a green vertical box) selected by the UTR algorithm. Details of how the UTR algorithm works are covered in the Methods and provided in Supplementary Method 3: UTR algorithm. A similar logic was used to compute polyA clusters and determine the 3' ends of transcripts.

Extended Data Fig. 3 Frequency of TSS signatures in RefSeq, Ensembl, and MANE transcripts.

A) Frequency of A, C, G, T nucleotides at each position (y-axis) relative to the transcription start site (x-axis). MANE transcripts show an enrichment of C at -1, and purine (A or G) at +1. **B)** Count of transcripts with a best Inr

motif (y-axis) placed relative to the TSS (x-axis). The peak of Inr motifs at -3 corresponds to the core CA motif located at -1 to $+1$. **C**) Count of transcripts with a TATA-box (y-axis) placed relative to the transcription start site (x-axis). The peak of TATA-box motifs at -31 corresponds to the core TATAAA box motif located at -28 to -23 upstream of the TSS. Details of the methods are available in Supplementary Methods [1](#).

[Source data](#)

[Extended Data Fig. 4 MANE Select coverage over time.](#)

(A) Graphical display of the percentage of all protein-coding genes (blue) and of the subset of clinical genes (orange) that have a defined MANE Select transcript per each MANE project release over time. **(B)** Number of genes that have a defined MANE Select transcript (MANE v0.95). The list includes 101 genes that will require the MANE Select to be defined using an ALT or PATCH (rather than the GRCh38 Primary Assembly). It does not include an additional set of 345 genes that require review due to conflicting gene types between RefSeq and Ensembl/Gencode.

[Extended Data Fig. 5 Commonly used resources that have adopted the MANE Select in their browsers and display.](#)

Top panel: A screenshot of the gene page of *PKP2* (HGNC:9024) in the DECIPHER database (<https://www.deciphergenomics.org/>). The transcript table on the gene page shows the MANE Select label with the RefSeq and Ensembl identifiers (marked by a red box). Middle panel: A ClinVar variant display (<https://www.ncbi.nlm.nih.gov/clinvar/variation/870075/>) page for the gene *PKP2* (allele ID 858255). The HGVS table in this page includes the RefSeq component of the MANE Select (indicated by red box). Bottom panel: A display page from the Genome Aggregation Database gnomAD v3.1. The MANE Select pair, along with the RefSeq and Ensembl identifiers, are displayed at the top of the page (indicated by red box). We note that UniProt, another commonly used resource, will update their browser soon to include flagged MANE Select proteins.

[Extended Data Fig. 6 Display of MANE data in Ensembl.](#)

(A) In Ensembl's Gene page, the Ensembl/GENCODE transcript(s) in the MANE set is highlighted with the “MANE Select” or “MANE Plus Clinical” flags, visible in the last column of the transcript table. The identical RefSeq transcript is highlighted in the same table, in the column titled “RefSeq Match”. **(B)** Graphical representation is visible in the Location page after configuring the view by adding the custom-made MANE Project track hub (<https://ftp.ncbi.nlm.nih.gov/refseq/MANE/trackhub/hub.txt>). **(C)** The list of MANE transcripts can be accessed and downloaded from Ensembl's Transcript Archive (Tark) MANE Project page (<http://tark.ensembl.org/web/manelist>) and programmatically using APIs available in the REST API page (http://tark.ensembl.org/api/#/transcript/transcript_manelist_list), or Ensembl's REST API e.g. <https://rest.ensembl.org/overlap/id/ENSG00000128573?feature=mane;content-type=text/xml>. **(D)** MANE data can also be downloaded from Ensembl BioMart (<https://www.ensembl.org/biomart/martview/c24cb3213fe65da552fcb8b755c2910c>) by choosing the ‘Human Genes (GRCh38.p13) dataset and the ‘MANE transcripts’ filter.

Extended Data Fig. 7 Access to MANE data in NCBI resources.

(A) Genome Data Viewer (GDV). The MANE track (green, at the top) shows RefSeq transcripts assigned as MANE Select and MANE Plus Clinical for the gene *SCN5A* (HGNC:10593). The middle section shows RefSeq and Ensembl identifiers included in the MANE sets, available by adding the MANE track hub using the ‘Configure Track Hubs’ menu. The bottom section shows a portion of RefSeq annotation release 109.20210514. **(B)** The gene search results page (shown here for the gene *SCN5A*), reached by searching for any human protein-coding gene in <https://www.ncbi.nlm.nih.gov/gene/>, flags the MANE Select in the expanded transcript list. **(C)** A portion of the transcript record of NM_000335.5, the MANE Select for *SCN5A*. The MANE Select tag (boxed) is included in the ‘KEYWORDS’ section. The keyword can be used in Nucleotide and Protein database queries to extract a list of MANE Select transcripts. For example: PALM[gene] AND MANE Select[keyword]. The entire list of MANE Select

transcripts can be obtained using the Entrez query “Homo sapiens[organism] AND MANE_select[keyword]”. MANE data can also be parsed from the annotation files available in the NCBI RefSeq FTP page (https://ftp.ncbi.nlm.nih.gov/refseq/H_sapiens/annotation/annotation_releases/109.20210514/GCF_000001405.39_GRCh38.p13/) using the “MANE Select” tag attribute (tag=MANE Select in GFF3, or tag ”MANE Select” in GTF), in the rows associated with the mRNA, CDS and exon features. In addition, column 9 also contains the matching Ensembl transcript identifier as an external database reference (Dbxref). Rows in the annotation files associated with the CDS feature contain the MANE Select tag, along with the matching Ensembl protein identifier.

Extended Data Fig. 8 Access to MANE Data in UCSC browser.

The MANE data are accessible in UCSC’s Genome Browser as a data track in the Genes and Gene Predictions section (bottom of figure). MANE data can also be viewed in this browser by adding the track hub (<https://ftp.ncbi.nlm.nih.gov/refseq/MANE/trackhub/hub.txt>), which displays the RefSeq and Ensembl identifiers of the MANE Select separately (top of figure), as shown in this display of the *SCN5A* (HGNC:10593).

Extended Data Fig. 9

MANE transcript display in LRG records. Screenshots of the LRG records for the genes *CYP3A5* (HGNC:2638) (http://ftp.ebi.ac.uk/pub/databases/lrgex/LRG_1431.xml) and *ATP1A2* (HGNC:800) (http://ftp.ebi.ac.uk/pub/databases/lrgex/LRG_6.xml) displaying MANE transcript annotations. As illustrated in this figure, if the LRG and MANE Select transcripts are identical (Panel A, LRG_1431 for *CYP3A5*), the MANE Select flag is displayed in the Fixed Reference Sequence and Transcript sections of the LRG. In the event that the LRG transcript is not the MANE Select (Panel B, LRG_6 for *ATP1A2*), there will be no flag in the Fixed reference section but the MANE Select transcript will be listed in the Transcript section for the user’s information.

Extended Data Table 1 Links to access MANE data from Ensembl, NCBI and UCSC

Supplementary information

Supplementary Methods

This file provides additional information on the methodology used to produce the MANE transcript sets.

Reporting Summary

Supplementary Table 1

This file provides a list of quality assurance criteria analysed to determine the suitability of a transcript for inclusion in the MANE Select set or for automatic updates to the 5' and 3' UTRs of transcripts.

Source data

Source Data Fig. 3

Source Data Extended Data Fig. 3

Rights and permissions

Open Access This article is licensed under a Creative Commons Attribution 4.0 International License, which permits use, sharing, adaptation, distribution and reproduction in any medium or format, as long as you give appropriate credit to the original author(s) and the source, provide a link to the Creative Commons license, and indicate if changes were made. The images or other third party material in this article are included in the article's Creative Commons license, unless indicated otherwise in a credit line to the material. If material is not included in the article's Creative Commons license and your intended use is not permitted by statutory regulation or exceeds the permitted use, you will need to obtain permission directly from the copyright holder. To view a copy of this license, visit <http://creativecommons.org/licenses/by/4.0/>.

Reprints and Permissions

About this article

Cite this article

Morales, J., Pujar, S., Loveland, J.E. *et al.* A joint NCBI and EMBL-EBI transcript set for clinical genomics and research. *Nature* **604**, 310–315 (2022). <https://doi.org/10.1038/s41586-022-04558-8>

- Received: 13 July 2021
- Accepted: 07 February 2022
- Published: 06 April 2022
- Issue Date: 14 April 2022
- DOI: <https://doi.org/10.1038/s41586-022-04558-8>

Share this article

Anyone you share the following link with will be able to read this content:

[Get shareable link](#)

Sorry, a shareable link is not currently available for this article.

[Copy to clipboard](#)

Provided by the Springer Nature SharedIt content-sharing initiative

This article was downloaded by **calibre** from <https://www.nature.com/articles/s41586-022-04558-8>

[Download PDF](#)

- Article
- Open Access
- [Published: 13 April 2022](#)

Thermophotovoltaic efficiency of 40%

- [Alina LaPotin](#) ORCID: [orcid.org/0000-0002-9002-4174¹](https://orcid.org/0000-0002-9002-4174),
- [Kevin L. Schulte](#) ORCID: [orcid.org/0000-0003-4273-6254²](https://orcid.org/0000-0003-4273-6254),
- [Myles A. Steiner](#)²,
- [Kyle Buznitsky](#)¹,
- [Colin C. Kelsall](#)¹,
- [Daniel J. Friedman](#)²,
- [Eric J. Tervo](#) ORCID: [orcid.org/0000-0002-8517-9649²](https://orcid.org/0000-0002-8517-9649),
- [Ryan M. France](#)²,
- [Michelle R. Young](#)²,
- [Andrew Rohskopf](#)¹,
- [Shomik Verma](#) ORCID: [orcid.org/0000-0002-0402-9930¹](https://orcid.org/0000-0002-0402-9930),
- [Evelyn N. Wang](#) ORCID: [orcid.org/0000-0001-7045-1200¹](https://orcid.org/0000-0001-7045-1200) &
- [Asegun Henry](#) ORCID: [orcid.org/0000-0002-9097-4882¹](https://orcid.org/0000-0002-9097-4882)

Nature volume **604**, pages 287–291 (2022)

- 18k Accesses
- 411 Altmetric
- [Metrics details](#)

Subjects

- [Devices for energy harvesting](#)
- [Energy storage](#)
- [Solar energy and photovoltaic technology](#)

Abstract

Thermophotovoltaics (TPVs) convert predominantly infrared wavelength light to electricity via the photovoltaic effect, and can enable approaches to energy storage^{1,2} and conversion^{3,4,5,6,7,8,9} that use higher temperature heat sources than the turbines that are ubiquitous in electricity production today. Since the first demonstration of 29% efficient TPVs (Fig. [1a](#)) using an integrated back surface reflector and a tungsten emitter at 2,000 °C (ref. [10](#)), TPV fabrication and performance have improved^{11,12}. However, despite predictions that TPV efficiencies can exceed 50% (refs. [11,13,14](#)), the demonstrated efficiencies are still only as high as 32%, albeit at much lower temperatures below 1,300 °C (refs. [13,14,15](#)). Here we report the fabrication and measurement of TPV cells with efficiencies of more than 40% and experimentally demonstrate the efficiency of high-bandgap tandem TPV cells. The TPV cells are two-junction devices comprising III–V materials with bandgaps between 1.0 and 1.4 eV that are optimized for emitter temperatures of 1,900–2,400 °C. The cells exploit the concept of band-edge spectral filtering to obtain high efficiency, using highly reflective back surface reflectors to reject unusable sub-bandgap radiation back to the emitter. A 1.4/1.2 eV device reached a maximum efficiency of $(41.1 \pm 1)\%$ operating at a power density of 2.39 W cm^{-2} and an emitter temperature of 2,400 °C. A 1.2/1.0 eV device reached a maximum efficiency of $(39.3 \pm 1)\%$ operating at a power density of 1.8 W cm^{-2} and an emitter temperature of 2,127 °C. These cells can be integrated into a TPV system for thermal energy grid storage to enable dispatchable renewable energy. This creates a pathway for thermal energy grid storage to reach sufficiently high efficiency and sufficiently low cost to enable decarbonization of the electricity grid.

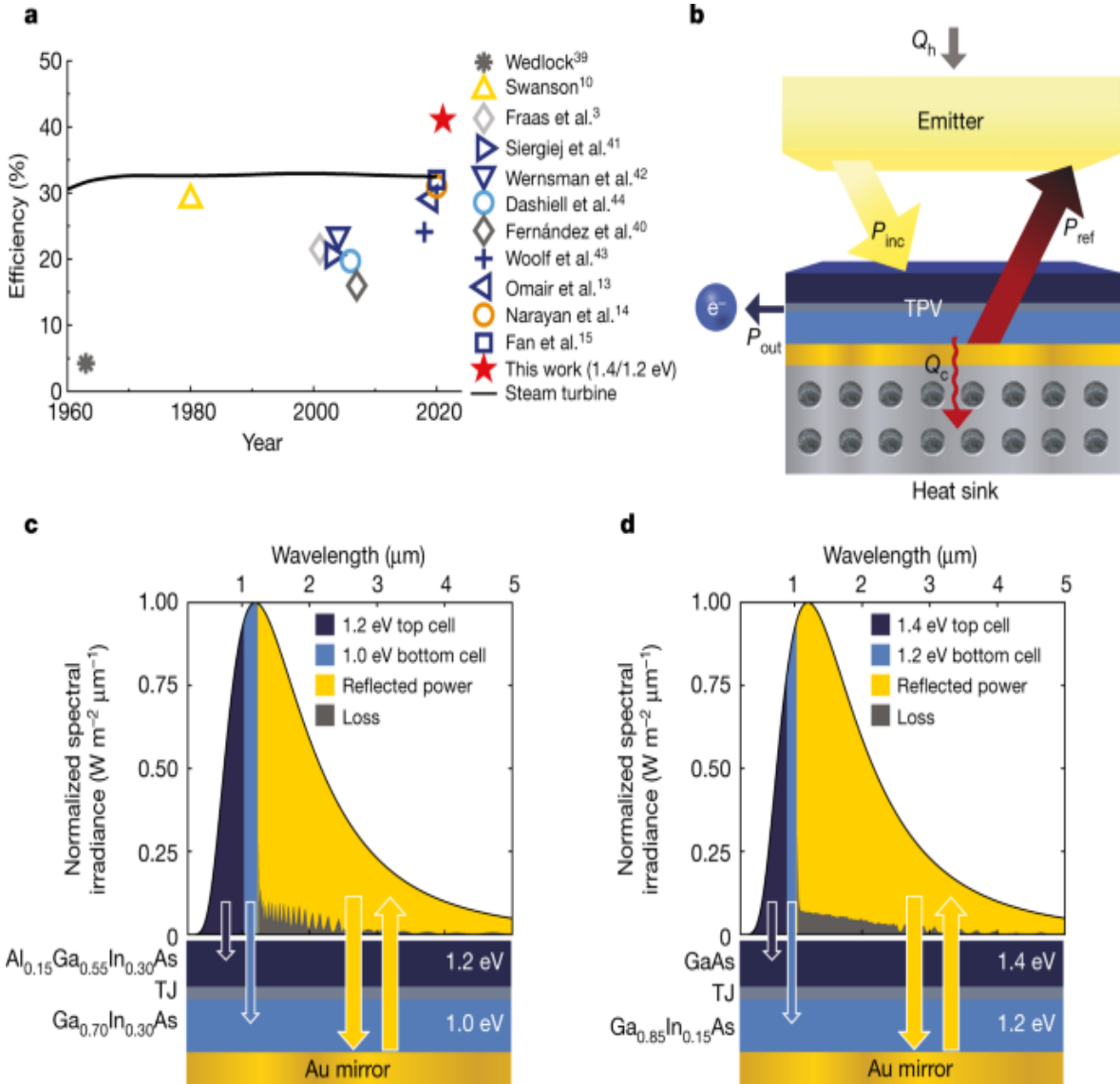
Main

Here we report TPV efficiency measurements of more than 40%, determined by simultaneous measurement of electric power output and heat dissipation

from the device by calorimetry. This record experimental demonstration of TPV efficiency was enabled by (1) the usage of higher bandgap materials in combination with emitter temperatures between 1,900 and 2,400 °C, (2) high-performance multi-junction architectures with bandgap tunability enabled by high-quality metamorphic epitaxy¹⁶ and (3) the integration of a highly reflective back surface reflector (BSR) for band-edge filtering^{11,13}.

The cells are 1.4/1.2 eV and 1.2/1.0 eV tandem devices optimized for the 1,900–2,400 °C emitter temperature range (Fig. 1) for the thermal energy grid storage (TEGS) application^{1,17}. TEGS is a low-cost, grid-scale energy storage technology that uses TPVs to convert heat to electricity above 2,000 °C, which is a regime inaccessible to turbines. It is a battery that takes in electricity, converts it to high-temperature heat, stores the heat and then converts it back to electricity by TPVs on demand. Although TEGS was initially conceived with a molten silicon storage medium¹⁸, a graphite storage medium is even lower cost (US\$0.5 per kg), and the projected capital cost per unit energy (CPE) is less than US\$10 per kWh (ref. ¹⁹). This cost is so low, it would enable TEGS to meet the proposed cost targets (<US\$20 per kWh) for long-duration energy storage that would allow renewable energy with storage to be cost-competitive with fossil fuels^{20,21,22}. As a result, the proliferation of TEGS could ultimately enable abatement of approximately 40% of global CO₂ emissions, by decarbonizing the electricity grid (approximately 25% of emissions) and then enabling CO₂-free electricity to charge vehicles in the transportation sector (approximately 15% of emissions)²³. Reaching a TPV efficiency of 40% is notable, because it means that TEGS, as well as a range of other potential applications, are now feasible. These applications include other energy storage technologies², natural gas, propane or hydrogen-fuelled power generation^{3,4,5,6,7,8,9}, and high-temperature industrial waste heat recovery (Methods and Extended Data Fig. 1).

Fig. 1: Tandem TPVs.



a, History of some TPV efficiencies¹² with different cell materials: Ge^{39,40} (dark grey), Si¹⁰ (yellow), GaSb³ (light grey), InGaAs^{13,15,41,42,43} (dark blue), InGaAsSb⁴⁴ (light blue) and GaAs¹⁴ (orange). The black line shows the average thermal efficiency of power generation in the United States using a steam turbine (coal and nuclear)^{36,37}. Before the year 2000, turbine efficiencies shown also include natural gas. **b**, Energy that is incident on the TPVs ($\{P\}_{inc}$) can be converted to electricity ($\{P\}_{out}$), reflected back to the emitter ($\{P\}_{ref}$), or thermalized because of inefficiencies in the cell and back reflector ($\{Q\}_c$). **c, d**, The 1.2/1.0 eV (**c**) and 1.4/1.2 eV (**d**) tandems that were fabricated and characterized in this work, and a representative

spectrum shape at the average emitter temperature (2,150 °C blackbody) indicating the spectral bands that can be converted to electricity by the top and bottom junction of a TPV cell. A gold mirror on the back of the cell reflects approximately 93% of the below bandgap photons, allowing this energy to be recycled. TJ represents the tunnel junction.

High-efficiency TPV cells

The efficiency of a TPV cell is defined differently from that of a solar cell because, unlike a solar cell, a TPV system can preserve and later convert the energy in sub-bandgap photons. This is because, in the contexts in which TPV is envisioned to be used, the TPV cell has a high view factor to the emitter. This means that sub-bandgap photons can be reflected back to the emitter by the TPV cell (Fig. 1b), which is different from a solar cell and the sun. By reflecting unconverted photons, the energy of the sub-bandgap light is preserved through reabsorption by the emitter. The reflected and subsequently reabsorbed light helps to keep the emitter hot, thereby minimizing the energy input required to heat the emitter. As a result, the efficiency of a TPV cell is given by

$$\eta_{\text{TPV}} = \frac{P_{\text{out}}}{P_{\text{out}} + Q_{\text{c}}} = \frac{P_{\text{out}}}{P_{\text{out}} + P_{\text{inc}} - P_{\text{ref}}} \quad (1)$$

In equation (1), P_{out} is the electric power generated by the TPV cell (that is, $V_{\text{oc}} I_{\text{sc}} F_{\text{FF}}$), where V_{oc} is the open circuit voltage, I_{sc} is the short-circuit current and F_{FF} is the fill factor of the current–voltage (IV) curve. The total heat absorbed and generated in the cell is denoted by Q_{c} , which is made up of the heat generated by parasitic absorption in the semiconductor or metal reflector, thermalization losses due to excess incident photon energy, Joule heating losses due to current flow and non-radiative recombination losses. The net energy received by the cell is equivalent to $P_{\text{out}} + Q_{\text{c}}$ and can also be expressed as $P_{\text{inc}} - P_{\text{ref}}$, where P_{inc}

$\{P\}_{inc}$) is the incident energy and $\{P\}_{ref}$) is the reflected energy. Based on equation (1), to increase TPV efficiency, one must increase the power output $\{P\}_{out}$) and/or reduce the amount of heat absorbed and generated in the cell ($\{Q\}_{c}$). The efficiency, $\{\eta\}_{TPV}$, is the metric we use here because it is the conventional and generalizable metric used to describe the performance of a cell–emitter pair independent of other system-level characteristics¹². The efficiency of a full system involving TPVs may be less than $\{\eta\}_{TPV}$ due to system-specific losses. However, these system-level losses can become negligible in the case of TEGS or a large-scale combustion-based electricity generation system^{1,24} (Methods and Extended Data Fig. 1).

The high emitter temperatures targeted here for TEGS and other applications allow higher bandgap cells of at least 1.0 eV to be used instead of the low-bandgap, InGaAs- or GaSb-based cells traditionally used for TPV. This is key, because the spectrum of light redshifts towards longer wavelengths as the radiator temperature is lowered, which is why traditional TPV cells that are paired with emitters of less than 1,300 °C are typically based on 0.74 eV InGaAs or 0.73 eV GaSb. Considerable work on low-bandgap semiconductors has been undertaken with the envisioned application of converting heat from natural gas combustion^{3,4,5,6,7,8,9}, concentrated solar power²⁴, space power applications^{25,26} and, more recently, energy storage^{1,2,27}. This pioneering body of work has led to the identification of three key features that now enable TPVs to become a competitive option for converting heat to electricity commercially: high-bandgap materials paired with high emitter temperatures, high-performance multi-junction architectures with bandgap tunability enabled by high-quality metamorphic epitaxy¹⁶ and the integration of a high-reflectivity BSR for band-edge filtering^{11,13}.

With respect to higher bandgaps, they increase efficiency because there is an almost constant penalty on voltage of around 0.3–0.4 V, due to the thermodynamic requirements on the radiative recombination rate²⁸. As a result, this unavoidable loss penalizes lower bandgap cells more than higher bandgap cells, because this loss makes up a smaller fraction of the voltage for higher bandgap materials. Using higher bandgap materials also needs to

be accompanied by operation at higher temperatures to maintain sufficiently high power density, which scales with the emitter temperature to the fourth power. Operation at high power density is critical for TPV economics because the cell costs scale with their area, and if the power generation per unit area increases, the corresponding cost per unit power (CPP) decreases²⁹.

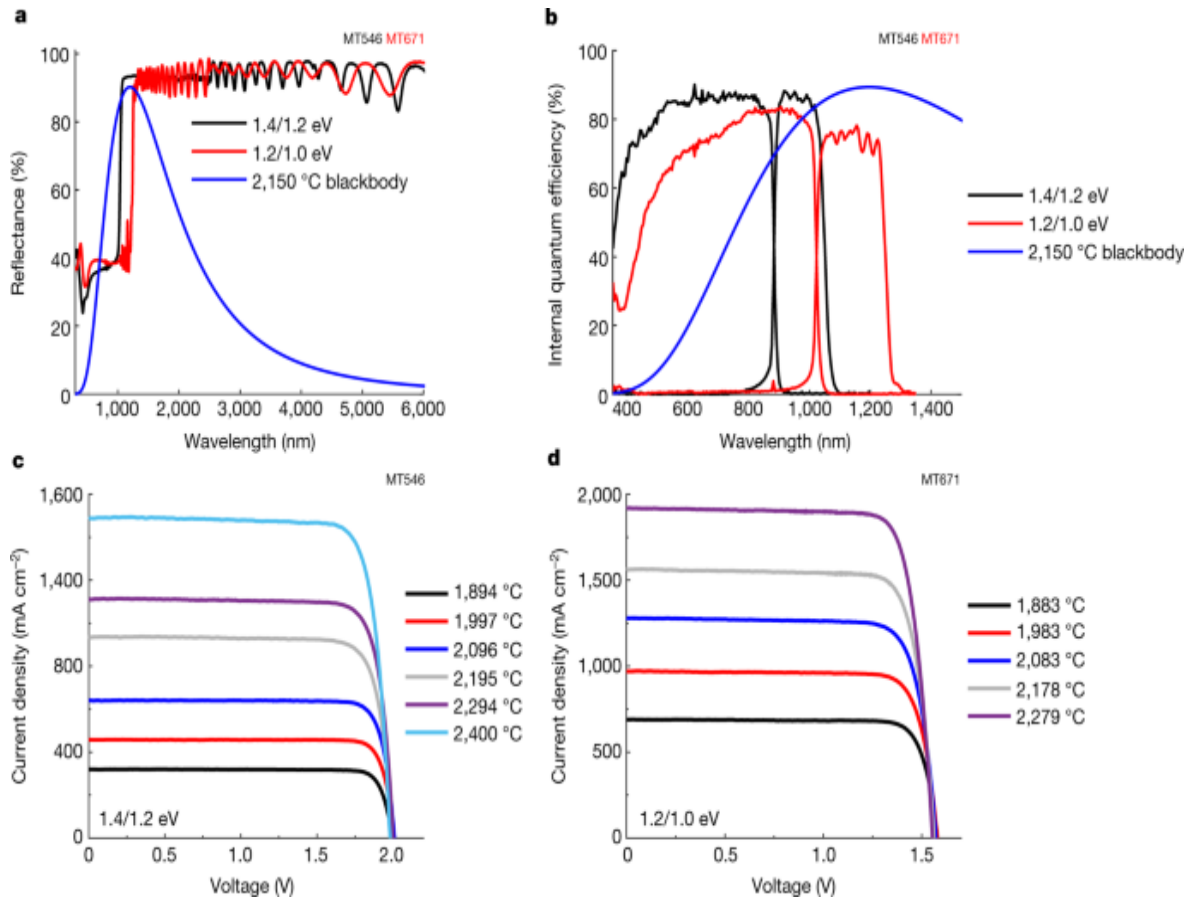
With respect to BSRs, a highly reflective BSR is critical to minimize $\langle\{Q\}_{\rm c}\rangle$. Highly reflective BSRs provide the additional benefit of boosting open-circuit voltage, because they also improve recycling of luminescent photons generated by radiative recombination^{30,31,32}. This effect has led to regular integration of BSRs with solar PV cells, which provides a template for their use in TPVs. With these important lessons from previous work in mind, the cells developed here are 1.2/1.0 eV and 1.4/1.2 eV two-junction designs intended for the TEGS application with emitter temperatures between 1,900 and 2,400 °C (ref. 1). Multi-junction cells increase efficiency over single junctions by reducing hot carrier thermalization losses and reducing resistive losses by operating at a lower current density. The cells were based on the inverted metamorphic multi-junction architecture pioneered at the National Renewable Energy Laboratory (NREL)^{33,34,35}.

The first cell design uses lattice-mismatched 1.2 eV AlGaInAs and 1.0 eV GaInAs top and bottom junctions, where the lattice mismatch is with respect to the crystallographic lattice constant of the GaAs substrate on which they are grown. The second design uses a lattice-matched 1.4 eV GaAs top cell and a lattice-mismatched 1.2 eV GaInAs bottom cell, taking advantage of the inherently higher material quality of lattice-matched epitaxy in the GaAs cell (Fig. 1c, Fig. 1d and Extended Data Fig. 2). The lower bandgap 1.2/1.0 eV tandem offers the potential for higher power density than the 1.4/1.2 eV tandem because it converts a broader band of the incident spectrum, and consequently the requirements on the BSR are less stringent to obtain high efficiency²⁷. Higher power density can also be a practical engineering advantage. On the other hand, although the 1.4/1.2 eV tandem has a lower power output, the reduced current density of this bandgap combination potentially enables higher efficiency than the 1.2/1.0 eV tandem if resistive losses are an issue.

TPV efficiency measurement results

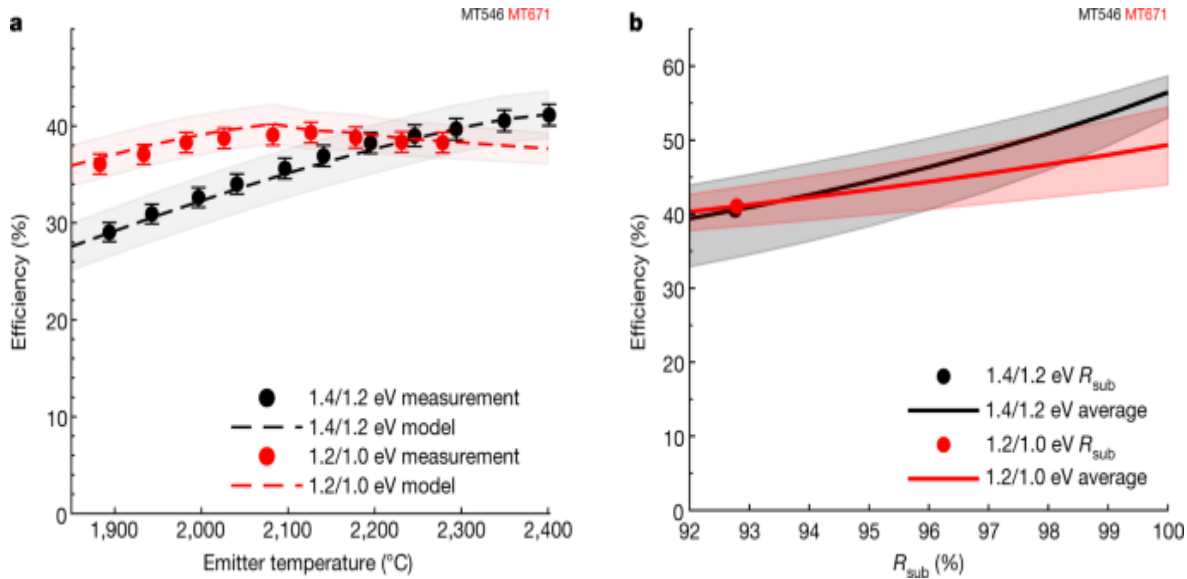
The TPV cell fabrication, measurement and modelling details are provided in the Methods. We refer to the two tandems by their bandgaps: 1.4/1.2 eV and 1.2/1.0 eV. Reflectance measurements are shown in Fig. 2a and internal quantum efficiency is given in Fig. 2b. The sub-bandgap spectral weighted reflectance for the 2,150 °C blackbody spectrum is 93.0% for the 1.4/1.2 eV tandem and 93.1% for the 1.2/1.0 eV tandem. The 2,150 °C blackbody spectrum shape is shown throughout for reference, because 2,150 °C is the average emitter temperature in the TECS application and in the measurements. See Extended Data Figs. 4 and 5a for the measured spectrum and a comparison between the blackbody spectrum shape and the spectrum under which the cells were characterized. Current density versus voltage measurements were performed under a tungsten halogen bulb emitter and results for a range of emitter temperatures relevant to the TECS application (approximately 1,900–2,400 °C) are shown in Fig. 2c, 2d. As expected, the 1.2/1.0 eV tandem had lower voltage but higher current density than the 1.4/1.2 eV tandem. The non-monotonic change in $\langle\langle V \rangle\rangle_{\{\{\rm{oc}\}\}}$ at the highest emitter temperatures was because of increasing cell temperature (Extended Data Fig. 6a) due to the presence of a heat flux sensor (HFS) used for the efficiency measurement, that undesirably also impeded heat flow. Figure 3a shows the efficiency measurement at the same range of emitter temperatures, which was accomplished by simultaneously measuring $\langle\langle Q \rangle\rangle_{\{\{\rm{c}\}\}}$ and $\langle\langle P \rangle\rangle_{\{\{\rm{out}\}\}}$.

Fig. 2: TPV characterization.



a, Reflectance of the 1.4/1.2 eV and 1.2/1.0 eV tandems. The 2,150 °C blackbody spectrum is shown for reference, which is the average emitter temperature in the TEGS application. **b**, Internal quantum efficiency (IQE) of the 1.4/1.2 eV and 1.2/1.0 eV tandems. The EQE is shown in Extended Data Fig. 3. **c**, **d**, Current density–voltage curves measured in the efficiency setup at varying emitter temperatures for the 1.4/1.2 eV (**c**) and 1.2/1.0 eV (**d**) tandems.

Fig. 3: TPV efficiency.



a, TPV efficiency measured at different emitter temperatures ranging from approximately 1,900 °C to 2,400 °C. The error bars indicate the uncertainty of the efficiency measurement, which is discussed in Methods. The dashed lines show the model predictions and the shaded regions show the uncertainty in the model predictions (see Methods). **b**, Predicted efficiency of the 1.4/1.2 eV and 1.2/1.0 eV tandems as the weighted sub-bandgap reflectance ($\langle\langle R \rangle\rangle_{\{ \{ \text{rm} \{ \text{sub} \} \} \}}$) is extrapolated assuming a W emitter with AR = 1 and VF = 1 and a 25 °C cell temperature (Extended Data Fig. 5). The solid lines show the average efficiency within the TEGS operating temperature range of 1,900 °C to 2,400 °C. The shaded bands show the maximum and minimum efficiencies within the temperature range. The dots show the present value of $\langle\langle R \rangle\rangle_{\{ \{ \text{rm} \{ \text{sub} \} \} \}}$ based on the measured reflectance in Fig. 2a weighted by the W AR = 1, VF = 1 spectrum.

The results for the 1.4/1.2 eV tandem showed increasing efficiency with increasing emitter temperature, and the efficiency exceeded 40% at 2,350 °C, which is within the target range of 1,900–2,400 °C needed for the TEGS application. At 2,400 °C, the efficiency was as high as $41.1 \pm 1\%$, whereas the average efficiency between 1,900 and 2,400 °C was 36.2%. The electrical power density was 2.39 W cm^{-2} at the maximum emitter temperature of 2,400 °C. The rate of increase of efficiency with temperature slowed at high emitter temperatures due to a reduction in FF, because of increasing series resistance losses and the diminishing increase in \

(η) due to the cell becoming current-limited by the bottom cell at approximately 2,250 °C.

The results for the 1.2/1.0 eV tandem showed greater efficiency than for the 1.4/1.2 eV tandem at lower emitter temperatures because of its lower bandgaps. The efficiency of the 1.2/1.0 eV tandem reached a maximum of $39.3 \pm 1\%$ at 2,127 °C, quite close to 2,150 °C, which is the temperature at which our device model predicted this bandgap combination would be optimal²⁷. The average efficiency between 1,900 and 2,300 °C was 38.2% and the efficiency remained high across a 400 °C range of emitter temperatures. This is particularly worth noting for the TEGS application because it indicates consistently high efficiency can be achieved even as the emitter temperature varies during the discharging process of the TEGS system. The reduction in efficiency beyond this temperature was due to the increasing series resistance losses and the diminishing increase in η (η) due to the cell becoming current-limited by the bottom cell at temperatures greater than 2,150 °C. The electrical power density was 2.42 W cm^{-2} at the maximum emitter temperature measured of 2,279 °C, and it was 1.81 W cm^{-2} at the maximum efficiency point at the emitter temperature of 2,127 °C. Comparing the performance of the two cells across the range of emitter temperatures, they exhibit different characteristics that are advantageous for TEGS. The efficiency of the 1.2/1.0 eV tandem is less sensitive to changes in emitter temperature, has a higher electrical power density at a given emitter temperature and has a higher efficiency averaged over the emitter temperatures. However, the 1.4/1.2 eV tandem can reach higher efficiency at the highest emitter temperatures.

Figure 3a also shows model predictions for efficiency and the corresponding uncertainty of the model prediction. The good agreement obtained between the modelled and measured performance supports and validates the accuracy of the efficiency measurement and of the calorimetry-based method used to measure efficiency. In addition, the good agreement indicates that the model can be extended to extrapolate how the performance would change with additional improvements or at other operating conditions. The most important TPV cell property that could be improved is its spectral-weighted sub-bandgap reflectance, R_{sub} . Figure 3b shows how the efficiency would change if R_{sub} could be increased. To

extrapolate the results to a real TPV system, here we assume that the emitter is tungsten (W), as it is in the TEGS system, and that the area ratio between the emitter and cell is $\text{AR} = 1$, the view factor is $\text{VF} = 1$ and the cell temperature is 25 °C (Extended Data Fig. 5). In this prediction, for a 2,200 °C emitter temperature, the efficiency of the 1.4/1.2 eV tandem exceeds 50% at $R_{\text{sub}} = 97 \%$. The reason this is worth noting is because the present value of R_{sub} is considerably lower than what was achieved with the air bridge approach recently demonstrated by Fan et al.¹⁵. Their work demonstrating a reflectivity of more than 98% charts a pathway towards further efficiency improvements. If the air bridge approach developed by Fan et al. could be combined with the advancements demonstrated here, it could lead to efficiencies greater than 56% at 2,250 °C, or greater than 51% averaged over the 1,900–2,400 °C temperature range.

Conclusions

We report two-junction TPV cells with efficiencies of more than 40% using an emitter with a temperature between 1,900 and 2,400 °C. The efficiency of the 1.4/1.2 eV tandem reaches $41.1 \pm 1\%$ at 2,400 °C, with an average of 36.2% over the target temperature range. The efficiency of the 1.2/1.0 eV tandem reaches $39.3 \pm 1\%$ and varies very little over a wide temperature range with an average efficiency over the 1,900–2,300 °C temperature range of 38.2%. This high performance is enabled by the usage of multi-junction cells with bandgaps of at least 1.0 eV, which are higher bandgaps than have been traditionally used in TPVs. The higher bandgaps enable the use of higher emitter temperatures, which correspond to the temperature range of interest for the low-cost TEGS energy storage technology¹. This temperature range is also applicable for natural gas or hydrogen combustion, and further demonstration of integrated systems is warranted.

Reaching 40% efficiency with TPVs is notable from the standpoint that it now renders TPV as a heat engine technology that can compete with turbines. An efficiency of 40% is already greater than the average turbine-based heat engine efficiency in the United States (Fig. 1a)^{36,37,38}, but what could make TPVs even more attractive than a turbine is the potential for lower cost (CPP < US\$0.25 per W)^{1,24}, faster response times, lower

maintenance, ease of integration with external heat sources and fuel flexibility. This is noteworthy because turbine costs and performance have already reached full maturity, so there are limited prospects for future improvement, as they are at the end of their development curve. TPVs, on the other hand, are very early in their progress down a fundamentally different development curve. Consequently, TPVs have numerous prospects for both improved efficiency (for example, by improving reflectivity and lowering series resistance) and lowering cost (for example, by reusing substrates and cheaper feedstocks). Thus, the demonstration of 40% efficiency represents an important step towards realizing the potential that can be achieved with increased attention and funding in the coming years as commercial applications emerge and become profitable.

Methods

TPV applications

Turbines proliferated because of their high efficiency (25–60%) and their low CPP generated (US\$0.5–1 per W). However, as turbines intrinsically require moving parts, there are corresponding requirements on the high-temperature mechanical properties of the materials of construction, as they are subject to centrifugal loads. Thus, they have reached their practical limits in terms of cost and efficiency, barring a materials discovery that would allow them to operate at substantially higher turbine inlet temperatures than the current values of approximately 1,500 °C for Brayton cycles and approximately 700 °C for Rankine cycles²⁹. Solid-state heat engines such as TPVs, which have no moving parts, possess an advantage in this sense, enabling operation at significantly higher temperatures than turbines. TPVs can enable new approaches to energy storage^{1,2} and conversion^{3,4,5,6,7,8,9} that use higher temperature heat sources.

In this section, we highlight two promising applications for high-bandgap tandem TPVs paired with high-temperature heat sources: (1) TEGS¹ and (2) combustion-driven electricity generation. We also discuss the importance of TPV efficiency in relation to the system-level efficiency metrics relevant to these applications.

TEGS, which is conceptually illustrated in Extended Data Fig. [1a](#), takes in electricity, converts it to heat by joule heating, stores the heat in a bank of large graphite blocks and then converts it back to electricity through TPVs. The heat is transferred to different parts of the system using mechanically pumped liquid metal tin⁴⁵ and a graphite infrastructure, as demonstrated by Amy et al.^{[1,17,18](#)}. The blocks store the heat and when electricity is desired, the liquid metal retrieves the heat and delivers it to a power block containing TPV cells that convert light emitted by the hot infrastructure. For a storage system, the primary efficiency metric is the round trip efficiency (RTE) described by the ratio of the output electrical power ($\{P\}_{\{out\}}$) to the input electrical power ($\{P\}_{\{in\}}$). For TEGS, $\{P\}_{\{in\}}$ is primarily the electricity supplied to the resistance heaters, but also includes a contribution from pumping power requirements for the liquid tin heat transfer fluid and the heat exchanger for cell cooling. The Sankey diagram of the TEGS system is shown in Extended Data Fig. [1b](#).

For any system using TPVs, a subsystem efficiency can be defined as the ratio of the electric power output to the energy input to the emitter at steady state, $\{Q\}_{\{h\}}$, such that $\{\eta_{\{TPV\}}\}_{\{rm{subsystem}\}} = \{P\}_{\{out\}} / Q_{\{h\}}$ (Fig. [1b](#) and Extended Data Fig. [1b](#)). $\{\eta_{\{TPV\}}\}_{\{rm{subsystem}\}}$ may be less than $\{\eta_{\{TPV\}}\}$ due to view factor or convective losses from the emitter or cell, or other heat losses from the emitter to the environment ($\{Q\}_{\{loss\}}_{\{rm{subsystem}\}}$). Therefore, $\{Q\}_{\{h\}} = \left(\{P\}_{\{out\}} / \{\eta_{\{TPV\}}\} \right) + \{Q\}_{\{loss\}}_{\{rm{subsystem}\}}$ and $\{\eta_{\{TPV\}}\}_{\{rm{subsystem}\}} = \{\eta_{\{TPV\}}\} (1 - \frac{\{Q\}_{\{loss\}}}{\{Q\}_{\{h\}}})$. Assuming no convective loss due to operation in a vacuum and negligible view-factor losses, then $\{\eta_{\{TPV\}}\}_{\{rm{subsystem}\}} \approx \{\eta_{\{TPV\}}\}$ if $\{Q\}_{\{loss\}}_{\{rm{subsystem}\}}$, which scales with the outer surface area of the power block, is small as compared with the energy conversion taking place inside the power block, which scales with its volume. This can be accomplished by increasing the scale of the system such that the heated material has a large volume to surface area ratio, Φ , and heat losses from the surfaces can be minimized with proper insulation²⁴, and

if the emitter surface and TPV module have a large surface area to perimeter ratio such that the view factor between them approaches one. This can be the case for TEGS or a large-scale combustion system, and it is a critically important aspect of achieving a high value for $\langle\eta_{\text{TPV}}\rangle$, $\langle\text{subsystem}\rangle$ (refs. [1,24](#)).

To illustrate the importance of Φ , Extended Data Fig. [1a](#) shows a single unit cell of the TEGS power block, which is composed of a tungsten cavity emitter heated by pumped liquid tin, emitting to an array of TPV cells. The nominal dimensions of the TPV array, $\langle L_{\text{TPV}}\rangle$, and emitter, $\langle L_{\text{emit}}\rangle$, are 10 cm and 40 cm, respectively. The area ratio $\langle AR \rangle = \frac{\langle A_{\text{emit}} \rangle}{\langle A_{\text{TPV}} \rangle} = 4$ and the emitter material is tungsten based on previous optimization^{[1](#)}. The graphite pipes, which carry the liquid tin heat transfer fluid and supply energy to the tungsten emitter surface, are 2 cm in diameter. Therefore, the side length of one unit cell of the power block is $\langle L_{\text{unit}} \rangle = 44 \text{ cm}$. We note that although fins on the emitter can be used to increase the volumetric power density of the system, in this example we assume no fins are used for simplicity. In this example, we also assume that the depth dimensions of all components are equivalent, and that convective losses and view factor losses are negligible.

Heat losses from the exterior surface of the power block to the environment can be expressed as $\langle Q_{\text{loss}} \rangle = hA_{\text{ext}}(T_{\text{ext}} - T_{\infty})$, where $\langle h \rangle$ is the overall heat transfer coefficient representing losses to the environment. The value of $\langle h \rangle$ is dominated by conduction through the graphite insulation such that $h \approx k/L_{\text{insulation}}$, where $\langle k \rangle$ is the thermal conductivity of graphite insulation ($k \approx 1 \text{ W m}^{-1} \text{ K}^{-1}$ at 2,150 °C) and $\langle L_{\text{insulation}} \rangle$ is the insulation thickness. Although its thermal conductivity is moderate, graphite insulation is the only economical option for insulating systems above 1,700 °C (ref. [46](#)). $\langle A \rangle$ is the external surface area of the power block, $\langle T_{\text{ext}} \rangle$ is the average temperature of the power block (2,150 °C) and $\langle T_{\infty} \rangle$ is the temperature of the environment (25 °C).

Considering a single unit cell of the dimensions discussed above and using tungsten spectral properties and an emitter temperature $\langle\{ T \} \rangle \{ \{ \rm{h} \} \}$ = 2,150 °C, our TPV model predicts $\langle\{ P \} \rangle \{ \{ \rm{out} \} \}$ = 11.4 W per cm² of cell area and $\langle\{ \eta \} \rangle \{ \{ \rm{TPV} \} \}$ = 40% for the 1.2/1.0 eV tandem. Considering the entire volume of the unit cell, this leads to a volumetric electric power density of 240 kW m⁻³. Assuming that the power block is a cube, Extended Data Fig. 1c shows $\langle\{ \eta \} \rangle \{ \{ \rm{TPV} \} \}$, $\{ \{ \rm{subsystem} \} \}$ as a function of the side length of the power block (excluding the insulation) as well as $\langle\{ \Phi \} \rangle$ for two different graphite insulation thicknesses. The results show that $\langle\{ \eta \} \rangle \{ \{ \rm{TPV} \} \}$, $\{ \{ \rm{subsystem} \} \}$ approaches $\langle\{ \eta \} \rangle \{ \{ \rm{TPV} \} \}$ for power block length scales of approximately 1 m when the system is appropriately insulated. The results also indicate that TPVs are well-suited for large-scale systems, as it is challenging to achieve high system efficiencies with power block length scales of less than 1 m. In characterizing the RTE of TECS (Extended Data Fig. 1b), other losses are due to the energy conversion of electricity to heat in the resistive heaters (<1%) and heat losses from the thermal storage media (approximately 1% per day), but they can be negligibly small¹. Therefore, the RTE can be dominated by $\langle\{ \eta \} \rangle \{ \{ \rm{TPV} \} \}$.

Here it is important to note that a RTE of 40–55% as is targeted in the TECS application is low as compared to other options, such as Li-ion batteries, which have RTEs of more than 70%. However, several studies have pointed out that to enable full penetration of renewables onto the grid, a one to two order of magnitude decrease in CPE is required, owing to the need for long storage durations^{20,21,22}. It is from this perspective that the RTE can be sacrificed, as long as it is above approximately 35% (ref. 1), provided it enables accession of much lower cost. Thus, techno-economic analyses indicate that a technology with a tenfold lower CPE, yet a twofold lower efficiency as compared with Li-ion batteries, is still more economically attractive^{1,20,21,22}.

Another promising application for TPVs is electricity generation in which the heat source is the combustion of fuel^{3,4,5,6,7,8,9,47}. The temperature regime examined here is accessible by combustion of natural gas or hydrogen, which could be made into an efficient power generation system

by using recuperators made from refractory metals and oxides^{3,47}. Extended Data Figure 1d shows a modular combustion-driven TPV concept. Air enters a recuperator and is preheated by exchanging heat with the outgoing exhaust. The preheated air mixes with fuel, combusts and transfers heat to the emitter wall, which irradiates to the TPVs. Here, the important metric is the first-law thermal efficiency defining the ratio of net work output to the primary energy input (Extended Data Fig. 1e). The net work output is $\langle P \rangle_{\{ \rm{out} \}} - \langle P \rangle_{\{ \rm{in} \}}$, where $\langle P \rangle_{\{ \rm{out} \}}$ is the electric power output from the TPVs and $\langle P \rangle_{\{ \rm{in} \}}$ is the work input for pumping required for gas circulation and the TPV liquid cooling. The primary energy input is the higher heating value of the fuel, $\langle Q \rangle_{\{ \rm{HHV} \}}$. The combustor modules are stacked to create an array of length scale of around 1 m (Extended Data Fig. 1c), the side walls of each module are adiabatic by symmetry and the entire block of modules can be insulated at the outermost edges. A TPV panel that is close and opposite the emitter array has an area to perimeter ratio that is large and minimizes view-factor losses from the edges. Other heat losses can occur through the exhaust because of an imperfect recuperator. However, the efficiency at which the chemical energy in the fuel, $\langle Q \rangle_{\{ \rm{HHV} \}}$, is converted to $\langle Q \rangle_{\{ \rm{h} \}}$ for TPV systems (that is, $\langle Q \rangle_{\{ \rm{h} \}} / \langle Q \rangle_{\{ \rm{HHV} \}}$) can be approximately 90% (ref. 3).

These two examples (TEGS and combustion-driven electricity generation) illustrate the importance of $\langle \eta \rangle_{\{ \rm{TPV} \}}$, which dominates system-level efficiencies for an appropriately designed system at scale. Assuming that the other losses can be made negligible, our work demonstrates a solid-state heat engine (terrestrial heat source) with an efficiency higher than the average heat engine efficiency in the United States, which is lower than 35% based on primary energy inputs and electricity output³⁸. An efficiency of 40% is also higher than most steam cycles, and is in the same range as simple cycle gas turbines⁴⁸. Thus, 40% represents a major step forward (Fig. 1a), as this is a type of heat engine that has the potential to compete with turbines by exhibiting comparable efficiency and potentially even lower CPP, for example less than \$0.25 per W (refs. 1,24). To properly contextualize why this has broad-reaching implications, it should be appreciated that over the last century a range of

alternative heat engines, such as thermoelectrics⁴⁹, thermionics⁵⁰, TPVs¹², thermally regenerative electrochemical systems⁵¹, thermoacoustic engines⁵² and Stirling engines^{53,54}, have been developed. All these technologies have some intrinsic advantage(s) over turbines, such as low maintenance, no moving parts and/or easier integration with an external heat source, yet none of them have previously been able to compete with the efficiency and CPP of turbines for large-scale heat to electricity conversion.

TPV cell growth and processing details

Extended Data Figure 2 shows the device structures of the tandem cells. All materials were grown by atmospheric pressure organometallic vapour phase epitaxy using trimethylgallium, triethylgallium, trimethylindium, triethylaluminium, dimethylhydrazine, arsine and phosphine. Diethylzinc and carbon tetrachloride were used as p-type dopant sources and hydrogen selenide and dislane were used as n-type dopant sources. Growth took place in a purified hydrogen gas flow of 6 litres per minute. Substrates were n-type (100) GaAs with a 2° offcut towards the (111)B plane, and all devices were grown in an inverted configuration. For both types of cells, the substrate was prepared by first etching in NH₄OH:H₂O₂:H₂O (2:1:10 by volume). The substrate was then mounted on a graphite susceptor and heated inductively to 700 °C under an arsine overpressure, followed by an approximately 10 min deoxidization under arsine.

Growth of the 1.4/1.2 eV tandem started with a 0.2 μm GaAs buffer and was then followed by a 0.5 μm GaInP etch stop layer. Then, 0.1 μm of GaInAsN:Se and 0.2 μm of GaAs:Se were deposited as the front contact layer. The top cell was grown, starting with a 0.02 μm AlInP window layer, then a 0.1 μm GaAs:Se emitter, a 0.1 μm undoped GaAs layer, a 2.8 μm GaAs:Zn base layer and a 0.12 μm GaInP back surface field (BSF) layer. Next, an AlGaAs:C/GaAs:Se/AlGaAs:Si quantum well tunnel junction was grown, followed by a GaInP compositionally graded buffer (CGB). The CGB consisted of 0.25 μm GaInP steps spanning the compositional range Ga_{0.51}In_{0.49}P to Ga_{0.34}In_{0.66}P at a rate of 1% strain per μm, with the final layer being a 1.0 μm Ga_{0.34}In_{0.66}P strain overshoot layer. The bottom cell was grown, consisting of a 1.0 μm Ga_{0.37}In_{0.63}P window, a 0.1 μm

$\text{Ga}_{0.85}\text{In}_{0.15}\text{As:Se}$ emitter, a $0.1\mu\text{m}$ $\text{Ga}_{0.85}\text{In}_{0.15}\text{As}$ i-layer, a $1.5\mu\text{m}$ $\text{Ga}_{0.85}\text{In}_{0.15}\text{As:Zn}$ base and a $0.05\mu\text{m}$ $\text{Ga}_{0.37}\text{In}_{0.63}\text{P:Zn}$ BSF. Finally, a $0.05\mu\text{m}$ $\text{Al}_{0.20}\text{Ga}_{0.66}\text{In}_{0.14}\text{As:Zn}^{++}$ back contact layer was grown.

For the $1.2/1.0\text{ eV}$ design²⁷, a $0.2\mu\text{m}$ GaAs buffer layer was grown first, then a GaInP CGB consisting of $0.25\mu\text{m}$ GaInP steps, spanning the range $\text{Ga}_{0.51}\text{In}_{0.49}\text{P}$ to $\text{Ga}_{0.19}\text{In}_{0.81}\text{P}$, with the final layers being a $1.0\mu\text{m}$ $\text{Ga}_{0.19}\text{In}_{0.81}\text{P}$ strain overshoot layer and a $0.9\mu\text{m}$ $\text{Ga}_{0.22}\text{In}_{0.78}\text{P}$ step back layer lattice matched to the in-plane lattice constant of the $\text{Ga}_{0.19}\text{In}_{0.81}\text{P}$. A $0.3\mu\text{m}$ $\text{Ga}_{0.70}\text{In}_{0.30}\text{As:Se}$ front contact layer was grown next, followed by the top cell, starting with a $0.02\mu\text{m}$ $\text{Ga}_{0.22}\text{In}_{0.78}\text{P:Se}$ window, a $1.0\mu\text{m}$ $\text{Al}_{0.15}\text{Ga}_{0.55}\text{In}_{0.30}\text{As:Se}$ emitter, an undoped $0.1\mu\text{m}$ $\text{Al}_{0.15}\text{Ga}_{0.55}\text{In}_{0.30}\text{As}$ i-layer, a $2.1\mu\text{m}$ $\text{Al}_{0.15}\text{Ga}_{0.55}\text{In}_{0.30}\text{As:Zn}$ base and a $0.07\mu\text{m}$ $\text{Ga}_{0.22}\text{In}_{0.78}\text{P:Zn}$ BSF. Then the tunnel junction, comprising a $0.2\mu\text{m}$ $\text{Al}_{0.15}\text{Ga}_{0.55}\text{In}_{0.30}\text{As:Zn}$ layer, a $0.05\mu\text{m}$ $\text{GaAs}_{0.72}\text{Sb}_{0.28}\text{:C}^{++}$ layer and a $0.1\mu\text{m}$ $\text{Ga}_{0.22}\text{In}_{0.78}\text{P:Se}^{++}$ layer, was grown. Finally, the bottom cell was grown, comprising a $0.05\mu\text{m}$ $\text{Ga}_{0.22}\text{In}_{0.78}\text{P:Se}$ window, a $1.5\mu\text{m}$ $\text{Ga}_{0.70}\text{In}_{0.30}\text{As:Se}$ emitter, a $0.1\mu\text{m}$ $\text{Ga}_{0.70}\text{In}_{0.30}\text{As:Zn}$ i-layer and a $0.02\mu\text{m}$ $\text{Ga}_{0.22}\text{In}_{0.78}\text{P:Zn}$ BSF. Finally, a $0.05\mu\text{m}$ $\text{Al}_{0.4}\text{Ga}_{0.30}\text{In}_{0.30}\text{As:Zn}^{++}$ back contact layer was grown.

After growth, an approximately $2\text{-}\mu\text{m}$ -thick reflective gold back contact was electroplated to the exposed back contact layer (the last semiconductor layer grown). The samples were bonded with low viscosity epoxy to a silicon handle and the substrates were etched away in $\text{NH}_4\text{OH:H}_2\text{O}_2$ (1:3 by volume). Gold front grids were electroplated to the front surfaces through a positive photoresist mask, using a thin layer of electroplated nickel as an adhesion layer. The grids were nominally $10\mu\text{m}$ wide, $100\mu\text{m}$ apart and at least $5\mu\text{m}$ thick. The samples were then isolated into individual devices using standard wet-chemical etchants and cleaved into single cell chips for characterization. The completed cells had mesa areas of 0.8075 cm^2 , with illuminated areas (discounting the single busbar but including the grid fingers) of 0.7145 cm^2 .

Efficiency measurement

To measure the TPV cell efficiency, we seek direct measurement of the two contributing quantities in equation (1), the power output \(\langle P \rangle_{\{ \text{out} \}} = \langle V \rangle_{\{ \text{oc} \}} \langle I \rangle_{\{ \text{sc} \}} \langle \text{FF} \rangle\)) and the heat generated in the cell, \(\langle Q \rangle_{\{ \text{c} \}}\)). To test the cells under a well-controlled and relevant spectrum (emission from tungsten between 1,900 and 2,400 °C for TECS), a tungsten halogen lamp was used in combination with a concentrator. The concentrator consisted of a silver-plated elliptical reflector behind the lamp and a compound parabolic reflector (CPC) obtained from Optiforms that further concentrated the light onto the cell. At the base of the CPC, a water-cooled aluminium aperture plate was suspended above the TPV cell (Extended Data Fig. 7). The area of the aperture was 0.312 cm² and the active area of the cell was 0.7145 cm².

To keep the TPV cell cool it was mounted on a microchannel copper heat sink (M2, Mikros) that was water-cooled. To measure \(\langle Q \rangle_{\{ \text{abs} \}}\)), a HFS, model gSKIN XP obtained from greenTEG, was placed between the cell and the heat sink. Thermally conductive adhesive tape held the HFS in place on the heat sink, and thermal paste provided thermal contact between the cell and the HFS. Electrical contact to the cell bus bars was accomplished using a pair of copper clips, which were both electrically and thermally isolated from the heat sink using a piece of insulation. A pair of wires was connected to the bottom of each copper clip to perform a four-wire measurement. The bottom side of the aluminium aperture plate was shielded with several layers of copper-coated Kapton and aluminium tape acting as a radiation shield to reduce the radiative transfer between the aperture plate and the TPV cell.

A d.c. power supply (Magna-Power) provided power to the tungsten halogen lamp and the voltage was controlled to achieve the desired emitter temperature. The lamp was rated for 5 kW at 3,200 K, but the temperature and power were tuned down to the desired emitter temperature by controlling the voltage to the lamp using the power supply. The emitter temperature was determined by measuring the resistance of the tungsten heating element in the lamp and using published correlations on the temperature dependence of the electrical resistivity and resistance of tungsten filaments in incandescent lamps⁵⁵. First, the cold resistance of the bulb was measured at the point of the bulb junction and at the point of contact with the power supply to determine the resistance of the electrical

leads to the bulb. The hot bulb resistance was measured by subtracting the electrical lead resistance from the total resistance as determined from the voltage and current input to the d.c. power supply. The heat sink was mounted onto the z-stage to allow for repeatable control of the TPV cell positioning with respect to the aperture, reflectors and lamp.

The TPV efficiency was measured by taking simultaneous measurements of $\langle P \rangle_{\text{out}}$ and $\langle Q_c \rangle$. The electric power was measured using a source meter (Keithley 2430) by sourcing the voltage and measuring the current density at the maximum power point, and $\langle Q_c \rangle$ was measured using the HFS beneath the cell. Owing to the temperature-dependent sensitivity of the HFS, the average HFS temperature, $\langle T_s \rangle$, was needed, which is taken from the average of the hot- and cold-side temperatures. The hot-side temperature was measured by a thermocouple placed underneath the cell. The cold-side temperature was determined iteratively using the thermal resistance of the sensor (4.167 K W^{-1}), the measured heat flux and the cell temperature. From the calibration certificate from the manufacturer, the sensitivity $S(\mu V/W)^{-1} \text{ m}^{-2}$ is given by $S = (T_s - 22.5)0.025 + 19.98$.

Emitter spectrum

The spectrum of the light source was measured using spectrometers in the visible (Ocean Insight FLAME) and in the near-infrared (NIR) (Ocean Insight NIRQUEST). The spectrometers were calibrated using a 1,000 W, 3,200 K quartz tungsten halogen bulb with known spectrum (Newport). Spectrum measurements at several temperatures can be found in Extended Data Fig. 4. To extrapolate the measured spectrum to a broader wavelength range, the spectrum was modelled by considering the literature values of the emission of tungsten⁵⁶, the filament material, and transmission of quartz, for the envelope surrounding the bulb. Quartz transmission was calculated for a 3-mm-thick piece of quartz using optical constants from the literature⁵⁷. The filament consists of tungsten coils with non-zero view factor to themselves. The coil geometry acts to smooth the spectral emission because light emitted by the inside of the coil has a high view factor to itself. Therefore, a geometric factor accounting for this smoothing was used as a fitting

parameter to model the spectrum to extend it beyond the spectrometer measurement range. Extended Data Figure 5a shows a comparison between the spectrum described by the emission of tungsten with $\text{AR} = 1$ and $\text{VF} = 1$, a blackbody spectrum shape and the model, which was found to agree well with the measured spectrum. Owing to the good agreement, the modelled spectrum was then used to form the efficiency predictions. We refer to this spectrum as $\langle\langle E \rangle\rangle_{\lambda,T}$ in the subsequent sections, where λ is wavelength.

Extended Data Figure 5b shows a comparison between the TPV model results under the lightbulb spectra with spectra corresponding to emitter/cell pairs with $\langle\langle \text{VF} \rangle\rangle = 1$, which allows the reflected light to be recycled (an example of these systems is shown in Extended Data Fig. 1). Modelling is shown for a tungsten emitter operating with $\langle\langle \text{AR} \rangle\rangle = 1$ and $\langle\langle \text{VF} \rangle\rangle = 1$, and for a blackbody emitter with $\langle\langle \text{VF} \rangle\rangle = 1$. The results show that the lightbulb spectra provide a characterization of TPV efficiency that is relevant to various higher intensity spectra experienced in TPV systems.

Effective view factor

To compare the measured TPV cell performance to model predictions, the effective view factor, $\langle\langle \text{VF} \rangle\rangle_{\text{eff}}$ was deduced from J_{sc} which was computed from Osterwald⁵⁸ and is shown in equations (2) and (3). We used an NREL-fabricated GaAs cell with measured EQE and a $\langle\langle J \rangle\rangle_{\text{sc}}$ that was measured at NREL on an XT-10 solar simulator (AM1.5D, $1,000 \text{ W m}^{-2}$) using a secondary calibration reference cell to set the intensity. Before an efficiency measurement, the GaAs cell was placed in the setup at the same location as the multi-junction cell using the z-stage. In equation (2), $\langle\langle J \rangle\rangle_{\text{sc}}$ is the short-circuit current of the GaAs cell measured in the efficiency setup, $\langle\langle J \rangle\rangle_{\text{sc}}$ is the short-circuit current of the cell measured using the XT-10 simulator at NREL, $\langle\langle E \rangle\rangle_{\lambda,T}$ is the spectral emissive power under the measured spectrum in the efficiency setup (Extended Data Fig. 4) and $\langle\langle E \rangle\rangle_{\text{G}} 173 \langle\langle d \rangle\rangle$ is the AM1.5D spectrum. Both spectra are in units of $\text{W m}^{-2} \text{ nm}^{-1}$. We define $\langle\langle \text{VF} \rangle\rangle_{\text{eff}}$

$\{\{\rm{VF}\}\}_{\{\rm{eff}\}}$) as the ratio of the actual irradiance in the efficiency setup, $\{E\}_{\{\rm{irradiance}\}}^{\{\rm{TPV}\}}$, to the full irradiance for the spectral emissive power at the same test temperature, $\{\int E\}_{\{\rm{TPV}\}} \left(\lambda\right) \{d\} / \lambda$ (equation (3)). The Emitter Spectrum section above discusses how $\{E\}_{\{\rm{TPV}\}} \left(\lambda\right)$ was determined. Measurements of $\{J\}_{\{\rm{sc}\}}^{\{\rm{TPV}\}}$ were averaged across the range of emitter temperatures.

$$\begin{aligned} \$\$ J_{\{\rm{s}\}}^{\{\rm{c}\}} &= \frac{\{V\}}{\{F\}} \\ &\times \frac{\{e\}}{\{f\}} \times \frac{\{f\}}{\{c\}} \times \frac{173\{d\}}{1,000\{W\}} \\ &\times \frac{\{m\}}{\{-2\}} \times \frac{\{E\}_{\{\rm{T}\}}^{\{\rm{P}\}}}{\{E\}_{\{\rm{T}\}}^{\{\rm{V}\}}} \\ &\times (\lambda, T) \{E\}_{\{\rm{Q}\}}^{\{\rm{E\lambda}\}} \lambda \\ &\times \{d\} \lambda \int \{E\}_{\{\rm{G}\}}^{\{d\}} (\lambda) \{E\}_{\{\rm{Q\lambda}\}}^{\{\rm{E\lambda}\}} \lambda \\ &\times \{G\}_{\{d\}} (\lambda) \{d\} \lambda \\ (2) \quad \$\$ \\ \$\$ \{VF\}_{\{\rm{eff}\}} &= \frac{\{E\}_{\{\rm{irradiance}\}}^{\{\rm{TPV}\}}}{\{\int E\}_{\{\rm{TPV}\}} \left(\lambda\right) \{d\} / \lambda} \\ (3) \end{aligned}$$

$\{\rm{VF}\}_{\{\rm{eff}\}}$ was then used to form the efficiency model predictions. A useful metric to enable comparisons with other systems is to define an effective view factor in relation to the blackbody spectrum.

Equation (4) compares the TPV irradiance in our efficiency setup with that of the Planck distribution blackbody spectrum at the same test temperature.

$$\begin{aligned} \$\$ \{VF\}_{\{\rm{eff}\}}, \\ \{black\} &= \frac{\{E\}_{\{\rm{irradiance}\}}^{\{\rm{TPV}\}}}{\{\int E\}_{\{\rm{B\lambda}\}} \left(\lambda\right) \{d\} / \lambda} \\ (4) \end{aligned}$$

Because the shape of $\{E\}_{\{\rm{TPV}\}} \left(\lambda\right)$ varies slightly with temperature, $\{\rm{VF}\}_{\{\rm{eff}\}}, \{black\}$ also changes slightly with temperature. Averaged across the emitter temperatures, for the 1.4/1.2 eV tandem $\{\rm{VF}\}_{\{\rm{eff}\}}, \{black\} = 10.07 \%$ and for the 1.2/1.0 eV tandem $\{\rm{VF}\}_{\{\rm{eff}\}}, \{black\}$

$\{\{\backslash rm\{VF\}\}\}_\text{eff, black} = 10.65 \%$). The differences are due to slight adjustments made to the setup between measurements of the two multi-junction cells.

Efficiency validation

Equation (1) for TPV efficiency can also be written in terms of equation (5), where $\{P\}_\text{inc}$ is the irradiance incident on the cell, $\{P\}_\text{ref}$ is the flux reflected by the cell, $\{P\}_\text{a}$ is the above-bandgap irradiance, $\{P\}_\text{inc}$, $\{P\}_\text{sub}$ is the sub-bandgap irradiance, $\{R\}_\text{a}$ is the spectral-weighted above-bandgap reflectance and $\{R\}_\text{sub}$ is the spectral-weighted sub-bandgap reflectance²⁷. The denominator of the efficiency expression represents the net flux to the cell.

$$\begin{aligned} \eta &= \frac{P_\text{o} u}{P_\text{t}} \\ Q_c &= \frac{V_o c}{J_s s} \\ P_r e f &= \frac{V_o c}{P_i i n} - \frac{P_r r}{P_e e} \\ R_a &= \frac{R_s s}{R_u u} \end{aligned} \quad (5)$$

The measured V_o , J_s and FF are shown in Extended Data Fig. 8 and Extended Data Tables 1 and 2. To model the numerator or electric power portion of the efficiency expression (Extended Data Fig. 8), we used a well-established analytical model that takes values extracted from experiments as input parameters⁵⁹. Using a flash simulator with known spectral irradiance, we first measured the cell performance under carefully controlled conditions of known spectrum with the cell temperature fixed at 25 °C. Using the model, we fit the data satisfactorily over an irradiance range of several orders of magnitude (shown for the 1.2/1.0 eV tandem in Extended Data Fig. 9a). The fitting was done using only three parameters: the geometric averaged dark current for the two

junctions in the form of $\{W\}_{oc} = \frac{E_g - (V_{oc} + W_{oc})}{R_{series}}$ (ref. [60](#)) where E_g is the bandgap and W_{oc} is the bandgap-voltage offset, the $n=2$ component of the dark current and the effective lumped series resistance $\{R\}_{series}$). We refer to these as the cell characteristic parameters.

We then measured the IV performance parameters ($\{J\}_{sc}$, $\{V\}_{oc}$, $\{FF\}$) of the device as a function of the ratio of the top to bottom junction photocurrents under a continuous 1 sun simulator for which the spectral content can be varied. Using the measured EQE of the cells (Extended Data Fig. [3](#)), the photocurrent ratio for a given emitter temperature can be calculated, and using reference cells^{[58](#)} the simulator was set to that photocurrent ratio for each emitter temperature. With the measured EQE and the cell characteristic parameters from above, we calculated the cell performance parameters and compared them to the measurements (shown for the 1.2/1.0 eV tandem in Extended Data Fig. [9b](#)). The agreement supports the validity of the modelling process and its ability to correctly predict performance trends under a wide range of conditions—for both irradiance and emitter temperature (that is, spectrum).

The measured spectra (Extended Data Fig. [4](#)) were used along with the measured EQE to calculate the top and bottom junction photocurrents (equation [\(6\)](#)). With those as inputs to the model, and the cell characteristic parameters determined above, we computed the cell performance parameters under the actual efficiency measurement conditions. The cell temperature varies (Extended Data Fig. [6a](#)). This was accounted for using a well-established model that works especially well for near-ideal devices, such as III–V devices. The model accounts for the temperature dependence through its effect on the intrinsic carrier density, and thus the dark current, and the effects of the bandgap variation with temperature^{[61,62](#)}. Extended Data Figure [9c](#) shows a comparison of the computed cell performance for a 25 °C cell and at the measured cell temperature for the 1.2/1.0 eV tandem.

$$\begin{aligned}
 J_{sc} &= \frac{q}{4\pi} \int_0^{\infty} \int_0^{2\pi} \int_0^{\pi} \left[\frac{F(\lambda) \cdot h\nu}{\pi} \right] \cdot \left[\frac{1}{1 + e^{(h\nu - E_g)/kT}} \right] \cdot Q(\lambda) \cdot E(\lambda) \cdot d\lambda \cdot d\theta \cdot d\phi
 \end{aligned}$$

$$\{E\}_{\lambda}(\{T\}, \{P\}, \{V\}) = (\lambda, T) \lambda d \lambda$$

\$\$

(6)

The spectral emissive power, $\{E\}_{\lambda}(\{TPV\})$, was used to determine $\{P\}_{\lambda}$ based on the emitter temperature, T , and $\{\{VF\}\}_{\lambda}$ (equation (7)). The reflectance, $\{\rho(\lambda)\}$, was measured on two different instruments owing to the range of the spectrum. The mid-infrared sub-bandgap reflectance was measured using a Fourier-transform infrared (FTIR) spectrometer (Nicolet iS50) with an integrating sphere accessory (PIKE Mid-IR IntegratIR). A copper aperture with area approximately 0.35 cm^2 was used over the sample port, and the spot encompassed both the cell and the front grids. The above-bandgap and NIR sub-bandgap reflectance was measured using an ultraviolet-visible-NIR spectrophotometer (Cary 7000) with the diffuse reflectance accessory and with a spot size approximately 0.4 cm^2 encompassing the cell and the front grids. $\{P\}_{\lambda}$ was then calculated according to equation (8).

$$\{P\}_{\lambda} = \{\{VF\}\}_{\lambda} \{\{eff\}\}_{\lambda} \int_0^{\infty} \{E\}_{\lambda}(\{TPV\}) \lambda d\lambda$$

\$\$

(7)

$$\{P\}_{\lambda} = \{\{VF\}\}_{\lambda} \{\{eff\}\}_{\lambda} \int_0^{\infty} \{E\}_{\lambda}(\{TPV\}) \lambda d\lambda$$

\$\$

(8)

This approach to modelling the cells was used to predict the cell performance under the tungsten filament lighting conditions. The decomposition of reflectance into $\{R\}_{\lambda}$ and $\{R\}_{\lambda}$ portions (equation (4)) enabled the subsequent predictions of efficiency at higher $\{R\}_{\lambda}$ shown in Fig. 3b.

Heat transfer considerations

We examined the influence of different parasitic heat flows on the efficiency measurement. A schematic of the different parasitic heat flows is shown in Extended Data Fig. 6b and they are quantified in Extended Data Fig. 6c.

Possible parasitic heat flows, $\{Q\}_{\rm parasitic}$, are given by equation (9). A positive value of $\{Q\}_{\rm parasitic}$ would act to increase the measured heat flow and reduce the measured efficiency, whereas a negative value of $\{Q\}_{\rm parasitic}$ would have the opposite effect.

$$\begin{aligned} \{Q\}_{\rm parasitic} = & \{Q\}_{\rm cond,clips} + \\ & \{Q\}_{\rm rad,gain} - \{Q\}_{\rm rad,loss} - \\ & \{Q\}_{\rm conv,loss} \end{aligned} \quad (9)$$

For example, the aperture does not block all the light hitting the electrical leads. $\{Q\}_{\rm cond,clips}$ arises owing to conduction from the electric leads into the cell that is cooled by the heat sink, which by design are thermally stranded from the heat sink using insulation. To quantify this value, we performed measurements of the heat flow both with and without the electrical leads attached to the cell. In both cases the cell was operating at $\{V\}_{\rm oc}$ to avoid differences in heating due to power being extracted by the cell. The difference between the two heat flows is $\{Q\}_{\rm cond,clips}$. The results show that, at most emitter temperatures, the heat flow in the presence of the leads is larger than without, because the leads are thermally stranded while the cell is actively cooled. Thus, inclusion of such a term would lead to a higher efficiency than what is reported.

The next parasitic heat flow is due to radiation from the aperture plate to the cell, $\{Q\}_{\rm rad,gain}$. The temperature of the bottom of the aperture plate was measured with a thermocouple at the different emitter temperatures. Aperture temperatures varied from 43 °C at the lowest emitter temperature to 125 °C at the highest. The view factor between the aperture plate and the cell, $\{F\}_{\rm ac}$, was calculated from their geometry and spacing. The heat transfer from the aperture to the cell was calculated using a diffuse grey approximation according to equation 10, where $A_{\rm ap}$ is the area of the aperture plate and $A_{\rm cell}$ is the area of the cell.

$$\{Q\}_{\rm rad,gain} = \frac{\sigma}{4} \left(\frac{A_{\rm ap}}{A_{\rm cell}} \right)^4 \left(\frac{T_{\rm ap}}{T_{\rm cell}} \right)^4$$

$$\{A\}_{\{\{\text{cell}\}\}} + \frac{1}{\{A\}_{\{\{\text{ap}\}\}}} \{F\}_{\{\{\text{ac}\}\}} + \frac{1 - \{\varepsilon\}_{\{\{\text{ap}\}\}}}{\{\varepsilon\}_{\{\{\text{ap}\}\}} \{A\}_{\{\{\text{ap}\}\}}} \quad (10)$$

The emissivity of the cell weighted by the spectrum at the aperture temperature is $\{\varepsilon\}_{\{\{\text{cell}\}\}}$ (0.15 for the 1.4/1.2 eV tandem and 0.11 for the 1.2/1.0 eV tandem) and the emissivity of the aperture is $\{\varepsilon\}_{\{\{\text{ap}\}\}} \approx 0.1$.

There is also radiative transfer between the cell and the ambient environment, $\{Q\}_{\{\{\text{rad}\}, \{\text{loss}\}\}}$, but this was found to be negligible at the cell temperature and the calculated view factor between the cell and the environment. Nonetheless, it was included in the calculation of $\{Q\}_{\{\{\text{parastic}\}\}}$ for completeness.

Another parasitic heat flow is convective heat loss from the cell to the ambient,

$$\$ \$ \{Q\}_{\{\{\text{c}\}, \{\text{o}\}, \{\text{n}\}, \{\text{v}\}, \{\text{l}\}, \{\text{o}\}, \{\text{s}\}, \{\text{s}\}} = h \{A\}_{\{\{\text{c}\}, \{\text{e}\}, \{\text{l}\}, \{\text{l}\}} (\{T\}_{\{\{\text{infty}\}\}} - \{T\}_{\{\{\text{c}\}, \{\text{e}\}, \{\text{l}\}, \{\text{l}\}\}}) \quad (11)$$

where h is the convective heat transfer coefficient, and $\{T\}_{\{\{\text{infty}\}\}}$ is the ambient temperature. The ambient temperature was measured with a thermocouple, which was blocked from irradiance by the light source using several layers of aluminium foil forming a radiation shield. Ambient temperatures were found to vary between 26 °C at the lowest emitter temperature and 33 °C at the highest emitter temperature. h was calculated using a Nusselt (Nu) correlation for natural convective heat transfer from a horizontal plate at the calculated Rayleigh (Ra) number⁶³. Heat transfer coefficients were calculated at each cell/ambient temperature, with the average being $(h=5.8, \{\text{W}\}, \{\text{m}\})^{-2}$, $\{\text{K}\}^{-1}$.

$\{Q\}_{\{\{\text{parastic}\}\}}$ is a small and positive quantity at most emitter temperatures. At lower emitter temperatures it is dominated by $\{Q\}_{\{\{\text{rad}\}, \{\text{loss}\}\}}$.

$\langle Q \rangle_{\rm cond}, \langle rm{clips} \rangle$), whereas at higher emitter temperatures $\langle Q \rangle_{\rm conv}, \langle rm{loss} \rangle$ and $\langle Q \rangle_{\rm rad}, \langle rm{gain} \rangle$ become more important. The potential impact of $\langle Q \rangle_{\rm parasitic}$ on the efficiency measurement is shown in Extended Data Fig. 6d. Overall, $\langle Q \rangle_{\rm parasitic}$ has a small impact on the efficiency because $\langle Q \rangle_{\rm parasitic}$ is two orders of magnitude lower than $\langle Q \rangle_c$. Because $\langle Q \rangle_{\rm parasitic}$ is largely derived from modelling and correlation, we do not include it in the efficiency measurement reported. In fact, our calculation of $\langle Q \rangle_{\rm parasitic}$ largely predicts a higher efficiency than the measured value, which indicates reported measured efficiency could be conservative.

Uncertainty propagation

Uncertainty in the efficiency measurement arises from the measurement of $\langle P \rangle_{\rm out}$ and the measurement of $\langle Q \rangle_c$ (equation 1). From the manufacturer, the calibration accuracy of the HFS is $\pm 3\%$. We include an additional 10°C temperature uncertainty in $\langle T \rangle_s$, the sensor temperature, which comes from the average temperature rise across the sensor as calculated from the thermal resistance of the sensor (4.167 K W^{-1}) and the average heat flux passing through the sensor. This leads to an uncertainty of heat absorbed of $\langle B \rangle_Q = 0.0325 \langle Q \rangle_c$. From the source meter, the voltage measurement uncertainty is 0.03% of the voltage ($B_v = 3 \times 10^{-4} V$) and the current measurement uncertainty is 0.06% of the current ($B_I = 6 \times 10^{-4} I$). This leads to an uncertainty in the electric power measurement of $\langle B \rangle_P = \sqrt{(I^2 B_v^2) + (V^2 B_I^2)}$, which is negligible due to the low uncertainty in voltage and current. The absolute uncertainty in measured efficiency, $\langle B \rangle_\eta = \langle rm{\partial \eta / \partial T} \rangle \langle rm{P} \rangle \langle rm{V} \rangle, \langle rm{m} \rangle \langle rm{e} \rangle \langle rm{a} \rangle \langle rm{s} \rangle \langle rm{u} \rangle \langle rm{r} \rangle \langle rm{e} \rangle$, was calculated as

$$\langle B \rangle_\eta = \sqrt{\left(\frac{\partial \eta}{\partial T}\right)^2 \langle P \rangle \langle V \rangle^2 + \langle m \rangle \langle e \rangle \langle a \rangle \langle s \rangle \langle u \rangle \langle r \rangle \langle e \rangle^2}$$

$$\begin{aligned}
& \left(\frac{\partial V}{\partial m} \right) \left(\frac{\partial m}{\partial e} \right) \left(\frac{\partial e}{\partial a} \right) \left(\frac{\partial a}{\partial s} \right) \left(\frac{\partial s}{\partial u} \right) \left(\frac{\partial u}{\partial r} \right) \\
& \left(\frac{\partial e}{\partial P} \right) \left(\frac{\partial P}{\partial B} \right) \left(\frac{\partial B}{\partial \eta} \right)^2 + \\
& \left(\frac{\partial \eta}{\partial T} \right) \left(\frac{\partial T}{\partial P} \right) \left(\frac{\partial P}{\partial V} \right), \\
& \left(\frac{\partial m}{\partial e} \right) \left(\frac{\partial e}{\partial a} \right) \left(\frac{\partial a}{\partial s} \right) \left(\frac{\partial s}{\partial u} \right) \left(\frac{\partial u}{\partial r} \right) \left(\frac{\partial r}{\partial e} \right) \\
& \left(\frac{\partial \eta}{\partial Q} \right) \left(\frac{\partial Q}{\partial c} \right) \left(\frac{\partial c}{\partial B} \right) \left(\frac{\partial B}{\partial Q} \right) \left(\frac{\partial Q}{\partial c} \right) \left(\frac{\partial c}{\partial r} \right)^2 \\
(12)
\end{aligned}$$

The uncertainty in the model prediction primarily arises from the uncertainty in predicted η ($\approx 0.03\%$) from the uncertainty of the EQE measurement of the multi-junction cell, and from the uncertainty of the FTIR reflectance measurement leading to $R \approx 0.013$. Propagating these errors through equation (4), the absolute uncertainty in the modelled efficiency, η , was calculated according to equation (13) and the model uncertainty is shown by the shaded regions in Fig. 3a.

$$\begin{aligned}
& \left(\frac{\partial \eta}{\partial T} \right) \left(\frac{\partial T}{\partial P} \right) \left(\frac{\partial P}{\partial V} \right) \left(\frac{\partial V}{\partial m} \right) \left(\frac{\partial m}{\partial o} \right) \\
& \left(\frac{\partial d}{\partial e} \right) \left(\frac{\partial e}{\partial l} \right) = \sqrt{\left(\frac{\partial \eta}{\partial T} \right)^2 \left(\frac{\partial T}{\partial P} \right)^2 \left(\frac{\partial P}{\partial V} \right)^2 \left(\frac{\partial V}{\partial m} \right)^2 \left(\frac{\partial m}{\partial o} \right)^2 \left(\frac{\partial d}{\partial e} \right)^2 \left(\frac{\partial e}{\partial l} \right)^2} \\
& \left(\frac{\partial \eta}{\partial l} \right) \left(\frac{\partial l}{\partial s} \right) \left(\frac{\partial s}{\partial c} \right) \left(\frac{\partial c}{\partial B} \right) \left(\frac{\partial B}{\partial J} \right) \left(\frac{\partial J}{\partial s} \right) \\
& \left(\frac{\partial \eta}{\partial c} \right) \left(\frac{\partial c}{\partial R} \right) \left(\frac{\partial R}{\partial s} \right) \left(\frac{\partial s}{\partial u} \right) \left(\frac{\partial u}{\partial b} \right) \left(\frac{\partial b}{\partial B} \right) \\
& \left(\frac{\partial \eta}{\partial b} \right) \left(\frac{\partial b}{\partial R} \right) \left(\frac{\partial R}{\partial s} \right)^2 \\
(13)
\end{aligned}$$

The uncertainty in the emitter temperature measurement was calculated from the variation in resistance of the bulb measured at each emitter temperature and the uncertainty in the temperature dependence of the resistance from the literature expression that was used, which is a 0.1% relative error on resistance as a function of temperature⁵⁵. The root mean square of these two yielded temperature measurement uncertainties of less than 4 °C, which had a negligible impact on model uncertainty.

Data availability

The data that support the findings of this study are available from the corresponding author upon reasonable request.

References

1. Amy, C., Seyf, H. R., Steiner, M. A., Friedman, D. J. & Henry, A. Thermal energy grid storage using multi-junction photovoltaics. *Energy Environ. Sci.* **12**, 334–343 (2019).
2. Datas, A., Ramos, A., Martí, A., del Cañizo, C. & Luque, A. Ultra high temperature latent heat energy storage and thermophotovoltaic energy conversion. *Energy* **107**, 542–549 (2016).
3. Fraas, L. M. et al. TPV generators using the radiant tube burner configuration. In *17th European PV Solar Energy Conference* Vol. 26(EUPVSEC, 2001).
4. Fraas, L. M., Avery, J. E. & Han Xiang, H. Thermophotovoltaics: Heat and electric power from low bandgap solar cells around gas fired radiant tube burners. In *Conference Record of the Twenty-Ninth IEEE Photovoltaic Specialists Conference* 1553–1556 (IEEE, 2002).
5. Yang, W. M., Chua, K. J., Pan, J. F., Jiang, D. Y. & An, H. Development of micro-thermophotovoltaic power generator with heat recuperation. *Energy Convers. Manage.* **78**, 81–87 (2014).
6. Jiang, D., Yang, W. & Tang, A. Development of a high-temperature and high-uniformity micro planar combustor for thermophotovoltaics application. *Energy Convers. Manage.* **103**, 359–365 (2015).
7. Chan, W. R. et al. Enabling efficient heat-to-electricity generation at the mesoscale. *Energy Environ. Sci.* **10**, 1367–1371 (2017).
8. Mustafa, K. F., Abdullah, S., Abdullah, M. Z. & Sopian, K. A review of combustion-driven thermoelectric (TE) and thermophotovoltaic (TPV) power systems. *Renew. Sustain. Energy Rev.* **71**, 572–584 (2017).

9. Gentillon, P. et al. A comprehensive experimental characterisation of a novel porous media combustion-based thermophotovoltaic system with controlled emission. *Appl. Energy* **254**, 113721 (2019).
10. Swanson, R. M. Recent developments in thermophotovoltaic conversion. In *1980 International Electron Devices Meeting* 186–189 (IEEE, 1980).
11. Ganapati, V., Xiao, T. P. & Yablonovitch, E. Ultra-efficient thermophotovoltaics exploiting spectral filtering by the photovoltaic band-edge. Preprint at <https://arxiv.org/abs/1611.03544> (2016).
12. Burger, T., Sempere, C., Roy-Layinde, B. & Lenert, A. Present efficiencies and future opportunities in thermophotovoltaics. *Joule* **4**, 1660–1680 (2020).
13. Omair, Z. et al. Ultraefficient thermophotovoltaic power conversion by band-edge spectral filtering. *Proc. Natl Acad. Sci. USA* **116**, 15356–15361 (2019).
14. Narayan, T. C. et al. World record demonstration of >30% thermophotovoltaic conversion efficiency. In *2020 47th IEEE Photovoltaic Specialists Conference (PVSC)* 1792–1795 (IEEE, 2020).
15. Fan, D. et al. Near-perfect photon utilization in an air-bridge thermophotovoltaic cell. *Nature* **586**, 237–241 (2020).
16. France, R. M. et al. Design flexibility of ultrahigh efficiency four-junction inverted metamorphic solar cells. *IEEE J. Photovolt.* **6**, 578–583 (2016).
17. Amy, C. et al. Thermal energy grid storage: liquid containment and pumping above 2000°C. *Appl. Energy* **308**, 118081 (2022).
18. Amy, C., Pishahang, M., Kelsall, C. C., LaPotin, A. & Henry, A. High-temperature pumping of silicon for thermal energy grid storage. *Energy* **233**, 121105 (2021).

19. Kelsall, C. C., Buznitsky, K. & Henry, A. Technoeconomic analysis of thermal energy grid storage using graphite and tin. Preprint at <https://arxiv.org/abs/2106.07624> (2021).
20. Ziegler, M. S. et al. Storage requirements and costs of shaping renewable energy toward grid decarbonization. *Joule* **3**, 2134–2153 (2019).
21. Sepulveda, N. A., Jenkins, J. D., Edington, A., Mallapragada, D. S. & Lester, R. K. The design space for long-duration energy storage in decarbonized power systems. *Nat. Energy* **6**, 506–516 (2021).
22. Albertus, P., Manser, J. S. & Litzelman, S. Long-duration electricity storage applications, economics, and technologies. *Joule* **4**, 21–32 (2020).
23. Pachauri, R. K. *et al.* in *Climate Change 2014: Synthesis Report* (eds Core Writing Team, Pachauri, R. K. & Meyer L. A.) (IPCC, 2014).
24. Seyf, H. R. & Henry, A. Thermophotovoltaics: a potential pathway to high efficiency concentrated solar power. *Energy Environ. Sci.* **9**, 2654–2665 (2016).
25. Wilt, D., Chubb, D., Wolford, D., Magari, P. & Crowley, C. Thermophotovoltaics for space power applications. *AIP Conf. Proc.* **890**, 335–345 (2007).
26. Datas, A. & Martí, A. Thermophotovoltaic energy in space applications: review and future potential. *Sol. Energy Mater. Sol. Cells* **161**, 285–296 (2017).
27. Schulte, K. L. et al. Inverted metamorphic AlGaInAs/GaInAs tandem thermophotovoltaic cell designed for thermal energy grid storage application. *J. Appl. Phys.* **128**, 143103 (2020).
28. King, R. R. et al. 40% efficient metamorphic GaInP/GaInAs/Ge multijunction solar cells. *Appl. Phys. Lett.* **90**, 183516 (2007).

29. Henry, A. & Prasher, R. The prospect of high temperature solid state energy conversion to reduce the cost of concentrated solar power. *Energy Environ. Sci.* **7**, 1819–1828 (2014).
30. Kayes, B. M. et al. 27.6% conversion efficiency, a new record for single-junction solar cells under 1 sun illumination. In *2011 37th IEEE Photovoltaic Specialists Conference* 000004–000008 (IEEE, 2011).
31. Steiner, M. A. et al. Optical enhancement of the open-circuit voltage in high quality GaAs solar cells. *J. Appl. Phys.* **113**, 123109 (2013).
32. Geisz, J. F., Steiner, M. A., García, I., Kurtz, S. R. & Friedman, D. J. Enhanced external radiative efficiency for 20.8% efficient single-junction GaInP solar cells. *Appl. Phys. Lett.* **103**, 041118 (2013).
33. Geisz, J. F. et al. High-efficiency GaInP/GaAs/InGaAs triple-junction solar cells grown inverted with a metamorphic bottom junction. *Appl. Phys. Lett.* **91**, 023502 (2007).
34. Geisz, J. F. et al. 40.8% efficient inverted triple-junction solar cell with two independently metamorphic junctions. *Appl. Phys. Lett.* **93**, 123505 (2008).
35. France, R. M., Dimroth, F., Grassman, T. J. & King, R. R. Metamorphic epitaxy for multijunction solar cells. *MRS Bull.* **41**, 202–209 (2016).
36. *US Electricity Generation by Major Energy Source, 1950–2020* Monthly Energy Review, Table 7.2a (US Energy Information Administration, 2021).
37. *Approximate Heat Rates for Electricity, and Heat Content of Electricity* Monthly Energy Review, Table A6 (US Energy Information Administration, 2021).
38. *Estimated US Energy Consumption in 2020: 92.9 Quads* (LLNL, DOE/EIA MER, 2020).
39. Wedlock, B. D. Thermo-photo-voltaic energy conversion. *Proc. IEEE* **51**, 694–698 (1963).

40. Fernández, J., Dimroth, F., Oliva, E., Hermle, M. & Bett, A. W. Back-surface optimization of germanium TPV cells. *AIP Conf. Proc.* **890**, 190–197 (2007).
41. Siergiej, R. R. et al. 20% efficient InGaAs/InPAs thermophotovoltaic cells. *AIP Conf. Proc.* **653**, 414–423 (2003).
42. Wernsman, B. et al. Greater than 20% radiant heat conversion efficiency of a thermophotovoltaic radiator/module system using reflective spectral control. *IEEE Trans. Electron Devices* **51**, 512–515 (2004).
43. Woolf, D. N. et al. High-efficiency thermophotovoltaic energy conversion enabled by a metamaterial selective emitter. *Optica* **5**, 213–218 (2018).
44. Dashiell, M. W. et al. Quaternary InGaAsSb thermophotovoltaic diodes. *IEEE Trans. Electron Devices* **53**, 2879–2891 (2006).
45. Amy, C. et al. Pumping liquid metal at high temperatures up to 1,673 kelvin. *Nature* **550**, 199–203 (2017).
46. Lang, S., Bestenlehner, D., Marx, R. & Drück, H. Thermal insulation of an ultra-high temperature thermal energy store for concentrated solar power. *AIP Conf. Proc.* **2033**, 090020 (2018).
47. Chan, W. R. et al. Towards a portable mesoscale thermophotovoltaic generator. *J. Phys. Conf. Ser.* **1052**, 012041 (2018).
48. *US Electric Power Annual 2019* (US Energy Information Administration, 2021).
49. Zebarjadi, M., Esfarjani, K., Dresselhaus, M. S., Ren, Z. F. & Chen, G. Perspectives on thermoelectrics: from fundamentals to device applications. *Energy Environ. Sci.* **5**, 5147–5162 (2012).
50. Go, D. B. et al. Thermionic energy conversion in the twenty-first century: advances and opportunities for space and terrestrial

applications. *Front. Mech. Eng.*
<https://doi.org/10.3389/fmech.2017.00013> (2017).

51. Chum, H. L. *Review of Thermally Regenerative Electrochemical Systems* Vol. 332 (Solar Energy Research Institute, 1981).
52. Timmer, M. A. G., Blok, K. D. & Meer, T. H. V. D. Review on the conversion of thermoacoustic power into electricity. *J. Acoust. Soc. Am.* **143**, 841–857 (2018).
53. Thombare, D. G. & Verma, S. K. Technological development in the Stirling cycle engines. *Renew. Sustain. Energy Rev.* **12**, 1–38 (2008).
54. Zare, S. & Tavakolpour-Saleh, A. Free piston Stirling engines: a review. *Int. J. Energy Res.* **44**, 5039–5070 (2020).
55. de Izarra, C. & Gitton, J.-M. Calibration and temperature profile of a tungsten filament lamp. *Eur. J. Phys.* **31**, 933–942 (2010).
56. Touloukian, Y. S. & DeWitt, D. P. *Thermophysical Properties of Matter — The TPRC Data Series. Volume 7. Thermal Radiative Properties — Metallic Elements And Alloys* (Thermophysical and Electronic Properties Information Center, 1970).
57. Kitamura, R., Pilon, L. & Jonasz, M. Optical constants of silica glass from extreme ultraviolet to far infrared at near room temperature. *Appl. Opt.* **46**, 8118–8133 (2007).
58. Osterwald, C. R. Translation of device performance measurements to reference conditions. *Sol. Cells* **18**, 269–279 (1986).
59. Geisz, J. F. et al. Generalized optoelectronic model of series – connected multijunction solar cells. *IEEE J. Photovolt.* **5**, 1827–1839 (2015).
60. King, R. R. et al. Band gap-voltage offset and energy production in next-generation multijunction solar cells. *Prog. Photovoltaics Res. Appl.* **19**, 797–812 (2011).

61. Fan, J. C. C. Theoretical temperature dependence of solar cell parameters. *Sol. Cells* **17**, 309–315 (1986).
62. Friedman, D. J. Modelling of tandem cell temperature coefficients. In *Conference Record of the Twenty Fifth IEEE Photovoltaic Specialists Conference* 89–92 (IEEE, 1996).
63. Raithby, G. D. & Hollands, K. G. T. in *Handbook of Heat Transfer* (eds Rohsenow, W. M. et al.) Ch. 4 (McGraw-Hill, 1998).

Acknowledgements

We thank W. Olavarria and A. Kibbler for organometallic vapour phase epitaxy growth work and C. Aldridge for earlier processing work. We thank T. McClure at MIT for the use of FTIR spectroscopy. We also thank Y. Salamin and R. Sakakibara at MIT for their assistance in the characterization of the light source. We acknowledge financial support from the US Department of Energy (DOE): Advanced Research Projects Agency – Energy (ARPA-E) cooperative agreement number DE-AR0001005; and the Office of Energy Efficiency and Renewable Energy grant numbers DE-EE0008381 and DE-EE0008375. This work was authored, in part, by the Alliance for Sustainable Energy, LLC, the manager and operator of the National Renewable Energy Laboratory for the US DOE under contract number DE-AC36-08GO28308. The views expressed in the article do not necessarily represent the views of the DOE or the US Government. The US Government retains and the publisher, by accepting the article for publication, acknowledges that the US Government retains a nonexclusive, paid-up, irrevocable, worldwide license to publish or reproduce the published form of this work, or allow others to do so, for US Government purposes.

Author information

Affiliations

1. Department of Mechanical Engineering, Massachusetts Institute of Technology, Cambridge, MA, USA

Alina LaPotin, Kyle Buznitsky, Colin C. Kelsall, Andrew Rohskopf, Shomik Verma, Evelyn N. Wang & Asegun Henry

2. National Renewable Energy Laboratory, Golden, CO, USA

Kevin L. Schulte, Myles A. Steiner, Daniel J. Friedman, Eric J. Tervo, Ryan M. France & Michelle R. Young

Contributions

A.L. conducted the efficiency measurement experiments and analysed the data. A.L, K.B. and C.C.K. designed, built and tested the experimental setup. K.L.S. developed and optimized the epitaxial growth of the cells. D.J.F., M.A.S. and K.L.S designed the cells, and M.A.S. and M.R.Y. fabricated them. D.J.F., M.A.S. and K.L.S., along with contributions from R.M.F., E.J.T., A.L. and A.R., characterized and modelled the cells. A.L. and S.V. characterized the light source. A.H. and E.N.W. supervised the work. All authors contributed intellectually to the work's execution and to preparation of the manuscript.

Corresponding author

Correspondence to [Asegun Henry](#).

Ethics declarations

Competing interests

M.A.S. and E.J.T. worked on a similar project with Antora Energy.

Peer review

Peer review information

Nature thanks Wenming Yang, Christos N. Markides and the other, anonymous, reviewer(s) for their contributionn to the peer review of this

work.

Additional information

Publisher's note Springer Nature remains neutral with regard to jurisdictional claims in published maps and institutional affiliations.

Extended data figures and tables

Extended Data Fig. 1 TPV applications.

a) Conceptual illustration of TEGS¹, which takes in electricity, converts it to heat via Joule heating, stores the heat in insulated graphite blocks, and then uses TPV for conversion of heat to electricity. A unit cell of the power block is also shown. B) Sankey diagram showing the energy flows in the TEGS system at scale and different efficiency metrics. c) The relationship between TPV sub-system efficiency and power block size or volume to surface area ratio, Φ , assuming the system is a cube. d) Conceptual illustration of a combustion-based electricity generation system using TPV. The system consists of an all-ceramic recuperator, similar to a printed circuit heat exchanger, with the end comprising of a combustion chamber. Air is preheated by exhaust and then combined with fuel for combustion near the end facing the TPV. The hot exhaust then delivers heat to the ceramic which radiates it to the TPV. e) Sankey diagram showing energy flows in a combustion-based TPV system at scale.

Extended Data Fig. 2 Tandem device structures.

Device structures of the 1.4/1.2-eV and the 1.2/1.0-eV tandems.

Extended Data Fig. 3 External Quantum Efficiency.

The external quantum efficiency (EQE) of the two cells. The blue curve shows the 2150 °C blackbody spectrum for reference.

Extended Data Fig. 4 Emitter spectrum measurements and model.

The emitter spectrum was measured at different emitter temperatures spanning the test temperature range. A model (Methods) was fit to the measurement and used to extend the spectra measurements to longer wavelengths. The spectral radiance goes to zero $>\sim 4500$ nm due to the presence of the quartz envelope around the bulb, as quartz is absorbing beyond this wavelength.

Extended Data Fig. 5 Comparison of spectra shapes.

a) A comparison between the spectrum shape at an intermediate test temperature (2130 °C). The red curve shows the modeled spectrum which agrees well with the measurement (see Extended Data Fig. 4). The gray curve shows comparison to a blackbody spectrum shape at the same emitter temperature. The blue curve shows comparison to the spectrum described by the literature emission of tungsten with $AR=1$, $VF=1$. All curves are normalized by their peak to show the comparison in spectra shapes. The spectrum shape under which the cells were characterized (red curve) is similar to that of a blackbody (gray curve), particularly above bandgap. Comparison of modeled TPV efficiency under the spectrum in this work with emitters which could be incorporated into a TPV system in which the $\langle\{AR\}\rangle$ and $\langle\{VF\}\rangle$ allow for the reflected light to be recycled. Shown is a tungsten (W) emitter with $\langle\{AR\}=1\rangle$ and $\langle\{VF\}=1\rangle$ as well as a blackbody emitter (cavity) with $\langle\{VF\}=1\rangle$. An example of systems which could have this geometry is shown in Extended Data Fig. 1. The W emitter results in a higher efficiency because the selective emissivity properties of W suppress some of the below-bandgap energy. Additionally, the W emitter causes the peak in efficiency to shift to lower temperature because the emissivity of W weights the spectrum towards shorter wavelengths. The blackbody emitter results in a lower efficiency because the high irradiance causes a larger penalty of series resistance loss due to the high current density. The comparison shows that the efficiency measured under the lightbulb spectrum in this work provides an appropriate and relevant characterization for TPV efficiency in a real TPV sub-system. In all cases, the cell temperature is 25 °C.

Extended Data Fig. 6 Cell temperature and parasitic heat flows.

a) Cell temperature vs emitter temperature. The cell temperature increases with emitter temperature due to the heat flux sensor which undesirably impedes heat flow. b) Schematic (not to scale) showing parasitic heat flows in the experiment. c) Calculated parasitic heat flows for the 1.4/1.2-eV device. A positive value would act to increase the measured heat flow and reduce the measured efficiency, while a negative value would have the opposite effect. d) Comparison of the efficiency measurement (solid circles) to the measurement with the addition of the modeled parasitic heat flows (open circles) for both tandems.

Extended Data Fig. 7 Experimental setup.

a) Schematic of the concentrator setup showing the relative placement of the ellipsoidal and compound parabolic reflectors, water-cooled aperture, TPV cell, HFS, and heat sink. b) Image of the concentrator setup. c) Schematic of the heat and electricity flows through the measurement device. Electric power is extracted by two copper clips which interface with the cell bus bars on the top surface of the cell and are thermally and electrically insulated from the heat sink. d) Image of the cell on the heatsink with electrical leads. The aperture was removed for clarity.

Extended Data Fig. 8 J_{sc} , V_{oc} , and FF.

Modeled vs measured a) $\langle J \rangle_{sc}$, b) $\langle V \rangle_{oc}$, and c) $\langle FF \rangle$. Good agreement can be seen between the measurement and model predictions. For each device, the $\langle FF \rangle$ measurement and model exhibit the same trend and the minimum in $\langle FF \rangle$ for 1.2/1.0-eV agrees well between the model and measurement which suggests good calibration of the emitter temperature.

Extended Data Fig. 9 Electric power modeling.

a) Measurements of $\langle V \rangle_{oc}$ and $\langle FF \rangle$ vs $\langle J \rangle_{sc}$ for the 1.2/1.0-eV device under the high irradiance flash simulator over a wide range of irradiances, but fixed spectrum and fixed cell temperature at 25 °C.

A model was fit to the data using the three fitting parameters to determine the cell characteristics. The measurement over a wide irradiance range is critical to extract the $\langle R \rangle_{\{series\}}$ parameter under the high-irradiance conditions of interest. b) Low irradiance measurements of $\langle V \rangle_{\{oc\}}$ and $\langle FF \rangle$ under a continuous 1 sun simulator in which the spectral content could be varied to produce photocurrent ratios of the two junctions corresponding to different emitter temperatures. Cell temperature was fixed at 25 °C. The model was determined using the cell characteristic parameters which were extracted from fitting to the data over a wide range of irradiances. The good agreement suggests that the model can be used to predict $\langle V \rangle_{\{oc\}}$, $\langle J \rangle_{\{sc\}}$, $\langle FF \rangle$ over a wide range of conditions (irradiance and spectra). c) Modeled cell performance parameters under the measured spectra showing a comparison between results for a 25 °C cell temperature and the measured cell temperature.

Extended Data Table 1 1.4/1.2-eV measurements of $\langle V \rangle_{\{oc\}}$, $\langle J \rangle_{\{sc\}}$, and $\langle FF \rangle$

Extended Data Table 2 1.2/1.0-eV measurements of $\langle V \rangle_{\{oc\}}$, $\langle J \rangle_{\{sc\}}$, and $\langle FF \rangle$

Rights and permissions

Open Access This article is licensed under a Creative Commons Attribution 4.0 International License, which permits use, sharing, adaptation, distribution and reproduction in any medium or format, as long as you give appropriate credit to the original author(s) and the source, provide a link to the Creative Commons license, and indicate if changes were made. The images or other third party material in this article are included in the article's Creative Commons license, unless indicated otherwise in a credit line to the material. If material is not included in the article's Creative Commons license and your intended use is not permitted by statutory regulation or exceeds the permitted use, you will need to obtain permission directly from the copyright holder. To view a copy of this license, visit <http://creativecommons.org/licenses/by/4.0/>.

[Reprints and Permissions](#)

About this article

Cite this article

LaPotin, A., Schulte, K.L., Steiner, M.A. *et al.* Thermophotovoltaic efficiency of 40%. *Nature* **604**, 287–291 (2022).
<https://doi.org/10.1038/s41586-022-04473-y>

- Received: 17 June 2021
- Accepted: 26 January 2022
- Published: 13 April 2022
- Issue Date: 14 April 2022
- DOI: <https://doi.org/10.1038/s41586-022-04473-y>

Share this article

Anyone you share the following link with will be able to read this content:

[Get shareable link](#)

Sorry, a shareable link is not currently available for this article.

[Copy to clipboard](#)

Provided by the Springer Nature SharedIt content-sharing initiative

This article was downloaded by **calibre** from <https://www.nature.com/articles/s41586-022-04473-y>

[Download PDF](#)

- Article
- [Published: 14 February 2022](#)

Synthesis of chiral sulfinate esters by asymmetric condensation

- [Xin Zhang](#) [ORCID: orcid.org/0000-0002-0767-9541¹](#),
- [Esther Cai Xia Ang¹](#),
- [Ziqi Yang¹](#),
- [Choon Wee Kee](#) [ORCID: orcid.org/0000-0003-1843-2189^{1,2}](#) &
- [Choon-Hong Tan](#) [ORCID: orcid.org/0000-0003-3190-7855¹](#)

[Nature](#) volume 604, pages 298–303 (2022)

- 8327 Accesses
- 72 Altmetric
- [Metrics details](#)

Subjects

- [Chemical libraries](#)
- [Synthetic chemistry methodology](#)
- [Organocatalysis](#)

Abstract

Achiral sulfur functional groups, such as sulfonamide, sulfone, thiol and thioether, are common in drugs and natural products. By contrast, chiral sulfur functional groups are often neglected as pharmacophores^{1,2,3},

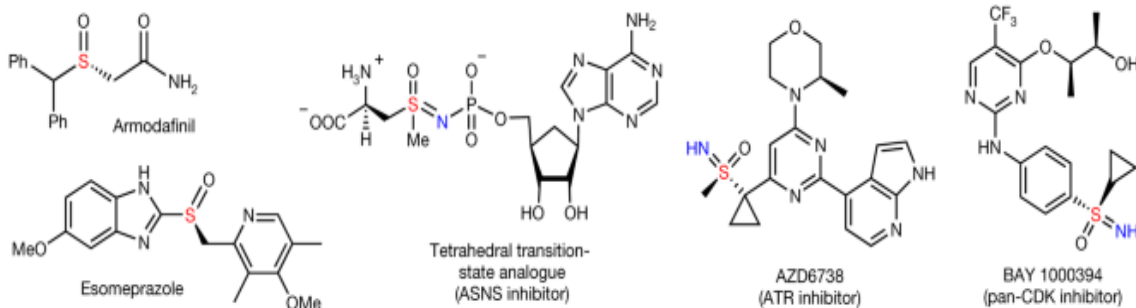
although sulfoximine, with its unique physicochemical and pharmacokinetic properties^{4,5}, has been recently incorporated into several clinical candidates. Thus, other sulfur stereogenic centres, such as sulfinate ester, sulfonamide, sulfonimidate ester and sulfonimidamide, have started to attract attention. The diversity and complexity of these sulfur stereogenic centres have the potential to expand the chemical space for drug discovery^{6,7,8,9,10}. However, the installation of these structures enantioselectively into drug molecules is highly challenging. Here we report straightforward access to enantioenriched sulfinate esters via asymmetric condensation of prochiral sulfinates and alcohols using pentanidium as an organocatalyst. We successfully coupled a wide range of sulfinates and bioactive alcohols stereoselectively. The initial sulfinates can be prepared from existing sulfone and sulfonamide drugs, and the resulting sulfinate esters are versatile for transformations to diverse chiral sulfur pharmacophores. Through late-stage diversification^{11,12} of celecoxib and other drug derivatives, we demonstrate the viability of this unified approach towards sulfur stereogenic centres.

Main

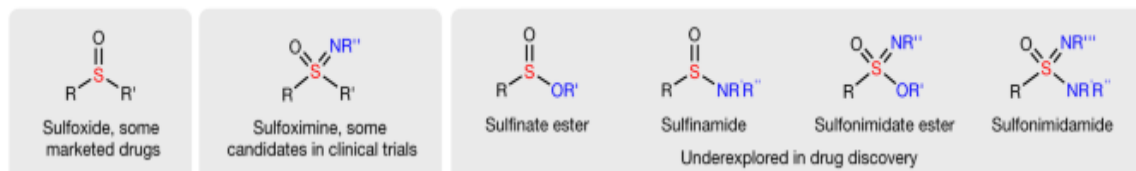
Diversity-oriented synthesis has facilitated drug discovery by efficiently generating compound collections with high structural complexity and diversity^{13,14}. Stereoisomeric compounds, with their different topographical features, usually result in distinct interactions with targeted proteins. Diverse molecular scaffolds based on carbon stereogenic centres have provided a wide range of chemical space for drug discovery¹⁵. Sulfur, with its multiple oxidation states, is widely present in biologically active compounds¹⁶. However, sulfur stereogenic centres are often overlooked as pharmacophores^{1,2,3}, apart from the marketed chiral sulfoxides esomeprazole and armodafinil (Fig. 1a).

Fig. 1 : Diverse chiral sulfur pharmacophores for drug discovery and their synthesis.

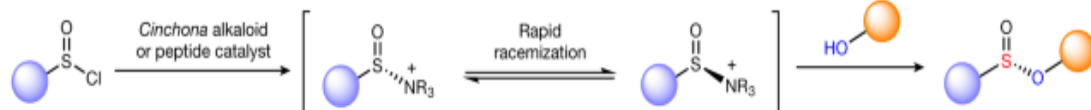
a Biologically active compounds containing S(IV) and S(VI) stereogenic centres



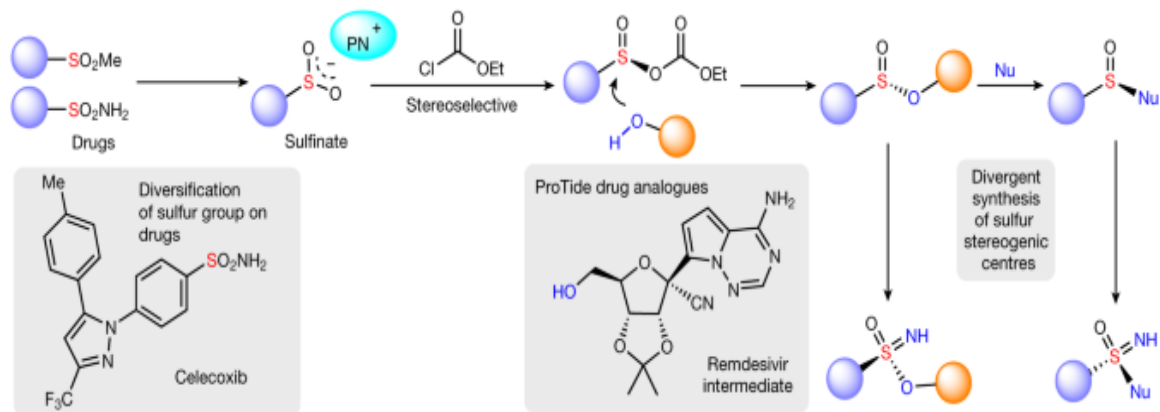
b Diverse S(IV) and S(VI) stereogenic centres for drug design and discovery



c Catalytic synthesis of chiral sulfinate esters through dynamic kinetic resolution



d This work: asymmetric condensation of sulfinites and alcohols with pentanidium (PN), a chiral cation catalyst



a, Examples of biologically active compounds containing S(IV) and S(VI) stereogenic centres. **b**, Examples of diverse chiral sulfur pharmacophores for drug design and discovery. **c**, Synthesis of chiral sulfinate esters through dynamic kinetic resolution with chiral amine catalysts. **d**, Synthesis of chiral sulfinate esters through asymmetric condensation of sulfinites and alcohols with pentanidium (this work). ASNS, L-asparagine synthase; ATR, ataxia telangiectasia and rad3-related; CDK, cyclin-dependent kinase; Et, ethyl; Me, methyl; Nu, nucleophile; Ph, phenyl.

Sulfoximine, a moiety with a S(VI) stereocentre, has become increasingly important in drug discovery owing to its unique physicochemical and

pharmacokinetic properties^{4,5}. Sulfoximine is tetrahedral and has been designed as a stable transition-state analogue to inhibit L-asparagine synthase⁶. Although no candidate containing sulfoximine has been approved as a drug, several compounds such as AZD6738 and BAY 1000394 have entered clinical trials (Fig. 1a)^{8,9}. Other sulfur stereogenic centres such as sulfinate ester, sulfinamide¹⁷, sulfonimidate ester and sulfonimidamide¹⁸ have started to attract attention owing to the advances made by sulfoximine (Fig. 1b). Although some methodologies have been developed for the racemic synthesis of these stereogenic centres^{19,20,21}, the preparation of enantiopure sulfur stereocentres is still a formidable challenge²². Established methods mainly rely on stoichiometric amounts of chiral reagents^{23,24,25} or kinetic resolution of racemic substrates^{26,27}. Only a handful of catalytic approaches have been reported and structural diversity is limited^{28,29,30,31,32}.

Among the sulfur stereogenic centres, sulfinate ester holds the linchpin position for two reasons. First, several enantiopure sulfinate esters can be reliably and affordably derived from chiral alcohols. Next, a variety of approaches have been developed to convert sulfinate esters to other sulfur stereogenic centres^{33,34,35}. Reports on the catalytic synthesis of enantioenriched sulfinate esters are scarce and all are based on dynamic kinetic resolution of sulfinyl chlorides with alcohols using peptides or *Cinchona* alkaloids as catalysts (Fig. 1c)^{36,37,38}. The community is still yearning for a general and efficient method for the catalytic synthesis of enantiopure sulfinate esters with broad substrate compatibility. Considering the increasing interest in using novel chiral sulfur stereogenic centres as pharmacophores, a catalytic method suitable for the late-stage manipulation of drugs with diverse sulfur stereocentres is imperatively required.

Here we report the desymmetrization of pro-chiral sulfinate to afford enantioenriched sulfinate esters using pentanidium (**PN**)^{39,40} as a catalyst (Fig. 1d). Sulfinate, a stable and easily accessible reagent, is well known as a carbon-radical source for coupling via desulfitation^{41,42} or as a sulfur-centred nucleophile⁴³. It is less known that sulfinate is an ambident nucleophile, and that the enantiotopic oxygen atoms are also potential nucleophilic sites. We realized this pathway through the use of ethyl chloroformate as the oxophilic electrophile. In the presence of pentanidium

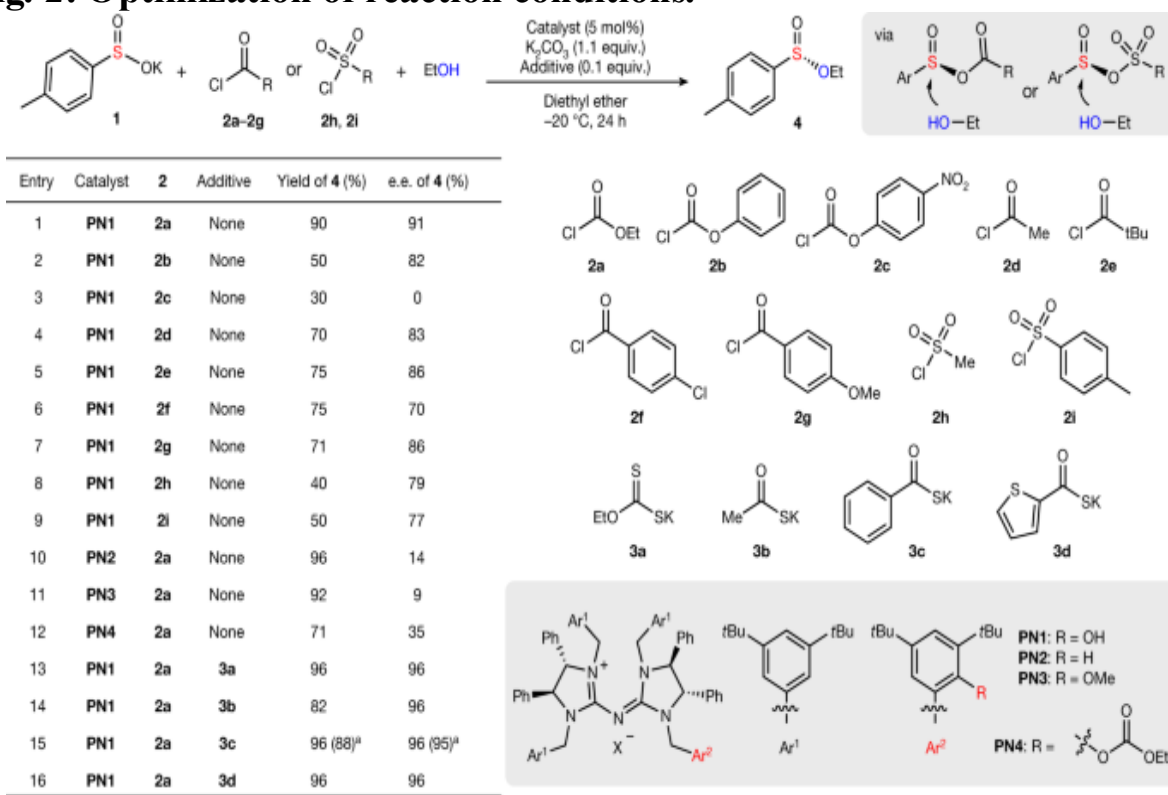
as a catalyst, sulfinate and ethyl chloroformate form a mixed anhydride intermediate, which in turn is converted to enantioenriched sulfinate ester through a replacement reaction with an alcohol. Sulfinate can also be easily derived from sulfur functional groups in drugs such as sulfonamide in celecoxib⁴⁴ or methylsulfone in etoricoxib⁴⁵. Thus, this methodology is suitable for late-stage diversification of existing drugs containing sulfur functional groups. In addition, drugs and drug intermediates containing an alcohol group, for example, the intermediate of remdesivir, an antiviral drug approved for the treatment of coronavirus disease 2019 (COVID-19), can be manipulated into novel analogues by replacing its phosphorus stereocentre (phosphoramidate) into a sulfur stereocentre. Phosphoramidate prodrugs, including remdesivir, are part of pronucleotide (ProTide) therapies for viral disease and cancer^{46,47,48}. Similar to phosphorus, sulfur is also available in multiple oxidation states and a diverse range of structures; its adoption in place of phosphorus may lead to new therapies.

Optimization of reaction conditions

We started our investigation using potassium 4-methylbenzenesulfinate **1** as a model for sulfinate (Fig. 2). Several acyl chlorides (**2a–2g**) and sulfonyl chlorides (**2h**, **2i**) were selected, and the respective mixed anhydrides were generated as intermediates, which were immediately replaced by ethanol at the sulfur stereocentre to afford sulfinate ester **4** (Fig. 2, entries 1–9). Ethyl chloroformate **2a** was found to give the most consistent and favourable results. Most of our earlier investigations were performed using pentanidium **PN2** (entry 10). Serendipitously, we discovered that pentanidium **PN1**, containing a phenol substituent, provided a high level of stereocontrol. We speculate that this may be due to the selective hydrogen bonding between the phenol group on **PN1** and sulfinate **1**. When the phenol group was methylated to form pentanidium **PN3**, enantioselectivity decreased substantially (entry 11). We also detected the formation of acylated pentanidium **PN4** during the reaction process when ethyl chloroformate **2a** was used. When we prepared pentanidium **PN4** separately and subjected it to the same reaction conditions, only low enantioselectivity was obtained (entry 12). It is likely that formation of pentanidium **PN4** was an undesirable pathway, which additives such as thiolates (**3a–3d**) mitigated to improve the reaction (entries 13–16; see [Supplementary Information](#) for details). Under

the optimized conditions, we were able to perform the reaction at gram scale with high yield and enantioselectivity (entry 15).

Fig. 2: Optimization of reaction conditions.



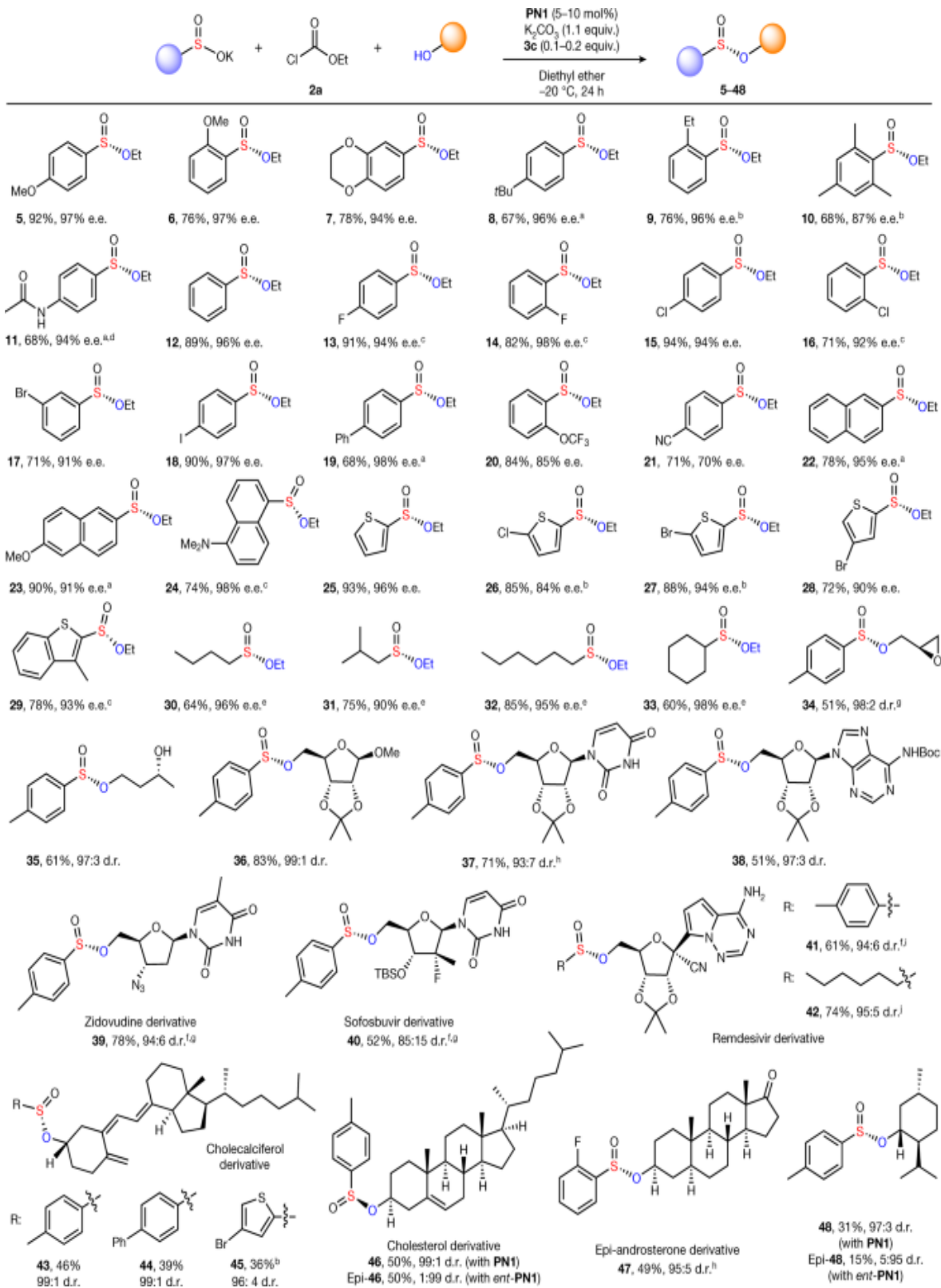
Reaction conditions: potassium sulfinate **1** (0.1 mmol), catalyst (5 mol%), **2a–2i** (1.6 equiv.), EtOH (1.2 equiv.), K_2CO_3 (1.1 equiv.), additive **3a–3d** (0.1 equiv.), Et_2O (0.5 ml), -20°C , 24 h. Isolated yields are reported, and e.e. values were determined by chiral high-performance liquid chromatography (HPLC) analysis. ^aReaction was performed on a 12.0 mmol scale and 1.94 g sulfinate ester **4** was isolated. Ar, aryl; *t*Bu, *tert*-butyl.

Reaction scope

On the basis of these results, we proceeded to investigate the scope of sulfinites suitable for our methodology (Fig. 3). Electron-rich phenyl sulfinites with different substitution patterns gave the desired sulfinate esters with high stereoselectivity. Phenyl sulfinate esters with alkoxy substitution (**5–7**), alkyl substitution (**8, 9**), bulky mesityl group (**10**) and *para*-acetamido substitution (**11**) were obtained with high enantiomeric excess (e.e.) values.

This reaction was also efficient to obtain a variety of phenyl sulfinate esters **13–18** substituted with halogen atoms. Phenyl substitution at the *para* position gave sulfinate ester **19** and 2-trifluoromethoxybenzenesulfinate gave sulfinate ester **20**, both with good levels of enantioselectivity. 4-Cyanobenzenesulfinate, which contained a strong electron-withdrawing cyano group, gave sulfinate ester **21** in moderate yield and with a moderate e.e. value. In general, strong electron-withdrawing aryl sulfinates gave moderate results. Several naphthyl sulfinates with different substitutions gave the corresponding sulfinate esters **22–24** with high enantioselectivities. Thiophene and benzothiophene sulfinate esters **25–29** were also obtained with excellent results. This methodology also worked well for alkyl sulfinates and enantioenriched products (**30–33**) were efficiently generated. During these investigations, we found that the catalyst **PN1** was quickly acylated to form **PN4** in reactions with electron-rich sulfinates, which resulted in decreased yields and enantioselectivity. This was solved by using dipotassium phosphate (K_2HPO_4) as a base and increasing the amount of catalyst or additive.

Fig. 3: Reaction scope.



Reaction conditions: potassium sulfinate (0.1 mmol), **PN1** (5–10 mol%), **2a** (1.3–1.6 equiv.), alcohol (1.0–1.2 equiv.), K_2CO_3 (1.1 equiv.), **3c** (0.1–0.2 equiv.), Et_2O (0.5–1.0 ml), –20 °C, 24 h. Isolated yields are reported, e.e. values were determined by chiral HPLC analysis, and d.r. values were determined by chiral HPLC or NMR analysis. ^a K_2HPO_4 (2.0 equiv.) instead of K_2CO_3 . ^b**3d** (0.1–0.2 equiv.) as additive. ^cSodium sulfinate was used. ^d**2a** (2.0 equiv.), **3d** (0.5 equiv.). ^e K_2HPO_4 (2.0 equiv.), **3d** (0.2 equiv.), additional H_2O (10 μl). ^fAlcohol (0.1 mmol), potassium sulfinate (0.15 mmol), **2a** (0.2 mmol), K_2CO_3 (0.15 mmol). ^gMTBE (1.0–2.0 ml) as solvent. ^h2.0 ml of mixed solvent $\text{Et}_2\text{O}/\text{EA}$ (1:1). ⁱ2.0 ml of mixed solvent MTBE/EA (2:1). ^jAlcohol (0.1 mmol), potassium sulfinate (0.2 mmol), **2a** (0.4 mmol), K_2HPO_4 (0.4 mmol), **3d** (0.04 mmol), H_2O (20 μl), Et_2O (2.0 ml).

See [Supplementary Information](#) for details. Boc, *tert*-butoxycarbonyl; EA, ethyl acetate; MTBE, methyl *tert*-butyl ether; TBS, *tert*-butyldimethylsilyl.

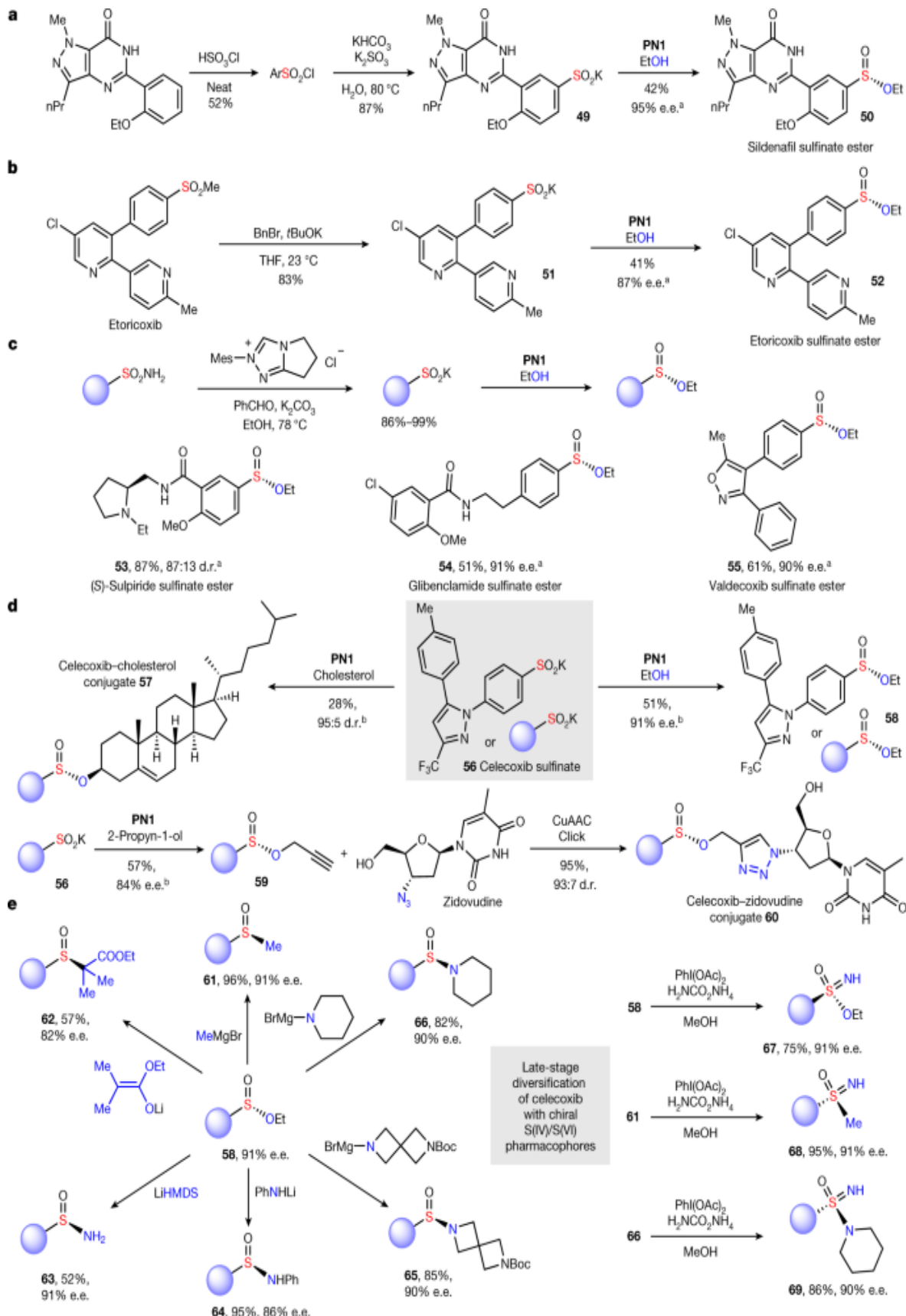
Next, we found that this methodology efficiently installed sulfur stereogenic centres to various alcohols with high functional group compatibility (Fig. 3). (*S*)-Glycidol was successfully functionalized, without affecting the epoxide moiety, to sulfinate ester **34** with a diastereomeric ratio (d.r.) of 98:2. With (*R*)-1,3-butanediol, primary alcohol was preferred over secondary alcohol with mono-sulfinylated product **35** obtained with d.r. of 97:3. To investigate the potential of using this methodology to complement the ProTide strategy, we investigated the functionalization of several nucleosides. The desired nucleoside sulfinate esters **36–42** were obtained with moderate to high yields and excellent stereoselectivity. Sulfur stereogenic centres were successfully installed on the corresponding alcoholic intermediates of several marketed antiviral drugs such as zidovudine, sofosbuvir and remdesivir. We also demonstrated stereoselective sulfinylation of several bioactive cyclic alcohols, including cholecalciferol, cholesterol, epi-androsterone and menthol, to their corresponding sulfinate esters **43–48**. With cholesterol and menthol, we also showed that when *ent*-**PN1** was used as the catalyst, the diastereomeric ratio is inverted, indicating catalyst control rather than substrate control of this reaction. Our methodology is suitable for primary and secondary alcohols including isopropanol; however, bulky *tert*-butanol,

phenols and amines were not viable nucleophiles ([Supplementary Information](#)).

Modification of drugs

To demonstrate the generality and efficiency of our methodology, we prepared several complex sulfinate salts from drugs or drug intermediates (Fig. 4). Using sildenafil as an example, chlorosulfonation of an electron-rich arene led to its sulfonyl chloride intermediate, which can be easily converted to sulfinate **49** (Fig. 4a). Using our asymmetric condensation condition with ethanol, sildenafil sulfinate ester **50** was obtained with high enantioselectivity. Next, we converted methylsulfone on etoricoxib to sulfinate **51** through alkylation and in situ elimination of styrene (Fig. 4b)⁴⁵. Subsequently, enantioenriched etoricoxib sulfinate ester **52** was obtained efficiently through our method. Recently, a group from Merck reported the preparation of sulfinites from primary sulfonamides through carbene-catalysed deamination⁴⁴. Using this approach, we transformed several bioactive primary sulfonamides into their corresponding sulfinites (Fig. 4c). Likewise, the respective (*S*)-sulpiride, glibenclamide and valdecoxib sulfinate esters (**53–55**) were afforded with high stereoselectivities.

Fig. 4: Functionalization and diversification of drugs.



a, Synthesis of sildenafil sulfinate ester. **b**, Synthesis of etoricoxib sulfinate ester. **c**, Functionalization of sulfonamide drugs into sulfinate esters. **d**, Synthesis of celecoxib sulfinate esters using different alcohols. **e**, Late-stage diversification of celecoxib into a plethora of derivatives with sulfur stereocentres. Reaction conditions: ^aPotassium sulfinate (0.1 mmol), EtOH (1.0 equiv.), **PN1** (20 mol%), **2a** (2.1 equiv.), K₂HPO₄ (2.0 equiv.), **3a** or **3d** (1.0 equiv.), Et₂O or toluene (1 ml), 0 °C or –20 °C, 24 h. ^b**56** (0.1 mmol), ROH (1.0 equiv.), **PN1** (5 mol%), **2a** (1.6 equiv.), K₂CO₃ (1.1 equiv.), **3c** (0.2 equiv.), H₂O (10 µl), MTBE (1.0 ml), –20 °C, 24 h. See [Supplementary Information](#) for details. CuAAC, copper-catalysed azide–alkyne cycloaddition; LiHMDS, lithium bis(trimethylsilyl)amide; *n*Pr, *n*-propyl; THF, tetrahydrofuran.

As mentioned, sulfinate ester is the ideal linchpin intermediate for late-stage diversification of drugs into a plethora of sulfur stereogenic centres. Therefore, we utilized celecoxib as a model to justify that our methodology is a valuable addition to the toolkit of drug discovery programmes (Fig. [4d](#), [e](#)). Primary sulfonamide on celecoxib was converted smoothly to celecoxib sulfinate **56**. Asymmetric condensation of sulfinate **56** with cholesterol gave celecoxib–cholesterol sulfinate ester conjugate **57** with a high diastereomeric ratio (95:5). Through condensation of celecoxib sulfinate **56** with 2-propyn-1-ol, we obtained enantioenriched propargyl sulfinate ester **59**. This nicely set it up for ‘click reaction’ with the azide group on zidovudine, generating celecoxib–zidovudine conjugate **60**. Celecoxib sulfinate ester **58** was obtained with a high e.e. value as a versatile precursor of other S(IV)/S(VI) stereogenic centres and able to be substituted by various nucleophiles at the sulfur centre with inverted configuration. Methyl Grignard reagent and lithium enolate are useful nucleophiles, providing respective enantioenriched sulfoxides (**61**, **62**). With lithium bis(trimethylsilyl)amide, we obtained directly unprotected sulfinamide **63**. Both primary and secondary amines are effective nucleophiles through formation of lithium amide or activation with Grignard reagents. Inversion at the sulfur stereocentre provided respective enantioenriched sulfinamides **64**–**66**. Further imidations^{[49,50](#)} of celecoxib sulfinate ester **58**, celecoxib sulfoxide **61** and celecoxib sulfinamide **66** gave the corresponding sulfonimidate ester **67**, sulfoximine **68** and sulfonimidamide **69** in high yields and without erosion of e.e. values. Many

of these enantioenriched S(IV)/S(VI) stereogenic centres have been previously deemed as synthetically challenging^{1,22}.

Conclusion

We have presented a viable and unified synthetic strategy for the stereoselective preparation of sulfinate esters and related sulfur stereogenic centres. This methodology is mild and tolerates a wide range of functional groups, allowing it to be compatible with late-stage diversification of celecoxib and other marketed drugs. In addition, several marketed antiviral drugs, for example, zidovudine, sofosbuvir and remdesivir, can be redecorated with sulfur stereogenic centres through sulfinylation of their alcoholic intermediates. This approach complements the ProTide strategy through replacement of the phosphorus stereogenic centre with sulfur stereogenic centres. In view of the increasing use of sulfur stereogenic centres as pharmacophores, we believe that this methodology will ameliorate the toolkits of drug discovery programmes for the exploration of these pharmacophores.

Data availability

The data supporting the findings of this study are available within the paper and its [Supplementary Information](#).

References

1. Tilby, M. J. & Willis, M. C. How do we address neglected sulfur pharmacophores in drug discovery? *Expert Opin. Drug Discov.* **16**, 1227–1231 (2021).
2. Lücking, U. Neglected sulfur(VI) pharmacophores in drug discovery: exploration of novel chemical space by the interplay of drug design and method development. *Org. Chem. Front.* **6**, 1319–1324 (2019).
3. Kitamura, S. et al. Sulfur(VI) fluoride exchange (SuFEx)-enabled high-throughput medicinal chemistry. *J. Am. Chem. Soc.* **142**, 10899–10904

(2020).

4. Mader, P. & Kattner, L. Sulfoximines as rising stars in modern drug discovery? Current status and perspective on an emerging functional group in medicinal chemistry. *J. Med. Chem.* **63**, 14243–14275 (2020).
5. Han, Y. et al. Application of sulfoximines in medicinal chemistry from 2013 to 2020. *Eur. J. Med. Chem.* **209**, 112885 (2021).
6. Koizumi, M., Hiratake, J., Nakatsu, T., Kato, H. & Oda, J. I. A potent transition-state analogue inhibitor of *Escherichia coli* asparagine synthetase A. *J. Am. Chem. Soc.* **121**, 5799–5800 (1999).
7. Altenburg, B. et al. Chiral analogues of PFI-1 as BET inhibitors and their functional role in myeloid malignancies. *ACS Med. Chem. Lett.* **11**, 1928–1934 (2020).
8. Foote, K. M. et al. Discovery and characterization of AZD6738, a potent inhibitor of ataxia telangiectasia mutated and rad3 related (ATR) kinase with application as an anticancer agent. *J. Med. Chem.* **61**, 9889–9907 (2018).
9. Lücking, U. et al. The lab oddity prevails: discovery of pan-CDK inhibitor (*R*)-S-cyclopropyl-S-(4-{[4-{[(1*R*,2*R*)-2-hydroxy-1-methylpropyl]oxy}-5-(trifluorome thyl)pyrimidin-2-yl]amino} phenyl)sulfoximide (BAY 1000394) for the treatment of cancer. *ChemMedChem* **8**, 1067–1085 (2013).
10. Bentley, R. Role of sulfur chirality in the chemical processes of biology. *Chem. Soc. Rev.* **34**, 609–624 (2005).
11. Börgel, J. & Ritter, T. Late-stage functionalization. *Chem* **6**, 1877–1887 (2020).
12. Guillemard, L., Kaplaneris, N., Ackermann, L. & Johansson, M. J. Late-stage C–H functionalization offers new opportunities in drug discovery. *Nat. Rev. Chem.* **5**, 522–545 (2021).

13. Schreiber, S. L. Target-oriented and diversity-oriented organic synthesis in drug discovery. *Science* **287**, 1964–1969 (2000).
14. Galloway, W. R., Isidro-Llobet, A. & Spring, D. R. Diversity-oriented synthesis as a tool for the discovery of novel biologically active small molecules. *Nat. Commun.* **1**, 80 (2010).
15. Quasdorf, K. W. & Overman, L. E. Catalytic enantioselective synthesis of quaternary carbon stereocentres. *Nature* **516**, 181–191 (2014).
16. Feng, M., Tang, B., Liang, S. H. & Jiang, X. Sulfur containing scaffolds in drugs: synthesis and application in medicinal chemistry. *Curr. Top. Med. Chem.* **16**, 1200–1216 (2016).
17. Finn, P., Charlton, M., Edmund, G., Jirgensons, A., & Loza, E. 2-Amino-N-(arylsulfinyl)-acetamide compounds as inhibitors of bacterial aminoacyl-tRNA synthetase. patent WO2018065611A1 (2018).
18. Chinthakindi, P. K. et al. Sulfonimidamides in medicinal and agricultural chemistry. *Angew. Chem. Int. Ed.* **56**, 4100–4109 (2017).
19. Yu, H., Li, Z. & Bolm, C. Copper-catalyzed transsulfinamidation of sulfinamides as a key step in the preparation of sulfonamides and sulfonimidamides. *Angew. Chem. Int. Edn* **57**, 15602–15605 (2018).
20. Chatterjee, S., Makai, S. & Morandi, B. Hydroxylamine-derived reagent as a dual oxidant and amino group donor for the iron-catalyzed preparation of unprotected sulfinamides from thiols. *Angew. Chem. Int. Edn* **60**, 758–765 (2021).
21. Davies, T. Q. et al. Harnessing sulfinyl nitrenes: a unified one-pot synthesis of sulfoximines and sulfonimidamides. *J. Am. Chem. Soc.* **142**, 15445–15453 (2020).
22. Wojaczynska, E. & Wojaczynski, J. Modern stereoselective synthesis of chiral sulfinyl compounds. *Chem. Rev.* **120**, 4578–4611 (2020).
23. Aota, Y., Kano, T. & Maruoka, K. Asymmetric synthesis of chiral sulfoximines via the S-arylation of sulfinamides. *J. Am. Chem. Soc.*

141, 19263–19268 (2019).

24. Mendonca Matos, P., Lewis, W., Argent, S. P., Moore, J. C. & Stockman, R. A. General method for the asymmetric synthesis of N–H sulfoximines via C–S bond formation. *Org. Lett.* **22**, 2776–2780 (2020).
25. Greed, S. et al. Synthesis of highly enantioenriched sulfonimidoyl fluorides and sulfonimidamides by stereospecific sulfur–fluorine exchange (SuFEx) reaction. *Chem. Eur. J.* **26**, 12533–12538 (2020).
26. Dong, S. et al. Organocatalytic kinetic resolution of sulfoximines. *J. Am. Chem. Soc.* **138**, 2166–2169 (2016).
27. Brauns, M. & Cramer, N. Efficient kinetic resolution of sulfur-stereogenic sulfoximines by exploiting $\text{Cp}^X\text{Rh}^{\text{III}}$ -catalyzed C–H functionalization. *Angew. Chem. Int. Edn* **58**, 8902–8906 (2019).
28. Shen, B., Wan, B. & Li, X. Enantiodivergent desymmetrization in the rhodium(III)-catalyzed annulation of sulfoximines with diazo compounds. *Angew. Chem. Int. Edn* **57**, 15534–15538 (2018).
29. Sun, Y. & Cramer, N. Enantioselective synthesis of chiral-at-sulfur 1,2-benzothiazines by $\text{Cp}^X\text{Rh}^{\text{III}}$ -catalyzed C–H functionalization of sulfoximines. *Angew. Chem. Int. Edn* **57**, 15539–15543 (2018).
30. Zhou, T. et al. Efficient synthesis of sulfur-stereogenic sulfoximines via Ru(II)-catalyzed enantioselective C–H functionalization enabled by chiral carboxylic acid. *J. Am. Chem. Soc.* **143**, 6810–6816 (2021).
31. Tang, Y. & Miller, S. J. Catalytic enantioselective synthesis of pyridyl sulfoximines. *J. Am. Chem. Soc.* **143**, 9230–9235 (2021).
32. Tilby, M. J., Dewez, D. F., Hall, A., Martinez Lamenca, C. & Willis, M. C. Exploiting configurational lability in aza-sulfur compounds for the organocatalytic enantioselective synthesis of sulfonimidamides. *Angew. Chem. Int. Edn* **60**, 25680–25687 (2021).

33. Kagan, H. B. & Rebiere, F. Some routes to chiral sulfoxides with very high enantiomeric excesses. *Synlett* **1990**, 643–650 (1990).
34. Fernandez, I., Khiar, N., Llera, J. M. & Alcudia, F. Asymmetric synthesis of alkane- and arenesulfinates of diacetone-D-glucose (DAG): an improved and general route to both enantiomerically pure sulfoxides. *J. Org. Chem.* **57**, 6789–6796 (1992).
35. Lu, B. Z. et al. New general sulfinylating process for asymmetric synthesis of enantiopure sulfinates and sulfoxides. *Org. Lett.* **7**, 1465–1468 (2005).
36. Evans, J. W., Fierman, M. B., Miller, S. J. & Ellman, J. A. Catalytic enantioselective synthesis of sulfinate esters through the dynamic resolution of *tert*-butanesulfinyl chloride. *J. Am. Chem. Soc.* **126**, 8134–8135 (2004).
37. Shibata, N. et al. Cinchona alkaloid/sulfinyl chloride combinations: enantioselective sulfinylating agents of alcohols. *J. Am. Chem. Soc.* **127**, 1374–1375 (2005).
38. Peltier, H. M., Evans, J. W. & Ellman, J. A. Catalytic enantioselective sulfinyl transfer using cinchona alkaloid catalysts. *Org. Lett.* **7**, 1733–1736 (2005).
39. Zong, L. & Tan, C. H. Phase-transfer and ion-pairing catalysis of pentanidiums and bisguanidiniums. *Acc. Chem. Res.* **50**, 842–856 (2017).
40. Zhang, X. et al. An enantioconvergent halogenophilic nucleophilic substitution (S_N2X) reaction. *Science* **363**, 400–404 (2019).
41. Fujiwara, Y. et al. Practical and innate carbon-hydrogen functionalization of heterocycles. *Nature* **492**, 95–99 (2012).
42. Smith, J. M., Dixon, J. A., deGruyter, J. N. & Baran, P. S. Alkyl sulfinates: radical precursors enabling drug discovery. *J. Med. Chem.* **62**, 2256–2264 (2019).

43. Goh, J., Maraswami, M. & Loh, T. P. Synthesis of vinylic sulfones in aqueous media. *Org. Lett.* **23**, 1060–1065 (2021).
44. Fier, P. S. & Maloney, K. M. NHC-catalyzed deamination of primary sulfonamides: a platform for late-stage functionalization. *J. Am. Chem. Soc.* **141**, 1441–1445 (2019).
45. Gauthier, D. R. Jr & Yoshikawa, N. A general, one-pot method for the synthesis of sulfinic acids from methyl sulfones. *Org. Lett.* **18**, 5994–5997 (2016).
46. DiRocco, D. A. et al. A multifunctional catalyst that stereoselectively assembles prodrugs. *Science* **356**, 426–430 (2017).
47. Wang, Y. et al. Remdesivir in adults with severe COVID-19: a randomised, double-blind, placebo-controlled, multicentre trial. *Lancet* **395**, 1569–1578 (2020).
48. Slusarczyk, M. et al. Application of ProTide technology to gemcitabine: a successful approach to overcome the key cancer resistance mechanisms leads to a new agent (NUC-1031) in clinical development. *J. Med. Chem.* **57**, 1531–1542 (2014).
49. Zenzola, M., Doran, R., Degennaro, L., Luisi, R. & Bull, J. A. Transfer of electrophilic NH using convenient sources of ammonia: direct synthesis of NH sulfoximines from sulfoxides. *Angew. Chem. Int. Edn* **55**, 7203–7207 (2016).
50. Izzo, F., Schafer, M., Stockman, R. & Lücking, U. A new, practical one-pot synthesis of unprotected sulfonimidamides by transfer of electrophilic NH to sulfinamides. *Chem. Eur. J.* **23**, 15189–15193 (2017).

Acknowledgements

We acknowledge support from Nanyang Technological University for Tier 1 grant (RG2/20). This research was supported by the Ministry of Education, Singapore, under its Academic Research Fund Tier 2 (MOE2019-T2-1-091).

This work was supported by the A*STAR Computational Resource Centre through the use of its high-performance computing facilities. The computational work for this article was partially performed on resources of the National Supercomputing Centre, Singapore (<https://www.nscc.sg>).

Author information

Affiliations

1. Division of Chemistry and Biological Chemistry, School of Physical and Mathematical Sciences, Nanyang Technological University, Singapore, Singapore

Xin Zhang, Esther Cai Xia Ang, Ziqi Yang, Choon Wee Kee & Choon-Hong Tan

2. Process and Catalysis Research, Institute of Chemical and Engineering Sciences, Singapore, Singapore

Choon Wee Kee

Contributions

C.-H.T. and X.Z. conceived the research; X.Z. is responsible for experimental design and data analysis; X.Z., E.C.X.A., and Z.Y. performed the experiments and compounds testing; C.W.K. contributed to mechanistic discussion; C.-H.T. and X.Z. prepared the manuscript with input from all authors.

Corresponding authors

Correspondence to [Xin Zhang](#) or [Choon-Hong Tan](#).

Ethics declarations

Competing interests

The authors declare no competing interests.

Peer review

Peer review information

Nature thanks Edward Anderson, Danielle Schultz and the other, anonymous, reviewer(s) for their contribution to the peer review of this work.

Additional information

Publisher's note Springer Nature remains neutral with regard to jurisdictional claims in published maps and institutional affiliations.

Supplementary information

Supplementary Information

This file contains Supplementary Sections 1–11 and references.

Rights and permissions

Reprints and Permissions

About this article

Cite this article

Zhang, X., Ang, E.C.X., Yang, Z. *et al.* Synthesis of chiral sulfinate esters by asymmetric condensation. *Nature* **604**, 298–303 (2022).
<https://doi.org/10.1038/s41586-022-04524-4>

- Received: 17 October 2021

- Accepted: 04 February 2022
- Published: 14 February 2022
- Issue Date: 14 April 2022
- DOI: <https://doi.org/10.1038/s41586-022-04524-4>

Share this article

Anyone you share the following link with will be able to read this content:

[Get shareable link](#)

Sorry, a shareable link is not currently available for this article.

[Copy to clipboard](#)

Provided by the Springer Nature SharedIt content-sharing initiative

This article was downloaded by **calibre** from <https://www.nature.com/articles/s41586-022-04524-4>

| [Section menu](#) | [Main menu](#) |

[Download PDF](#)

- Article
- [Published: 16 February 2022](#)

Bat coronaviruses related to SARS-CoV-2 and infectious for human cells

- [Sarah Temmam^{1,2}](#) na1,
- [Khamsing Vongphayloth³](#) na1,
- [Eduard Baquero⁴](#) na1,
- [Sandie Munier⁵](#) na1,
- [Massimiliano Bonomi](#) ORCID: orcid.org/0000-0002-7321-0004⁶ na1,
- [Béatrice Regnault^{1,2},](#)
- [Bounsavane Douangboubpha⁷,](#)
- [Yasaman Karami](#) ORCID: orcid.org/0000-0001-8413-2665⁶,
- [Delphine Chrétien^{1,2},](#)
- [Daosavan Sanamxay⁷,](#)
- [Vilakhan Xayaphet⁷,](#)
- [Phetphoumin Paphaphanh⁷,](#)
- [Vincent Lacoste](#) ORCID: orcid.org/0000-0002-3173-4053³,
- [Somphavanh Somlor³,](#)
- [Khaithong Lakeomany³,](#)
- [Nothasin Phommavanh³,](#)
- [Philippe Pérot](#) ORCID: orcid.org/0000-0002-5194-8200^{1,2},
- [Océane Dehan^{6,8},](#)
- [Faustine Amara⁵,](#)
- [Flora Donati](#) ORCID: orcid.org/0000-0003-2862-9751^{6,8},
- [Thomas Bigot](#) ORCID: orcid.org/0000-0001-8504-4675^{1,9},
- [Michael Nilges](#) ORCID: orcid.org/0000-0002-1451-8092⁶,

- [Félix A. Rey](#) [ORCID: orcid.org/0000-0002-9953-7988⁴](#),
- [Sylvie van der Werf](#) [ORCID: orcid.org/0000-0002-1148-4456^{6,8}](#),
- [Paul T. Brey³](#) &
- [Marc Eloit](#) [ORCID: orcid.org/0000-0002-1853-7207^{1,2,10}](#)

[*Nature*](#) volume **604**, pages 330–336 (2022)

- 58k Accesses
- 4 Citations
- 938 Altmetric
- [Metrics details](#)

Subjects

- [SARS-CoV-2](#)
- [Virus–host interactions](#)

Abstract

The animal reservoir of SARS-CoV-2 is unknown despite reports of SARS-CoV-2-related viruses in Asian *Rhinolophus* bats^{1,2,3,4}, including the closest virus from *R. affinis*, RaTG13 (refs. [5,6](#)), and pangolins^{7,8,9}. SARS-CoV-2 has a mosaic genome, to which different progenitors contribute. The spike sequence determines the binding affinity and accessibility of its receptor-binding domain to the cellular angiotensin-converting enzyme 2 (ACE2) receptor and is responsible for host range^{[10,11,12](#)}. SARS-CoV-2 progenitor bat viruses genetically close to SARS-CoV-2 and able to enter human cells through a human ACE2 (hACE2) pathway have not yet been identified, although they would be key in understanding the origin of the epidemic. Here we show that such viruses circulate in cave bats living in the limestone karstic terrain in northern Laos, in the Indochinese peninsula. We found that the receptor-binding domains of these viruses differ from that of SARS-CoV-2 by only one or two residues at the interface with ACE2, bind more efficiently to the hACE2 protein than that of the SARS-CoV-2 strain isolated

in Wuhan from early human cases, and mediate hACE2-dependent entry and replication in human cells, which is inhibited by antibodies that neutralize SARS-CoV-2. None of these bat viruses contains a furin cleavage site in the spike protein. Our findings therefore indicate that bat-borne SARS-CoV-2-like viruses that are potentially infectious for humans circulate in *Rhinolophus* spp. in the Indochinese peninsula.

Main

The origin of SARS-CoV-2, as well as its mode of introduction into the human population, are unknown at present. Since its emergence, numerous animal species have been studied to identify possible reservoirs and/or intermediate hosts of the virus, including a large diversity of insectivorous bats of the genus *Rhinolophus*. Despite the recent report of various SARS-CoV-2-related viruses in *R. shameli* (isolated in Cambodia in 2010¹³), *R. pusillus* and *R. malayanus* (China, 2020 and 2019, respectively²), *R. acuminatus* (Thailand, 2020³) and *R. cornutus* (Japan, 2013⁴), the closest SARS-CoV-2 bat-borne genome still remains the one from *R. affinis*, RaTG13 (China, 2013^{5,6}), with 96.1% identity at the whole-genome level. Several studies also suggested the involvement of pangolin coronaviruses in the emergence of SARS-CoV-2 (refs. ^{7,8,9}). Since its appearance in humans, SARS-CoV-2 has evolved through sporadic mutations and recombination events¹⁴, some of which correspond to gains in fitness allowing the virus to spread more widely, or to escape neutralizing antibodies¹⁵.

To decipher the origin of SARS-CoV-2, it is therefore essential to ascertain the diversity of animal coronaviruses, and more specifically, that of bat coronaviruses. Although the identification of SARS-CoV-2 in bats is a main goal, a more realistic objective is to identify the sequences that contribute to its mosaicism. The spike sequence seems essential, as it determines the binding affinity and accessibility of the receptor-binding domain (RBD) to the cellular ACE2 receptor and is therefore responsible for host range^{10,11,12}. The closest related bat strain identified so far (RaTG13) has a low RBD sequence similarity to SARS-CoV-2, and with only 11/17 hACE2 contact amino acid residues conserved with SARS-CoV-2, its affinity for hACE2 is very limited¹⁶. Moreover, SARS-CoV-2 poorly infects bats and bat cells

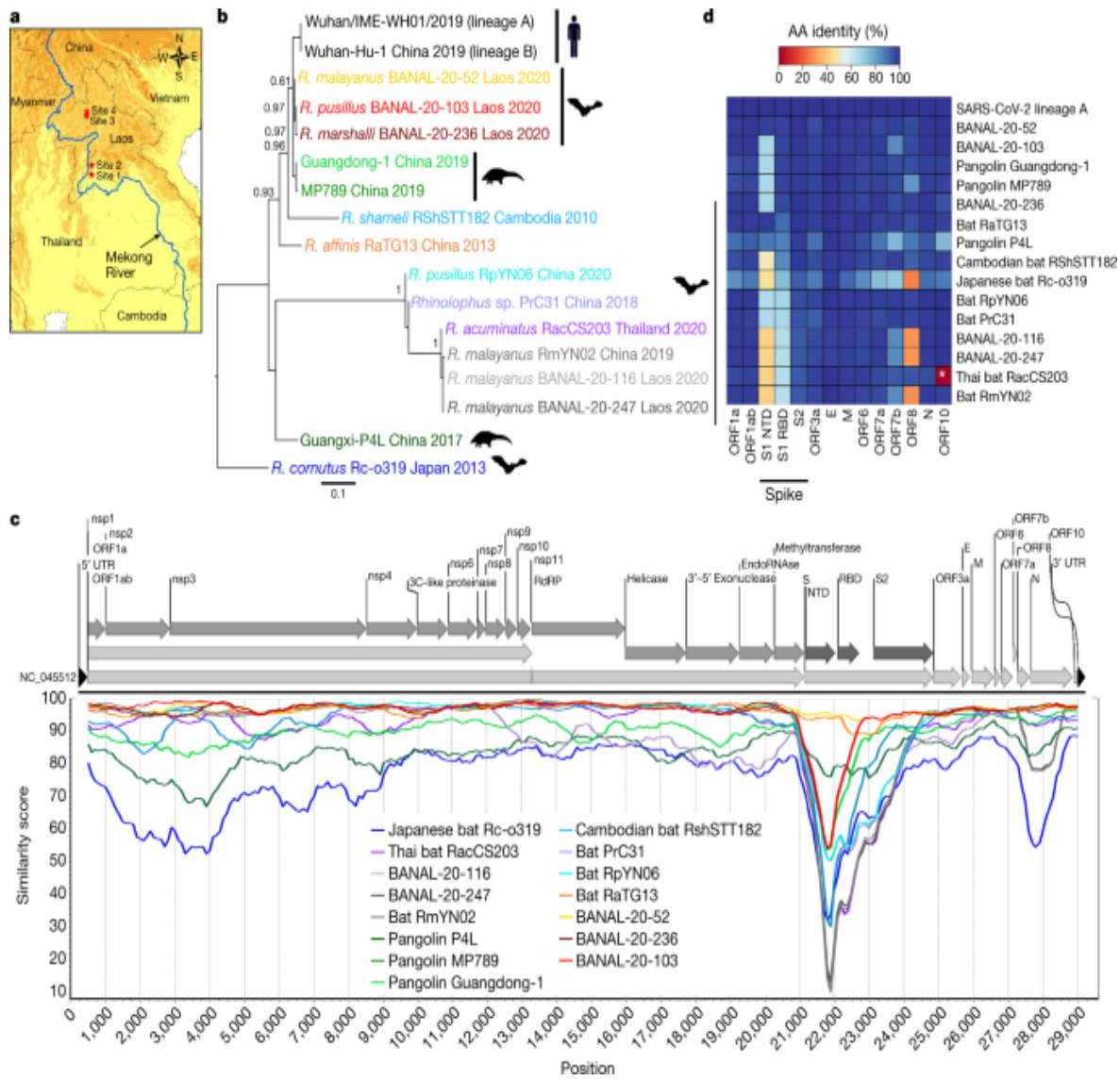
tested so far¹⁷. In addition, no bat SARS-CoV-2-like virus has been shown to use hACE2 to efficiently enter human cells, and none has the furin cleavage site that is associated with an increased pathogenicity in humans¹⁸. The SARS-CoV-2 RBD binds to *R. macrotis* ACE2 with a lower affinity than to hACE2 (ref. ¹⁹). An essential piece of information—finding bat viruses with an RBD motif genetically close to that of SARS-CoV-2 and capable of binding to hACE2 with high affinity—is therefore missing.

We speculated that this type of virus could be identified in bats living in the limestone karstic terrain common to China, Laos and Vietnam in the Indochinese peninsula. Here we report the presence of sarbecoviruses close to SARS-CoV-2 whose RBDs differ from that of SARS-CoV-2 by only one or two contact residues, strongly bind to the hACE2 protein and mediate hACE2-dependent entry and replication into human cells. Despite the absence of the furin cleavage site, these viruses may have contributed to the origin of SARS-CoV-2 and may intrinsically pose a future risk of direct transmission to humans.

Diversity of bat and coronavirus species

A total of 645 bats belonging to 6 families and 46 species were captured (Supplementary Table ¹). Two hundred and forty-seven blood samples, 608 saliva, 539 anal/faecal and 157 urine swabs were collected from bats in the northern part of Laos (Supplementary Table ²). We first screened all 539 faecal samples through a pan-coronavirus nested RT-PCR analysis²⁰. Overall, 24 individuals of 10 species were positive, and 1 individual (BANAL-27) was concomitantly infected by an alphacoronavirus and a betacoronavirus (Supplementary Table ³). BLAST analysis of amplicons identified alphacoronavirus sequences of the *Decacovirus*, *Pedacovirus* and *Rhinacovirus* subgenera and betacoronavirus sequences of the *Nobecovirus* and *Sarbecovirus* subgenera. Sequences of the *Sarbecovirus* subgenus were all identified from *Rhinolophus* individuals belonging to three different species (*R. malayanus*, *R. marshalli* and *R. pusillus*). Positive individuals were trapped in three different districts, and those infected with a sarbecovirus were all from the Fueng district in Vientiane province (Fig. ^{1a}, site 1).

Fig. 1: Genomic description of bat-borne sarbecoviruses identified in Laos.



a, Map of sampling sites. All BANAL isolates were collected from the same site (site 1). The map was downloaded from DIVA-GIS (<https://www.diva-gis.org/gdata>). **b**, Phylogenetic analysis of the protein sequence of the RBD of Laotian and representative human, bat, and pangolin sarbecoviruses. Sequences were aligned with MAFFT (ref. 49) in auto mode, and maximum-likelihood phylogenetic reconstruction was performed with PhyML implemented through the NGPhylogeny portal⁵⁰ with the LG + G substitution model. Branch support was evaluated with the aBayes parameter. Bat species are specified in the name of the sequences. Sequences are coloured according to Fig. 1c. **c**, Similarity plot analysis of Laotian and

representative bat and pangolin sarbecoviruses based on the full-length genome sequence of the SARS-CoV-2 human prototype strain ([NC_045512](#), Wuhan-Hu-1) used as a reference. The analysis was performed with the SimPlot program version 3.5.1 (ref. [51](#)) with the Kimura two-parameter model, a window size of 1,000 base pairs, a step size of 100 base pairs, a transition/transversion rate (T/t) of 2.0, and a Gap/Strip parameter: on⁵¹. nsp, non-structural protein; RdRP, RNA-dependent RNA polymerase. **d**, Heat map of identities at the protein level of representative human, bat and pangolin sarbecoviruses compared to human SARS-CoV-2 lineage B ([NC_045512](#)). Spike protein has been divided into functional domains, and the sequences are ordered according to percentage of identity of the RBD domain. The asterisk marks the absence of a functional ORF10 in Thai bat RacCS203 (accession number [MW251308](#)). The heat map was created using the gplots package in R (version 3.6.3). AA, amino acid.

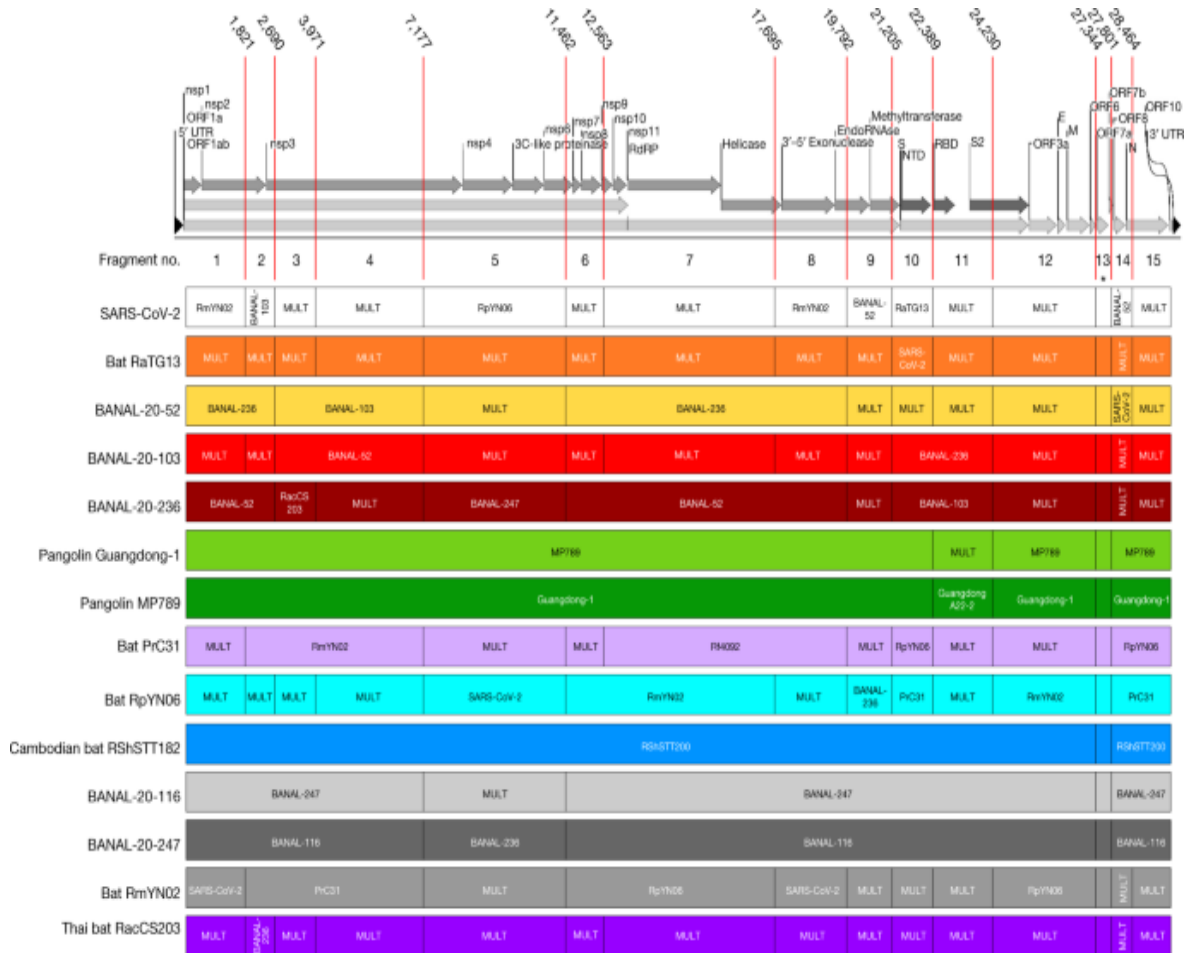
Next-generation sequencing (NGS) and Sanger sequencing were used to obtain a complete genomic sequence of five of the seven sarbecoviruses (Fig. [1](#) and Supplementary Table [4](#)). The coverage of the genome of the remaining two sarbecoviruses (BANAL-27 and BANAL-242 sampled from *R. pusillus* and *R. malayanus* bats, respectively) was 90%; therefore, they were not included in the final analyses. Phylogenetic analyses performed on the receptor-binding protein domain of lineages A and B human SARS-CoV-2 (ref. [21](#)), and on representative bat and pangolin sarbecoviruses, placed the Laotian *R. malayanus* BANAL-52, *R. pusillus* BANAL-103 and *R. marshalli* BANAL-236 coronaviruses close to human SARS-CoV-2 and pangolin coronaviruses collected in 2019, whereas *R. malayanus* BANAL-116 and BANAL-247 coronaviruses belonged to a sister clade with other bat coronaviruses (RmYN02, RacCS203, RpYN06 and PrC31) from different *Rhinolophus* species. Pangolin coronaviruses sampled in 2017 exhibited a basal position relative to these strains (Fig. [1b](#)). Very similar SARS-CoV-2-like viruses are shared by different bat species, suggesting possible circulation of viruses between different species living sympatrically in the same caves. These results are consistent with the similarity plot analysis showing that RaTG13 and BANAL-52 bat coronaviruses exhibit high nucleotide identity with SARS-CoV-2 throughout the length of the genome (96.8% for BANAL-52 and 96.1% for RaTG13). Notably, BANAL-52 has a higher level of nucleotide conservation than RaTG13 in the S1 domain of

the spike protein, and especially in the amino-terminal domain (NTD) and RBD of the spike protein (Fig. 1c). These observations are congruent with amino acid identities between human SARS-CoV-2 and representative bat and pangolin coronaviruses, which have a high level of conservation, except for the open reading frame 8 (ORF8) of bat BANAL-116, BANAL-247, Rc-0319 and RmYN02 (Supplementary Fig. 1). The S1 domain of the spike protein (and especially the NTD) has a lower degree of conservation in several bat coronaviruses, suggesting that this domain may reflect a relative degree of adaptation of the virus to its mammalian host (Fig. 1d and Extended Data Fig. 1).

Bat Sarbecovirus evolutionary history

Following analysis using a genetic algorithm for recombination detection (GARD), we identified 14 recombinant breakpoints during the evolutionary history of sarbecoviruses, which were further confirmed by phylogenetic analyses performed on the 15 fragments of sequences defined by the breakpoints (Fig. 2 and Supplementary Fig. 2). No specific signature was identified in the breakpoints (Supplementary Table 5). SARS-CoV-2 has a mosaic genome, to which more than five sequences close to sequences published or determined during this study contributed: *R. malayanus* RmYN02 and *R. pusillus* RpYN06 viruses found in China in 2019, *R. affinis* RaTG13 coronavirus found in China in 2013, and *R. malayanus* BANAL-52 and *R. pusillus* BANAL-103 found in northern Laos in 2020 (this study). No pangolin coronavirus sequence was immediately associated with a recombination event at the origin of SARS-CoV-2. Laotian *Rhinolophus* bat coronaviruses had a lower degree of recombination compared to SARS-CoV-2. Such recombination events occurred between other BANAL viruses isolated from bats living sympatrically in caves in the same area.

Fig. 2: Recombination events in the evolutionary history of sarbecoviruses.



Representation of the 15 recombinant fragments of relevant *Sarbecovirus* genomes compared to the SARS-CoV-2 human prototype strain ([NC_045512](#)). The coordinates of the breakpoints refer to the nucleotide position in the alignment. Where possible, the closest viral sequence is indicated for each fragment. In other cases, MULT indicates a group of multiple sequences. The asterisk marks unresolved fragment phylogeny (fragment 13, from positions 27,344 to 27,800 in the alignment). Sequences are coloured as in Fig. 1. The complete phylogenetic analyses are presented in Supplementary Fig. 2.

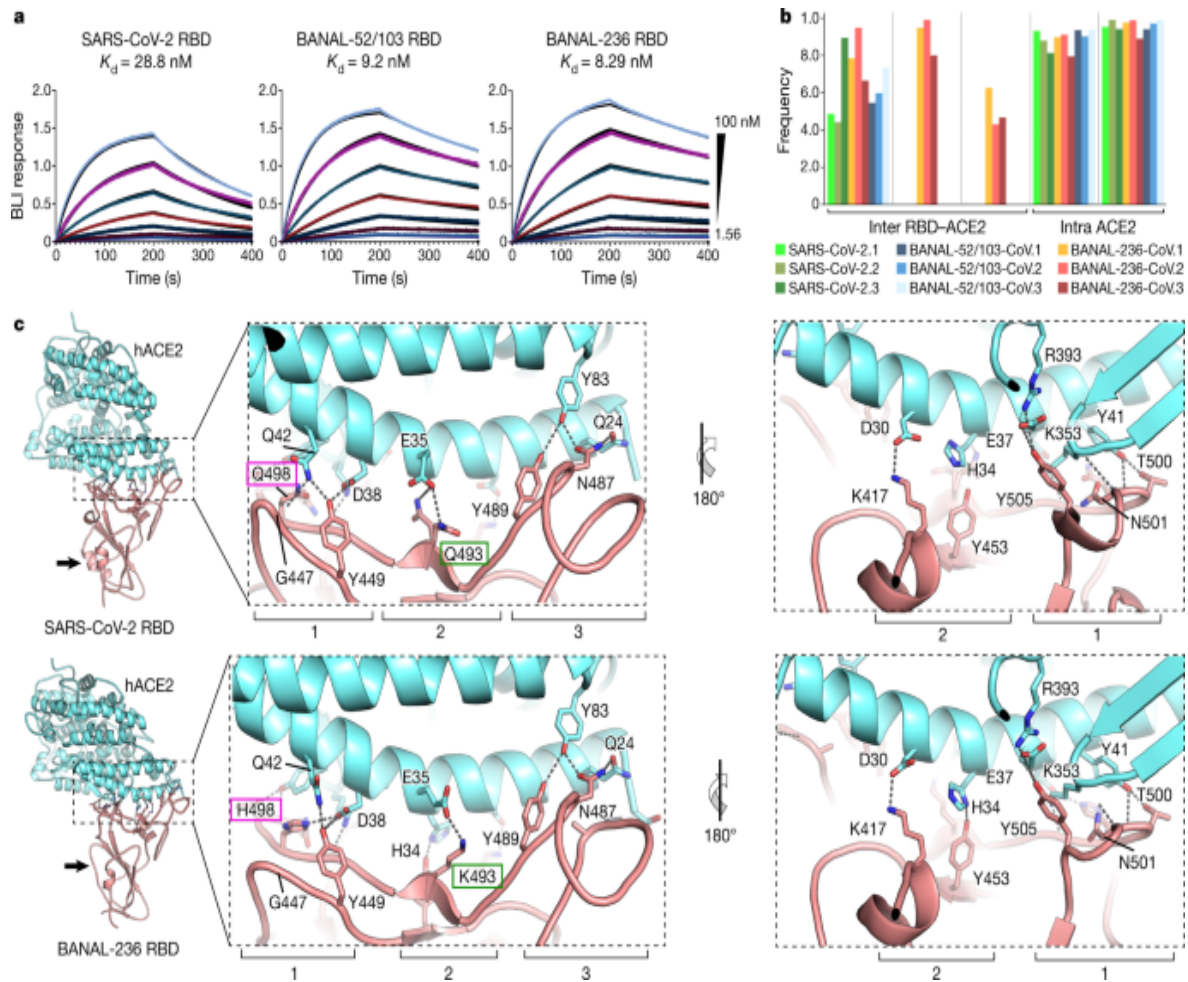
Notably, the origin of several fragments of SARS-CoV-2 genomes could be assigned to several donor strains and not a unique donor sequence. For example, a breakpoint was identified seven nucleotides upstream of the RBD region of S1: the downstream fragment of SARS-CoV-2, which comprises the RBD and the beginning of S2, could involve the *R. malayanus* BANAL-52, *R. pusillus* BANAL-103 and *R. marshalli* BANAL-236 viruses,

which formed a highly supported sister clade of SARS-CoV-2 (fragment 11, Supplementary Fig. 2). In a more basal position are *R. shamelii* bat coronaviruses and pangolin-2019 coronaviruses, consistent with the conservation of RBD amino acid sequences among SARS-CoV-2 and representative bat and pangolin coronaviruses (Extended Data Fig. 2). Among the 17 residues that interact with hACE2, 16 are conserved between SARS-CoV-2 and BANAL-52 or BANAL-103 (one mismatch, H498Q), and 15/17 are conserved for BANAL-236 (two mismatches, K493Q and H498Q) whereas only 13/17 residues are conserved for the Cambodian bat *R. shamelii* virus and 11/17 for the Chinese bat *R. affinis* RaTG13 virus. At the full spike protein level, bat *R. affinis* RaTG13 and pangolin-2017 P4L viruses seemed closer to SARS-CoV-2 than bat *R. malayanus* BANAL-52, but this effect is due to a higher degree of conservation in S2. All of these viruses shared the absence of a furin cleavage site and the conservation of the internal fusion peptide (Supplementary Figs. 1 and 3 and Extended Data Fig. 3).

Interaction of BANAL RBDs with ACE2

Biolayer interferometry experiments to measure the interaction between hACE2 and the RBDs of BANAL-52/103 (which have identical residues in the receptor-binding motif; Extended Data Fig. 2), BANAL-236 and SARS-CoV-2 (residues 233–524) resulted in a dissociation constant K_d three times lower for the BANAL RBDs compared to SARS-CoV-2 (Fig. 3a). This higher affinity can be attributed to the Q498H mismatch that has been reported to increase the affinity of the SARS-CoV-2 RBD for hACE2, and also to be involved in the host range expansion of SARS-CoV-2 and SARS-CoV-2-like viruses^{22,23,24,25,26,27,28,29}.

Fig. 3: Dynamics of the binding of hACE2 to bat-sarbecovirus-borne RBDs and insight into the structure of the complex.



a, Biolayer interferometry (BLI) binding analysis of the hACE2 peptidase domain to immobilized BANAL-52/103, BANAL-236 or SARS-CoV-2 RBDs. Black lines correspond to a global fit of the data using a 1:1 binding model. **b**, Frequency of formation of salt bridges close to the RBD–ACE2 interface (from left to right: D30/K417, E35/K493, D38/K493, K31/E35 and D38/K353) during the course of the MD simulations. The analysis was performed for nine different MD simulations (three replicates for each complex) of hACE2 in complex with RBDs from SARS-CoV-2 (SARS-CoV-2.1, SARS-CoV-2.2 and SARS-CoV-2.3, shades of green), BANAL-236 (BANAL 236-CoV.1, BANAL 236-CoV.2 and BANAL 236-CoV.3, shades of red) and BANAL-52/103 (BANAL 52/103-CoV.1, BANAL 52/103-CoV.2 and BANAL 52/103-CoV.3, shades of blue). **c**, Ribbon representations of the crystal structures of the hACE2 peptidase domain (cyan) in complex with SARS-CoV-2 (PDB [6M0J](#)) or BANAL-236 (this study, PDB [7PKI](#)) RBDs (pink). Black arrows in the overall structures

indicate the structural difference between the two complexes at the level of helix H4. The magnifications show the main interactions in the ACE2–RBD interfaces. Residues in the receptor-binding motif altered between SARS-CoV-2 and BANAL-236 are highlighted with coloured outlines. Numbers 1, 2 and 3 indicate the three main clusters of interactions between hACE2 and RBDs.

To study the effect of the alterations at the interface between these RBDs and hACE2, we performed molecular dynamics (MD) simulations of the complexes between the RBDs of SARS-CoV-2, BANAL-236 and BANAL-52/103 and hACE2 initiated from the crystal structure and homology models of these systems, respectively (Supplementary Table 6). Cluster analysis of the MD trajectories showed that, at the RBD–hACE2 interface, both BANAL complexes were identical to the complex between the SARS-CoV-2 RBD and hACE2 within 2 Å backbone root mean square deviation (RMSD; Extended Data Fig. 4), except for one of the BANAL-52/103 simulations that exhibited larger conformational variability of the RBD residues S443–Y449 ([Supplementary Methods](#) and Extended Data Fig. 5). Empirical scoring functions predicted a similar RBD–hACE2 binding energy in all three complexes (Extended Data Fig. 6).

The analysis of the persistence of hydrogen bonds and salt bridges provided further insights into the effect of the substitutions at the RBD–hACE2 interface (Fig. 3b and Extended Data Fig. 7). The H498Q mismatch present in both BANAL-52/103 and BANAL-236 RBDs disrupted the hydrogen bonds between RBD Q498 and both hACE2 K353 and Q42. However, these hydrogen bonds were only transiently formed in the SARS-CoV-2 complex: more persistent hydrogen bonds in this region (RBD T500 to hACE2 D355; RBD G502 to hACE2 K353; and RBD Y505 to hACE2 E37) were not affected. The K493Q mismatch enabled the formation of two salt bridges between RBD and hACE2 that were not present in the SARS-CoV-2 complex (RBD K493 to hACE2 E35 and RBD K493 to hACE2 D38).

For further insight into the molecular details of these interactions, we determined the crystal structure of the complex between the BANAL-236 RBD and the hACE2 peptidase domain to 2.9 Å resolution (Supplementary Table 7). The overall structure of this RBD is identical to that of SARS-CoV-2 (RMSD 0.360 Å, 150 Ca). The only significant difference is in the

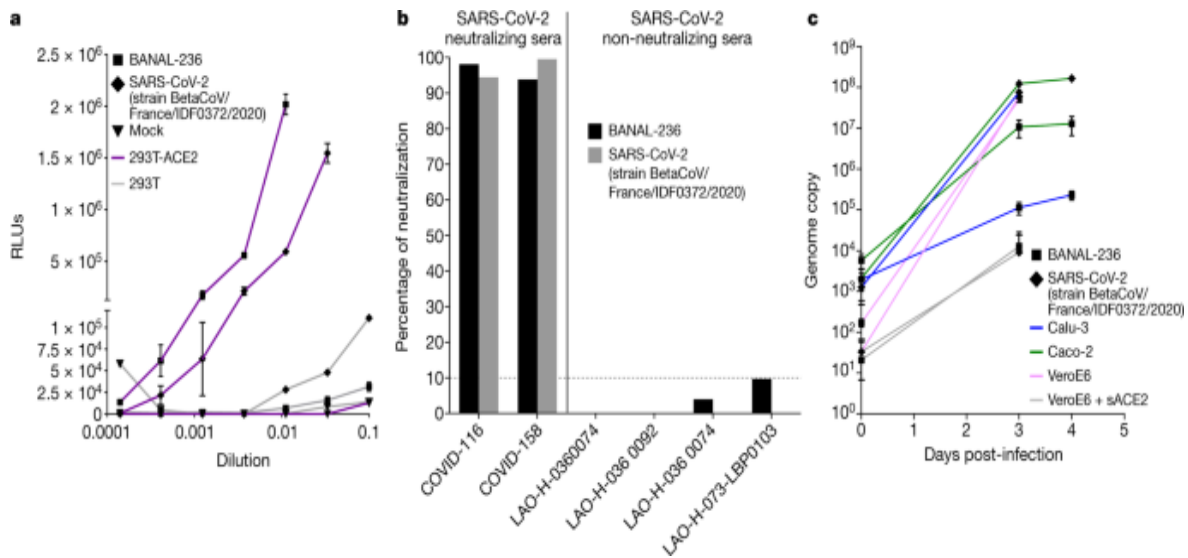
region between amino acids D363 and S375 (Fig. 3c, arrow). In this region, BANAL spikes have the A372T mismatch, which converts the sequence $^{370}\text{NSA}^{372}$ to $^{370}\text{NST}^{372}$, an *N*-linked glycosylation sequon. The crystals indeed showed clear electron density for the first *N*-acetylglucosamine residue of glycan attached to N370. The main chain at residue T372 makes a hydrogen bond with the glycan residue, altering the conformation of the main chain downstream, which results in partial unwinding of helix H4 in RBD 236. The calculation of a simulated annealing composite omit map for the segment D363–S375 confirms the correct assignment of the structure for this polypeptide segment and the *N*-glycosylation at residue N370 (Extended Data Fig. 8).

As expected, most of the interactions observed in the SARS-CoV-2 RBD–hACE2 complex³⁰ are also present in the structure of the complex between the BANAL-236 RBD and hACE2. In these interfaces, there are three main clusters of interactions as indicated in Fig. 3c (insets). The sequence mismatches are in clusters 2 (making the salt bridge between RBD K493 and hACE2 E35) and 3 (hydrogen bond between RBD H498 and D38). Although the interaction K493–E35 contributes to stabilizing the complex, it does not seem to markedly affect the binding to hACE2 because both BANAL RBDs have similar K_d values.

Virus replication in human cells

To assess whether the BANAL-236 spike protein could mediate entry into cells expressing hACE2, we generated lentiviral particles pseudotyped with spike from the SARS-CoV-2 strain first detected in Wuhan or BANAL-236 (Supplementary Fig. 4). We detected spike-mediated entry of the BANAL-236 spike-pseudotyped lentivirus into hACE2-expressing HEK-293T cells, but no such entry into control cells not expressing hACE2 (Fig. 4a). Entry was blocked by human sera neutralizing SARS-CoV-2, but not by control non-neutralizing sera, demonstrating that neutralization of BANAL-236 was specific for epitopes shared with the spike protein of SARS-CoV-2 (Fig. 4b).

Fig. 4: BANAL-236 entry and propagation in human cells.



a, Results of spike-pseudotyped BANAL-236 (squares) and SARS-CoV-2 (strain BetaCoV/France/IDF0372/2020, GISAID accession number EPI_ISL_406596, diamonds) pseudovirus entry assay in HEK-293T cells expressing (purple lines) or not (grey lines) the hACE2 receptor, shown in relative luminescence units (RLUs) produced by the firefly luciferase present in the lentiviral backbone and the Bright-Glo luciferase substrate. A single experiment performed in triplicate representative of two experiments is shown. Centre values represent the average of the three replicates and error bars indicate s.d. **b**, Results of spike-pseudotyped BANAL-236 (black) and SARS-CoV-2 (strain BetaCoV/France/IDF0372/2020, grey) neutralization assay expressed as a percentage of neutralization of luciferase activity in the absence of serum. Sera neutralizing SARS-CoV-2 were from patients with confirmed infections whereas non-neutralizing sera samples were collected before the spread of SARS-CoV-2 Laos. The dashed line marks the neutralization threshold. A single experiment representative of three independent experiments is shown. **c**, Human cell lines expressing endogenous ACE2, Calu-3 (blue lines) and Caco-2 (green lines), were infected at an MOI of 0.01 with the BANAL-236 virus (squares) and the virus first detected in Wuhan (diamonds). VeroE6 cells were infected at an MOI of 0.0001 with BANAL-236 virus (squares) and SARS-CoV-2 (strain BetaCoV/France/IDF0372/2020, diamonds) pre-incubated with (grey lines) or without (pink lines) soluble hACE2 (sACE2) at 25 μ g ml⁻¹ for 30 min. Genome copy number was determined by quantitative RT-PCR in the supernatants recovered 3 and 4 days post-infection. A single experiment

performed in triplicate is shown. Centre values represent the average of the three replicates and error bars indicate s.d.

Source data

To isolate infectious viruses, rectal swabs were inoculated on VeroE6 cells. No cytopathic effect (CPE) was observed 3 and 4 days after infection, but viral RNAs were detected for one of the two wells inoculated with the BANAL-236 sample (cycle threshold (Ct) = 25.1 at day 3, Ct = 21.7 at day 4). The culture supernatant (C1) formed plaques on VeroE6 and the titre was 3,800 pfu ml⁻¹. A C2 viral stock was prepared by amplification on VeroE6 at a multiplicity of infection (MOI) of 10⁻⁴. The culture supernatant was collected on day 4 when CPE was observed and titrated on VeroE6 (Extended Data Fig. 9). The plaques' phenotype was small, but the titre reached 2.6.10⁶ pfu ml⁻¹. The random NGS performed on the RNA extracted from this stock confirmed that the culture was pure and corresponded to the BANAL-236 virus, without any non-synonymous mutations between the original BANAL-236 genome and the C2 viral stock. Replication of BANAL-236 in VeroE6 was efficiently inhibited by soluble hACE2, thus showing that entry and propagation was largely ACE2 dependent (Fig. 4c and Extended Data Fig. 9). Furthermore, BANAL-236 replicated in human cell lines expressing endogenous levels of ACE2, Calu-3 and Caco-2 (Fig. 4c). The kinetics of RNA synthesis were slower compared to those for SARS-CoV-2. Infectious viral particles were produced at day 4 in the supernatant of Caco-2 and Calu-3 cells (respectively 10^{4.7} and 10^{2.9} pfu ml⁻¹).

Discussion

Many sarbecoviruses circulate in *Rhinolophus* colonies living in caves in China and probably also in neighbouring countries further south^{31,32,33}. During the course of a prospective study in northern Laos, we have identified, among other coronaviruses, five sarbecoviruses for which we obtained full-length sequences. Among these, three (BANAL-52, BANAL-103 and BANAL-236) were considered to be close to SARS-CoV-2 because of the similarity of one of the S1 domains (NTD or RBD) or S2 to that of SARS-CoV-2.

As genomic regions subject to recombination are probably contributing to host–virus interactions, we compared SARS-CoV-2 strains from the two lineages identified at the onset of the coronavirus disease 2019 (COVID-19) outbreak²¹ to these new bat sarbecoviruses and to pangolin strains in the SARS-CoV-2 clade. Strains close to *R. pusillus* RpYN06, *R. malayanus* RmYN02 and *Rhinolophus* sp. PrC31 isolated in China in 2018–2019, along with *R. malayanus* BANAL-52, *R. pusillus* BANAL-103 and *R. marshalli* BANAL-236 isolated in Laos in 2020, contributed to the appearance of SARS-CoV-2 in different regions of the genome. No closer viral genome has yet been identified as a possible contributor, and pangolin coronaviruses seem more distantly related than bat coronaviruses. We identified potential recombination sites, allowing for the reconstruction of the phylogenetic history of early isolated SARS-CoV-2 strains between homologous regions defined by recombination points. We identified a breakpoint at the beginning of the SARS-CoV-2 RBD, resulting in a downstream fragment key for the virus tropism and host spectrum composed of the RBD and the furin cleavage site, and ending in the N-terminal region of S2. Despite the absence of the furin site, phylogenetic reconstruction of this fragment showed that the Laotian *R. malayanus* BANAL-52, *R. pusillus* BANAL-103 and *R. marshalli* BANAL-236 coronaviruses are the closest ancestors of SARS-CoV-2 known so far. ORF8 was highly divergent between SARS-CoV-2 related genomes. The ORF8 genes from the strains BANAL-52, BANAL-103 and BANAL-236, like that of RaTG13, were closer to that of SARS-CoV-2 than to those of pangolin strains. *ORF8* encodes a protein that has been proposed to participate in immune evasion³⁴ and is deleted in many human SARS-CoV-2 strains that appeared after March 2020³⁵, which is reminiscent of the deletions identified during the 2003 severe acute respiratory syndrome epidemic³⁶. Therefore, the presence of ORF8 is consistent with bats acting as a natural reservoir of early strains of SARS-CoV-2.

Structural and functional biology studies have identified the RBD domain that mediates the interaction with hACE2 and host range, as well as the main amino acids that are involved^{30,37,38}. The RBDs (BANAL-52, BANAL-103 and BANAL-236) are closer to that of SARS-CoV-2 than that of any other bat strain described so far, including that of RaTG13, the virus identified in *R. affinis* from the Mojiang mineshaft where pneumonia cases with clinical

characteristics a posteriori interpreted as similar to COVID-19 (ref. ⁶) were recorded in 2012^{39,40}. Overall, one (H498Q (BANAL-103 and BANAL-52)) or two (K493Q and H498Q (BANAL-236)) amino acids interacting with hACE2 are substituted in these strains in comparison to SARS-CoV-2. These substitutions did not destabilize the interface between BANAL-236 and hACE2, as shown by the biolayer interferometry experiments (Fig. ^{3a}) and analysed by MD simulations.

Our results therefore support the hypothesis that SARS-CoV-2 could originally result from a recombination of sequences pre-existing in *Rhinolophus* bats living in the extensive limestone cave systems of Southeast Asia and South China^{41,42}. Many species forage in the same cave areas, including *R. malayanus* and *R. pusillus*⁴³. In addition, the distributions of *R. marshalli*, *R. malayanus* and *R. pusillus* overlap in the Indochinese subregion (Supplementary Fig. ⁵), which means that they may share caves as roost sites and foraging habitats⁴⁴. With the new viruses described here, understanding the emergence of SARS-CoV-2 does not require speculation of recombination or natural selection for increased RBD affinity for hACE2 in an intermediate host such as the pangolin before spillover⁴⁵, nor natural selection in humans following spillover⁴⁶. However, we found no furin cleavage site in any of these viruses on sequences determined directly from original faecal swab samples, which prevent from any risk of counterselection of the furin site by amplification in Vero cells¹⁸. The lack of the furin cleavage site may be explained by insufficient sampling in bats. On the basis of comparison of the sequences around the cleavage site between S1 and S2 (Extended Data Fig. ³), it has been suggested that the furin cleavage site in SARS-CoV-2 could originate from recombination events between SARS-CoV-2-related coronaviruses co-circulating in bats^{2,47}, meaning that BANAL-116, BANAL-247, bat RmYN02 (ref. ²) and bat RacCS203 (ref. ³) coronaviruses may share a common history with SARS-CoV-2. Alternatively, the furin cleavage site could have been acquired through passages of the virus in an alternative host or during an early poorly symptomatic unreported circulation in humans. Finally, the epidemiological link between these bat viruses and the first human cases remains to be established.

As expected from the high affinity for hACE2 of the S ectodomain of BANAL-236, pseudoviruses expressing it were able to efficiently enter human cells expressing endogenous hACE2 using an ACE2-dependent pathway. However, alternative routes of entry may still exist, especially in cells that do not express ACE2 (ref. [48](#)). Entry was blocked by a serum neutralizing SARS-CoV-2. The RaTG13 strain, the closest to SARS-CoV-2 known previously, had never been isolated. By contrast, preliminary studies show that BANAL-236 replicated in primate VeroE6 cells with a small plaque phenotype compared to that of SARS-CoV-2. Further analysis may indicate more clearly which steps shape infectivity.

To conclude, our results pinpoint the presence of new bat sarbecoviruses that seem to have the same potential for infecting humans as early strains of SARS-CoV-2. Guano collectors, certain ascetic religious communities who spend time in or very close to caves and tourists visiting caves are particularly at risk of being exposed. Further investigations are needed to assess whether such exposed populations have been infected, symptomatically or not, by one of these viruses, and whether infection could confer protection against subsequent SARS-CoV-2 infections. In this context, it is noteworthy that SARS-CoV-2 with the furin site deleted replicates in hamsters and in transgenic mice expressing hACE2, but leads to less severe disease and protects from rechallenge with wild-type SARS-CoV-2 (ref. [18](#)).

Methods

Ethical and legal statements

The bat study was approved by the wildlife authorities of the Department of Forest Resource Management (DFRM), and the Ministry of Agriculture and Forestry (MAF), Lao People's Democratic Republic, no. 2493/DFRM, issued on 21 May 2020 and no. 0755/MAF issued on 2 June 2020. All animals were captured, handled and sampled following previously published protocols and ASM guidelines [52,53](#). Exportation from Laos and importation in France were conducted according to national regulations. Human serum samples used for neutralization assays were already available [54](#) and selected on the basis of their status regarding seroneutralization of SARS-CoV-2.

They were collected following a protocol approved by the Lao National Ethics Committee for Health Research (NECHR; reference no. 052/2020).

Biosafety

Both the Institut Pasteur du Laos (IPL) and the Faculty of Environmental Science have extensive experience in safely collecting bats (appropriate biosafety training and personal protective equipment (PPE) for collectors). In this study, training before field work was organized once for field work participants. The aim was to teach participants the transmission risks of infectious agents from bats and how to identify, assess and mitigate these risks, as well to practice the use of PPE.

During field collection, sampling stations were selected to minimize potential exposure to infectious agents and stress on the animals during the handling time by selecting: an area easy to disinfect; an area out of view of the general public; a location that would not cause exposure of the general population (such as a picnic area); and procedures that reduce time and stress on bats caused by handling. For handling bats and bat samples, the following minimum PPE was required: eye protection, an N95 respirator, long clothing/coverall and latex gloves (2 pairs). All waste was disposed of in biohazard bags and was transported to a disposal site of IPL in Vientiane capital. Each sample box containing 81 cryovial tubes was placed inside an individual plastic ziplock and transported from the field to IPL on dry ice in a polystyrene foam box. At IPL, samples were stored in a specific -80 °C freezer until analysis.

For initial sample analysis at IPL, samples were transferred to a BSL-3 room for nucleic acid extraction. Initial coronavirus screening by nested RT-PCR was then performed under internal regulation on biosafety and security of IPL. Sample-extracted products (50 µl) were stored in NucleoSpin 8 sample boxes (8 × 12) and sent to IP-Paris packed in individual plastic ziplock bags on dry ice. Aliquots of anal swab samples were sent individually triple packaged on dry ice in a separate box.

All experiments on potentially infectious samples performed at Institut Pasteur (Paris) were conducted in BSL-3 laboratories according to procedures adapted for respiratory viruses.

Bat sampling areas and sample collection

Trapping sessions were conducted at four sites, in the Fueng and Meth districts, Vientiane province, and in the Namor and Xay districts, Oudomxay province, between July 2020 and January 2021 (Fig. 1a and Supplementary Tables 1 and 2). Bats were captured using four-bank harp traps⁵⁵ and mist nets set in forest patches between rice fields or orange/banana plantations and karst limestone formations, for 5–8 nights depending on accessibility. Harp traps were set across natural trails in patches of forest understorey. Mist nets were set across natural trails, at the edges of forests, at entrances of caves and in areas near cave entrances, as well as in open areas or those with high forest canopy. Bats were morphologically identified following morphological criteria^{55,56,57}. Other data such as forearm length (FA), sex, developmental stage (adult or juvenile) and reproductive condition (pregnant or lactating) were also recorded. Bats were sampled for saliva, faeces and/or urine, and blood before release at the capture site. Species identification of PCR-positive individuals was confirmed by sequencing the mitochondrial cytochrome oxidase 1 (ref. 20).

Initial coronavirus screening

Total RNA was extracted from faecal samples using the NucleoSpin 8 virus kit (Macherey Nagel). cDNA was synthesized using the Maxima H minus first strand cDNA synthesis kit (Thermo Scientific) and random hexamers following the manufacturer’s instructions. The presence of coronaviruses was tested by a nested RT-PCR approach using PCR master mix (Promega) and by targeting the RNA-dependent RNA Polymerase gene using combinations of degenerate and non-degenerate consensus primers as previously described²⁰. PCR products of the expected size were directly sequenced on both strands by Sanger sequencing using the nested PCR primers. The sequences obtained were confirmed by similarity analysis using the NCBI BLASTn search (<http://www.ncbi.nlm.nih.gov/BLAST>).

Primer design for *Betacoronavirus* enrichment before NGS

Betacoronavirus enrichment was performed at the genus level by adapting a previously described protocol⁵⁸ based on *k*-mers for targeted-sequence

enrichment before NGS. Briefly, 2,000 complete *Betacoronavirus* genomes were downloaded from the GenBank and GISAID databases and then clustered to a 95% sequence identity using CD-HIT-EST (ref. [59](#)). Overall, 185 representative sequences of all betacoronaviruses were used for further analysis. Owing to the high diversity in the genus *Betacoronavirus*, the full genomes belonging to the subgenera *Sarbecovirus*, *Nobecovirus*, *Merbecovirus* and *Embecovirus* were separately aligned using MAFFT multiple sequence alignment software and used to design 13-mer spiked primers for each cluster. The genomic position of the full set of primers was extracted from some representative subgenera sequences and close primers were removed. Finally, 416 spiked primers were synthesized by Eurofins Genomics.

Sample preparation for sequencing

Reverse transcription was performed using the mix of spiked primers and random hexamers at a 10:1 ratio using the SuperScript IV First-Strand Synthesis System (Invitrogen). After a denaturation step at 95 °C for 3 min in the presence of dNTPs (500 µM), DTT (5 mM) and RNaseOUT inhibitor, the reverse transcription reaction was incubated for 10 thermal cycles consisting of 6 steps at 8 °C for 12 s, 15 °C for 45 s, 20 °C for 45 s, 30 °C for 30 s, 35 °C for 2 min and 42 °C for 3 min, followed by a final incubation step at 42 °C for 20 min, as previously described^{[60](#)}. Double-stranded cDNA was generated using the Sequenase 2.0 DNA Polymerase kit (Applied Biosystems) in the presence of dNTPs and then purified using the Beckman Coulter Agencourt AMPure XP.

For samples with a low nucleic acid content, a random amplification step was performed using the MALBAC Single Cell WGA kit (Yikon Genomics, Promega). The amplified product was then purified using AMPure XP Beads, eluted in a final volume of 20 µl of low TE (10 mM Tris-HCl (pH 8,0), 0,1 mM EDTA), and quantified with the Qubit DNA HS Assay (Life Technologies, Thermo Fisher Scientific).

Libraries were generated using the NEBNext Ultra II DNA Library Prep kit (New England Biolabs) after a fragmentation step using the Covaris M220 Focused-ultrasonicator using microTUBE-15 (peak incident power = 18 W,

duty factor = 20%, cycles per burst = 50, treatment time = 60 s). The PCR-amplified libraries were cleaned up using 0.9× AMPure XP Beads and checked on the 2100 Bioanalyzer system with the High-Sensitivity DNA kit (Agilent Technologies) and quantified with the Qubit DNA HS Assay. Finally, the dual-multiplexed libraries were pooled (six samples per pool) and run on the Illumina NextSeq500 platform with High Output Kit version 2.5 (150 cycles).

Amplicon sequencing

In addition to enrichment-based sequencing, cDNA was amplified using the AmpliSeq for Illumina SARS-CoV-2 Research Panel (catalogue number 20020496), applying 26 amplification cycles in PCR1 and 9 cycles in PCR2. Primers at the end of the amplicons were partially digested during the library preparation, following the manufacturer's instructions. Libraries were barcoded individually using the Illumina UD dual indices and normalized with the AmpliSeq Library Equalizer for Illumina (catalogue number 20019171), and then pooled and sequenced on the Illumina NextSeq500 instrument using a Mid Output version 2.5 kit (SR 150 cycles). To eliminate residual PCR primer sequences, raw reads were trimmed by 15 bases at each end and special attention was paid to checking that internal sequences corresponding to primer regions in overlapping amplicons did not derive from primer sequences of the multiplex PCR. As an internal control, we verified that sequences of the complete genome of sample BANAL-236 obtained from the enrichment-based sequencing approach and from the AmpliSeq approach were identical.

Genome assembly and finishing

Raw reads from the enrichment-based sequencing were processed with an in-house bioinformatics pipeline (Microseek; Bigot T. et al., unpublished observations) comprising quality check and trimming, read normalization, de novo assembly, and ORF prediction of contigs and singletons, followed by three levels of taxonomic assignation⁶¹. Sequences identified as *Sarbecovirus* were then mapped onto appropriate reference sequences using CLC Genomics Workbench 20.0 (Qiagen). Trimmed reads from the amplicon sequencing were mapped to the SARS-CoV-2 genome first, and

then mapped again (refined mapping) to the closest genome relative. When needed, complete genomes were obtained by conventional PCR and Sanger sequencing. Briefly, viral RNA was reverse transcribed using SuperScript IV reverse transcriptase (Invitrogen) and cDNA was subsequently used to fill the gaps in the genomes using Phusion High Fidelity DNA polymerase (New England Biolabs) and specific primers flanking the missing regions. Positive PCR products were further purified and sequenced by Sanger sequencing at Eurofins Genomics.

Recombination and phylogenetic analyses

Identification of recombination events occurring during the evolutionary history of bat sarbecoviruses was performed using the IDPlot package⁶², a web-based workflow that includes multiple sequence alignment and phylogeny-based breakpoint prediction using the GARD algorithm from the HyPhy genetic analysis suite⁶³. First, a comprehensive analysis comprising 106 sequences and covering all non-human *Sarbecovirus* and *Sarbecovirus*-related complete genomes available in GenBank and GISAID databases was performed, including prototype strains of SARS-CoV-2 isolated in 2019. Special attention was paid to including bat-borne and pangolin-borne viral sequences to maximize the ability to capture a large diversity of the sarbecoviruses. Then, a reduced set of 36 sequences was chosen because of their phylogenetic proximity to SARS-CoV-2, and the GARD algorithm was run to identify recombination breakpoints in Laotian and representative human, bat and pangolin sarbecoviruses. Breakpoint coordinates were confirmed by performing phylogenetic analyses on the corresponding fragments using PhyML implemented through the NGPhylogeny portal⁵⁰. Branch support was evaluated with the aBayes parameter.

Generation of lentiviral pseudoviruses

The synthetic genes encoding spike in BANAL-236 and in SARS-CoV-2 (strain BetaCoV/France/IDF0372/2020, GISAID accession number EPI_ISL_406596) were cloned into the pVAX1 vector with a cytoplasmic tail truncation of 19 amino acids. Pseudotyped lentiviral particles were prepared using HEK-293T cells (ATCC CRL-3216) seeded in 10-cm dishes. HEK-293T cells were co-transfected with 5 µg of spike-encoding plasmid,

10 µg of lentiviral backbone plasmid expressing the firefly luciferase (pHAGE-CMV-Luc2-IRES-ZsGreen-W) and 3.3 µg of each lentiviral helper plasmid expressing HIV Gag-Pol (HDM-Hgpm2), Tat (HDM-tat1b) and Rev (pRC-CMV-Rev1b) using calcium phosphate precipitation⁶⁴. The medium was replaced 5 h post-transfection by 6 ml of DMEM without fetal calf serum (FCS) and phenol red. Pseudotyped particles were collected 48 h post-transfection, clarified by centrifugation at 2,500g for 5 min and frozen at -80 °C. Mock pseudotyped lentivirus was generated as above but in the absence of an S-expressing plasmid.

Spike-pseudotyped lentivirus entry assays

HEK-293T cells stably expressing hACE2 were transduced in suspension by mixing 50 µl of threefold serial dilutions of S-pseudotyped lentiviruses with 50 µl of cells at 4×10^5 cells per ml in 96-well white culture plates⁶⁵. At 60–72 h post-transduction, 100 µl of Bright-Glo luciferase substrate (Promega) was added to the wells and luminescence was measured using a Berthold Centro XS luminometer.

Neutralization assays

Sera neutralizing SARS-CoV-2 and non-neutralizing sera were described in ref. ⁵⁴. They were decomplemented at 56 °C for 30 min and 2.5 µl was incubated with 0.5 µl of S-pseudotyped lentiviruses in a final volume of 50 µl DMEM–10% FCS without phenol red in 96-well white culture plates. After 30 min at room temperature, 50 µl of hACE2-expressing HEK-293T cells in suspension at 4×10^5 cells per ml was mixed into the wells. Luminescence was measured at 60–72 h post-transduction as described above. Neutralization was calculated using the following formula: $1 - (\text{RLU in presence of serum}/(\text{mean of RLU in absence of serum determined in 12 wells} - 3 \times \text{s.d.}))$.

Virus isolation and multiplication

Rectal swabs were inoculated in duplicate in 24-well plates containing VeroE6 cells (ATCC CRL-1586) (1/5 dilution in 100 µl DMEM without FCS supplemented with 1% penicillin–streptomycin, 1% Fungizone and 1 µg

ml^{-1} TPCK-treated trypsin). After 1 h of adsorption at 37 °C, inoculum was removed and 1 ml of the medium described above was added. At 3 and 4 days after infection, CPE was monitored and 100 μl of supernatant was collected for RNA extraction. Quantitative RT-PCR targeting a conserved sequence in the E gene was performed as described previously⁶⁶. Culture supernatant (C1) was collected at day 4 and titrated by plaque assay on VeroE6 overlaid with 0.5% carboxymethylcellulose containing 1 $\mu\text{g ml}^{-1}$ TPCK-treated trypsin. A viral stock was prepared by amplification on VeroE6 cells at an MOI of 10^{-4} . Culture supernatant (C2) was collected at day 4 when a massive CPE was observed and titrated by plaque assay on VeroE6 as described above. A C3 viral stock was produced by a subsequent viral amplification at an MOI of 10^{-4} for 3 days on VeroE6. RNA was extracted from the viral stock and submitted to random NGS analysis using the SMARTer Stranded Total RNA-Seq Kit version 3 - Pico Input Mammalian (Takara Bio). Raw reads were processed with the Microseek pipeline, as described above.

For infection experiments, VeroE6 or the human cell lines Calu-3 (lung cells, ATCC HTB-55) and Caco-2 (intestinal cells, ATCC HTB-37) were infected in triplicate in 24-well plates with viral stocks of BANAL-236 (C3) or SARS-CoV-2 (strain BetaCoV/France/IDF0372/2020) at an MOI of 0.0001 and 0.01, respectively. Human soluble ACE2 was pre-incubated at 25 $\mu\text{g ml}^{-1}$ (ref. ⁶⁷) for 30 min with the viral inoculum before VeroE6 infection. Infections were carried out without TPCK in the medium described above for 3 and 4 days. Supernatants were recovered at 0, 3 and 4 days post-infection and genome copy number and viral titres were quantified as described above.

Protein expression and purification

BANAL-52/103, BANAL-236 and SARS-CoV-2 RBDs (residues 233–524, with carboxy-terminal 8×His-Strep and AVI tags) and hACE2 peptidase domain (residues 19–615, with C-terminal 8×His tag) were expressed in Expi293F cells at 37 °C and 8% CO₂ (GnTI- Expi293, ThermoFisher Scientific). Cell culture supernatants were collected 5 days post transfection and purified by affinity chromatography followed by size-exclusion

chromatography (SEC) using a 200 10/300 GL column pre-equilibrated in 20 mM Tris-HCl pH 8.0, 100 mM NaCl.

For crystallization experiments, the same constructs were expressed in Expi293F GnTI cells. The protein tags were cleaved overnight with thrombin and deglycosylated with EndoH. The RBD was mixed with a 1.3 molar excess of hACE2 and the complex was purified by SEC.

Biolayer interferometry

Purified Avi-tagged RBD was biotinylated using a BirA biotin–protein ligase kit according to the manufacturer’s instructions (Avidity). The biotinylated RBDs at 100 nM were immobilized to SA sensors. A 1:2 dilution series of hACE2 starting at 100 nM in PBS–BSA buffer was used in cycles of 200-s association followed by 200-s dissociation steps to determine protein–protein affinity. The data were baseline-subtracted and the plots were fitted using the Pall FortéBio/Sartorius analysis software (version 12.0). Data were plotted in Prism 9.1.0.

Crystallization and data collection

Crystals of the complex BANAL-236 RBD–hACE2 were obtained at 4 °C in sitting drops by mixing 200 nl of the protein complex at 8 mg ml⁻¹ with 200 nl of reservoir solution containing 0.2 M lithium sulfate, 0.1 M Tris 8.5, 30% w/v PEG 4000. The crystals were soaked in reservoir solution containing 20% glycerol as a cryoprotectant before being flash-frozen in liquid nitrogen. X-ray diffraction data were collected on the beamline PROXIMA 1 at the SOLEIL synchrotron (St Aubin, France) and reduced using the XDS package⁶⁸. The structure of the complex was determined by molecular replacement with Phaser software⁶⁹ using the coordinates of the SARS-CoV-2 RBD in complex with hACE2 as a search template (Protein Data Bank (PDB) [6M0J](#)). The model was manually corrected in COOT (ref. [70](#)) and refined with phenix.refine (ref. [71](#)). The final coordinates were deposited in the PDB with the accession code [7PKI](#).

MD simulations of RBD–hACE2 complexes

Generation of homology models

Homology models of the complexes between the RBDs of BANAL-236 and BANAL-52/103 and hACE2 were constructed using the X-ray structure of the complex between the SARS-CoV-2 RBD and hACE2 (PDB code [6M0J](#); resolution 2.45 Å) as a template using MODELLER version 10.1 (ref. [72](#)). These models included the fragments S19–D615 and T333–G526 of hACE2 and RBD, respectively, which were the regions resolved in the template. In these regions, BANAL-236 and BANAL-52/103 RBDs have a sequence identity to SARS-CoV-2 RBD equal to 96.9% and 97.4%, respectively. The alignment reported in Extended Data Fig. [3](#) was used. The zinc and chloride atoms in the template were retained during homology modelling; N-acetylglucosamine (NAG) and water residues were removed. Seven disulfide bonds were detected by MODELLER in the template (three in hACE2 and four in the RBD) and enforced in the generation of the homology models using CHARMM-like distance and dihedral angles restraints. For each construct, 100 homology models were built and ranked on the basis of the normalized DOPE score^{[73](#)}. The top three scoring models of each complex were used as starting points of three independent MD simulations, as described in the following section.

Set-up, equilibration and production of the MD simulations

The six homology models described in the previous section along with the X-ray structure of the SARS-CoV-2 RBD–hACE2 complex (PDB code [6M0J](#)) were used as input to the CHARMM-GUI server^{[74](#)}. In the case of the X-ray structure, for consistency with the homology models, the zinc and chloride atoms in [6M0J](#) were retained whereas the NAG and water residues were removed. The seven systems were solvated in a triclinic box of initial xyz dimensions of ~13.5 nm × 9.2 nm × 8.3 nm. Potassium and chloride ions were added to ensure charge neutrality at a salt concentration of 0.15 M. The total number of atoms was ~104,000. Further details of the systems are reported in Supplementary Table [4](#). The CHARMM36m force field^{[75](#)} was used for the protein and ions, and the TIP3P model^{[76](#)} was used for the water molecules. CHARMM36m force field parameters for the seven pairs of cysteines linked by disulfide bonds were used. The CHARMM-GUI models were first energy-minimized using the steepest descent algorithm. After

minimization, the systems were equilibrated using a 1-ns-long simulation in the NPT ensemble followed by a 1-ns-long simulation in the NVT ensemble. The temperature T was set at 300 K and the pressure P was set to 1 atm using the Bussi–Donadio–Parrinello thermostat⁷⁷ and the Berendsen barostat⁷⁸, respectively. During equilibration, harmonic restraints on the positions of the protein backbone and sidechain heavy atoms were applied. For each system studied, production simulations were performed in the NVT ensemble for 1 μ s. A time step of 2 fs was used together with LINCS constraints on hydrogen bonds⁷⁹. The van der Waals interactions were gradually switched off at 1.0 nm and cut off at 1.2 nm; the particle mesh Ewald method was used to calculate electrostatic interactions with a cutoff at 1.2 nm (ref. ⁸⁰). Production simulations were performed at room temperature for consistency with the bilayer interferometry experiments.

Details of the analysis

To evaluate the stability of the starting model during the production simulations, we calculated the backbone RMSD with respect to the energy-minimized structure for each frame of the trajectories. The RMSD was calculated separately for the residues in the RBD (Extended Data Fig. 4a), the hACE2 (Extended Data Fig. 4b), the RBD–hACE2 interface (Extended Data Fig. 4c) and the entire complex (Extended Data Fig. 4d). Interfacial residues were defined as the residues in one subunit closer than 0.8 nm to the residues in the other subunit in the X-ray structure of the complex between the SARS-CoV-2 RBD and hACE2. RMSD calculations were performed using the driver utility of PLUMED version 2.7 (ref. ⁸¹). To characterize conformational heterogeneity at the RBD–hACE2 interface, we performed a cluster analysis of the MD trajectories using as similarity metrics the backbone RMSD of the interfacial residues and the GROMOS clustering approach⁸² with a cutoff equal to 0.2 nm. The nine trajectories were first concatenated, clustering was then performed, and finally the population of each cluster was calculated separately for each trajectory (Extended Data Fig. 4e). To estimate the binding energy between RBD and hACE2, we used the InterfaceAnalyzer tool in ROSETTA version 3.11 (ref. ⁸³; Extended Data Fig. ^{6a}) and the AnalyseComplex tool in FoldX version 4 (ref. ⁸⁴; Extended Data Fig. ^{6b}). To identify relevant interactions at the RBD–hACE2 interface

that could contribute to the binding affinity of the complex, we quantified the frequency of formation of inter-subunit salt bridges (Fig. 3b) and hydrogen bonds (Extended Data Fig. 7) during the course of the MD simulations. For each frame of the trajectories, we used PLUMED to calculate the distances between the side-chain charged groups of aspartic acids (OD1/OD2), glutamic acids (OE1/OE2), lysines (NZ) and arginines (NH1/NH2). An inter-subunit salt bridge was then defined as formed if the distance between groups with opposite charge was lower than 0.32 nm. We confirmed this calculation using the Salt Bridges tool available in VMD (ref. 85). To monitor the formation of inter-subunit hydrogen bonds, we used the Hydrogen Bond Analysis module of the MDAnalysis library version 1.0.0 (ref. 86). A donor–acceptor distance and angular cutoff of 0.3 nm and 150° were used to define the formation of a hydrogen bond. We confirmed this calculation using the Hydrogen Bonds tool available in VMD.

Reporting summary

Further information on research design is available in the [Nature Research Reporting Summary](#) linked to this paper.

Data availability

Sequence data that support the findings of this study have been deposited in the GenBank and [GISAID](#) (<https://www.gisaid.org/>) databases with the following accession numbers: [MZ937000](#)/EPI_ISL_4302644 (BANAL-52), [MZ937001](#)/EPI_ISL_4302645 (BANAL-103), [MZ937002](#)/EPI_ISL_4302646 (BANAL-116), [MZ937003](#)/EPI_ISL_4302647 (BANAL-236) and [MZ937004](#)/EPI_ISL_4302648 (BANAL-247). Raw sarbecovirus NGS reads and Sanger sequencing .ab1 files have been deposited in the National Center for Biotechnology Information Sequence Read Archive repository under the BioProject code [PRJNA796968](#) (SAMN24959173–SAMN24959177). The crystal structure presented in this manuscript has been deposited in the PDB with the accession code [7PKI](#). The GROMACS topology and input files as well as the analysis scripts used are freely available on PLUMED-NEST (www.plumed-nest.org) under accession ID [plumID:21.037](#). [Source data](#) are provided with this paper.

Code availability

MODELLER version 10.1 (<https://salilab.org/modeller/>) and GROMACS version 2020.4 (<http://www.gromacs.org>) were used for MD simulations. XDS (version 5 February 2021), CCP4 (v 7.0), COOT (version 0.8.6) and PHENIX (version 1.19.2-4158) software programs were used for X-ray diffraction data processing, model building and refinement of the complex between the BANAL-236 RBD and hACE2. PyMOL (version 2.4.2) was used for structural image rendering. PLUMED version 2.7 (<https://www.plumed.org>), ROSETTA version 3.11 (<https://www.rosettacommons.org/>), FoldX version 4 (<http://foldxsuite.crg.eu/>), MDAnalysis version 1.0.0 (<https://www.mdanalysis.org/>), MDTraj version 1.9.5 (<https://www.mdtraj.org/1.9.5/index.html>) and in-house scripts available at <https://github.com/maxbonomi/bat-MD> were used for MD simulations.

hyphy 2.5.31, PhyML and MAFFT implemented through NGPphylogeny (<https://ngphylogeny.fr/>) and Simplot 3.5.1 were used for phylogenetic and recombination analyses. MSSPE 1 was used for *Betacoronavirus* primer enrichment design and is available at <https://github.com/chiulab/MSSPE-design>. MICROSEEK is an in-house pipeline that uses ALIENTRIMMER version 2.0 (<https://gitlab.pasteur.fr/GIPhy/AlienTrimmer>) for read trimming/clipping, BBNORM from BBMAP version 38.86 package (<https://sourceforge.net/projects/bbmap/>) for coverage normalization, MEGAHIT version 1.2.9 (<https://github.com/voutcn/megahit>) for assembly, an in-house ORF-finder (https://figshare.com/articles/code/translateReads_py/7588592), and then DIAMOND version 2.0.4 (<https://github.com/bbuchfink/diamond/>) and NCBI BLAST version 2.12.0+ (<ftp://ftp.ncbi.nlm.nih.gov/blast/executables/blast+/2.12.0/>) both for sequence searching.

References

1. Delaune, D. et al. A novel SARS-CoV-2 related coronavirus in bats from Cambodia. *Nat. Commun.* **12**, 6563 (2021).

2. Zhou, H. et al. Identification of novel bat coronaviruses sheds light on the evolutionary origins of SARS-CoV-2 and related viruses. *Cell* **184**, 4380–4391 (2021).
3. Wacharapluesadee, S. et al. Evidence for SARS-CoV-2 related coronaviruses circulating in bats and pangolins in Southeast Asia. *Nat. Commun.* **12**, 972 (2021).
4. Murakami, S. et al. Detection and characterization of bat sarbecovirus phylogenetically related to SARS-CoV-2, Japan. *Emerg. Infect. Dis.* **26**, 3025–3029 (2020).
5. Zhou, P. et al. A pneumonia outbreak associated with a new coronavirus of probable bat origin. *Nature* **579**, 270–273 (2020).
6. Rahalkar, M. C. & Bahulikar, R. A. Lethal pneumonia cases in Mojiang miners (2012) and the mineshaft could provide important clues to the origin of SARS-CoV-2. *Front. Public Health* <https://doi.org/10.3389/fpubh.2020.581569> (2020).
7. Liu, P. et al. Are pangolins the intermediate host of the 2019 novel coronavirus (SARS-CoV-2)? *PLoS Pathog.* **16**, e1008421 (2020).
8. Xiao, K. et al. Isolation of SARS-CoV-2-related coronavirus from Malayan pangolins. *Nature* **583**, 286–289 (2020).
9. Wahba, L. et al. An extensive meta-metagenomic search identifies SARS-CoV-2-homologous sequences in pangolin lung viromes. *mSphere* **5**, e00160-20 (2020).
10. Letko, M., Marzi, A. & Munster, V. Functional assessment of cell entry and receptor usage for SARS-CoV-2 and other lineage B betacoronaviruses. *Nat. Microbiol.* **5**, 562–569 (2020).
11. Shang, J. et al. Structural basis of receptor recognition by SARS-CoV-2. *Nature* **581**, 221–224 (2020).
12. Wang, Q. et al. Structural and functional basis of SARS-CoV-2 entry by using human ACE2. *Cell* **181**, 894–904 (2020).

13. Delaune, D. et al. A novel SARS-CoV-2 related coronavirus in bats from Cambodia. *Nat. Commun.* **12**, 6563 (2021).
14. Jackson, B. et al. Generation and transmission of interlineage recombinants in the SARS-CoV-2 pandemic. *Cell* **184**, 5179–5188 (2021).
15. Rochman, N. D. et al. Ongoing global and regional adaptive evolution of SARS-CoV-2. *Proc. Natl Acad. Sci. USA* **118**, e2104241118 (2021).
16. Liu, K. et al. Binding and molecular basis of the bat coronavirus RaTG13 virus to ACE2 in humans and other species. *Cell* **184**, 3438–3451 (2021).
17. Aicher, S.-M. et al. Species-specific molecular barriers to SARS-CoV-2 replication in bat cells. Preprint at *bioRxiv* <https://doi.org/10.1101/2021.05.31.446374> (2021).
18. Johnson, B. A. et al. Loss of furin cleavage site attenuates SARS-CoV-2 pathogenesis. *Nature* **591**, 293–299 (2021).
19. Liu, K. et al. Cross-species recognition of SARS-CoV-2 to bat ACE2. *Proc. Natl Acad. Sci. USA* **118**, e2020216118 (2020).
20. Chu, D. K. W. et al. Avian coronavirus in wild aquatic birds. *J. Virol.* **85**, 12815–12820 (2011).
21. Rambaut, A. et al. A dynamic nomenclature proposal for SARS-CoV-2 lineages to assist genomic epidemiology. *Nat. Microbiol.* **5**, 1403–1407 (2020).
22. Wrapp, D. et al. Cryo-EM structure of the 2019-nCoV spike in the prefusion conformation. *Science* **367**, 1260–1263 (2020).
23. Laffeber, C., de Koning, K., Kanaar, R. & Lebbink, J. H. G. Experimental evidence for enhanced receptor binding by rapidly spreading SARS-CoV-2 variants. *J. Mol. Biol.* **433**, 167058 (2021).

24. Lei, C. et al. Neutralization of SARS-CoV-2 spike pseudotyped virus by recombinant ACE2-Ig. *Nat. Commun.* **11**, 2070 (2020).
25. Walls, A. C. et al. Structure, function, and antigenicity of the SARS-CoV-2 spike glycoprotein. *Cell* **181**, 281–292 (2020).
26. Niu, S. et al. Molecular basis of cross-species ACE2 interactions with SARS-CoV-2-like viruses of pangolin origin. *EMBO J.* **40**, e107786 (2021).
27. Zhang, Y. et al. SARS-CoV-2 rapidly adapts in aged BALB/c mice and induces typical pneumonia. *J. Virol.* **95**, e02477–20 (2021).
28. Huang, K. et al. Q493K and Q498H substitutions in Spike promote adaptation of SARS-CoV-2 in mice. *EBioMedicine* **67**, 103381 (2021).
29. Zhang, S. et al. Bat and pangolin coronavirus spike glycoprotein structures provide insights into SARS-CoV-2 evolution. *Nat. Commun.* **12**, 1607 (2021).
30. Lan, J. et al. Structure of the SARS-CoV-2 spike receptor-binding domain bound to the ACE2 receptor. *Nature* **581**, 215–220 (2020).
31. Hu, B. et al. Discovery of a rich gene pool of bat SARS-related coronaviruses provides new insights into the origin of SARS coronavirus. *PLoS Pathog.* **13**, e1006698 (2017).
32. Ge, X.-Y. et al. Isolation and characterization of a bat SARS-like coronavirus that uses the ACE2 receptor. *Nature* **503**, 535–538 (2013).
33. Latinne, A. et al. Origin and cross-species transmission of bat coronaviruses in China. *Nat. Commun.* **11**, 4235 (2020).
34. Tan, Y., Schneider, T., Leong, M., Aravind, L. & Zhang, D. Novel immunoglobulin domain proteins provide insights into evolution and pathogenesis of SARS-CoV-2-related viruses. *mBio* <https://doi.org/10.1128/mBio.00760-20> (2020).

35. Su, Y. C. F. et al. Discovery and genomic characterization of a 382-nucleotide deletion in ORF7b and ORF8 during the early evolution of SARS-CoV-2. *mBio* **11**, e01610-20 (2020).
36. Chinese SARS Molecular Epidemiology Consortium. Molecular evolution of the SARS coronavirus during the course of the SARS epidemic in China. *Science* **303**, 1666–1669 (2004).
37. Conceicao, C. et al. The SARS-CoV-2 Spike protein has a broad tropism for mammalian ACE2 proteins. *PLoS Biol.* **18**, e3001016 (2020).
38. Damas, J. et al. Broad host range of SARS-CoV-2 predicted by comparative and structural analysis of ACE2 in vertebrates. *Proc. Natl Acad. Sci. USA* **117**, 22311–22322 (2020).
39. Cohen, J. Wuhan coronavirus hunter Shi Zhengli speaks out. *Science* **369**, 487–488 (2020).
40. Ge, X.-Y. et al. Coexistence of multiple coronaviruses in several bat colonies in an abandoned mineshaft. *Virol. Sin.* **31**, 31–40 (2016).
41. Clements, R., Sodhi, N. S., Schilthuizen, M. & Ng, P. K. L. Limestone karsts of Southeast Asia: imperiled arks of biodiversity. *BioScience* **56**, 733–742 (2006).
42. Hassanin, A., Tu, V. T., Curaudeau, M. & Csorba, G. Inferring the ecological niche of bat viruses closely related to SARS-CoV-2 using phylogeographic analyses of *Rhinolophus* species. *Sci. Rep.* **11**, 14276 (2021).
43. Soisook, P. et al. A taxonomic review of *Rhinolophus stheno* and *R. malayanus* (Chiroptera: Rhinolophidae) from continental Southeast Asia: an evaluation of echolocation call frequency in discriminating between cryptic species. *Acta Chiropt.* **10**, 221–242 (2008).
44. Francis, C. *Field Guide to the Mammals of South-east Asia* 2nd edn (Bloomsbury Wildlife, 2019).

45. Makarenkov, V., Mazoure, B., Rabusseau, G. & Legendre, P. Horizontal gene transfer and recombination analysis of SARS-CoV-2 genes helps discover its close relatives and shed light on its origin. *BMC Ecol. Evol.* **21**, 5 (2021).
46. Andersen, K. G., Rambaut, A., Lipkin, W. I., Holmes, E. C. & Garry, R. F. The proximal origin of SARS-CoV-2. *Nat. Med.* **26**, 450–452 (2020).
47. Lytras, S. The Sarbecovirus origin of SARS-CoV-2's furin cleavage site. Virological <https://virological.org/t/the-sarbecovirus-origin-of-sars-cov-2-s-furin-cleavage-site/536/6> (2021).
48. Puray-Chavez, M. et al. Systematic analysis of SARS-CoV-2 infection of an ACE2-negative human airway cell. *Cell Rep.* **36**, 109364 (2021).
49. Katoh, K., Rozewicki, J. & Yamada, K. D. MAFFT online service: multiple sequence alignment, interactive sequence choice and visualization. *Brief. Bioinform.* **20**, 1160–1166 (2019).
50. Lemoine, F. et al. NGPhylogeny.fr: new generation phylogenetic services for non-specialists. *Nucleic Acids Res.* **47**, W260–W265 (2019).
51. Lole, K. S. et al. Full-length human immunodeficiency virus type 1 genomes from subtype C-infected seroconverters in India, with evidence of intersubtype recombination. *J. Virol.* **73**, 152–160 (1999).
52. PREDICT One Health Consortium. *Protocol for Bat and Rodent Sampling Methods* (2013).
53. Sikes, R. S., Gannon, W. L. & the Animal Care and Use Committee of the American Society of Mammalogists. Guidelines of the American Society of Mammalogists for the use of wild mammals in research. *J. Mammal.* **92**, 235–253 (2011).
54. Virachith, S. et al. Low seroprevalence of COVID-19 in Lao PDR, late 2020. *Lancet Reg. Health West Pac.* **13**, 100197 (2021).

55. Francis, C. A comparison of mist nets and two designs of harp traps for capturing bats. *J. Mammal.* **70**, 865–870.
56. Corbet, G. B. & Hill, J. E. *Mammals of the Indomalayan Region: a Systematic Review* (Oxford Univ. Press & Natural History Museum, 1992).
57. Csorba, G., Ujhelyi, P. & Thomas, N. *Horseshoe Bats of the World (Chiroptera: rhinolophidae)* (Alana Books, 2003).
58. Deng, X. et al. Metagenomic sequencing with spiked primer enrichment for viral diagnostics and genomic surveillance. *Nat. Microbiol.* **5**, 443–454 (2020).
59. Fu, L., Niu, B., Zhu, Z., Wu, S. & Li, W. CD-HIT: accelerated for clustering the next-generation sequencing data. *Bioinformatics* **28**, 3150–3152 (2012).
60. Regnault, B. et al. Deep impact of random amplification and library construction methods on viral metagenomics results. *Viruses* **13**, 253 (2021).
61. Bratuleanu, B. E. et al. The virome of *Rhipicephalus*, *Dermacentor* and *Haemaphysalis* ticks from Eastern Romania includes novel viruses with potential relevance for public health. *Transbound. Emerg. Dis.* <https://doi.org/10.1111/tbed.14105> (2021).
62. Kosakovsky Pond, S. L., Posada, D., Gravenor, M. B., Woelk, C. H. & Frost, S. D. W. Automated phylogenetic detection of recombination using a genetic algorithm. *Mol. Biol. Evol.* **23**, 1891–1901 (2006).
63. Kosakovsky Pond, S. L., Posada, D., Gravenor, M. B., Woelk, C. H. & Frost, S. D. W. GARD: a genetic algorithm for recombination detection. *Bioinformatics* **22**, 3096–3098 (2006).
64. Crawford, K. H. D. et al. Protocol and reagents for pseudotyping lentiviral particles with SARS-CoV-2 spike protein for neutralization assays. *Viruses* **12**, E513 (2020).

65. Anna, F. et al. High seroprevalence but short-lived immune response to SARS-CoV-2 infection in Paris. *Eur. J. Immunol.* **51**, 180–190 (2021).
66. Corman, V. M. et al. Detection of 2019 novel coronavirus (2019-nCoV) by real-time RT-PCR. *Euro Surveill.* **25**, 2000045 (2020).
67. Monteil, V. et al. Inhibition of SARS-CoV-2 infections in engineered human tissues using clinical-grade soluble human ACE2. *Cell* **181**, 905–913 (2020).
68. Kabsch, W. XDS. *Acta Crystallogr. D* **66**, 125–132 (2010).
69. McCoy, A. J. et al. Phaser crystallographic software. *J. Appl. Crystallogr.* **40**, 658–674 (2007).
70. Emsley, P. & Cowtan, K. Coot: model-building tools for molecular graphics. *Acta Crystallogr. D* **60**, 2126–2132 (2004).
71. Liebschner, D. et al. Macromolecular structure determination using X-rays, neutrons and electrons: recent developments in Phenix. *Acta Crystallogr. D* **75**, 861–877 (2019).
72. Sali, A. & Blundell, T. L. Comparative protein modelling by satisfaction of spatial restraints. *J. Mol. Biol.* **234**, 779–815 (1993).
73. Shen, M.-Y. & Sali, A. Statistical potential for assessment and prediction of protein structures. *Protein Sci.* **15**, 2507–2524 (2006).
74. Jo, S., Kim, T., Iyer, V. G. & Im, W. CHARMM-GUI: a web-based graphical user interface for CHARMM. *J. Comput. Chem.* **29**, 1859–1865 (2008).
75. Huang, J. et al. CHARMM36m: an improved force field for folded and intrinsically disordered proteins. *Nat. Methods* **14**, 71–73 (2017).
76. Jorgensen, W. L., Chandrasekhar, J., Madura, J. D., Impey, R. W. & Klein, M. L. Comparison of simple potential functions for simulating liquid water. *J. Chem. Phys.* **79**, 926–935 (1983).

77. Bussi, G., Donadio, D. & Parrinello, M. Canonical sampling through velocity rescaling. *J. Chem. Phys.* **126**, 014101 (2007).
78. Berendsen, H. J. C., Postma, J. P. M., van Gunsteren, W. F., DiNola, A. & Haak, J. R. Molecular dynamics with coupling to an external bath. *J. Chem. Phys.* **81**, 3684–3690 (1984).
79. Hess, B., Bekker, H., Berendsen, H. J. C. & Fraaije, J. G. E. M. LINCS: a linear constraint solver for molecular simulations. *J. Comput. Chem.* **18**, 1463–1472 (1997).
80. Essmann, U. et al. A smooth particle mesh Ewald method. *J. Chem. Phys.* **103**, 8577–8593 (1995).
81. The PLUMED consortium. Promoting transparency and reproducibility in enhanced molecular simulations. *Nat. Methods* **16**, 670–673 (2019).
82. Daura, X. et al. Peptide folding: when simulation meets experiment. *Angew. Chem. Int. Ed.* **38**, 236–240 (1999).
83. Stranges, P. B. & Kuhlman, B. A comparison of successful and failed protein interface designs highlights the challenges of designing buried hydrogen bonds. *Protein Sci.* **22**, 74–82 (2013).
84. Schymkowitz, J. et al. The FoldX web server: an online force field. *Nucleic Acids Res.* **33**, W382–W388 (2005).
85. Humphrey, W., Dalke, A. & Schulten, K. VMD: visual molecular dynamics. *J. Mol. Graph.* **14**, 33–38 (1996).
86. Michaud-Agrawal, N., Denning, E. J., Woolf, T. B. & Beckstein, O. MDAnalysis: a toolkit for the analysis of molecular dynamics simulations. *J. Comput. Chem.* **32**, 2319–2327 (2011).

Acknowledgements

We thank S. Mohamed Ali, N. Da Rocha, A. Brisebarre, T. Xaybounou and S. Chonephetsarath for their help at the bench; A. Haouz and the staff of the

protein crystallogenesis facility at Institut Pasteur for help with crystallization trials; P. England from the Molecular Biophysics facility at Institut Pasteur for his support and access to the BLI equipment; P. Legrand from the PX1 beamline at Synchrotron SOLEIL for data collection support; and P. Guardado-Calvo for discussion and support with BLI experiments. NGS was performed with the help of the Biomics Platform, Center for Technological Resources and Research, Institut Pasteur, Paris, France, supported by France Génomique (ANR-10-INBS-09-09), Inclusive Blockchain Insurance using Space Assets and the Illumina COVID-19 Projects' offer. The work was granted access to the High Performance Computing resources of the Institute for Development and Resources in Intensive Scientific Computing under the allocation 2020-101592 made by Grand Équipement National de Calcul Intensif. We thank the Ministry of Health and the Ministry of Natural Resources and Environments, Lao People's Democratic Republic, for their authorization of the field work and the Faculty of Environmental Science for its authorization of the field research collaboration. The work was supported by an Institut Pasteur 'Covid Taskforce' and in part by the H2020 project 101003589 (RECOVER) and Labex IBEID (ANR-10-LABX62-IBEID) grants. Field and laboratory work at IPL was also supported by a UK embassy grant (grant no. INT 2021/LOV C19 02) and a Luxembourg Development special grant (grant no. LAO/030-202324).

Author information

Author notes

1. These authors contributed equally: Sarah Temmam, Khamsing Vongphayloth, Eduard Baquero, Sandie Munier, Massimiliano Bonomi

Affiliations

1. Institut Pasteur, Université de Paris, Pathogen Discovery Laboratory, Paris, France

Sarah Temmam, Béatrice Regnault, Delphine Chrétien, Philippe Pérot, Thomas Bigot & Marc Eloit

2. Institut Pasteur, Université de Paris, The OIE Collaborating Center for the Detection and Identification in Humans of Emerging Animal Pathogens, Paris, France

Sarah Temmam, Béatrice Regnault, Delphine Chrétien, Philippe Pérot & Marc Eloit

3. Institut Pasteur du Laos, Vientiane, Lao People's Democratic Republic

Khamsing Vongphayloth, Vincent Lacoste, Somphavanh Somlor, Khaithong Lakeomany, Nothasin Phommavanh & Paul T. Brey

4. Institut Pasteur, Université de Paris, CNRS UMR 3569, Structural Virology Unit, Paris, France

Eduard Baquero & Félix A. Rey

5. Institut Pasteur, Université de Paris, CNRS UMR 3569, Molecular Genetics of RNA Viruses Unit, Paris, France

Sandie Munier & Faustine Amara

6. Institut Pasteur, Université de Paris, CNRS UMR 3528, Structural Bioinformatics Unit, Paris, France

Massimiliano Bonomi, Yasaman Karami, Océane Dehan, Flora Donati, Michael Nilges & Sylvie van der Werf

7. Faculty of Environmental Sciences, National University of Laos, Vientiane, Lao People's Democratic Republic

Bounsavane Douangboubpha, Daosavanh Sanamxay, Vilakhan Xayaphet & Phetphoumin Paphaphanh

8. Institut Pasteur, Université de Paris, National Reference Center for Respiratory Viruses, Paris, France

Océane Dehan, Flora Donati & Sylvie van der Werf

9. Institut Pasteur, Université de Paris, Bioinformatic and Biostatistic Hub
- Computational Biology Department, Paris, France

Thomas Bigot

10. Ecole Nationale Vétérinaire d'Alfort, University of Paris-Est, Maisons-Alfort, France

Marc Eloit

Contributions

S.T., K.V., P.T.B. and M.E. conceived the study design. K.V., B.D., K.L., N.P., D.S., V.X. and P. Paphaphanh carried out sample procurement and bat species identification. S.M. and F.D. performed virus isolation, entry and neutralization assays. B.R., D.C. and P. Pérot prepared the NGS libraries and carried out the NGS. S.T., B.R. and T.B. carried out the genome assembly, recombination and phylogenetic analyses. V.L., S.S., K.L. and N.P. implemented the pan-coronavirus PCR testing. E.B.S. and F.A.R. performed and analysed the structure and binding studies. M.B., Y.K. and M.N. performed and analysed the MD simulations. M.E. and S.T. wrote the manuscript with input from all other authors.

Corresponding author

Correspondence to [Marc Eloit](#).

Ethics declarations

Competing interests

All authors of the manuscript are listed as inventors on US provisional patent number entitled 'New isolated bat SARS-COV able to infect human cells and harboring receptor-binding domains close to SARS-COV-2'. The patent covers medical applications (including diagnostics and vaccination) for the sequences described in the manuscript.

Peer review

Peer review information

Nature thanks Michael Worobey and the other, anonymous, reviewer(s) for their contribution to the peer review of this work. Peer reviewer reports are available.

Additional information

Publisher's note Springer Nature remains neutral with regard to jurisdictional claims in published maps and institutional affiliations.

Extended data figures and tables

[Extended Data Fig. 1 Spike identity matrices at the genus level of representative sarbecoviruses.](#)

Amino-acid (lower) and nucleotide (upper) identity matrices of Laotian and representative human, bat, and pangolin sarbecoviruses. Spike N-terminal (NTD), Receptor-binding (RBD) and S2 nucleotide and amino-acid sequences were aligned with MAFFT, and identity matrices were constructed using CLC Main Workbench 21.0.4 (Qiagen). Matrices were colored according to the identity scale, from 25% (red) to 100% (green) of nucleotide or amino-acid identity.

[Extended Data Fig. 2 Alignment of the spike RBD domain.](#)

Protein alignment of the Receptor Binding Domain (RBD) of Laotian and representative human, bat and pangolin sarbecoviruses. Sequences were aligned with MAFFT in G-iNS-I mode. Residues interacting with human ACE2 receptor are highlighted in grey. The domain used for interactions modeling, based on the X-ray structure 6M0J (residues T333 to G526), is highlighted by a black line.

Extended Data Fig. 3 Nucleotide and amino-acid alignments of the furin cleavage site region.

Complete nucleotide and amino-acid spike sequences of representative bat SARS-CoV-2-like coronaviruses were downloaded from GenBank and GISAID and aligned with MAFFT (G-INS-I parameter) (**A & C**).

Alignments were manually edited as proposed by Zhou² and Lytras⁴⁷ with CLC Main Workbench (Qiagen) (**B & D**). Alignments of the furin cleavage region are presented at the nucleotide (**A & B**) and the amino-acid (**C & D**) level, respectively.

Extended Data Fig. 4 Analysis of the stability and conformational heterogeneity of RBD–hACE2 complexes.

Time series (left column) and violin plots (right column) of backbone Root Mean Square Deviation (RMSD) from the initial, energy-minimized model calculated on the residues in RBD (**A**), hACE2 (**B**), at the interface of RBD and hACE2 (**C**), and on the entire complex (**D**). In the violin plots, the white circle corresponds to the median value, the black rectangle extends from the first to the third quantiles, and the thin black line represents the 95% confidence intervals. Population of the 3 most significant clusters visited during the course of the MD simulations (**E**). The analysis is performed for 9 different MD simulations: 3 replicates of the SARS-CoV-2 (shades of green), BANAL-236 (shades of red), and BANAL-52/103 (shades of blue) RBD–hACE2 complexes.

Extended Data Fig. 5 Additional analysis of the MD simulations of the BANAL-52/103 RBD–hACE2 complex.

Comparison of the time series of interface RMSD during the course of two MD simulations of the BANAL-52/103 RBD–hACE2 complex with short (BANAL-52/103-CoV.1) and long (BANAL-52/103-CoV.1*) equilibration phase. The large fluctuations of the interface RMSD are due to the flexibility of the RBD loop between residues S443 and Y449 (insets, in yellow). When these residues were not included in the calculation of the interface RMSD,

the time series displayed a more stable behavior (BANAL-52/103-CoV.1-L and BANAL-52/103-CoV.1*-L).

Extended Data Fig. 6 Estimation of RBD–hACE2 binding energy.

Time series (left column) and violin plots (right column) of the RBD–hACE2 binding energy estimated using ROSETTA (**A**) and FoldX (**B**). In the violin plots, the white circle corresponds to the median value, the black rectangle extends from the first to the third quantiles, and the thin black line represents the 95% confidence intervals. The analysis is performed for 9 different MD simulations: 3 replicates of the SARS-CoV-2 (shades of green), BANAL-236 (shades of red), and BANAL-52/103 (shades of blue) RBD–hACE2 complexes.

Extended Data Fig. 7 Analysis of the inter-subunits hydrogen bonds at the interface of RBD and hACE2.

Frequency of formation of hydrogen bonds at the interface of RBD and hACE2 in the knob (**A**), base (**B**), and tip regions (**C**). The analysis is performed for 9 different MD simulations: 3 replicates of the SARS-CoV-2 (shades of green), BANAL-236 (shades of red), and BANAL-52/103 (shades of blue) RBD–hACE2 complexes.

Extended Data Fig. 8 Stick representation.

Stick representation of segments D364-S375 of BANAL-236 (left panel) and SARS-CoV-2 (right panel) RBDs. A 2Fo–Fc composite omit map (contoured at 3σ) is shown for this region in BANAL-236 RBD.

Extended Data Fig. 9 Isolation of BANAL-236 on VeroE6 cells.

(**A**) CPE observed on VeroE6 4 days after inoculation at an MOI of 10-4 from the C1. (**B**) Uninfected VeroE6 cells layer. (**C**) Plaque assay performed from the C2 stock on VeroE6 cells. (**D**) Comparative CPE observed on VeroE6 cells infected with SARS-CoV-2 ('Wuhan', top panel) or BANAL-236 (bottom panel) in absence (left) or in presence (right) of soluble ACE2.

Photos were taken with a EVOS XL Core microscope at x10. A single experiment performed in triplicate is shown for each cell line.

Supplementary information

Supplementary Information

This file contains Supplementary Methods, Tables 1–8, Figs. 1–5 and References.

Reporting Summary

Peer Review File

Supplementary Data

This file contains the full wwPDB X-ray structure validation report.

Source data

Source Data Fig. 4

Rights and permissions

Reprints and Permissions

About this article

Cite this article

Temmam, S., Vongphayloth, K., Baquero, E. *et al.* Bat coronaviruses related to SARS-CoV-2 and infectious for human cells. *Nature* **604**, 330–336 (2022). <https://doi.org/10.1038/s41586-022-04532-4>

- Received: 03 September 2021

- Accepted: 08 February 2022
- Published: 16 February 2022
- Issue Date: 14 April 2022
- DOI: <https://doi.org/10.1038/s41586-022-04532-4>

Share this article

Anyone you share the following link with will be able to read this content:

[Get shareable link](#)

Sorry, a shareable link is not currently available for this article.

[Copy to clipboard](#)

Provided by the Springer Nature SharedIt content-sharing initiative

This article was downloaded by **calibre** from <https://www.nature.com/articles/s41586-022-04532-4>

| [Section menu](#) | [Main menu](#) |

[Download PDF](#)

- Article
- Open Access
- [Published: 06 April 2022](#)

Compartmentalized metabolism supports midgestation mammalian development

- [Ashley Solmonson](#)¹,
- [Brandon Faubert](#) ORCID: orcid.org/0000-0002-2886-886X^{1,2},
- [Wen Gu](#) ORCID: orcid.org/0000-0002-3003-8945¹,
- [Aparna Rao](#)¹,
- [Mitzy A. Cowdin](#) ORCID: orcid.org/0000-0003-0549-2473³,
- [Ivan Menendez-Montes](#) ORCID: orcid.org/0000-0001-5252-9502⁴,
- [Sherwin Kelekar](#)¹,
- [Thomas J. Rogers](#)¹,
- [Chunxiao Pan](#)¹,
- [Gerardo Guevara](#)¹,
- [Amy Tarangelo](#)¹,
- [Lauren G. Zacharias](#)¹,
- [Misty S. Martin-Sandoval](#)¹,
- [Duyen Do](#)¹,
- [Panayotis Pachnis](#)¹,
- [Dennis Dumesnil](#)¹,
- [Thomas P. Mathews](#)¹,
- [Alpaslan Tasdogan](#)^{1,5},
- [An Pham](#)⁶,
- [Ling Cai](#)^{1,7},
- [Zhiyu Zhao](#) ORCID: orcid.org/0000-0001-6308-6997¹,

- [Min Ni¹](#),
- [Ondine Cleaver³](#),
- [Hesham A. Sadek](#) [ORCID: orcid.org/0000-0002-4745-366X^{3,4}](#),
- [Sean J. Morrison](#) [ORCID: orcid.org/0000-0003-1587-8329^{1,8}](#) &
- [Ralph J. DeBerardinis](#) [ORCID: orcid.org/0000-0002-2705-7432^{1,6,8}](#)

[*Nature*](#) volume **604**, pages 349–353 (2022)

- 7788 Accesses
- 109 Altmetric
- [Metrics details](#)

Subjects

- [Developmental biology](#)
- [Metabolic diseases](#)

Abstract

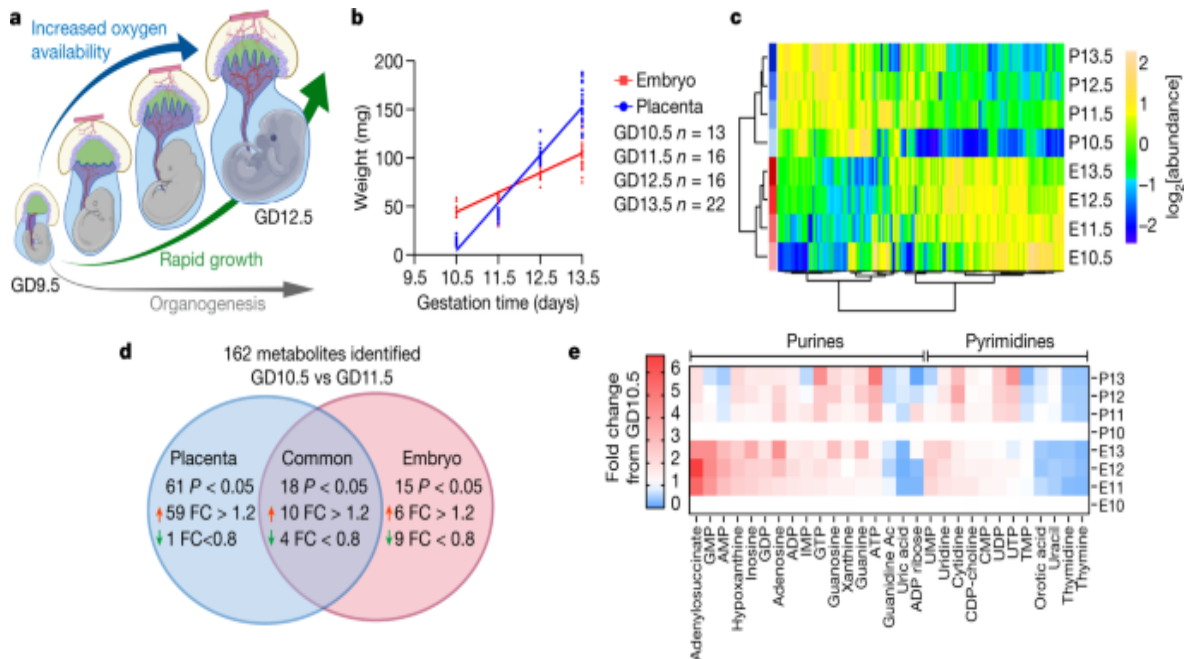
Mammalian embryogenesis requires rapid growth and proper metabolic regulation¹. Midgestation features increasing oxygen and nutrient availability concomitant with fetal organ development^{2,3}. Understanding how metabolism supports development requires approaches to observe metabolism directly in model organisms *in utero*. Here we used isotope tracing and metabolomics to identify evolving metabolic programmes in the placenta and embryo during midgestation in mice. These tissues differ metabolically throughout midgestation, but we pinpointed gestational days (GD) 10.5–11.5 as a transition period for both placenta and embryo. Isotope tracing revealed differences in carbohydrate metabolism between the tissues and rapid glucose-dependent purine synthesis, especially in the embryo. Glucose's contribution to the tricarboxylic acid (TCA) cycle rises throughout midgestation in the embryo but not in the placenta. By GD12.5, compartmentalized metabolic programmes are apparent within the embryo, including different nutrient contributions to the TCA cycle in different organs. To contextualize developmental anomalies associated with

Mendelian metabolic defects, we analysed mice deficient in LIPT1, the enzyme that activates 2-ketoacid dehydrogenases related to the TCA cycle^{4,5}. LIPT1 deficiency suppresses TCA cycle metabolism during the GD10.5–GD11.5 transition, perturbs brain, heart and erythrocyte development and leads to embryonic demise by GD11.5. These data document individualized metabolic programmes in developing organs in utero.

Main

Metabolism supports tissue development by supplying metabolic intermediates for energy production, anabolism, epigenetic regulation of gene expression and the formation of metabolic gradients that inform embryonic patterning^{6,7,8}. The post-implantation embryo and placenta initially develop in relative hypoxia⁹ (1–5% O₂). During this period, both the placenta and embryo require hypoxia-inducible gene-expression programmes, and disrupting these pathways or prolonging exposure to hypoxia results in improper cell differentiation and premature lethality^{10,11,12} around GD10. Midgestation is marked by an increased transfer of nutrients and oxygen from the maternal circulation as fetal erythropoiesis begins and the vasculature matures in the placenta and embryo. This period is characterized by accelerating growth of placenta and embryo, and morphogenesis in the heart, brain and liver^{2,13} (Fig. 1a), both of which suggest that midgestation is a metabolically dynamic period. Genetic and environmental alterations of metabolism result in developmental defects in humans^{14,15,16}, although the mechanism of many such anomalies is unknown. Most previous analyses of mouse embryonic metabolism has relied on ex vivo models or inferred metabolic requirements indirectly from the developmental consequences of genetic loss-of-function experiments¹. We set out to observe metabolism directly in the intact fetal–placental unit in vivo during midgestation to identify metabolic transitions and to test the effects of perturbing them.

Fig. 1: Metabolic transition at GD10.5–GD11.5.



a, Midgestation is a dynamic period of development. **b**, Tissue weights from pregnant dams, aged 13.6 ± 3.8 weeks. **c**, Group average heat map of metabolomics data. **d**, Metabolites with $P < 0.05$ and fold change (FC) > 1.2 or < 0.8 between GD10.5 and GD11.5. **e**, Heat map of purines and pyrimidines, plotted as fold change relative to GD10.5. Statistical tests: straight-line least-squares fitting followed by the extra sum-of-squares F -test (**b**); Student's t -tests (**d**). Data are mean \pm s.d. Statistical tests were two-sided. Guanidine Ac, guanidine acetate; IMP, inosine monophosphate (additional abbreviations, Supplementary Table 1).

[Source data](#)

Distinct metabolic transitions at GD10.5

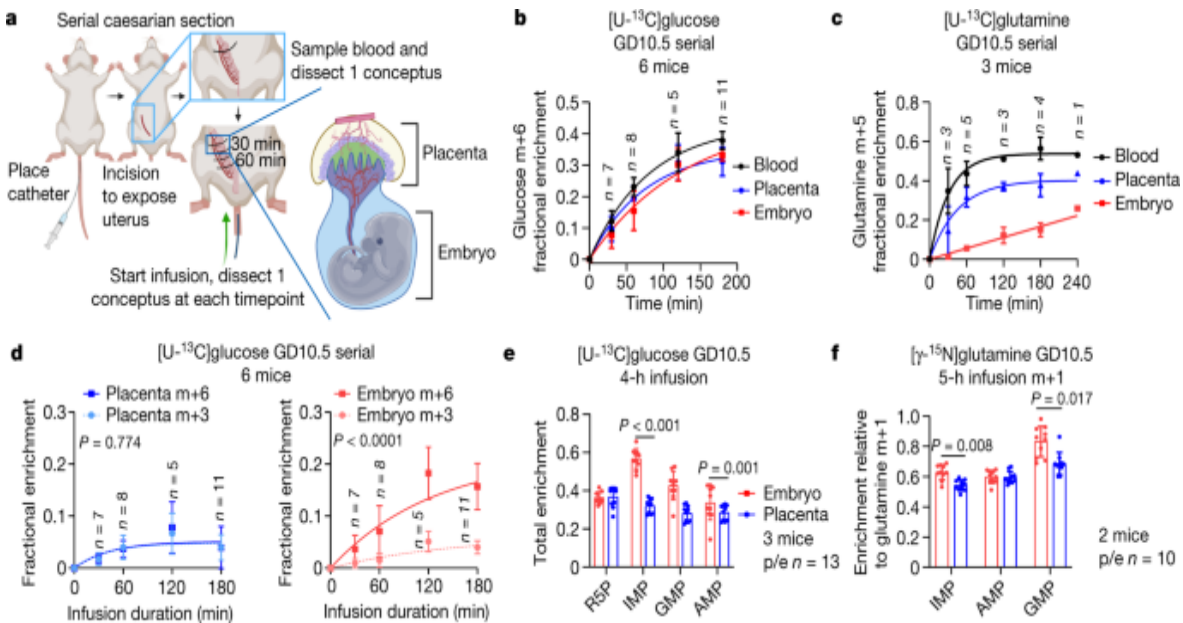
In mice, placentation begins² at GD3.5 and facile dissection of the placenta from the embryo is possible by GD9.5. To characterize metabolism during midgestation, we collected embryos and placentas from naively pregnant C57BL/6J dams from GD10.5 to GD13.5 and performed metabolomics. Tissue mass increased rapidly in both the placenta and embryo over this period (Fig. 1b). Placenta and embryo metabolomics differ throughout midgestation, as expected given their divergent cellular composition and functions (Fig. 1c, Extended Data Fig. 1). In both tissues, GD10.5 was

metabolically different from subsequent days, indicating transitions between GD10.5 and GD11.5 (Fig. 1c, Extended Data Fig. 1). These transitions were largely distinct between embryo and placenta, with most metabolites changing in one tissue but not the other (Fig. 1d, Extended Data Fig. 2a–d). Metabolic set overrepresentation analysis (MSOA) identified numerous pathways that change in the placenta between GD10.5 and GD11.5, particularly pathways related to nitrogen and amino acid metabolism (Extended Data Fig. 2d). Urea cycle-related metabolites increased abruptly but transiently in the placenta at GD11.5 (Extended Data Fig. 2e), possibly reflecting the role of arginine in stimulating placental–fetal blood flow¹⁷. In the embryo, MSOA between GD10.5 and GD11.5 identified purine and pyrimidine metabolism as two of the top-scoring pathways (Extended Data Fig. 2c). Most purines displayed a sustained increase after GD10.5 in the embryo, whereas pyrimidines showed little change or decreased in both tissues (Fig. 1e).

Rapid and localized metabolism in utero

To assess metabolite turnover in utero, we adapted previous methods¹⁸ to infuse uniformly labelled [¹³C]-glucose ([U-¹³C]glucose) into pregnant mice at GD10.5. Embryos and adjoined placentas were removed every 30 min while uterine blood flow was maintained so that nutrient transport and metabolism could be assessed kinetically (Fig. 2a). This analysis revealed rapid labelling in maternal blood, placenta and embryo, indicating efficient glucose transfer from maternal circulation to embryo, as expected (Fig. 2b). By contrast, embryonic glutamine was labelled slowly from [U-¹³C]glutamine in the maternal circulation (Fig. 2c), indicating distinct transport kinetics for different nutrients.

Fig. 2: Carbohydrate metabolism in midgestation.



a, Serial caesarian-section procedure. **b, c**, Time-dependent enrichment of $[U-^{13}C]glucose$ (**b**) and $[U-^{13}C]glutamine$ (**c**). **d**, Major glucose-6-phosphate isotopologues during serial caesarian-section infusion. **e**, Total enrichment (1 – unlabelled) of purines from $[U-^{13}C]glucose$. **f**, M+1 enrichment in purines from $[{\gamma}-^{15}N]glutamine$. ^{15}N -glutamine enrichments are normalized to glutamine m+1 to account for differences among compartments (see Fig. 2c). Statistical tests: plateau followed by one-phase decay least-squares fitting followed by the Holm–Sidak’s multiple-comparisons adjustment (**b–d**) (**b**: embryo vs placenta $P = 0.09$, embryo vs blood $P = 0.0001$, placenta vs blood $P = 0.003$; **c**: embryo vs placenta $P < 0.0001$, embryo vs blood $P < 0.0001$, placenta vs blood $P < 0.0001$); paired *t*-tests or Wilcoxon matched-pairs signed-rank tests followed by Holm–Sidak’s multiple-comparisons adjustment (**e**); log₂ paired *t*-tests followed by Holm–Sidak’s multiple-comparisons adjustment (**f**). Data are mean \pm s.d. Statistical tests were two-sided. p/e, placenta/embryo.

Source data

Rapid labelling of downstream metabolites indicates robust metabolism in the conceptus, and distinct labelling features in the embryo and placenta indicate metabolic differences between the tissues. Levels of ¹³C enrichment in glucose-derived metabolites reflect the combined contribution of labelled and unlabelled substrates through intersecting pathways (Extended Data Fig.

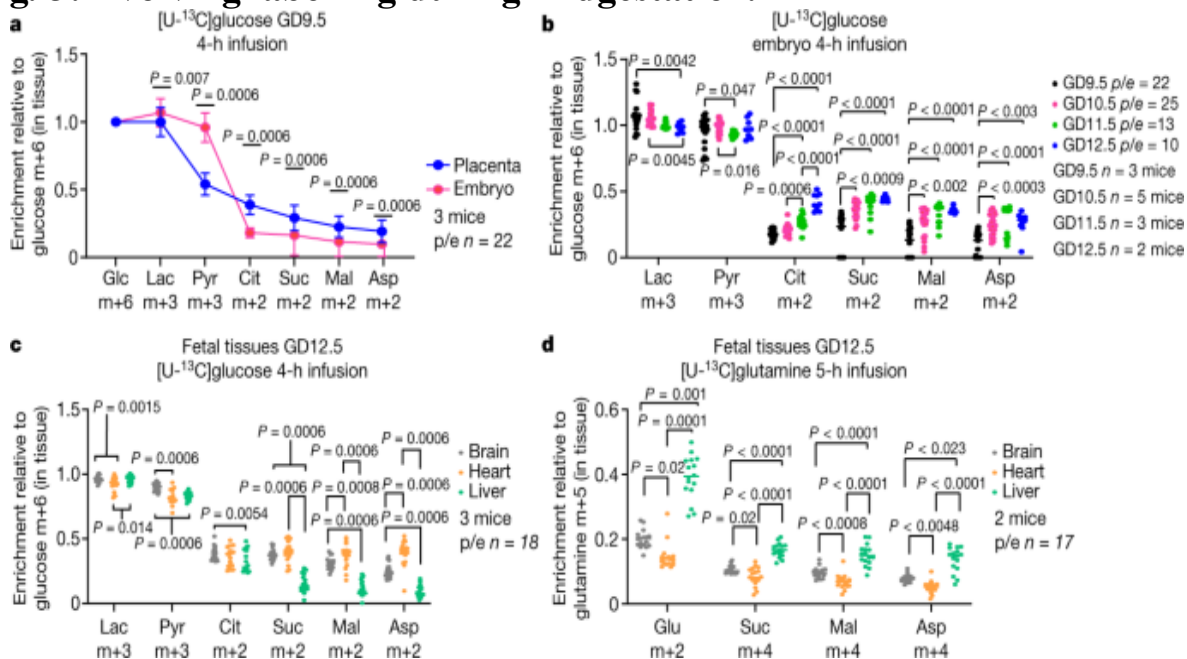
[3a](#)). Glucose-6-phosphate (G6P) appeared rapidly in the embryo as m+6, indicating conversion from maternal glucose (Fig. [2d](#)). However, placental G6P was labelled differently in the same mice. Overall G6P enrichment was lower than in the embryo, and G6P m+6 and m+3 appeared over similar time scales (Fig. [2d](#)). A complete understanding of carbohydrate metabolism will require compartment-specific enzyme knockouts, but the placental labelling pattern suggests contributions from glycogenolysis, gluconeogenesis and other pathways previously reported in mammalian placentas¹⁹ (Extended Data Fig. [3a](#)).

The pentose phosphate pathway intermediate and nucleotide precursor ribose-5-phosphate (R5P) also turned over rapidly. R5P was similar to G6P in that labelling was distributed across several isotopologues, and fully labelled R5P (m+5) was the predominant labelled form in the embryo but not the placenta (Extended Data Fig. [3b,c](#)). After 4 h, purines were extensively labelled in both placenta and embryo, but again labelling was higher in embryos (Fig. [2e](#), Extended Data Fig. [3d–f](#)). The total enrichment (that is, 1.0 – the unlabelled fraction, incorporating all ¹³C-labelled forms) was above 0.3 in all purines analysed, indicating that within 4 h, at least 30% of the embryo purine pools contained carbon originating in the maternal circulation (Fig. [2e](#)). Although much of the purine labelling appeared to arise from R5P, purine bases in the embryo also contained ¹³C; evidence for labelling in the bases included higher total labelling in purines than R5P (Fig. [2e](#)), and the presence of inosine monophosphate, GMP and AMP containing more than five ¹³C nuclei (Extended Data Fig. [3d–f](#)). In the context of the expanding purine pool (Fig. [1e](#)) and extensive labelling of serine and glycine (Extended Data Fig. [3g](#)), these data point to de novo purine synthesis in embryos. As an orthogonal labelling approach, we infused pregnant mice with [γ -¹⁵N]glutamine. The labelled nitrogen is incorporated into the purine ring during de novo synthesis. Again, higher relative enrichments were detected in inosine monophosphate and GMP in the embryos (Fig. [2f](#)). Pyrimidines were also labelled by both [U-¹³C]glucose and [γ -¹⁵N]glutamine, but with less consistent differences between embryo and placenta (Extended Data Fig. [3h,i](#)). Overall, the data indicate rapid metabolism during midgestation, including prominent utilization of maternal glucose and glutamine for embryonic purines, and distinct patterns of metabolic labelling between embryo and placenta.

Compartmentalized embryonic metabolism

Increases in vascularization, erythropoiesis and cardiac function^{2,20} predict enhanced oxidative metabolism in the embryo during midgestation. We performed [$U-^{13}C$]glucose infusions between GD9.5 and GD12.5, when oxygen levels increase⁹. On GD9.5, the placenta displayed higher labelling of tricarboxylic acid (TCA) cycle intermediates than the embryo (Fig. 3a). Labelling in the placental TCA cycle intermediates changed minimally over the next 3 days, but labelling in embryonic intermediates increased such that by GD12.5, labelling was similar or higher in the embryo than the placenta (Fig. 3b, Extended Data Fig. 4a, b). The citrate m+2/pyruvate m+3 ratio reports transfer of labelled two-carbon units from glucose to citrate via pyruvate dehydrogenase (PDH), whereas the citrate m+3/pyruvate m+3 ratio reports transfer of labelled three-carbon units via pyruvate carboxylase. In both tissues on all days, citrate m+2/pyruvate m+3 exceeds citrate m+3/pyruvate m+3, indicating that pyruvate enters the TCA cycle predominantly by PDH (Extended Data Fig. 4c, d). Both ratios increased between GD9.5 and GD12.5 in the embryos, but not in placenta, where labelling declined slightly. These data indicate that pyruvate oxidation is timed differently in the embryo and placenta, lagging in the embryo by a few days.

Fig. 3: Evolving labelling during midgestation.



a, Enrichments normalized to glucose m+6. **b**, Labelling from [U-¹³C]glucose between GD9.5 and GD12.5. **c, d**, Organ-specific enrichments at GD12.5. Statistical tests: paired *t*-tests followed by Holm–Sidak’s multiple-comparisons adjustment (**a**); Kruskal-Wallis test followed by Dunn’s multiple-comparisons adjustment or one-way ANOVA followed by Tukey’s multiple-comparisons adjustment (**b**); linear mixed-effects analysis followed by Holm-Sidak’s multiple-comparisons adjustment (**c**, between-tissue comparisons); or Welch’s one-way ANOVA followed by the Dunnett’s T3 multiple-comparisons adjustment or Kruskal–Wallis test followed by the Dunn’s multiple comparisons adjustment (**d**). Data are mean ± s.d. Statistical tests were two-sided. Asp, aspartate; Cit, citrate; Glc, glucose; Lac, lactate; Mal, malate; Pyr, pyruvate; Suc, succinate.

Source data

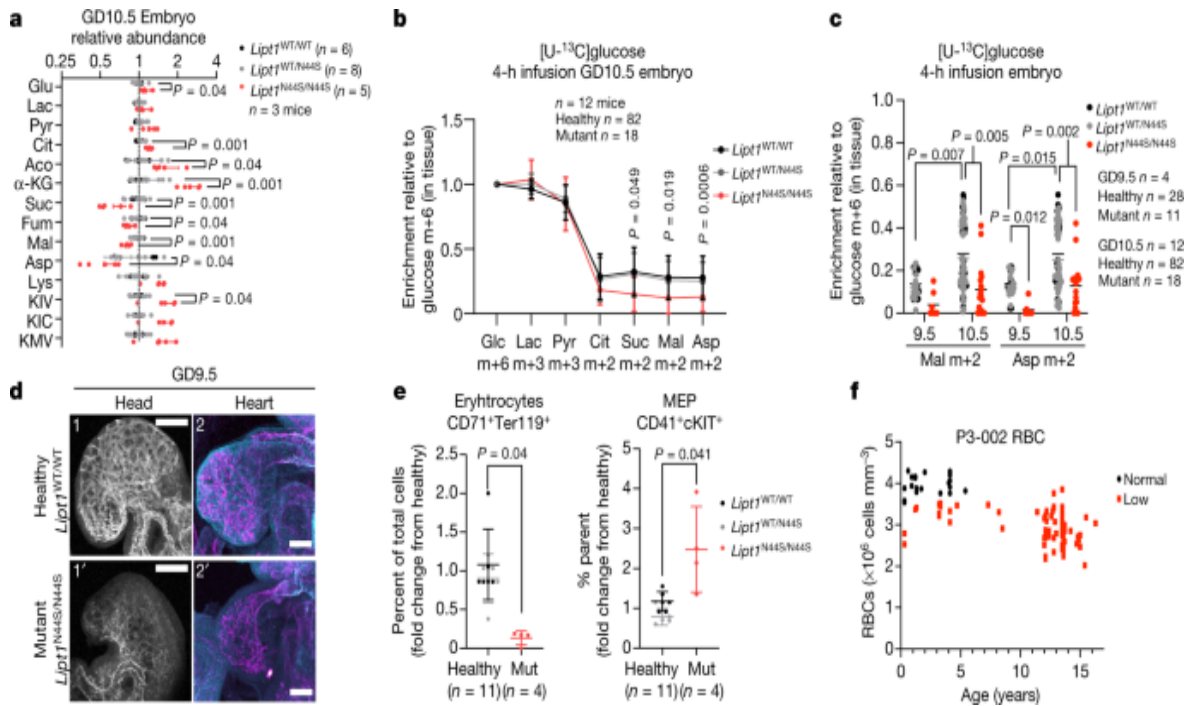
The increased contribution of glucose to the TCA cycle in the embryo may reflect the development of oxidative organs such as the liver, heart and brain. To assess gene-expression signatures relevant to mitochondrial function, we analysed polyA plus RNAseq data from the ENCODE portal²¹ from each of these organs across GD10.5–GD13.5. This revealed increased electron transport chain (ETC)-related transcript abundance over this period, particularly in the heart (Extended Data Fig. [4e](#)). By contrast, most ETC-related transcripts declined in placenta over midgestation (Extended Data Fig. [4g](#)). We then performed [U-¹³C]glucose infusions and analysed labelling in the brain, heart and liver. On GD12.5, TCA cycle intermediates displayed uniformly high labelling in the brain and heart, with less labelling in the liver (Fig. [3c](#)). The ratio of citrate to pyruvate labelling in the heart increased during midgestation, corresponding to enhanced expression of ETC subunits (Extended Data Fig. [4e,f](#)); this is notable because heart development requires increased oxygenation and reduced HIF1α expression^{2,22,23}. We also infused [U-¹³C]glutamine to assess metabolism of an alternative fuel. In contrast to [U-¹³C]glucose, infusion with [U-¹³C]glutamine resulted in higher labelling in metabolites from the GD12.5 liver compared with brain or heart (Fig. [3d](#)). Kinetic experiments revealed consistent glutamine labelling in each organ, but higher labelling in glutamate in the liver throughout the time course (Extended Data Fig. [4h](#)).

These data indicate distinct patterns of fuel metabolism in developing embryonic organs.

LIPT1 enables developmental metabolism

To test the importance of enhanced oxidative metabolism during midgestation, we examined the impact of lipoyltransferase-1 (LIPT1) deficiency in utero. LIPT1 transfers the essential lipoic acid cofactor onto mitochondrial 2-ketoacid dehydrogenases related to the TCA cycle, including PDH, α -ketoglutarate dehydrogenase (AKGDH), branched-chain ketoacid dehydrogenase (BCKDH) and 2-oxoadipate dehydrogenase^{4,5}. We reported a patient with compound heterozygosity for pathogenic LIPT1 variants (N44S and S292X) and a phenotype of neurodevelopmental disability and seizures⁵. Mice homozygous for the N44S variant are detected at close to the expected Mendelian ratio at GD10.5 but absent by GD11.5, indicating embryonic lethality occurs between these days⁵. *Lipt1*^{WT/N44S} mice are healthy, born at the expected frequency⁵ and have similar metabolomic signatures to *Lipt1*^{WT/WT} embryos at GD10.5 (Fig. 4a, Extended Data Fig. 5a), so we grouped *Lipt1*^{WT/WT} and *Lipt1*^{WT/N44S} together as ‘healthy’ in statistical analyses. *Lipt1*^{N44S/N44S} conceptuses are viable but small on GD10.5 (Extended Data Fig. 5b). On GD10.5, *Lipt1*^{N44S/N44S} conceptuses had metabolomic patterns consistent with deficiencies in lipoylation and the TCA cycle. A defect in AKGDH was apparent from accumulation of α -ketoglutarate in the placenta and embryo; depletion of products downstream of AKGDH also occurred in the embryos (Fig. 4a, Extended Data Fig. 5c). Other abnormalities related to 2-ketoacid dehydrogenase dysfunction included accumulation of lysine and branched-chain ketoacids, particularly in the embryos (Fig. 4a Extended Data Fig. 5c).

Fig. 4: *Lipt1* deficiency impairs embryo metabolism, growth and erythropoiesis.



a, Relevant metabolites in embryos of the indicated genotypes. **b, c**, Labelling from [^{13}C]glucose. **d**, Endothelial cells in the head stained for PECAM1 and endomucin (1 and 1'; scale bar, 200 μm), and endothelial cells in the heart stained for PECAM1 and endomucin (magenta) and connexin 40 (cyan) (2 and 2'; scale bar, 100 μm). Images are representative of $n = 3$ dams, and the following numbers of embryos: *Lipt1*^{WT/WT} ($n = 5$), *Lipt1*^{WT/N44S} ($n = 4$), *Lipt1*^{N44S/N44S} ($n = 8$). **e**, Quantification of cells from dissociated GD10.5 whole embryos stained with antibodies against CD71, TER119, CD41 and c-Kit. Erythrocytes express CD71 and TER119, and myeloid-erythroid progenitors (MEP) express CD41 and c-Kit. '% parent' indicates the proportion of CD71⁺TER119⁺ cells that stained CD41⁺c-Kit⁺. **f**, Longitudinal red blood cell (RBC) measurements in a LIPT1-deficient patient. Statistical tests: Student's *t*-tests (**a**); log₂-transformation followed by Holm-Sidak's multiple-comparisons adjustment (**b**); Mann-Whitney tests followed by Holm-Sidak's multiple-comparisons adjustment (**e**); Kruskal-Wallis tests followed by the Dunn's multiple-comparisons adjustment (**c**). Data are \pm s.d. Statistical tests were two-sided. α-KG, α-ketoglutarate; Aco, aconitase; Fum, fumarate; Lys, lysine; KIV, a-ketoisovalerate; KIC, α-ketoisocaproate; KMV, α-keto-β-methylvalerate.

[Source data](#)

We next performed infusions in pregnant dams at GD9.5 and GD10.5, first evaluating the capacity of *Lipt1*^{N44S/N44S} placentas to take up and transfer nutrients to the embryo. *Lipt1*^{N44S/N44S} placentas had no defects in taking up [$\text{U-}^{13}\text{C}$]glucose or [$\text{U-}^{13}\text{C}$]glutamine from the maternal circulation or transferring the label to the embryos (Extended Data Fig. 5d, e). Placental differentiation markers were largely conserved between healthy and *Lipt1*^{N44S/N44S} placentas (Extended Data Fig. 5f). From this, we conclude that although LIPT1 deficiency alters placental metabolism, placental dysfunction is not the primary cause of lethality in the *Lipt1*^{N44S/N44S} embryos.

We also investigated the effects of LIPT1 deficiency on TCA cycle labelling at GD9.5 and GD10.5 (Fig. 4b, c, Extended Data Fig. 5g), just before the point of demise. *Lipt1*^{N44S/N44S} embryos were metabolically active and indistinguishable from healthy embryos in pyruvate or lactate labelling from ^{13}C -glucose (Fig. 4b). However, TCA cycle labelling was suppressed in *Lipt1*^{N44S/N44S} tissues, particularly downstream of AKGDH, at both GD9.5 and GD10.5 (Fig. 4b, c, Extended Data Fig. 5g). Thus, *Lipt1*^{N44S/N44S} embryos do not induce TCA cycle labelling just prior to their midgestation demise.

Finally, we assessed development in these embryos. Somite counts were indistinguishable among the genotypes at GD9.5 (Extended Data Fig. 6a). The initial formation and patterning of blood vessels was normal, and blood vessels were present throughout the *Lipt1*^{N44S/N44S} embryos (Extended Data Fig. 6b). Vessel maturation as assessed by the flow-responsive marker Connexin 40, was also normal (Extended Data Fig. 6b). However, both the brain and heart were smaller in the mutants (Fig. 4d, Extended Data Fig. 6b). We also assessed erythropoiesis by performing flow cytometry on cells from dissociated embryos using cell surface markers. We observed a decreased abundance of CD71⁺TER119⁺ fetal erythrocytes and an increased abundance of CD41⁺c-Kit⁺ myeloid–erythroid progenitors in *LIPT1*^{N44S/N44S} embryos, suggesting impaired erythrocyte differentiation (Fig. 4e, Extended Data Figs. 6c, d, 7). To examine the human relevance of this observation, we reviewed 15 years of clinical records from our LIPT1-deficient patient, and found that she suffers from chronic, unexplained anaemia (Fig. 4f) despite normal iron, folate and vitamin B12 levels. Her platelet and white blood cell

counts are preserved (Extended Data Fig. 6e,f), suggesting a particular defect in the erythroid lineage.

Conclusions

Metabolic defects and exposure to metabolic inhibitors¹⁶ can result in human congenital anomalies, emphasizing the importance of precise metabolic control during fetal development. Although resources exist to assess gene-expression and epigenetic signatures throughout development^{24,25}, understanding the developmental consequences of metabolic defects will benefit from methods to assess metabolism directly in utero. In this Article, we report metabolic features that evolve during midgestation in placenta and embryo, with both tissues undergoing extensive but largely distinct changes. The metabolic differences are consistent with requirements for rapid growth, dramatically divergent cellular composition of these tissues, and evolving cellular environments. Compartment-specific labelling differences in G6P and other metabolites indicate localized placental carbohydrate metabolism that may have little direct effect on embryonic glucose metabolism and possible differences in how each compartment meets its growth requirements. In the embryo, glucose supplies glycolysis, the pentose phosphate pathway and an expanding purine pool, all of which are rapidly labelled from glucose in the maternal circulation.

The contribution of maternally derived nutrients to the embryonic TCA cycle increases as midgestation progresses beyond GD9.5²⁶. We thus sought to examine the metabolic effects of a human genomic variant that interrupts this process. LIPT1 activates multiple enzymes responsible for providing respiratory substrates to the TCA cycle, and human LIPT1 deficiency results in developmental anomalies in oxidative organs including the brain. In mice, we find that LIPT1 is required for precisely timed changes in mitochondrial metabolism necessary for development past GD10.5; LIPT1 mutants persist for about one day after TCA cycle labelling increases in wild-type counterparts, and then die. Embryonic demise involves delayed or defective development in tissues such as the heart that have enhanced pyruvate oxidation over this gestational time frame, and erythrocytes, whose development requires mitochondrial function²⁷. Of note, the metabolic fate of pyruvate has been suggested to inform development in some contexts,

with persistent conversion to lactate associated with stem cell expansion and oxidation in the TCA cycle associated with differentiation^{28,29,30}. Observing metabolic pathways at the level of individual embryonic organs should provide an efficient approach to identify pathways that support spatiotemporal developmental programmes.

Methods

Materials

Materials were obtained as follows: [U-¹³C]glucose (Cambridge Isotopes, CLM-1396), [U-¹³C]glutamine (Cambridge Isotopes, CLM-1822), C57BL/6J (UTSW Mouse Breeding Core or Jackson Labs) and *Lipt1*^{N44S} knock-in mice (developed in-house)⁵.

Subject information and clinical data

The LIPT1-deficient individual who provided clinical data in Fig. 4f, Extended Data Fig. 6e,f was described previously⁵. This patient was enrolled in a prospective, non-randomized, non-blinded observational study whose overarching goal is to discover new metabolic disease-associated genes in patients of any age, and to characterize the metabolic phenotype in these patients (NCT02650622). The study was approved by the Institutional Review Board (IRB) at University of Texas Southwestern Medical Center (UTSW), and written informed consent was obtained from the patient's parents. Patients and family members eligible for the study are identified at UTSW, its affiliated hospitals, and other collaborating hospitals. After enrollment, study subjects provide blood for metabolomics and genomics, and a research-based integrated analysis of the data allows potentially pathogenic genomic variants to be prioritized for functional analysis in the laboratory. The study is purely observational in that no therapeutic interventions are proposed, although patients are followed longitudinally to understand each disease's natural history and the effects of therapies instituted as a part of routine clinical care. A total enrollment of over 1,500 patients is planned with the intention of representing many rare conditions within the cohort.

Reference datasets and data processing

Data for fetal tissues during midgestation are available from the ENCODE^{21,35,40} project Mouse Development Matrix (<https://www.encodeproject.org/mouse-development-matrix>). We downloaded the tsv files from the polyA plus RNAseq assay with the following identifiers: ENCFF262TPS (E11.5 liver -1), ENCFF414APX (E11.5 liver-2), ENCFF173NFQ (E12.5 liver-1), ENCFF144DHB (E12.5 liver-2), ENCFF971KKK (E13.5 liver-1), ENCFF042DVY (E13.5 liver-2), ENCFF770SOB (E10.5 heart-1), ENCFF351QKG (E10.5 heart-2), ENCFF159DWP (E11.5 heart-1), ENCFF168UJM (E11.5 heart-2), ENCFF484QWQ (E12.5 heart-1), ENCFF329HOZ (E12.5 heart-2), ENCFF148BEQ (E13.5 heart-1), ENCFF836QQS (E13.5 heart-2), ENCFF145PTV(E10.5 forebrain-1), ENCFF476ADM (E10.5 forebrain-2), ENCFF606UHO (E11.5 forebrain-1), ENCFF434CSI (E11.5 forebrain-2), ENCFF928MQD (E12.5 forebrain-1), ENCFF046RSQ (E12.5 forebrain-2), ENCFF960KJV (E13.5 forebrain-1), ENCFF356CTG (E13.5 forebrain-2). Placenta RNA transcript abundance was obtained from Gene Expression Omnibus (GEO) accession code [GSE100053](#). Expression data were filtered based on known metabolic genes^{37,38,39} and human–mouse gene mapping was based on the HomoloGene database (<https://www.ncbi.nlm.nih.gov/homologene>).

Placental gene-expression data were obtained from the GEO repository (<https://www.ncbi.nlm.nih.gov/gds>) using the GEOquery package³⁶ (<https://doi.org/10.18129/B9.bioc.GEOquery>) v2.62.1 from BioConductor release (3.14) (<https://www.bioconductor.org/>). Data were filtered based on known metabolic genes^{37,38,39} and sorted by Kyoto Encyclopedia of Genes and Genomes pathway annotation in the metaboAnalyst_KEGG R package (<https://github.com/xia-lab/MetaboAnalystR>). Human–mouse gene mapping was based on the HomoloGene database (<https://www.ncbi.nlm.nih.gov/homologene>).

Animal studies

All procedures were approved by the UT Southwestern Animal Care and Use Committee (IACUC) in accordance with *The Guide for the Care and*

Use of Laboratory Animals. All mice were housed in a pathogen free environment (temperature 20–26 °C, humidity 30–70%) with a 12 h:12 h light:dark cycle and fed chow diet (Teklad 2916) ad libitum. Healthy 8–15 week old, naïve pregnant females were set up for mating between 05:00 and 07:00 with proven studs of the appropriate genotype. The following morning, females displaying vaginal plugs were identified as pregnant and moved to a new cage until the indicated gestational day.

Metabolomic analysis

All sample collection took place between 09:00 and 11:00 with no prior fasting of the pregnant dams. Mice were initially anaesthetized using isoflurane and samples were dissected in cold sodium chloride irrigating solution (Baxter) and snap frozen in liquid nitrogen. Whole embryos and placentas were homogenized manually with a rubber dounce homogenizer in ice-cold acetonitrile:water (80:20). Samples were flash frozen 3 times in liquid nitrogen and then centrifuged at 16,000g for 10 min at 4 °C.

Supernatants were subject to BCA analysis and normalized to 70 µg ml⁻¹ and placed in LC–MS vials. Metabolite analysis used a Vanquish UHPLC coupled to a Thermo Scientific QExactive HF-X hybrid quadrupole orbitrap high-resolution mass spectrometer (HRMS) as performed previously³¹. Pooled samples were generated from an equal mixture of all individual samples and analysed using individual positive- and negative-polarity spectrometry ddHRMS/MS acquisition methods for high-confidence metabolite ID. Metabolite identities were confirmed in three ways: (1) precursor ion *m/z* was matched within 5 ppm of theoretical mass predicted by the chemical formula; (2) fragment ion spectra were matched within a 5 ppm tolerance to known metabolite fragments; and (3) the retention time of metabolites was within 5% of the retention time of a purified standard run with the same chromatographic method. LC-MS/MS data were collected using SCIEX Analyst v1.6.3 and Thermo Scientific XCalibur 4.1.50 and data analysed using SCIEX MultiQuant v2.1.1, and Thermo Scientific Trace Finder v5.1. Relative metabolite abundance was determined by integrating the chromatographic peak area of the precursor ion searched within a 5 ppm tolerance and then normalized to total ion count (TIC). Statistical analysis for generation of PCA plots, heatmaps, differential abundances and MSOA were performed using MetaboAnalyst 5.0 (<https://www.metaboanalyst.ca>).

Data were log-transformed and auto-scaled prior to the analysis. Additional heatmaps (Fig. 1e, Extended Data Fig. 2e) were generated using GraphPad Prism 9.0.1. For ¹³C studies, observed distributions of mass isotopologues were corrected for natural isotope abundances using a customized R script, which can be found at the GitHub repository (<https://github.com/wencgu/nac>). The script was written by adapting the AccuCor algorithm v0.2.4³².

Pregnant mouse infusions

All infusions took place between 09:00 and 11:00 with no prior fasting of the pregnant dams. Mice were initially anaesthetized using ketamine and xylazine (120 mg kg⁻¹ and 16 mg kg⁻¹, respectively, intraperitoneally) and maintained under anaesthesia using subsequent doses of ketamine (20 mg kg⁻¹, intraperitoneally) as needed. Catheters (25-gauge) were inserted into the tail vein and isotope infusions began immediately after a retro-orbital blood draw to mark time zero. In the glucose infusions, the total dose was 2.48 g kg⁻¹ dissolved in 750 µl normal saline and administered with a bolus of 62.5 µl min⁻¹ for 1 min followed by an infusion rate of 2.5 µl min⁻¹ for 3–4 h. Retro-orbital blood draws were taken throughout the infusion to monitor tracer enrichment in maternal blood. Glutamine infusions used a total dose of 1.73 g kg⁻¹ dissolved in 1,500 µl normal saline administered as a bolus of 147 µl min⁻¹ for 1 min followed by an infusion rate of 3 µl min⁻¹ for 5 h. Mice were euthanized at the end of the infusion, then the uterus was removed and placentas and embryos dissected in cold sodium chloride irrigating solution and frozen in liquid nitrogen. Care was taken during infusions not to increase nutrient concentrations over pre-infusion levels.

Serial caesarian-section surgery

For serial caesarian sections, the infusion parameters were the same as described above with the following alterations: (1) Serial caesarian-section infusions did not include a bolus; (2) the infusion rate was increased to 5 µl min⁻¹ in order to obtain sufficient labelling. Although the patterns of data for serial caesarian-sections matched what we observed in the 4 h

infusions, the overall labelling was somewhat lower and for this reason we did not compare serial caesarian-section data to data from longer infusions. After cannulation of the tail vein and retro-orbital blood draw for time zero, the lower abdomen of the pregnant dam was opened with a small incision. The uterus was removed from the peritoneal cavity and the conceptus nearest to one of the ovaries was dissected away from the uterus and further dissected into placenta and embryo in cold sodium chloride irrigating solution and then frozen in liquid nitrogen. The peritoneal cavity was flushed with sodium chloride irrigating solution, covered with gauze, and periodically rinsed with irrigating solution throughout the remainder of the surgery. The infusion was initiated and a single conceptus was dissected in a similar manner at the indicated time points until all embryos had been dissected or the 3 h time point was reached.

Gas chromatography mass spectrometry (GCMS)

Gas chromatography–mass spectrometry (GCMS) was used to identify glucose, pyruvate, lactate, citrate, succinate, malate and aspartate. These metabolites were also identified using liquid chromatography–mass spectrometry (LC–MS) and enrichment values were similar. Blood samples obtained during the infusion were chilled on ice for 5–10 min and then flash frozen in liquid nitrogen. Aliquots of 10–20 μ l were added to 80:20 acetonitrile:water for extraction. Frozen tissues (whole embryo and whole placenta) were added to 80:20 acetonitrile:water and extracted to analyse ^{13}C enrichment. Samples were manually disrupted using a rubber dounce homogenizer, subjected to three freeze–thaw cycles, then centrifuged at 16,000g for 15 min to precipitate macromolecules. For GCMS, 1 μ l D₂₇-myristic acid was added as an internal control, supernatants were evaporated, then re-suspended in 30 μ l anhydrous pyridine with 10 mg ml^{−1} methoxyamine and incubated at room temperature overnight. The following morning, the samples were incubated at 70 °C for 10–15 min and then centrifuged at 16,000g for 10 min. The supernatant was transferred to a pre-prepared GC/MS autoinjector vial containing 70 μ l *N*-(*tert*-butyldimethylsilyl)-*N*-methyltrifluoroacetamide (MTBSTFA) derivatization reagent. The samples were incubated at 70 °C for 1 h after which aliquots of 1 μ l were injected for analysis. Samples were analysed using either an Agilent 6890 or 7890 gas chromatograph coupled to an Agilent 5973N or

5975C Mass Selective Detector, respectively. GC–MS data were collected and analysed using Agilent ChemStation E02.02.1431. The observed distributions of mass isotopologues were corrected for natural isotope abundances using a customized R script, which can be found at the GitHub repository (<https://github.com/wencgu/nac>). The script was written by adapting the AccuCor algorithm v0.2.4³².

Gene expression

Total RNA was extracted from placental tissue using TRIzol Reagent (Thermo Fisher Scientific cat. no. 15596026). RNA (3,250 ng) was used as a template for a 70 µl cDNA synthesis reaction using TaqMan Reverse Transcription Reagents (Thermo Scientific cat. no. N8080234) according to the manufacturer’s instructions. cDNA was diluted 1:1 in nuclease-free water and plated at a final volume of 4 µl in a 384-well plate. Primers for placental markers were as described³³ and diluted to a final concentration of 2.5 µM. Primers were mixed with iTaq Universal SYBR Supermix (Bio-Rad cat. no. 1725121) and plated at a volume of 6 µl for a total reaction volume of 10 µl. Plates were run in a Bio-Rad CFX384 Touch Real-Time PCR Detection machine using the following protocol: (1) polymerase activation: 95 °C hold for 30 min; (2) PCR phase, 40 cycles: 95 °C hold for 5 s, 60 °C hold for 30 s; (3) melt curve, instrument default settings. Relative fold induction was computed using the $\Delta\Delta C_T$ method, as described³⁴.

Embryo RNA sequencing data were downloaded from the ENCODE Mouse Development Matrix³⁵ (<https://www.encodeproject.org/>). PolyA plus RNA-seq data were obtained for fetal heart, forebrain and liver from GD10.5-GD12.5 (not all days are available for liver). Placenta RNA transcript abundance was obtained from GEO accession code [GSE100053](#) using the GEOquery package³⁶ (<https://doi.org/10.18129/B9.bioc.GEOquery>) v2.62.1 from BioConductor release (3.14) (<https://www.bioconductor.org/>). Data were filtered based on known metabolic genes^{37,38,39} and sorted by Kyoto Encyclopedia of Genes and Genomes pathway annotation in the metaboAnalyst_KEGG R package (<https://github.com/xia-lab/MetaboAnalystR>). Human–mouse gene mapping was based on the HomoloGene database (<https://www.ncbi.nlm.nih.gov/homologene>).

Flow cytometry

Whole embryos were collected from GD10.5 pregnant mice into 1× PBS and mechanically disrupted using disposable pestles (VWR) and then filtered through a 40-µM cell strainer to remove clumps. Antibody staining was performed for 20 min on ice, followed by washing with HBSS (Invitrogen) and centrifugation at 200g for 5 min. Cells were stained with directly conjugated antibodies against mouse CD71 (FITC-R17.217.1.4 Biolegend, 1:100), mouse Ter119 (APC-TER-119 TONBO, 1:100), mouse CD41 (PE/Cy7-MWReg30 Biolegend, 1:100) and mouse CD117 (cKIT-APC-eFlour 780-Invitrogen, 1:100). All cells were gated for forward and side scatter and gated for live cells based on DAPI (1 µg ml⁻¹; Sigma, eFlour-450A). Erythrocytes were cells that were negative for CD117 (c-KIT), and positive for CD71 and Ter119. Myeloid–erythroid progenitors were negative for CD71 and TER119 and positive for CD41 and CD117 (c-KIT). Cells were examined on an LSRFortessa cell analyser (Becton Dickinson) and figures were generated using BD FACSDiva 8.0 and FlowJo v10.

Whole-mount immunofluorescent staining

Pregnant females at the desired developmental stage were euthanized by carbon dioxide asphyxiation and the uterus and extra-embryonic tissues were removed. Yolk sacs were used for genotyping and somites were counted. Embryos were fixed in 4% paraformaldehyde for 1 h at 25 °C or 4 °C overnight. Fixed embryos were washed at least 3 times with 1× PBS and dehydrated through a series of methanol or ethanol (25%, 50%, 75% and 100%, two times), permeabilized using 1% Triton X-100 (Fisher Bioreagents, cat. no. BP151-100) in PBS for 1.5–2 h at 25 °C, then blocked using CAS Block (Life Technologies, cat. no. 008120) for 2 h. Embryos were incubated in primary antibodies diluted in CAS Block overnight at 4 °C: Rat-anti-PECAM1 (1:100, BD, Biosciences, cat. no. 553370), Rat-anti-endomucin (1:100, Santa Cruz, sc-65495) and Rabbit-anti-connexin 40 (1:100, Alpha Diagnostics International, cat. no. CX-40A). Embryos were washed with 1× PBS then incubated with secondary antibodies diluted in CAS Block at 1:250 overnight at 4 °C: donkey-anti-rat 488 (Invitrogen, cat. no. A21208), donkey-anti-rabbit 555 (Invitrogen, cat. no. A31572). Embryos were washed in 1× PBS, then dehydrated to 100% methanol through a

methanol series (25%, 50%, 75%, 100% two times, 10 min each), cleared in a 1:2 benzyl alcohol:benzyl benzoate (BABB) solution, and mounted in BABB in 5 mm Thick Microscopy slides (Chang Biosciences, Rb167104D_1) and cover slipped. Images were obtained using a LSM700 Ziess confocal microscope with the Carl Zeiss ZEN 2011 software. If images of the dissected heart were desired, whole embryos were rehydrated through a methanol series into PBS, hearts were dissected and placed in a 1.5 mm 2-well concavity slide (Electron Microscopy Sciences, cat. no. 71878-03) containing PBS. Whole-heart images were obtained using a Ziess Images M2 with an Axiocam 506 mono camera attached with the Carl Zeiss ZEN 2011 software. For sectioned samples, paraffin embedded samples were transverse sectioned at 5 μ m and stained with haematoxylin and eosin.

Statistical analysis

During flow cytometry, isotope tracing, metabolomics, quantitative PCR, tissue weights, somite counts and histology experiments, the data were analysed in a manner blinded to sample genotype. A.S. collected the samples and then passed them to A. Tasdogan. for flow cytometry, or to I.M.-M. and M.A.C. for histology and immunofluorescence, and A. Tarangelo. for quantitative PCR. A.S. processed samples for mass spectrometry and analysed data. After the patterns had been analysed in each of these experiments, D. Dumesnil. provided the genotype information so results could be interpreted. For experiments in wild-type mice, no blinding was performed on placentas versus embryos because A.S. performed these experiments and analysed the data. For gene-expression studies from publicly available datasets, no blinding was performed.

Mice were allocated to experiments randomly and samples were processed in an arbitrary order, but formal randomization techniques were not used. Samples sizes were not pre-determined based on statistical power calculations but were based on our experience with these assays. For most experiments, the minimum number of mice was 3, with some exceptions where the embryo/placenta numbers were $n \geq 10$. No data were excluded; however, sometimes the small sample size was below the threshold for metabolomic analysis. In those instances, data that could be obtained from maternal blood or other tissues were used. These samples were not used

during direct comparisons of embryo relative to its own placenta if one of the samples was absent.

Prior to analysing the statistical significance of differences among groups, we tested whether data were normally distributed and whether variance was similar among groups. To test for normality, we performed the Shapiro–Wilk tests when $3 \leq n < 20$ or D’Agostino omnibus tests when $n \geq 20$. To test whether variability significantly differed among groups we performed F -tests (for experiments with two groups) or Levene’s median tests (for experiments with more than two groups). When the data significantly deviated from normality or variability significantly differed among conditions, we \log_2 -transformed the data and tested again for normality and variability. If the transformed data no longer significantly deviated from normality and equal variability, we performed parametric tests on the transformed data. If \log_2 -transformation was not possible or the transformed data still significantly deviated from normality or equal variability, we performed non-parametric tests on the non-transformed data.

When data or \log_2 -transformed data were normal and equally variable, statistical analyses were performed using Student’s t -tests or paired t -tests (when there were two groups), one-way ANOVAs or repeated measures one-way ANOVAs (when there were more than two groups), two-way repeated measures ANOVAs (when there were two or more groups with multiple metabolites or time points), or mixed effects models (when there were missing values but the data otherwise met the assumptions for a one-way or two-way repeated measures ANOVA). When the data or \log_2 -transformed data were normal but unequally variable, statistical analyses were performed using Welch’s t -tests (when there were two groups) or Welch’s one-way ANOVAs followed by the Dunnett’s T3 tests for multiple-comparisons adjustment (when there were more than two groups). When the data and \log_2 -transformed data were abnormal or unequally variable, statistical analysis was performed using Mann–Whitney or Wilcoxon matched pairs signed rank tests (when there were two groups) or Kruskal–Wallis tests (when there were more than two groups). P -values from multiple comparisons were adjusted using Tukey’s (when there were more than two groups and all of the comparisons were of interest) or Sidak’s method (when there were more than two groups and planned comparisons) after ANOVAs

or mixed effects models, or Dunn's method after Kruskal–Wallis tests. Holm–Sidak's method was used to adjust comparisons involving multiple metabolites between two conditions. A linear regression or nonlinear curve fitting method, plateau followed by one-phase association, was used to fit the time series data and the extra sum-of-squares F -test was used to assess if there was difference between two fitted lines/curves. Multiple line/curve fitting P -values were adjusted using the Holm–Sidak method. Statistical tests were performed using GraphPad Prism V9.0.1 or R 4.0.2.

Reporting summary

Further information on research design is available in the [Nature Research Reporting Summary](#) linked to this paper.

Data availability

[Source data](#) are provided with this paper.

Code availability

Mass isotopologues were corrected for natural isotope abundances using a customized R script, which can be found at the GitHub repository (<https://github.com/wencgu/nac>). The script was written by adapting the AccuCor algorithm v0.2.4³².

References

1. Johnson, M. T., Mahmood, S. & Patel, M. S. Intermediary metabolism and energetics during murine early embryogenesis. *J. Biol. Chem.* **278**, 31457–31460 (2003).
2. Dunwoodie, S. L. The role of hypoxia in development of the mammalian embryo. *Dev. Cell* **17**, 755–773 (2009).
3. Hansen, J. M., Jones, D. P. & Harris, C. The redox theory of development. *Antioxid. Redox Signal.* **32**, 715–740 (2020).

4. Solmonson, A. & DeBerardinis, R. J. Lipoic acid metabolism and mitochondrial redox regulation. *J. Biol. Chem.* **293**, 7522–7530 (2018).
5. Ni, M. et al. Functional assessment of lipoyltransferase-1 deficiency in cells, mice, and humans. *Cell Rep.* **27**, 1376–1386.e1376 (2019).
6. Lu, C. & Thompson, C. B. Metabolic regulation of epigenetics. *Cell Metab.* **16**, 9–17 (2012).
7. Oginuma, M. et al. A gradient of glycolytic activity coordinates FGF and Wnt signaling during elongation of the body axis in amniote embryos. *Dev. Cell* **40**, 342–353.e310 (2017).
8. Bulusu, V. et al. Spatiotemporal analysis of a glycolytic activity gradient linked to mouse embryo mesoderm development. *Dev. Cell* **40**, 331–341.e334 (2017).
9. Rodesch, F., Simon, P., Donner, C. & Jauniaux, E. Oxygen measurements in endometrial and trophoblastic tissues during early pregnancy. *Obstet. Gynecol.* **80**, 283–285 (1992).
10. Maltepe, E., Schmidt, J. V., Baunoch, D., Bradfield, C. A. & Simon, M. C. Abnormal angiogenesis and responses to glucose and oxygen deprivation in mice lacking the protein ARNT. *Nature* **386**, 403–407 (1997).
11. Iyer, N. V. et al. Cellular and developmental control of O₂ homeostasis by hypoxia-inducible factor 1 alpha. *Genes Dev.* **12**, 149–162 (1998).
12. Cowden Dahl, K. D. et al. Hypoxia-inducible factors 1α and 2α regulate trophoblast differentiation. *Mol. Cell. Biol.* **25**, 10479–10491 (2005).
13. Thion, M. S., Ginhoux, F. & Garel, S. Microglia and early brain development: an intimate journey. *Science* **362**, 185–189 (2018).
14. Patel, K. P., O'Brien, T. W., Subramony, S. H., Shuster, J. & Stacpoole, P. W. The spectrum of pyruvate dehydrogenase complex deficiency:

- clinical, biochemical and genetic features in 371 patients. *Mol. Genet. Metab.* **106**, 385–394 (2012).
15. Coman, D., Coman, D., Kranc, K. R. & Christodoulou, J. in *GeneReviews* (eds Adam, M. P. et al.) (Univ. of Washington, 1993).
 16. Coscia, L. A. et al. Update on the teratogenicity of maternal mycophenolate mofetil. *J. Pediatr. Genet.* **4**, 42–55 (2015).
 17. Hsu, C. N. & Tain, Y. L. Impact of arginine nutrition and metabolism during pregnancy on offspring outcomes. *Nutrients* **11**, 1452 (2019).
 18. Faubert, B. et al. Lactate metabolism in human lung tumors. *Cell* **171**, 358–371.e359 (2017).
 19. Tunster, S. J., Watson, E. D., Fowden, A. L. & Burton, G. J. Placental glycogen stores and fetal growth: insights from genetic mouse models. *Reproduction* **159**, R213–R235 (2020).
 20. Kumaravelu, P. et al. Quantitative developmental anatomy of definitive haematopoietic stem cells/long-term repopulating units (HSC/RUs): role of the aorta-gonad-mesonephros (AGM) region and the yolk sac in colonisation of the mouse embryonic liver. *Development* **129**, 4891–4899 (2002).
 21. He, P. et al. The changing mouse embryo transcriptome at whole tissue and single-cell resolution. *Nature* **583**, 760–767 (2020).
 22. Menendez-Montes, I. et al. Myocardial VHL–HIF signaling controls an embryonic metabolic switch essential for cardiac maturation. *Dev. Cell* **39**, 724–739 (2016).
 23. Beutner, G., Eliseev, R. A. & Porter, G. A. Jr Initiation of electron transport chain activity in the embryonic heart coincides with the activation of mitochondrial complex 1 and the formation of supercomplexes. *PLoS ONE* **9**, e113330 (2014).
 24. Cao, J. et al. The single-cell transcriptional landscape of mammalian organogenesis. *Nature* **566**, 496–502 (2019).

25. Liu, Y. et al. Single-cell RNA-seq reveals the diversity of trophoblast subtypes and patterns of differentiation in the human placenta. *Cell Res.* **28**, 819–832 (2018).
26. Miyazawa, H. et al. Rewiring of embryonic glucose metabolism via suppression of PFK-1 and aldolase during mouse chorioallantoic branching. *Development* **144**, 63–73 (2017).
27. Liu, X. et al. Regulation of mitochondrial biogenesis in erythropoiesis by mTORC1-mediated protein translation. *Nat. Cell Biol.* **19**, 626–638 (2017).
28. Schell, J. C. et al. Control of intestinal stem cell function and proliferation by mitochondrial pyruvate metabolism. *Nat. Cell Biol.* **19**, 1027–1036 (2017).
29. Flores, A. et al. Lactate dehydrogenase activity drives hair follicle stem cell activation. *Nat. Cell Biol.* **19**, 1017–1026 (2017).
30. Anso, E. et al. The mitochondrial respiratory chain is essential for haematopoietic stem cell function. *Nat. Cell Biol.* **19**, 614–625 (2017).
31. Tasdogan, A. et al. Metabolic heterogeneity confers differences in melanoma metastatic potential. *Nature* **577**, 115–120 (2020).
32. Su, X., Lu, W. & Rabinowitz, J. D. Metabolite spectral accuracy on orbitraps. *Anal. Chem.* **89**, 5940–5948 (2017).
33. Rhee, C. et al. ARID3A is required for mammalian placenta development. *Dev. Biol.* **422**, 83–91 (2017).
34. Livak, K. J. & Schmittgen, T. D. Analysis of relative gene expression data using real-time quantitative PCR and the $2^{-\Delta\Delta CT}$ method. *Methods* **25**, 402–408 (2001).
35. The ENCODE Project Consortium. Expanded encyclopaedias of DNA elements in the human and mouse genomes. *Nature* **583**, 699–710 (2020).

36. Davis, S. & Meltzer, P. S. GEOquery: a bridge between the Gene Expression Omnibus (GEO) and BioConductor. *Bioinformatics* **23**, 1846–1847 (2007).
37. Possemato, R. et al. Functional genomics reveal that the serine synthesis pathway is essential in breast cancer. *Nature* **476**, 346–350 (2011).
38. Birsoy, K. et al. An essential role of the mitochondrial electron transport chain in cell proliferation is to enable aspartate synthesis. *Cell* **162**, 540–551 (2015).
39. Zhu, X. G. et al. Functional genomics *in vivo* reveal metabolic dependencies of pancreatic cancer cells. *Cell Metab.* **33**, 211–221.e216 (2021).
40. Davis, C. A. et al. The Encyclopedia of DNA elements (ENCODE): data portal update. *Nucleic Acids Res.* **46**, D794–D801 (2018).

Acknowledgements

This manuscript is dedicated to Gerardo Guevara who was an excellent laboratory member and friend and whom we miss dearly. K. Dickerson helped interpret the patient's anaemia and A. B. Jaffe provided critical feedback. A.S. is a Ruth L. Kirschstein National Research Service Award Postdoctoral Fellow from the Eunice Kennedy Shriver National Institute of Child Health and Human Development (F32HD096786-01). B.F. is supported by a Career Transition Award from the National Cancer Institute (K99CA237724-01A1). R.J.D. is supported by the H.H.M.I. Investigator Program, N.C.I. Grant R35CA22044901, the Baldridge Family and the Robert L. Moody Sr Faculty Scholar endowment. A.R. is supported by the Victorian Cancer Agency Early Career Research Fellowship. S.K. is a Ruth L. Kirschstein National Research Service Award Predoctoral Fellow (F30CA254150-01A1). T.J.R. (K00CA212230) and A. Tarangelo. (K00CA234650) are NCI Predoctoral to Postdoctoral Fellows. The schematic of the midgestation (Fig. 1a) and infusion (Fig. 2a) procedures were generated using BioRender (<https://biorender.com/>). We also

acknowledge the ENCODE Consortium^{[35,40](#)} and the ENCODE production laboratory(s) for generating the datasets used in this study^{[21](#)}.

Author information

Affiliations

1. Children's Medical Center Research Institute, University of Texas Southwestern Medical Center, Dallas, TX, USA

Ashley Solmonson, Brandon Faubert, Wen Gu, Aparna Rao, Sherwin Kelekar, Thomas J. Rogers, Chunxiao Pan, Gerardo Guevara, Amy Tarangelo, Lauren G. Zacharias, Misty S. Martin-Sandoval, Duyen Do, Panayotis Pachnis, Dennis Dumesnil, Thomas P. Mathews, Alpaslan Tasdogan, Ling Cai, Zhiyu Zhao, Min Ni, Sean J. Morrison & Ralph J. DeBerardinis

2. Section of Hematology and Oncology, Department of Medicine, The University of Chicago, Chicago, IL, USA

Brandon Faubert

3. Department of Molecular Biology, University of Texas Southwestern Medical Center, Dallas, TX, USA

Mitz A. Cowdin, Ondine Cleaver & Hesham A. Sadek

4. Division of Cardiology, Department of Internal Medicine, University of Texas Southwestern Medical Center, Dallas, TX, USA

Ivan Menendez-Montes & Hesham A. Sadek

5. Department of Dermatology, University Hospital Essen and German Cancer Consortium, Partner Site Essen, Essen, Germany

Alpaslan Tasdogan

6. Department of Pediatrics, University of Texas Southwestern Medical Center, Dallas, TX, USA

An Pham & Ralph J. DeBerardinis

7. Quantitative Biomedical Research Center, Department of Population and Data Sciences, University of Texas Southwestern Medical Center, Dallas, TX, USA

Ling Cai

8. Howard Hughes Medical Institute, University of Texas Southwestern Medical Center, Dallas, TX, USA

Sean J. Morrison & Ralph J. DeBerardinis

Contributions

A.S., B.F. and R.J.D. conceived of the project, designed experiments and interpreted data. A.S., W.G., A.R., S.K., A. Tarangelo., A. Tasdogan, G.G., I.M.-M., M.A.C. and D. Dumesnil performed experiments. T.P.M., L.G.Z., M.S.M.-S. and D. Do, performed metabolomics and LCMS experiments. A.S., T.J.R., P.P. and L.C. performed metabolic tracing and gene-expression analysis. A.S., M.N. and C.P. generated and bred mice for LIPT1 experiments. Z.Z. performed statistical analyses. A.S. and R.J.D. wrote and edited the manuscript with help from B.F., A.P., O.C., S.J.M. and H.A.S.

Corresponding author

Correspondence to [Ralph J. DeBerardinis](#).

Ethics declarations

Competing interests

R.J.D. is an advisor for Agios Pharmaceuticals and Vida Ventures and a co-founder of Atavistik Bio. The other authors declare no competing interests.

Peer review

Peer review information

Nature thanks Nicola Zamboni and the other, anonymous reviewer(s) for their contribution to the peer review of this work. Peer review reports are available.

Additional information

Publisher's note Springer Nature remains neutral with regard to jurisdictional claims in published maps and institutional affiliations.

Extended data figures and tables

[Extended Data Fig. 1 Dynamic metabolism in developmental tissues during midgestation.](#)

(a) Principal component analysis and (b) Dendrogram analysis generated using Metaboanalyst 5.0 (<https://www.metaboanalyst.ca/>).

[Extended Data Fig. 2 Tissue specific metabolic changes from gd10.5-gd11.5.](#)

(a) Heatmap of top 50 metabolites significantly different between embryo and placenta. (b) Top 25 metabolites that contribute to the separation of gd10.5 embryo and placenta metabolic profiles. (c-d) Metabolic set overrepresentation analysis using metabolites in embryos (c) and placentas (d) differing in abundance ($p < 0.05$) between gd10.5-gd11.5. (e) Metabolites associated with the urea cycle transiently increase at gd11.5 and decrease the following two days. Statistical significance was determined using Student's t-tests. All data represent mean \pm s.d. Statistical tests were two-sided.

[Extended Data Fig. 3 Glucose feeds purine synthesis in developmental tissues.](#)

(a) Possible pathways contributing to labeling from [U-¹³C]glucose. (b-f) Isotopologues of G6P (b), R5P (c), IMP (d), GMP (e) and AMP (f) labeled with [U-¹³C]glucose. (g) Total enrichment (1-unlabeled fraction) of serine and glycine relative to total glucose enrichment. (h) Total enrichment in R5P (isobar with Ri5P/X5P), UMP and CMP labeled with [U-¹³C]glucose. (i) UMP and CMP m+1 enrichment from [γ -¹⁵N]glutamine. ¹⁵N-glutamine enrichment is normalized to glutamine m+1 to account for differences among compartments (see Fig. 2c). Statistical significance was determined using paired t-tests (b, c, h, and i) or Wilcoxon matched-pairs signed rank tests (b-g) followed by the Holm-Sidak's multiple comparisons adjustment (b-i). All data represent mean \pm s.d. Statistical tests were two-sided.

[Source data](#)

Extended Data Fig. 4 Tissue-specific TCA cycle metabolism in midgestation.

(a) Labeling from [U-¹³C]glucose between gd9.5-gd12.5 in placenta. (b) Enrichments normalized to glucose m+6 on gd12.5. (c-d) Daily citrate m+2/pyruvate m+3 (c) and citrate m+3/pyruvate m+3 (d) enrichment ratios. (e) ETC-related transcript counts ($n = 2$) in fetal tissues normalized to gd10.5 (gd11.5 in liver). (f) Daily total citrate/pyruvate enrichment ratio in fetal heart. (g) Placental ETC complex gene expression. (h) Enrichment ratio of glutamate m+5/glutamine m+5 in fetal tissues infused with [U-¹³C]glutamine. Statistical significance was determined using Mann-Whitney tests (a, g), paired t-tests (b), or straight line least squares fitting (h) followed by the Holm-Sidak's multiple comparisons adjustment (a, b, g, and h), linear mixed-effects analysis (c,d) followed by the Sidak's (c-d; between-tissue comparisons) or Tukey's (c-d; between-time comparisons) multiple comparisons adjustment, or one-way ANOVA followed by the Tukey's multiple comparisons adjustment (f). All data represent mean \pm s.d. Statistical tests were two-sided.

[Source data](#)

Extended Data Fig. 5 LIPT1 activity is critical for transition from gd10.5-gd11.5.

(a) PCA plots of metabolomics data and (b) tissue weights in litters arising from *Lipt1*^{WT/N44S} intercrosses. (c) Relevant metabolites in placentas of the indicated genotypes. (d-e) Placental uptake (left) and embryo transfer (right) of [U-¹³C]glucose (d) and [U-¹³C]glutamine (e). (f) Expression of placental markers. (g) Labeling from [U-¹³C]glucose in placentas of various *Lipt1* genotypes. Statistical significance was determined using two-way repeated measures ANOVA followed by the Sidak's multiple comparisons adjustment (b), Student's t-tests (c) or Mann-Whitney tests (d-g) followed by Holm-Sidak's multiple comparisons adjustment. All data represent mean ± s.d. Statistical tests were two-sided.

[Source data](#)

Extended Data Fig. 6 LIPT1 deficiency hinders organogenesis and erythropoiesis.

(a) Somite counts in embryos from litters arising from *Lipt1*^{WT/N44S} intercrosses at gd9.5. (b) Brightfield whole mount images, scale bar = 500µm (1,1'); Dorsal Aortae stained with Connexin 40, scale bar = 100µm (2,2'); PE staining of whole hearts, scale bar = 300µm (3,3'); H&E staining of hearts, scale bar = 50µM (4,4'). All images from gd9.5 embryos. (c-d) Gd10.5 whole embryo cells stained with antibodies against the erythroid lineage markers CD71 and TER119 (c) and myeloid/erythroid progenitor markers, cKIT and CD41 (d). Flow cytometry was performed in 24 individual embryos (Healthy n = 11, Mutant n = 7) White blood cell (WBC) (e) and platelet (f) counts from a LIPT1-deficient patient. Statistical significance was determined using Student's t-tests followed by Holm-Sidak's multiple comparisons adjustment. All data represent mean ± s.d. Statistical tests were two-sided.

[Source data](#)

Extended Data Fig. 7 Flow cytometry gating strategies.

(a) Single cell suspensions from whole embryos were gated by forward and side scatter area (P1) then by forward scatter height and width (P2), then by side scatter height and width (P3). Cells had been stained with DAPI and

live cells were gated as DAPI negative (P4), and then by CD117 (cKIT) negative (P5). Fetal erythrocytes were identified as CD71⁺/TER119⁺ (red box – P5:Q2), and myeloid/erythroid progenitors were gated as CD71⁻/TER119⁻ (blue box - P5:Q3) and also gated as cKIT⁺/CD41⁺ (P6).

Supplementary information

[Supplementary Table 1](#)

A list of abbreviations.

[Reporting Summary](#)

[Peer Review File](#)

Source data

[Source Data Fig. 1](#)

[Source Data Fig. 2](#)

[Source Data Fig. 3](#)

[Source Data Fig. 4](#)

[Source Data Extended Data Fig. 3](#)

[Source Data Extended Data Fig. 4](#)

[Source Data Extended Data Fig. 5](#)

[Source Data Extended Data Fig. 6](#)

Rights and permissions

Open Access This article is licensed under a Creative Commons Attribution 4.0 International License, which permits use, sharing, adaptation, distribution and reproduction in any medium or format, as long as you give appropriate credit to the original author(s) and the source, provide a link to the Creative Commons license, and indicate if changes were made. The images or other third party material in this article are included in the article's Creative Commons license, unless indicated otherwise in a credit line to the material. If material is not included in the article's Creative Commons license and your intended use is not permitted by statutory regulation or exceeds the permitted use, you will need to obtain permission directly from the copyright holder. To view a copy of this license, visit <http://creativecommons.org/licenses/by/4.0/>.

Reprints and Permissions

About this article

Cite this article

Solomonson, A., Faubert, B., Gu, W. *et al.* Compartmentalized metabolism supports midgestation mammalian development. *Nature* **604**, 349–353 (2022). <https://doi.org/10.1038/s41586-022-04557-9>

- Received: 01 March 2021
- Accepted: 08 February 2022
- Published: 06 April 2022
- Issue Date: 14 April 2022
- DOI: <https://doi.org/10.1038/s41586-022-04557-9>

Share this article

Anyone you share the following link with will be able to read this content:

[Get shareable link](#)

Sorry, a shareable link is not currently available for this article.

[Copy to clipboard](#)

Provided by the Springer Nature SharedIt content-sharing initiative

This article was downloaded by **calibre** from <https://www.nature.com/articles/s41586-022-04557-9>

| [Section menu](#) | [Main menu](#) |

[Download PDF](#)

- Article
- Open Access
- [Published: 06 April 2022](#)

Capturing a rhodopsin receptor signalling cascade across a native membrane

- [Siyun Chen](#)^{1,2},
- [Tamar Getter](#)³,
- [David Salom](#)³,
- [Di Wu](#) [ORCID: orcid.org/0000-0001-9748-4408](#)^{1,2},
- [Daniel Quetschlich](#)^{1,2},
- [Dror S. Chorev](#) ¹,
- [Krzysztof Palczewski](#) [ORCID: orcid.org/0000-0002-0788-545X](#)^{3,4,5,6}
&
- [Carol V. Robinson](#) [ORCID: orcid.org/0000-0001-7829-5505](#)^{1,2}

Nature volume **604**, pages 384–390 (2022)

- 6599 Accesses
- 144 Altmetric
- [Metrics details](#)

Subjects

- [Biological techniques](#)
- [Membrane biophysics](#)

Abstract

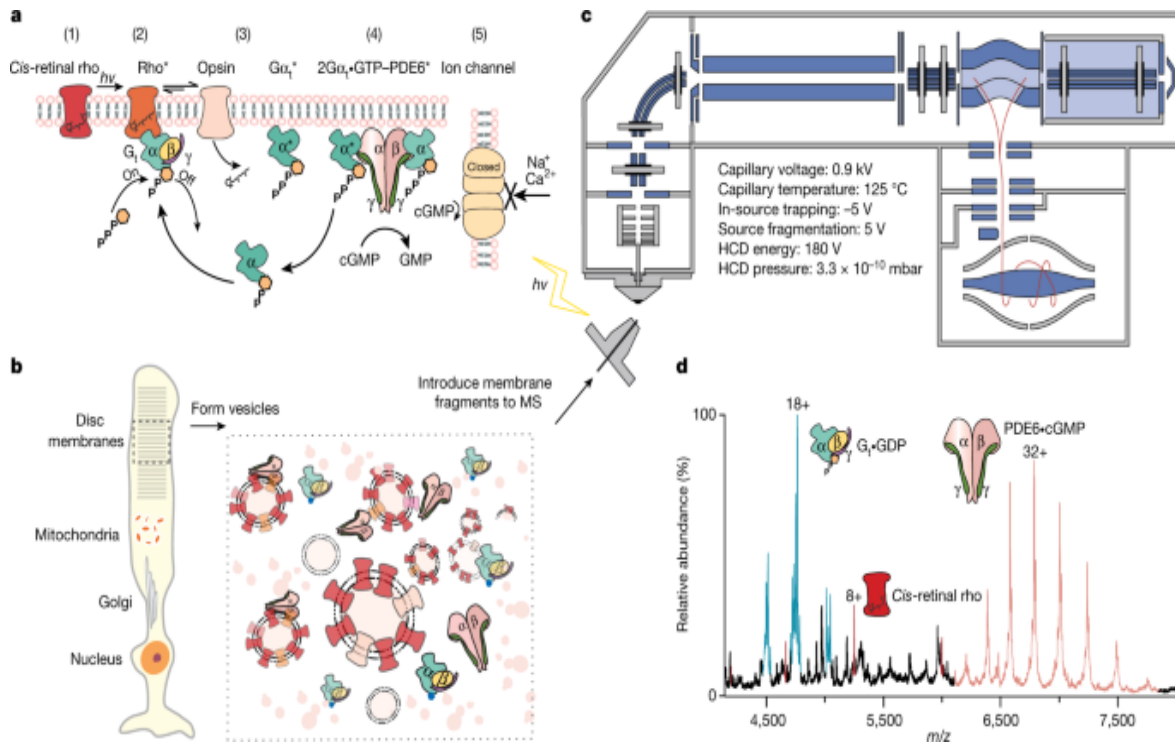
G protein-coupled receptors (GPCRs) are cell-surface receptors that respond to various stimuli to induce signalling pathways across cell membranes. Recent progress has yielded atomic structures of key intermediates^{1,2} and roles for lipids in signalling^{3,4}. However, capturing signalling events of a wild-type receptor in real time, across a native membrane to its downstream effectors, has remained elusive. Here we probe the archetypal class A GPCR, rhodopsin, directly from fragments of native disc membranes using mass spectrometry. We monitor real-time photoconversion of dark-adapted rhodopsin to opsin, delineating retinal isomerization and hydrolysis steps, and further showing that the reaction is significantly slower in its native membrane than in detergent micelles. Considering the lipids ejected with rhodopsin, we demonstrate that opsin can be regenerated in membranes through photoisomerized retinal–lipid conjugates, and we provide evidence for increased association of rhodopsin with unsaturated long-chain phosphatidylcholine during signalling. Capturing the secondary steps of the signalling cascade, we monitor light activation of transducin (G_t) through loss of GDP to generate an intermediate apo-trimeric G protein, and observe $G\alpha_t$ •GTP subunits interacting with PDE6 to hydrolyse cyclic GMP. We also show how rhodopsin-targeting compounds either stimulate or dampen signalling through rhodopsin–opsin and transducin signalling pathways. Our results not only reveal the effect of native lipids on rhodopsin signalling and regeneration but also enable us to propose a paradigm for GPCR drug discovery in native membrane environments.

Main

Molecular details of GPCRs, their G protein coupling and arrestin interactions are providing unprecedented insight into signalling cascades and are often achieved through judicious antibody stabilization or protein engineering¹. Meanwhile, recognition of the importance of lipids in mediating GPCR signalling interactions has been derived from the use of lipid nanodiscs and peptidiscs to recreate membrane environments^{5,6,7}. Capturing signalling of unmodified GPCRs, in native membrane environments, has so far eluded biophysical measurement. Here, selecting

the best-characterized GPCR rhodopsin, the dim light receptor of the mammalian visual system⁸, we formed lipid vesicles from disc membranes of dark-adapted bovine retinal rod outer segments (ROSs) and ejected this GPCR directly from fragments of its native membrane environment into a mass spectrometer (Fig. 1a–c, [Supplementary Video 1](#)). We monitored signalling by operating our mass spectrometer in a dark room and controlling light exposure to prompt photoisomerization of 11-*cis*-retinylidene (*cis*-retinal rho) to form activated all-*trans*-retinylidene (rho*). The Schiff base of rho* was then hydrolysed to the apo-protein opsin and all-*trans*-retinal^{9,10}. During photoactivation, rho* interacted with GDP-bound transducin (heterotrimeric G protein (G_t)), leading to GDP–GTP exchange and subsequent dissociation and formation of Gα_t•GTP, which then interacted with phosphodiesterase 6 (PDE6), displacing the PDE6 γ-subunit, releasing inhibition of catalysis and resulting in rapid hydrolysis of cytoplasmic cGMP¹¹. Here we show that all components of this signalling pathway (protein, downstream effectors, cofactors and lipids) can be ejected simultaneously and their response to photon activation in the native membrane captured by native mass spectrometry directly and in real time (Fig. 1d).

Fig. 1: Established signalling pathway of rho, experimental conditions for preparation of vesicles for GPCR signalling and representative mass spectrum.



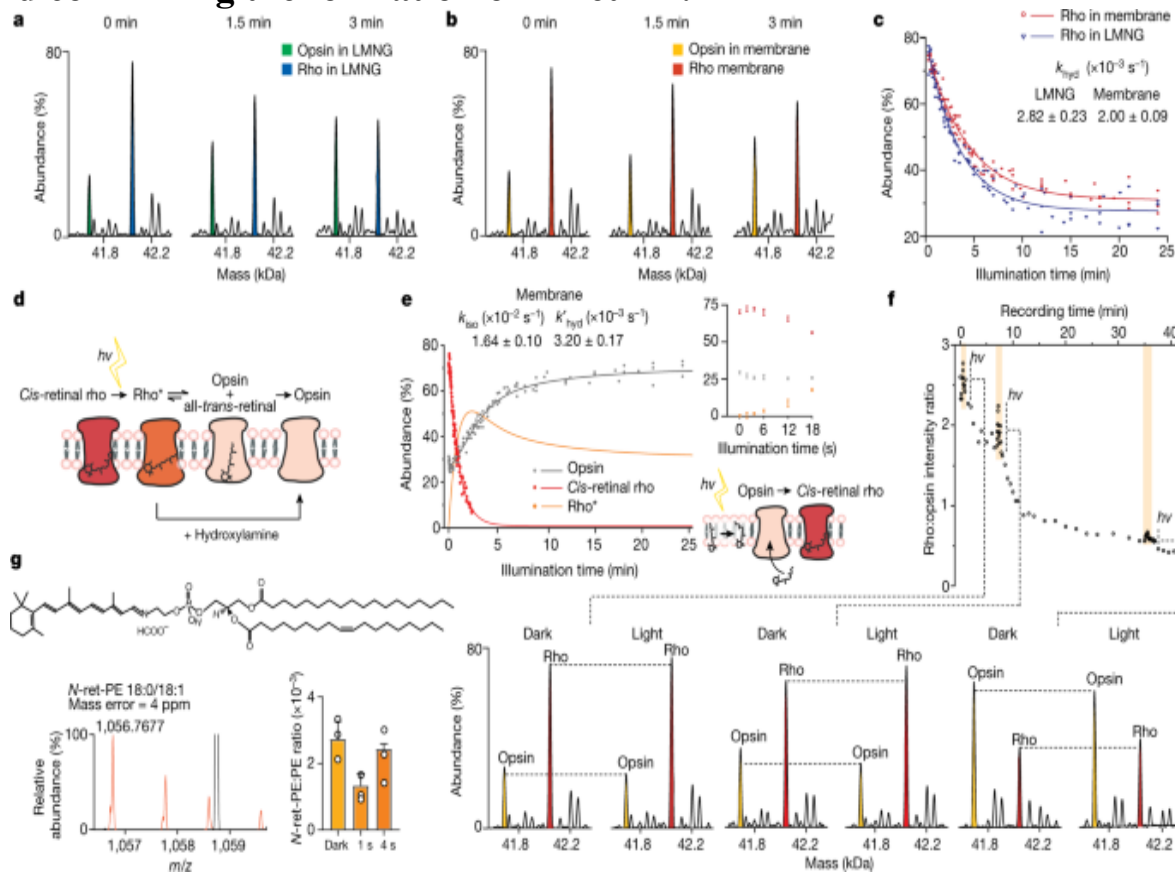
a, Following absorption of a photon of light $h\nu$ (1), 11-*cis*-retinal of rho isomerizes to the all-*trans* isomer (2). The activated states of rho (rho*) engage with transducin (G_t), consisting of G α_t •GDP $\beta\gamma_t$, and exchange GDP for GTP. G_t dissociates to form G α_t •GTP and G $\beta\gamma_t$; loss of retinal from rho* leads to the formation of opsin (3). α -Subunits of G_t interact with the γ -subunits in the PDE6 enzyme, with γ -subunits undergoing a conformational change, relieving inhibition and thereby activating PDE6 to cause hydrolysis of cGMP (4). Depletion of cGMP then closes the ion channel and the ‘dark current’ is terminated (5). The resulting change in the membrane potential produces the sensation of light. **b**, Disc membranes of rod cells are homogenized to form a heterogeneous distribution of vesicles that are introduced directly into the mass spectrometer (MS). The spectrum shown was recorded using the parameters stated above, which led to the dissociation of lipids from proteins. **c**, An LED light source is configured to apply timed light intervals before the electrospray ionization of the vesicles into an Orbitrap mass spectrometer under the conditions noted. HCD, higher-energy collisional dissociation. **d**, Following the addition of a soluble fraction containing PDE6 and G_t, all proteins along the signalling pathway were detected. The proteins were ejected intact as rho/opsin (red), trimeric G α_t •GDP (cyan) and tetrameric PDE6•cGMP (pink). The mass

spectrum shown from m/z 4,000 to m/z 8,000 represents the raw data. The experiment was repeated three times.

To establish mass spectrometry and light conditions that enable monitoring of rhodopsin signalling, and before instituting our approach in native membranes, we used membrane solubilization and detergents to extract rhodopsin from dark-adapted ROS membrane, as previously described for analysis via mass spectrometry^{12,13,14}. Following extraction into lauryl maltose neopentyl glycol (LMNG), we identified illumination conditions (LED-emitting cold white light; Extended Data Fig. 1) and mass spectrometry conditions to release rho from membrane lipids and detergents and to monitor rho* signalling through the mass change associated with conversion of rho to opsin (Δ mass = 266 Da). Before illumination, $73 \pm 1\%$ rho (11-cis-retinal or *trans*-retinal) and $27 \pm 1\%$ opsin were present. Recording of spectra in real time was synchronized with illumination; equal population of both species was achieved after 3 min (Fig. 2a), reaching a plateau with $27 \pm 1\%$ rho remaining at 20 min in this detergent micelle preparation (Fig. 2c). We next established mass spectrometry conditions that enabled ejection of rho and opsin (rho/opsin) directly from disc membrane fragments while activated with light. To do this, we adapted and applied a sonicated lipid vesicle approach^{15,16} to purified ROS disc membranes, forming vesicles for direct introduction into the mass spectrometry. Under these conditions, monomeric rho was ejected. No dimeric population was observed, attributed to the relatively small dimer interface observed via cryo-electron microscopy in nanodiscs¹⁷ that dissociates under these mass spectrometry conditions. Comparing the post-translational modification status of dark-adapted and light-exposed rho/opsin extracted in detergent or ejected from membranes, we found that glycosylation, palmitoylation and cysteinylation status are largely indistinguishable (Extended Data Fig. 2a–d, Extended Data Table 1). An increase in phosphorylation of opsin was observed 20 min after signalling was initiated, both in detergent-extracted and membrane-ejected rho/opsin, consistent with progress towards termination of this signalling pathway through eventual interaction with arrestin¹⁸.

Fig. 2: Monitoring real-time conversion of rho to opsin in detergent micelles and in native membranes, probing the effects of pulses of light

and confirming the formation of N-ret-PE.



a, b, Changes in the population of rho and opsin in LMNG (blue and green, respectively; **a**) and in native membranes (red and yellow, respectively; **b**). Individual spectra are shown as zero-charge plots with illumination times stated. **c**, Plot of the relative abundance of rho during illumination, in either LMNG detergent micelles (blue) or native membranes (red) monitored as a change in mass as a function of time. Rate constants for hydrolysis are shown for the reaction in detergent micelles or in membranes (Extended Data Fig. 3). **d**, Schematic of the dark-adapted state undergoing light-activated conversion of *cis*-retinal to all-*trans*-retinal, hydrolysis of the Schiff base and dissociation from rho to form opsin. **e**, Monitoring the decay of *cis*-retinal rho in membranes pretreated with hydroxylamine (red), the generation of opsin in native membranes (grey) and the change of rho* calculated over the illumination period (orange). The inset, which is an expansion of the illumination period from 0–18 s, shows a less than 18-s increase in rho abundance at the expense of opsins. The schematic depicts a possible regeneration mechanism through isomerization of *trans*-retinal. **f**, Monitoring the conversion of rho to opsin and the regenerative reaction of

opsin to rho following pulses of light at 0.51 min, 7 min and 35 min for time periods of 3 s, 12 s and 32 s, respectively. Zero-charge mass spectra are shown at time points during this conversion reaction, before illumination (dark) and at the peak of the three light pulses. **g**, Spectrum (orange) of *N*-ret-PE (18:0/18:1 representative structure shown) extracted from native membranes; the bar graph shows changes in the equilibrium between conjugated and free PE in response to illumination time. Data are presented as mean \pm s.d. ($n = 3$).

Monitoring rho/opsin populations during continuous light exposure in membrane vesicle fragments, we found that after 3 min rho remained predominant over opsin (Fig. 2b). The reaction in membranes proceeds until a plateau is reached with approximately 32% rho remaining after 20 min (compared with approximately 27% in detergent micelles after the same time period (Fig. 2c)). We next calculated and compared the rates of chromophore hydrolysis (k_{hyd} ; at pH 7.0 and 28 °C) in LMNG micelles and from ROS membrane vesicles according to a kinetic model (Fig. 2c, Extended Data Fig. 3, eq. 7). As the hydrolysis of all-*trans*-retinal from rho* is a slower step than photoisomerization of 11-*cis*-retinal to *trans*-retinal in rho, our results allow us to conclude that hydrolysis of all-*trans*-retinylidene from rho* is slower in vesicles than in detergent micelles. Considering the isomerization reaction, loss of all-*trans*-retinal from the binding pocket of rho* is monitored through a change in mass following hydrolysis of the Schiff base. The extent of *cis*-retinal or *trans*-retinal bound to opsin before hydrolysis, however, is not apparent via mass alone. To delineate these isomeric populations, we adopted a well-established protocol in which ROS membrane preparations were pre-incubated in the dark with 5 mM hydroxylamine (Fig. 2d). Rho in its ground state is insensitive to hydroxylamine but, upon photoisomerization of *cis*-retinal to all-*trans*-retinal, hydroxylamine is able to attack and cleave the Schiff base in the photoactivated rhodopsin to form all-*trans*-retinyl oxime¹⁹. As expected, rho* in membranes decayed significantly faster in the presence of hydroxylamine (Extended Data Fig. 2e). This hydroxylamine experiment, together with the rho/opsin photoconversion of untreated membranes mentioned above (k_{hyd}), enabled us to subtract the two decay curves and consequently obtain the rates of retinal isomerization (k_{iso}) and hydrolysis

without isomerization (k'_{hyd}) in native membranes (Fig. 2e, Extended Data Fig. 3).

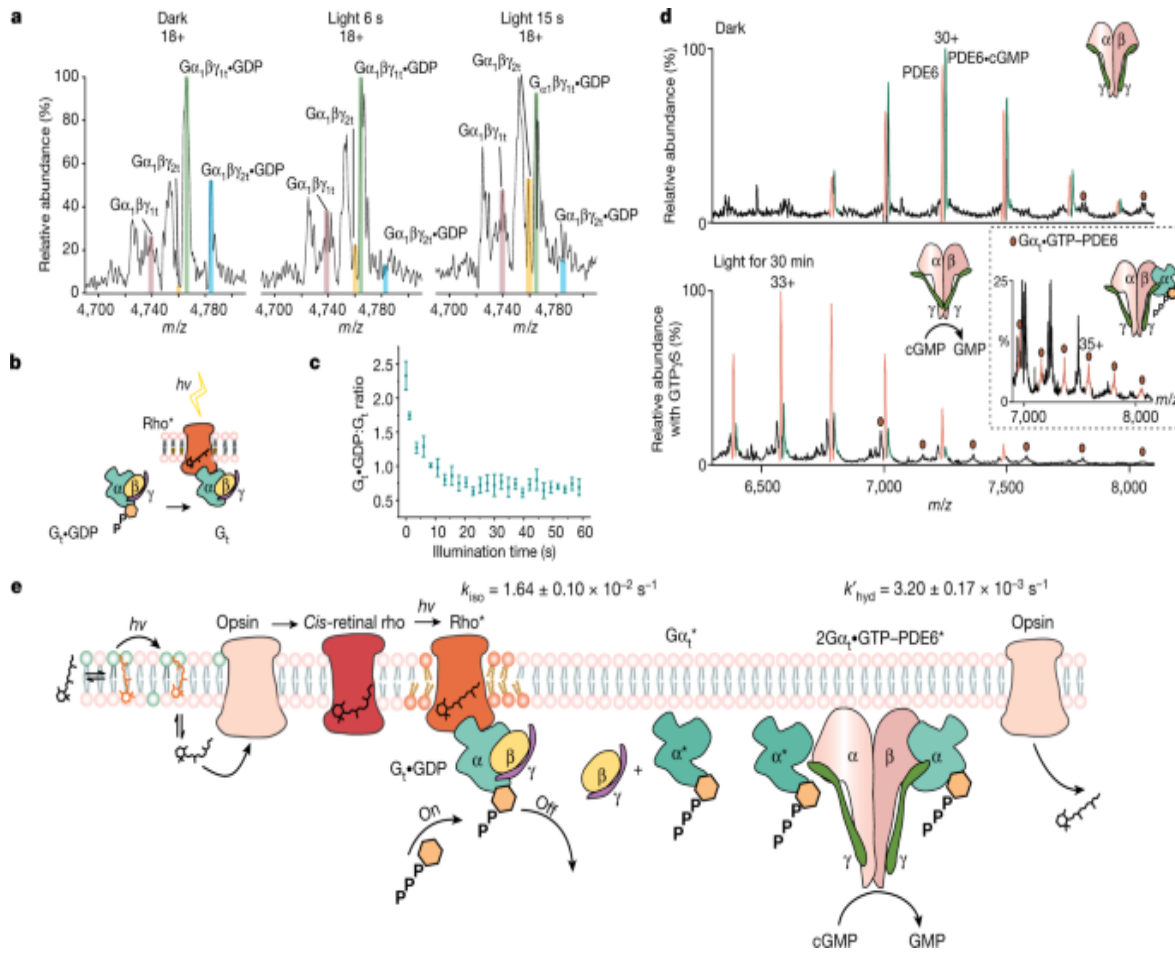
Careful examination of the data reveals an initial phase in which opsin regenerates to rho (less than 18 s) in competition with the overall rho/opsin conversion. The increase in *cis*-retinal rho at 2.7 ± 1 s is coincident with the lowest level of opsin at 3.6 ± 1 s (Fig. 2e, inset). This initial reaction, in the absence of hydroxylamine, must therefore arise primarily from *cis*-retinal binding to opsin. To determine whether this observation was a feature of the membrane, we applied short-term illumination on disc membrane preparation and to rho purified in LMNG detergent micelles. Upon each transient illumination of rho from ROS, a rapid rise of rho was observed together with the general trend of rho transforming to opsin (Fig. 2f). Some evidence for regeneration of rho in micelles was observed, although to a much lower extent (Extended Data Fig. 4). The ability to regenerate is a known property of the visual system, which requires the conversion of all-*trans*-retinal to 11-*cis*-retinal and has been shown to be carried out by enzyme pathways in neighbouring cells¹⁰. Our proteomics experiments (Supplementary Table 1) were unable to detect key enzymes from the regeneration cycle, such as retinal GPCR (RGR) or the retinoid isomerase RPE65 (ref. 20), prompting us to consider the possibility that this rapid regeneration (less than 18 s) may be a feature of the membrane itself.

Previous reports have implicated an *N*-all-*trans*-retinyl-PE conjugate that can undergo photoisomerization to form *cis*-retinals (primarily 11-*cis*-retinal (85–86%) with small contributions from 9-*cis*-retinal (12–13%) and 13-*cis*-retinal (1–2%))²¹. Although our mass spectrometry approach cannot readily distinguish these structural isomers, our lipidomics data reveal the presence of high concentrations of polyunsaturated fatty acids including PE (Extended Data Fig. 5a–c). To explore the formation of retinal conjugated to PE, we extracted lipids into isopropanol directly from dark-exposed and controlled-light-exposed ROS disc membranes. We selected three representative lipids (PE 18:0/18:1, 18:0/20:4 and 18:0/22:5) with minimal overlap in mass spectra, and searched for their respective retinyl conjugation. We found direct evidence for the formation of *N*-retinyl-PE (*N*-ret-PE) in all cases and monitored its change as a function of exposure to light. After 1 s of illumination, a significant decrease in conjugation was

observed (more than 2.5-fold for PE 18:0/18:1), consistent with light-stimulated retinal dissociation from PE (Fig. 2g, Extended Data Fig. 5d–f). Peaks assigned to *N*-ret-PE increased after 4 s of light exposure to similar levels as the dark-adapted membrane, suggesting further conjugation events. Significantly reduced rho regeneration was observed for rho purified in micelles, where a lack of the conjugation system for retinal and PE would be anticipated (Extended Data Fig. 4). Moreover, regeneration of rho might be expected to be limited by the availability of *cis*-retinal. To investigate this possibility, we incubated intact ROS disc membranes with a tenfold excess of all-*trans*-retinal. Following illumination, regeneration of rho from 79% to 91% was observed after 3.8 min (Extended Data Fig. 6). Together, these results imply that conversion of opsin to rho in membranes can be supplemented by the addition and photoisomerization of all-*trans*-retinal and that conjugation of PE provides a source of *cis*-retinal for regeneration in membranes, a mechanism that has been suggested for sustained vision in daylight²¹.

Turning our attention to the next step in the signalling cascade, rho* signals through G_t, releasing GDP and dissociating to form Gα_t•GTP for interaction with PDE6. Before illumination, GDP-bound heterotrimeric G_t•GDP and cGMP-bound heterotetrameric PDE6 (PDE6•cGMP) were observed as the predominant species (Fig. 1d). To monitor real-time signalling through transducin, excess soluble fraction containing G_t and PDE6 was added to our membrane preparation (see [Methods](#)). We monitored the decrease in the ratio of G_t•GDP:G_t as a function of time, initially for periods of up to 1 min (Fig. 3c), but found little change beyond the first 15 s of light stimulation. The spectra of G_t are complicated by the presence of additional proteoforms (α₂ from cone G_t (Extended Data Fig. 7a–c)). Control experiments in the absence of light or ROS membranes (Extended Data Fig. 7d–f) confirm that light activation of rho in the membrane is required to decrease the population of G_t•GDP during signalling (Fig. 3a).

Fig. 3: Light activation of rho in ROS disc membrane signalling through G_t to release Gα_t•GDP to effect hydrolysis of cGMP and its release from PDE6.



a, Native mass spectra of $G_t \bullet GDP$ with no additional GTP added containing two α -isoforms (α_1 and α_2) and two γ -isoforms (γ_1 and γ_2) are catalysed to apo- G_t during a 15-s time course of illumination. **b**, Reaction scheme: ρ^* catalysed the nucleotide exchange of G_t . **c**, The ratio of ground-state $G_t \bullet GDP$ to intermediate apo- G_t decreases rapidly during the first 15 s after illumination. Data are presented as mean \pm s.e. ($n = 3$). **d**, Native mass spectra of PDE6 ejected from ROS disc membrane vesicles under dark conditions reveal that cGMP binds to intact tetrameric PDE6 with an approximately 1:1 ratio (top). A low population of PDE6– $G\alpha_t \bullet GTP$ is also observed (red circles). After exposure to light in the presence of ROS disc membranes, the population of PDE6 bound to cGMP is reduced considerably, consistent with the release of GMP following its hydrolysis via activated PDE6 with addition of a molar equivalent of GTP γ S to G_t (bottom). **e**, Schematic shows the ρ^* signalling cascade that involves the conjugation of all-trans-retinal with PE and its light activation to form *cis*-retinal rho*. This leads to the formation of Rho^* , which activates $G\alpha_t$ by catalyzing the exchange of GDP for GTP. The activated $G\alpha_t \bullet GTP$ then activates PDE6, leading to the hydrolysis of cGMP to GMP. The released GMP is then used by the activated PDE6 to hydrolyze another molecule, resulting in the release of α' , β' , and γ' subunits.

retinal that is able to interact with opsin. Light-activated conversion of rho to an intermediate state takes place with rho* capable of interacting with G_t. Changes in the lipid bilayer are depicted as unsaturated lipids that are recruited during rho* signalling (lipids, orange). The Gα_t•GTP subunit produced following hydrolysis of Gα_t•GDP interacts with PDE6, relieving its inhibition via the γ-subunit and effecting the hydrolysis of cGMP, which is then released from PDE6. Gα_t•GDP is formed for the regeneration of G_t•GDP. All experiments shown in this figure were repeated at least three times. Data are presented as mean ± s.e. ($n = 3$).

To explore the relationship between Gt-dependent rho* signalling and PDE6•cGMP hydrolysis, we investigated three different GTP conditions: (1) with endogenous levels of GTP in the soluble fraction, (2) following the addition of a molar equivalent of GTP to G_t, and (3) in the presence of a molar equivalent of non-hydrolysable GTPγS to G_t. After illumination, the levels of G_t•GDP decreased in all three cases but were replenished in condition 2, the supplementary GTP experiment (Extended Data Fig. 7g–i). Linking G_t signalling with PDE6•cGMP hydrolysis, we monitored the release of the hydrolysed GMP product via the ratio PDE6:PDE6•cGMP. For dark-adapted membranes, before illumination, a PDE6:PDE6•cGMP ratio of approximately 1:1 was observed, consistent with full occupancy of one substrate-binding site in PDE6 (Fig. 3d, top). Signalling of rho* through G_t prompts further hydrolysis of cGMP with supplementary GTP (PDE6:PDE6•cGMP ratio of approximately 1:0.25) compared with endogenous levels (PDE6:PDE6•cGMP ratio of approximately 1:0.85) (Extended Data Fig. 7g, h). As Gα_t•GTPγS is also able to interact with PDE6 (ref. 22), an intermediate level of hydrolysis of cGMP was observed in the presence of an equimolar aliquot of Gα_t•GTPγS (PDE6:PDE6•cGMP of approximately 1:0.4) (Fig. 3d, bottom, Extended Data Fig. 7i). An additional PDE6–Gα_t•GTP complex with 1:1 stoichiometry can also be discerned at low intensity in the presence of Gα_t•GTPγS (Fig. 3d, inset). Under these experimental conditions, 1:2 complexes of PDE6•(Gα_t•GTP)₂ and PDE6•(cGMP)₂ were not observed, consistent with existing mechanistic models. According to one model, although controversial²³, one catalytic

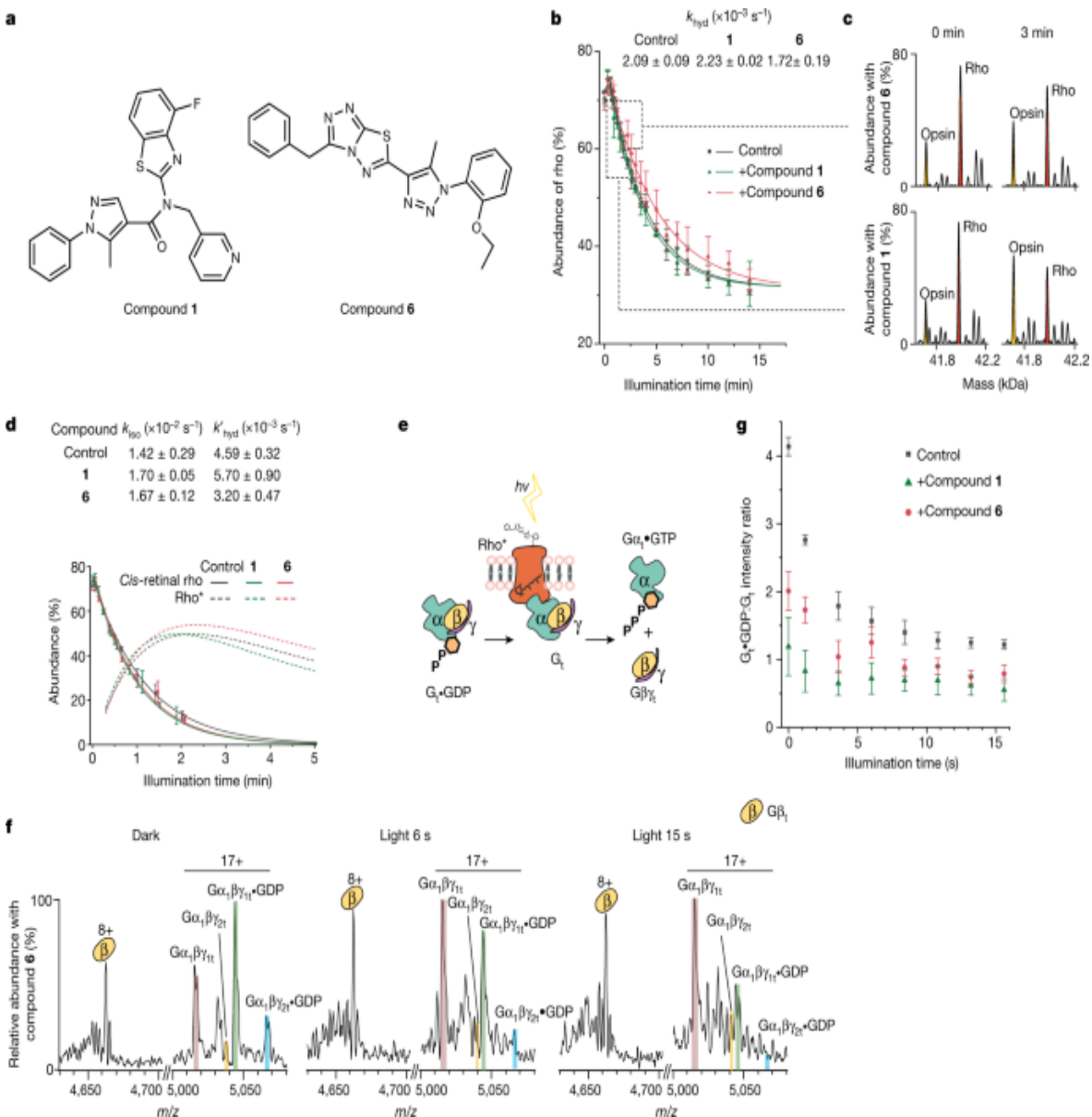
subunit of PDE6 binds to $G\alpha_t$ -GTP with high affinity but low activity for hydrolysing cGMP, whereas the other catalytic subunit of PDE6 binds to $G\alpha_t$ -GTP with low affinity but is able to hydrolyse cGMP at a high rate¹¹. Our data, with only one $G\alpha_t$ -GTP subunit binding to PDE6 and with a high intensity for a single binding site of cGMP, are in accordance with the asymmetry of the activated complex and its ability to hydrolyse one cGMP to GMP per PDE6 tetramer. This reaction in turn is regulated by available GTP, activation of rho* through G_t and causes decreased concentrations of cGMP for closure of the ion channel.

Having established a means of capturing the entire signalling cascade we considered further the influence of the membrane through the effect of lipid microenvironments on rho* signalling through G_t . We examined lipids in the spectrum of dark-adapted rho expelled from membranes in the presence of G_t and PDE6 (see [Methods](#)) and found a predominance of long-chain polyunsaturated phosphatidylcholinelipids (PC 40:6, 40:8, 38:6, 38:8, 34:1, 34:2) (Extended Data Fig. [8a](#)) in line with observations of distinct regions of retinal rods in nanodisc experiments⁷. After exposure to light (6–18 s) in the presence of G_t and PDE6, we observed a notable increase in the ratio of unsaturated to saturated PC lipids compared with initial and later time points (Extended Data Fig. [8a, b](#)). Initial contact with unsaturated lipids is in line with findings of a molecular dynamic simulation study of a GPCR in an inactive or partially active state receptor²⁴ and NMR experiments²⁵. The increase of unsaturated lipid chains associated to rho during light activation provides evidence to support earlier proposals²⁴ that polyunsaturated chains associate specifically with rho* to enable its conformational change from its ground state and thereby facilitate swift signalling.

Monitoring signalling in a membrane environment provides us with a unique opportunity to probe the effects of rho-targeting molecules, identified through cell-based assays designed to select compounds that enhance or perturb rho dimerization^{26,27} (see [Methods](#)). We tested nine compounds individually and measured their effect on rho k_{hyd} against a control (compounds **1–9**; Extended Data Fig. [9a, b](#)). The results allowed these ligands to be divided into two groups that were capable of either accelerating

with a marginal effect or, more commonly, slowing retinal hydrolysis. Compounds **1** and **6** represent these two capabilities and were selected for further study (Fig. 4a). Clear differences emerge post-illumination (3 min) as rho and opsin predominate in the presence of **1** and **6**, respectively (Fig. 4b, c). After 15 min, noticeable differences occur in the rho to opsin conversion, which is faster when modulated by **1** than by **6**, with **1** being marginally faster than the control. As we see no evidence for displacement of retinal by these compounds or changes in the conformation of rhodopsin²⁷, we speculate that **1** and **6** act as allosteric modulators. Calculating rates of hydrolysis and isomerization in the presence of hydroxylamine, we found that **1** accelerates both hydrolysis and isomerization, whereas rho* bound to **6** has an accelerated isomerization rate but retains retinal by decelerating hydrolysis, thereby potentially maintaining active signalling states for extended periods.

Fig. 4: The effects of rho-targeting compounds on the rho to opsin conversion and the hydrolysis of G_t•GDP.



a, Structures of the two rho-targeting compounds (**1** and **6**) used here. **b**, Monitoring the conversion of rho to opsin via the change in mass following illumination in the presence of **1** or **6** and in a control under the same conditions. Data are presented as mean \pm s.e. ($n = 3$). **c**, Time points for spectra of rho (red) and opsin (yellow) ejected from membranes at 0 and 3 min in the presence of **1** (bottom) and **6** (top) are shown on a zero-charge scale. **d**, Abundance of *cis*-retinal rho and rho* as a function of time in the absence (grey) or presence of **6** (pink) or **1** (green). The function for *cis*-retinal rho is derived from fitting data from more than 3.6 s (dashed lines) and the function for rho* is derived from the fit of the data from 18 s to 300

s (solid lines) and extrapolated (dotted lines). Data are presented as mean \pm s.e. ($n = 3$). **e**, Reaction scheme: following activation with light, rho* signals through G_t to the nucleotide-free form (G_t^*), which then dissociates to form $\beta\gamma$ and α . **f**, Mass spectra of G_t^* in the presence of compound **6** added to the native membrane in the absence of light (dark), and after exposure to light for 6 s and 15 s. **g**, Monitoring signalling through G_t^* via changes in the ratio of $G_t^*\text{-GDP}:G_t^*$ in the presence or absence of compound **1** or compound **6** as a function of illumination time. Data are presented as mean \pm s.e. ($n = 3$).

Anticipating that the prolonged activation state of rho* in the presence of **6**, and the rapid isomerization and hydrolysis of **1**, would affect signalling differently through G_t^* , we established a further assay in which we measured the ability of **1** and **6** to affect phototransduction. As above, we monitored their impact by measuring the change in mass of the conversion of $G_t^*\text{-GDP}$ to apo- G_t^* . Before illumination, in the presence of **1** or **6** and a control under dark conditions, the ratio of $G_t^*\text{-GDP}:G_t^*$ was 1.2, 2.0 and 4.1, respectively. In the presence of the ROS membrane, both ligands had caused significant conversion of $G_t^*\text{-GDP}:G_t^*$ compared with the control (Fig. [4f](#), Extended Data Fig. [10](#)). Unexpectedly, **1** and **6** induced transduction in the dark, implying that their enhanced isomerization rates enable them to signal through the initial *trans*-retinal rho population before illumination. Once illuminated, phototransduction proceeded further ($G_t^*\text{-GDP}:G_t^*$ ratios of 0.6, 0.8 and 1.2 after 15 s for **1**, **6** and the control, respectively; Fig. [4g](#)). We conclude that **1** and **6** target rho and amplify signalling through G_t^* , making them ideal starting points for further chemical development. More generally, the fact that we can separate these reactions into isomerization, hydrolysis and influence on a downstream effector enables us to study rho-targeting compounds in molecular detail via their effects on phototransduction, in real time and within their native membrane environments.

Together, our native mass spectrometry data document that we have conserved a signalling cascade for an archetypal class A GPCR across its native membrane. We have shown that all three key players in the cascade can be ejected simultaneously from vesicles formed from native ROS disc membranes. In so doing, we have captured the conversion of rho to opsin in real time and have shown that it is significantly slower in the membrane than

in the detergent micelle. We observed regeneration of rho following exposure to light and detected changes in the level of *N*-ret-PE and depletion of the conjugated chromophore following illumination. The importance of the membrane also prompted us to consider the changing lipid microenvironment during signalling and documented changes in the association of unsaturated long-chain PC lipids in the vicinity of signalling rho. Considering the effects of rho-targeting compounds, we demonstrated their ability to accelerate the rho to opsin conversion or slow down the reaction, and we hypothesize that the latter would stabilize a signalling-competent state. In line with this hypothesis, we demonstrated the ability to modulate the G_t signalling pathway through an increase in the turnover of G_t•GDP to G_t and the subsequent dissociation to the Gβγ_t complex and Gα_t•GTP primed for interaction with PDE6. We observed the static intermediate Gα_t–PDE6, as well as the effects of endogenous GTP levels on the hydrolysis of cGMP through light-activated signalling across the membrane. By capturing the entire signalling process, we have demonstrated the importance of the lipid microenvironment for signalling, coupling, effector targeting and regeneration. We anticipate that similar approaches will be applicable to other cell-surface receptors (for example, olfactory receptors) present at high density, enabling kinetic studies of molecular events, and identification of endogenous and synthetic receptor ligands that perturb signalling. Overall, we have highlighted an approach to drug discovery in which different stages of a signalling cascade can be targeted across native membranes.

Methods

Preparation of bovine rod disc membrane vesicles, detergent solubilized rho and purified rho

Bovine eyes were obtained from a commercial slaughterhouse. ROSSs were obtained from a batch of 50–100 eyes each time, with dark-adapted retinas, and purified as previously described^{28,29}. To prepare vesicles, rho disc membranes containing 81 µg rho were suspended in 250 µl of 200 mM ammonium acetate. An earlier protocol was adapted¹⁶ to homogenize disc membranes using a probe sonicator with a stepped tip microtip (2 mm;

Vibra-Cell VCX-500 Watt, Sonics) and a maximal amplitude (40%) (1 s on, 2 s off) applying 2 J per cycle for 1.5 min. Disc membrane vesicles containing rho (approximately 9 μ M) were ready for study via native mass spectrometry (MS) either directly, or alternatively following addition of hydroxylamine to a final concentration 5 mM, at pH 7.0.

For detergent-solubilized rho, collected ROS was solubilized with 20 mM LMNG overnight. The solution was then diluted into 50 μ l 200 mM ammonium acetate with 0.004% LMNG and buffer exchanged with 200 mM ammonium acetate and 0.002% LMNG using a micro bio-spin column (6,000 Da MW cut-off) before native MS. The resulting solution (approximately 9 μ M rho in LMNG ammonium acetate solution) was exposed to light for MS measurement of rho/opsin kinetics (Fig. 2).

For rho purification, to remove the majority of lipids for the regeneration experiments (Extended Data Fig. 4), ROS, washed with isotonic and hypotonic buffers, was solubilized in 5 mM LMNG. Rho was then purified with an immobilized 1D4 antibody as previously described³⁰, with the modification that LMNG was used as the detergent. Purified rho was then dialysed (10 kDa cut-off) to remove the nonapeptide TETSQVAPA.

All above procedures were carried out in the dark under dim red light (more than 670 nm).

Purification of bovine rod G_t and PDE6

Trimeric G_t and PDE6 were prepared as previously described³¹. In brief, bovine ROSSs were suspended in isotonic buffer containing 20 mM 4-(2-hydroxyethyl)-1-piperazineethanesulfonic acid (HEPES), pH 7.5, 100 mM NaCl, 1 mM DTT and 5 mM MgCl₂ and centrifuged at 31,000g for 25 min at 4 °C. The pellet was homogenized in a hypotonic buffer containing 5 mM HEPES, pH 7.5, 1 mM EDTA and 1 mM DTT and centrifuged at 40,000g for 30 min at 4 °C multiple times. The ratio between G_t and PDE6 in the supernatant was analysed by ImageJ software on a Coomassie blue staining SDS-PAGE. For addition of the soluble fraction to the membrane, G_t and PDE6, as purified above, were first buffer exchanged three times with 200 mM ammonium acetate using an Amicon filter (10 kDa cut-off). Under dim

red light, rho, G_t and PDE6 were mixed at a molar ratio of 13:4:1 for 15 min on ice to allow diffusion of G_t and PDE6 before analyses by native MS. To capture post-signalling PDE6 for native MS, rho, G_t and PDE6 at a molar ratio of 32.5:4:1 were illuminated under cold white LED for 30 min at room temperature and centrifuged at 20,000g for 20 min to remove the membrane (presented in Fig. 3d, Extended Data Fig. 7g-i).

Native MS set-up and illumination conditions

The native membrane preparation (2–3 µl) was placed directly in a gold-coated nano-electrospray capillary before the source of the mass spectrometer (Fig. 1c). The cold LED light source (120 µW at a 10 cm distance with a surface area of illumination of 3 mm²) was assembled via a bracket to illuminate the tip of the capillary for a defined interval in a dim red-light environment. For a real-time dynamic process, the membrane was first recorded in the dark and then illuminated with light pulses, or continuously, depending on the experiment. Native MS experiments were carried out on a Q-Exactive adapted for membrane proteins³². The following parameters were used typically and adjusted to release the membrane protein from the detergents and membrane lipids: capillary voltage of 0.8–1.4 kV, capillary temperature of 125–200 °C, higher-energy collisional dissociation (HCD) energy of 125–200 V, desolvation voltage of –5 to 0 V, source fragmentation of 5–100 V, HCD pressure of 3.8×10^{-10} to 8.5×10^{-10} mbar, C-trap entrance lens tune offset was set to 2, injection flatapole was set to 7 V, inter-flatapole lens was at 0 V, and the bent flatapole was set at 1 V. Threshold was set to 3. These MS conditions were modified to focus on the individual components of the spectrum. For example, the following parameters were used for Fig. 1d: capillary voltage of 0.9 kV, desolvation voltage of –5 V, source fragmentation of 5 V and HCD energy of 180 V. HCD pressure was typically 3.3×10^{-10} mbar. The spectra of rho/opsin (Fig. 2) were collected at a capillary voltage of 1.1 kV, desolvation voltage of 0 V, source fragmentation of 100 V and HCD energy of 200 V. HCD pressure was typically 5.5×10^{-10} mbar. For optimized spectra of G_t (Figs. 3c, 4f) the following parameters were used: capillary voltage of 0.9–1.1 kV, desolvation voltage of 0 V, source fragmentation of 25 V and HCD energy of 175 V. HCD pressure was typically 8.5×10^{-10} mbar. For the measurement of

PDE6 spectra (Fig. 4d, e), the following parameters were used: capillary voltage of 1.1 kV, desolvation voltage of 0 V, source fragmentation of 50 V and HCD energy of 175 V. HCD pressure was typically 7.3×10^{-10} mbar.

Polyunsaturated PC lipids surrounding rho identified with multistage native MSⁿ

The mixture of rho, G_t and PDE6 at a molar ratio of 32.5:4:1 (described above) was used to identify the polyunsaturated PC surrounding rho during light-induced signalling. PC lipids are released from rho and detected in positive mode using an Orbitrap Eclipse tribrid mass spectrometer (Thermo Fisher Scientific)³³. In general, in-source activation (100 V) was applied to rho in membranes and the resulting ions were transferred to the ion-routing multipole (IRM) for activation (HCD normalized collision energy (NCE) of 100%, IRM pressure of 8 mM) to promote dissociation into lipids. Automatic gain control (AGC) target values (100–150%) and maximum injection time (100 ms) were adjusted manually to maximize the normalized level. Detection at this stage was typically performed in the Orbitrap at a high *m/z* range 500–8,000. High resolution at 60,000 can be used to enhance the intensity of lipid signals at low *m/z*. Data were analysed using the Xcalibur software package 4.1 (Thermo Fisher Scientific).

Data analysis

Raw data were first analysed manually using Xcalibur 4.1 (Thermo Fisher Scientific). The relative abundance of each species in a real-time measurement was quantified using Lig2Apo, a simple jupyter notebook. A folder of text files (format *m/z* versus intensity) was exported from Xcalibur 4.1 (Thermo Fischer Scientific) and two series of *m/z* values were defined corresponding to the molecular species of interest. The program then read all text files and calculated the relative intensity of the series and the intensity ratio of two species (see Code availability). The zero charge spectra presented in Fig. 2 were analysed by Unidec v.2.7.3³⁴. The rate constants were analysed by OriginPro 2020 SR1 9.7.0.188.

Proteomics and protein identification

Protein bands were excised from gels and processed as previously described³⁵. Peptides generated were resuspended in 0.1% formic acid and separated on an Ultimate 3000 UHPLC system (Thermo Fisher Scientific) and electrosprayed directly into a Q Exactive mass spectrometer (Thermo Fisher Scientific) through an EASY-Spray nano-electrospray ion source (Thermo Fisher Scientific). The peptides were trapped on a C18 PepMap100 pre-column (300 µm i.d. × 5 mm, 100 Å; Thermo Fisher Scientific) using solvent A (0.1% formic acid in water). The peptides were separated on an analytical column (75 µm i.d. packed with ReproSil-Pur 120 C18-AQ, 1.9 µm, 120 Å, by Dr Maisch GmbH) using a gradient (15–38% for 30 min, solvent B – 0.1% formic acid in acetonitrile, flow rate: 200 nl min⁻¹) for 15 min. The raw data were acquired in a data-dependent acquisition mode. Full-scan mass spectra were acquired in the Orbitrap (scan range of 350–1,500 *m/z*, resolution of 70,000, AGC target of 3×10^6 , maximum injection time of 50 ms). After the MS scans, the ten most intense peaks were selected for HCD fragmentation at 30% of the normalized collision energy. HCD spectra were also acquired in the Orbitrap (resolution of 17,500, AGC target of 5×10^4 , maximum injection time of 120 ms) with the first fixed mass at 180 *m/z*. Charge exclusion was selected for 1+ and 2+ ions. The dynamic exclusion was set to 5 s. All peptides were manually validated. Peptide identification and data analysis were carried out using the MASCOT Daemon client program and server (version 2.7.0)³⁶, and the Maxquant software (version 1.6.3.4)³⁷.

Lipidomics and N-ret-PE identification

N-ret-PEs and lipids were extracted by 90% isopropanol with 0.1% formic acid from the disc membrane vesicles in dark, illuminated for 1 s and 4 s, respectively. The supernatant was transferred into a new glass tube and dried using a SpeedVac vacuum concentrator (Thermo Fisher Scientific). The evaporated lipid mixture was dissolved in a 50 µl buffer and sonicated for 10 min. For liquid chromatography–MS/MS analysis, lipids were loaded onto a C8 column (Acclaim PepMap 100, C8, inner diameter of 75 µm, particle size of 3 µm, length of 150 mm; Thermo Scientific) using a Dionex UltiMate 3000 RSLC nano System connected to an Eclipse Tribrid Orbitrap mass spectrometer (Thermo Scientific). A binary buffer system was used with buffer A of acetonitrile:H₂O (60:40), 10 mM ammonium formate and

0.1% formic acid, and buffer B of isopropanol:acetonitrile (90:10), 10 mM ammonium formate and 0.1% formic acid. Lipids were separated at 40 °C with a gradient from 30% to 99% buffer B at a flow rate of 300 nl min⁻¹ over 30 min. The electrospray voltage was set to 2.2 kV with funnel RF level at 40 and heated capillary temperature at 320 °C. For data-dependent acquisition, full MS mass range was set to 300–2,000 with a resolution of 120,000 and AGC target of 100%. Fragment spectra were acquired in the Orbitrap with a resolution of 15,000 using HCD with stepped collision energy of 25%, 30% and 35%. Phospholipids were detected in negative-ion mode. The raw data were processed by LipiDex³⁸ and MZmine 2 (ref. ³⁹) for phospholipid identification and quantification. Identification of *N*-ret-PE was processed manually. The extracted ion chromatogram of ret-PE was integrated using Xcalibur 4.1 (Thermo Fisher Scientific) and the area under the curve (AUC) was used for quantification.

Selection and evaluation of rho-targeting molecules

Compounds used in this study were selected via high-throughput screening of a diverse library of 50,000 small molecules. The high-throughput screening approach used cells expressing tagged rho with β-galactosidase complementary and BRET detection systems. To validate the identified hits further, rho photobleaching assays were carried out along with ex vivo electrophysiology recordings^{26,27}.

Hit compounds F2515-3945 (**1**), F3382-0749 (**2**), F2502-0030 (**3**), F3215-0002 (**6**), F5103-0385 (**7**), F5097-2767 (**8**) and F0834-0928 (**9**) were obtained from Life Chemicals. The racemic mixture of sulconazole (**4** and **5**) was purchased from MilliporeSigma and separated as previously described on an Agilent 1100 HPLC system (Agilent Technologies) using a cellulose tris 3,5-dimethylphenyl carbamate chiralcar column (Chiral Technologies)²⁶.

For MS, these compounds were dissolved individually in DMSO and diluted 1,000-fold in disc membrane vesicle preparations in 200 mM ammonium acetate buffer to give a concentration for each compound of 90 μM, and a 10:1 final molar ratio of compound to rhodopsin. The disc membranes and compound were incubated for 30 min on ice, allowing for complete diffusion

before native MS measurement of rho/opsin. Disc membrane supplemented with G_t and PDE6 at a molar ratio of 6.5:4:1 (rho:G_t:PDE6) were also incubated with 90 μM compound in 200 mM ammonium acetate for 30 min on ice before native MS measurement of G_t. A control experiment in the absence of membranes was performed with G_t and PDE6 incubated with 90 μM compound at 4:1:50 for 30 min on ice before native MS measurement of G_t. Data were analysed as described above.

Reporting summary

Further information on research design is available in the [Nature Research Reporting Summary](#) linked to this paper.

Data availability

The data that support the findings of this study are available as follows: native MS/proteomics data and lipidomics data have been deposited to Figshare at <https://doi.org/10.25446/oxford.16901326> and <https://doi.org/10.6084/m9.figshare.18319361.v1>, respectively.

Code availability

The script for calculating the opsin:rho ratio in mass spectra can be accessed at <https://github.com/d-que/Lig2Apo>.

References

1. Hilger, D., Masureel, M. & Kobilka, B. K. Structure and dynamics of GPCR signaling complexes. *Nat. Struct. Mol. Biol.* **25**, 4–12 (2018).
2. Weis, W. I. & Kobilka, B. K. The molecular basis of G protein-coupled receptor activation. *Annu. Rev. Biochem.* **87**, 897–919 (2018).
3. Lee, Y. et al. Molecular basis of β-arrestin coupling to formoterol-bound β₁-adrenoceptor. *Nature* **583**, 862–866 (2020).

4. Zhang, M. et al. Cryo-EM structure of an activated GPCR–G protein complex in lipid nanodiscs. *Nat. Struct. Mol. Biol.* **28**, 258–267 (2021).
5. Van Eps, N. et al. Conformational equilibria of light-activated rhodopsin in nanodiscs. *Proc. Natl Acad. Sci. USA* **114**, E3268–E3275 (2017).
6. Xu, P. et al. Structural insights into the lipid and ligand regulation of serotonin receptors. *Nature* **592**, 469–473 (2021).
7. Sander, C. L. et al. Nano-scale resolution of native retinal rod disk membranes reveals differences in lipid composition. *J. Cell Biol.* **220**, e202101063 (2021).
8. Palczewski, K. G protein-coupled receptor rhodopsin. *Annu. Rev. Biochem.* **75**, 743–767 (2006).
9. Heck, M. et al. Signaling states of rhodopsin. Formation of the storage form, metarhodopsin III, from active metarhodopsin II. *J. Biol. Chem.* **278**, 3162–3169 (2003).
10. Palczewski, K. & Kiser, P. D. Shedding new light on the generation of the visual chromophore. *Proc. Natl Acad. Sci. USA* **117**, 19629–19638 (2020).
11. Irwin, M. J. et al. The molecular architecture of photoreceptor phosphodiesterase 6 (PDE6) with activated G protein elucidates the mechanism of visual excitation. *J. Biol. Chem.* **294**, 19486–19497 (2019).
12. Schey, K. L., Papac, D. I., Knapp, D. R. & Crouch, R. K. Matrix-assisted laser desorption mass spectrometry of rhodopsin and bacteriorhodopsin. *Biophys. J.* **63**, 1240–1243 (1992).
13. Whitelegge, J. P., Gundersen, C. B. & Faull, K. F. Electrospray-ionization mass spectrometry of intact intrinsic membrane proteins. *Protein Sci.* **7**, 1423–1430 (1998).

14. Norris, C. E. et al. Native mass spectrometry reveals the simultaneous binding of lipids and zinc to rhodopsin. *Int. J. Mass Spectrom.* **460**, 116477 (2021).
15. Chorev, D. S. et al. Protein assemblies ejected directly from native membranes yield complexes for mass spectrometry. *Science* **362**, 829–834 (2018).
16. Chorev, D. S. et al. The use of sonicated lipid vesicles for mass spectrometry of membrane protein complexes. *Nat. Protoc.* **15**, 1690–1706 (2020).
17. Zhao, D. Y. et al. Cryo-EM structure of the native rhodopsin dimer in nanodiscs. *J. Biol. Chem.* **294**, 14215–14230 (2019).
18. Kang, Y. et al. Crystal structure of rhodopsin bound to arrestin by femtosecond X-ray laser. *Nature* **523**, 561–567 (2015).
19. Sakmar, T. P., Franke, R. R. & Khorana, H. G. Glutamic acid-113 serves as the retinylidene Schiff base counterion in bovine rhodopsin. *Proc. Natl Acad. Sci. USA* **86**, 8309–8313 (1989).
20. Kiser, P. D. & Palczewski, K. Pathways and disease-causing alterations in visual chromophore production for vertebrate vision. *J. Biol. Chem.* **296**, 100072 (2021).
21. Kaylor, J. J. et al. Blue light regenerates functional visual pigments in mammals through a retinyl-phospholipid intermediate. *Nat. Commun.* **8**, 16 (2017).
22. Wang, X., Plachetzki, D. C. & Cote, R. H. The N termini of the inhibitory γ -subunits of phosphodiesterase-6 (PDE6) from rod and cone photoreceptors differentially regulate transducin-mediated PDE6 activation. *J. Biol. Chem.* **294**, 8351–8360 (2019).
23. Gulati, S. & Palczewski, K. New focus on regulation of the rod photoreceptor phosphodiesterase. *Curr. Opin. Struct. Biol.* **69**, 99–107 (2021).

24. Grossfield, A., Feller, S. E. & Pitman, M. C. A role for direct interactions in the modulation of rhodopsin by omega-3 polyunsaturated lipids. *Proc. Natl Acad. Sci. USA* **103**, 4888–4893 (2006).
25. Soubias, O. & Gawrisch, K. Probing specific lipid–protein interaction by saturation transfer difference NMR spectroscopy. *J. Am. Chem. Soc.* **127**, 13110–13111 (2005).
26. Getter, T. et al. Stereospecific modulation of dimeric rhodopsin. *FASEB J.* **33**, 9526–9539 (2019).
27. Getter, T., Kemp, A., Vinberg, F. & Palczewski, K. Identification of small-molecule allosteric modulators that act as enhancers/disrupters of rhodopsin oligomerization. *J. Biol. Chem.* **297**, 101401 (2021).
28. Jastrzebska, B. et al. Functional and structural characterization of rhodopsin oligomers. *J. Biol. Chem.* **281**, 11917–11922 (2006).
29. Kevany, B. M. et al. Structural and functional analysis of the native peripherin–ROM1 complex isolated from photoreceptor cells. *J. Biol. Chem.* **288**, 36272–36284 (2013).
30. Gulati, S. et al. Photocyclic behavior of rhodopsin induced by an atypical isomerization mechanism. *Proc. Natl Acad. Sci. USA* **114**, E2608–E2615 (2017).
31. Gulati, S. et al. Targeting G protein-coupled receptor signaling at the G protein level with a selective nanobody inhibitor. *Nat. Commun.* **9**, 1996 (2018).
32. Gault, J. et al. High-resolution mass spectrometry of small molecules bound to membrane proteins. *Nat. Methods* **13**, 333–336 (2016).
33. Gault, J. et al. Combining native and 'omics' mass spectrometry to identify endogenous ligands bound to membrane proteins. *Nat. Methods* **17**, 505–508 (2020).

34. Marty, M. T. et al. Bayesian deconvolution of mass and ion mobility spectra: from binary interactions to polydisperse ensembles. *Anal. Chem.* **87**, 4370–4376 (2015).
35. Shevchenko, A., Tomas, H., Havlis, J., Olsen, J. V. & Mann, M. In-gel digestion for mass spectrometric characterization of proteins and proteomes. *Nat. Protoc.* **1**, 2856–2860 (2006).
36. Perkins, D. N., Pappin, D. J., Creasy, D. M. & Cottrell, J. S. Probability-based protein identification by searching sequence databases using mass spectrometry data. *Electrophoresis* **20**, 3551–3567 (1999).
37. Tyanova, S., Temu, T. & Cox, J. The MaxQuant computational platform for mass spectrometry-based shotgun proteomics. *Nat. Protoc.* **11**, 2301–2319 (2016).
38. Hutchins, P. D., Russell, J. D. & Coon, J. J. LipiDex: an integrated software package for high-confidence lipid identification. *Cell Syst.* **6**, 621–625 (2018).
39. Pluskal, T., Castillo, S., Villar-Briones, A. & Oresic, M. MZmine 2: modular framework for processing, visualizing, and analyzing mass spectrometry-based molecular profile data. *BMC Bioinformatics* **11**, 395 (2010).

Acknowledgements

All MS research was funded by a Wellcome Trust Investigator Award (221795/Z/20/Z) and an ERC Advanced Grant ENABLE (695511) to C.V.R. A grant from the National Institutes of Health (R01EY030912) and unrestricted grants from Research to Prevent Blindness (RPB) to the Department of Ophthalmology at UCI are gratefully acknowledged by the K.P. laboratory. We acknowledge discussions with M. Galpin and T. El-Baba on the interpretation of kinetic data. For the purpose of Open Access, the authors have applied for a CC BY public copyright license to any Author Accepted Manuscript version arising from this submission.

Author information

Affiliations

1. Chemistry Research Laboratory, University of Oxford, Oxford, UK

Siyun Chen, Di Wu, Daniel Quetschlich, Dror S. Choren & Carol V. Robinson

2. Kavli Institute for Nanoscience Discovery, University of Oxford, Oxford, UK

Siyun Chen, Di Wu, Daniel Quetschlich & Carol V. Robinson

3. Gavin Herbert Eye Institute, Department of Ophthalmology, University of California, Irvine, Irvine, CA, USA

Tamar Getter, David Salom & Krzysztof Palczewski

4. Department of Physiology and Biophysics, University of California, Irvine, Irvine, CA, USA

Krzysztof Palczewski

5. Department of Chemistry, University of California, Irvine, Irvine, CA, USA

Krzysztof Palczewski

6. Department of Molecular Biology and Biochemistry, University of California, Irvine, Irvine, CA, USA

Krzysztof Palczewski

Contributions

C.V.R. and K.P. conceived the idea through the CIFAR network and provided overall supervision for the study. S.C. performed all of the

experiments described in this paper under the supervision of D.S.C. and D.W. for the SoLVe and lipidomics experiments, respectively. D.Q. provided computational support for analysis. T.G., D.S. and K.P. prepared and provided ROS disc membranes and purified rho, identified rho-targeting compounds and prepared PDE6 and transducin complexes. C.V.R., S.C. and K.P. wrote the paper with contributions from other authors.

Corresponding authors

Correspondence to [Dror S. Chorev](#), [Krzysztof Palczewski](#) or [Carol V. Robinson](#).

Ethics declarations

Competing interests

K.P. is Chief Scientific Officer of Polgenix and C.V.R. is a founding director of OMass Therapeutics. All other authors declare no competing interests.

Peer review

Peer review information

Nature thanks Ka Young Chung, Julian Whitelegge and the other, anonymous, reviewer(s) for their contribution to the peer review of this work. Peer reviewer reports are available.

Additional information

Publisher's note Springer Nature remains neutral with regard to jurisdictional claims in published maps and institutional affiliations.

Extended data figures and tables

Extended Data Fig. 1 Photographic images of the electrospray set-up showing the relationship between the light source, the electrospray capillary and MS inlet and UV visible emission spectrum of the LED light source used here.

a, The relationship between the electrospray interface, the cold white LED light source and the mass spectrometer. The glass capillary was displayed on the same axis of source aperture. The light stimulation set up was set orthogonally onto the capillary and the sample was at the illuminating centre. **b**, (i) and (ii) membrane fragments are placed in the glass needle prepared in-house and secured in the needle holder. (iii) shows the orientation of the light source orthogonal to the electrospray plume. (iv) to (vi) high voltage is applied to the needle holder and the distance between the needle tip and the MS inlet is adjusted to produce a stable electrospray ion current. Once this is achieved the electrospray interface is illuminated ($t = 0$) and spectra are recorded in real-time either with continuous illumination or as a function of the post illumination period. **c**, UV-visible emission spectrum of the cold white light source used here. The spectrum was recorded on an Andor Shamrock 303i Spectrograph equipped with an Andor Newton 920 camera. The wavelength maximum is at 460 nm.

Extended Data Fig. 2 Native mass spectra of rho extracted in detergent (left-hand side) or ejected directly from membranes (right-hand side), dark-adapted or following 20 min of illumination, and decay curve following treatment with hydroxylamine.

a, From dark-adapted membranes extracted into LMNG 73% rho (blue) and 27% opsin (green) are observed in spectra initially consistent with a small population of opsin in dark-adapted bovine retinae. Inset: Expansion of the 7+ charge state reveals glycans (hexoses: hex1, hex2, hex3 and hex4), cysteinylation (cys) and palmitoylation (pal). ~95% rho /opsin has two pal sites occupied, while 5% have only one pal. **b**, After 20 min of exposure to light the population of opsin has increased and ~5% of opsin is observed with at least one phosphorylation (pho). All other PTMs remain unchanged, 7+ charge state expanded (inset). **c**, MS of rho/opsin expelled from

membrane fragments reveals 73% rho and 27% opsin, as in the detergent extraction, and an identical pattern of PTMs is observed (inset). **d**, After 20 min exposure to light in membranes the majority of rho has converted to opsin. 5% of opsin is phosphorylated while all other PTMs remain unchanged (7+ charge state (inset)). **e**, Plot of the photoconversion of 11-*cis*-retinal rho to opsin in membranes either pre-treated with 5 mM hydroxylamine (red) or without pre-treatment (grey) monitored by mass spectrometry under the conditions described for Fig. 2 (main text). The experiments were performed under continuous illumination conditions and the data are presented as mean values \pm SE ($n = 3$).

[Extended Data Fig. 3 Kinetic model for the photoconversion and regeneration of rho in disc membranes.](#)

The photoconversion and regeneration processes involve a number of reactions outlined above. To simplify our kinetic model, we have divided the light response process into three phases. **a**, First, < 18 s when a rapid increase of rho is observed, prior to a steady decrease. **b**, This initial fast reaction $0 - 18$ s is attributed to the rapid regeneration of *cis*- retinal rho competing with photoconversion ($\text{rho} \rightarrow \text{ops}$). Dark-adapted membranes possess *N*-ret-PE which responds rapidly to light such *N*-all-*trans*-ret-PE is activated and dissociates into *cis*-retinal and PE. Regenerated *cis*-retinal is then able to interact with opsin to form *cis*-retinal rho. Concurrently, existing *cis*-retinal rho photoconverts to active rho* and then deactivated opsin. **c**, During the second phase (> 18 s), after the original *N*-ret-PE is consumed, isomerization of *cis*-retinal rho to rho* continues with minimal regeneration of *cis*-retinal rho. rho* hydrolyses into opsin and all-*trans*-retinal.

([Supplementary Notes](#)).

[Extended Data Fig. 4 Monitoring the conversion of purified bovine rho to opsin through its mass change in LMNG micelles during applied illumination pulses \(shaded orange\) at pH 7.0 and 28 °C.](#)

Pulses were applied at 1.1 min, 7.6 min, 15 min and 20 min for 4.6 min, 18 s, 40 s and 35 s respectively. The experimental noise makes it challenging to

measure the increase in these illumination pulses in micelles compared to the experiments in the ROS membrane. However, a clear trend is observed after *circa* 20 min. The experiment was repeated twice.

Extended Data Fig. 5 Extraction of lipids from the ROS membrane, identification of phosphatidylethanolamines and formation of N-ret-PE under controlled illumination conditions.

a, Analysis of lipids through tandem MS in the negative ion mode and assignment using the program LipiDex³⁸. Shown is the fragmentation pattern of PE 40:6 confirming unsaturation in one chain. **b**, Profile and abundance of phosphatidylethanolamine in ROS membranes. Data are presented as mean values \pm SD ($n = 3$). A high degree of unsaturation is observed with the most abundant lipid assigned to PE 40:6. **c**, The reaction scheme of the formation of *N*-ret-PE. **d**, Detection of the formation of *N*-ret-PE 36:1. **e**, *N*-retinylidene-38:4 and **f**, *N*-retinylidene-40:5 under controlled illumination conditions and extraction into organic solvent for lipidomics. Negative ion mass spectra, monitoring the formate ion of the conjugated lipid, reveals a low intensity peak assigned through accurate mass to the *N*-retinylidene conjugate. Bar charts abundance ratio of *N*-ret-PE to free PE was monitored as a function of the illumination time and shows a clear decrease after 1 s for all three *N*-ret-PE lipids. Data are presented as mean values \pm SD ($n = 3$).

Extended Data Fig. 6 Rho regeneration in the presence of excess all-trans-retinal.

a, Schematic process of ROS opsin regenerated into rho in 10-fold excess of all-*trans*-retinal under continuous illumination. **b**, The intensity ratio of rho to opsin increases until it reaches a plateau at 3.8 min (red). Comparatively, rho remains constant in the presence of exogenous all-*trans*-retinal in the dark (blue). **c**, Zero-charge spectra of rho and opsin with 10-fold excessive all-*trans*-retinal present before and following 3.8 min illumination. This experiment was repeated twice.

Extended Data Fig. 7 In-gel digestion proteomics and native mass spectra of G_t and PDE6 complexes isolated from dark-adapted rod outer segments under different conditions.

a, Separation of the component subunits of the Gt and PDE6 complex on a 2D page gel, pre-stained with protein standards. **b**, Unique peptides of G α 1 (GNAT1) and **c**, G α 2 (GNAT2) are identified by proteomics (see [Methods](#)). **d**, Gt with rho-containing membrane in the absence of light reveals the initial extent of endogenous GDP binding to Gt (blue and green for γ^1 and γ^2 isoforms respectively) and without GDP (pink and yellow). **e**, Gt preparation illuminated in the absence of membranes was found to be bound to GDP predominantly for both isoforms. No reaction is observed in the absence of the membrane. **f**, with rho in membranes following illumination, GDP bound forms have declined in favour of *apo* states (pink and yellow). **g**, with endogenous levels of GTP, the PDE6:PDE6•cGMP complex remains ~ 1:1 after activation of Gt though rho*. The endogenous quantity of GTP is insufficient to produce sufficient G α ._{GTP} to interact with PDE6 and promote hydrolysis of cGMP. **h**, in the presence of an additional molar amount of GTP, G α .GDP is replenished and further cGMP hydrolysis takes place. **i**, in the presence of an additional molar aliquot of GTPs further cGMP hydrolysis has occurred but G α .GDP is not replenished. The SDS-page electrophoresis (**a**) was performed twice; in-gel proteomics experiment (**b**, **c**) was performed once and the real-time native MS experiments (**d–f**) and bulk reactions (**g–i**) were repeated three times and twice respectively.

Extended Data Fig. 8 Monitoring the lipids that are released with rho while signalling through G_t over the illumination period from dark to light.

a, PC lipids released as rho and opsin are ejected from disc membranes during signalling through Gt. Unsaturated lipids are designated as PC 34:1, 38:6 and 40:8 (orange) their more saturated counterparts 34:0, 38:4 and 40:6 (blue/purple). A decrease in the saturated lipids (blue and purple) relative to unsaturated is observed at the early stages of illumination (< 18 s). Lipids were detected in the positive ion mode. **b**, The intensities of PC 38:6 and

40:8 were manually selected to be compared with PC 38:4 and PC 40:6. Plotted is the ratio of unsaturated over saturated lipids as a function of illumination time. After 6 s and 18 s of illumination the extent of unsaturation increases. Data are presented as mean values +/- SE (n = 3).

Extended Data Fig. 9 Chemical structures of rho targeting compounds and their effects k_{hyd} of rho.

a, Chemical structures of the compounds **1–9**. **b**, comparison of the rate of hydrolysis of rho for **1–9** and a control comprising ROS vesicles in 200 mM ammonium acetate with 0.1% DMSO at pH 7.0. **1–9** were solubilised in DMSO and diluted to give a final concentration of 90 μ M in ROS vesicles in 0.1% DMSO, 200 mM ammonium acetate, pH 7.0. Data are presented as mean values +/- SE (n = 3).

Extended Data Fig. 10 G_t activation across native membranes during illumination of a control and in the presence of **1 and **6**.**

The ratio of GDP bound Gt to intermediate Gt represents a measure of the activation of transducin. Upon light absorption, rho activated G protein releases GDP **a**, at 6 s **b**, and after 15 s of the reaction. **c**, In the presence of **1** or **6** G protein signalling was accelerated and commenced even under dim red-light conditions when compared to the control experiment. Two different control experiments were performed in the absence of compounds (left hand column) but with the same concentration of DMSO used to dissolve **1** and **6**. **d**, The second control in the presence of the same concentration of DMSO, and **1** and **6**, but in the absence of rho* establish that the agonists do not compete with the nucleotide (GDP) and that signalling occurs through rho* in the native membrane. Two replicate experiments were performed for **a–c** and three replicate experiments were performed for **d**.

Extended Data Table 1 Measured mass with standard error and abundance of ROS rho/opsin ejected from LMNG micelles and disc membranes from either dark-adapted membranes (dark) or following 20 min of illumination (light)

Supplementary information

Supplementary Information

This file contains Supplementary Figure 1: Uncropped gel image of the soluble fraction; Supplementary Notes for Extended Data Figure 3; and Supplementary Table 1: Proteomics of purified bovine ROS disc membrane.

Reporting Summary

Peer Review File

Supplementary Video 1

A video of the experimental set-up begins with the positioning of the gold-coated nanoflow capillary close to the source aperture of the UHMR mass spectrometer. Red-light conditions are employed at this time while we establish a stable nanoflow electrospray mass spectrum for rho/opsin from native membrane vesicles. Once a stable signal is established, the capillary is illuminated with white light and the photoconversion is initiated. The rho/opsin ratio can be seen to transition from rho to the lower molecular mass species (opsin) as a function of real-time light exposure. Expansion across charge states in the mass spectrum shows the two peaks assigned to rho/opsin, with the same charge state, revealing the changing population as a function of time. In the mass spectral recording shown here, a pulse of light is applied for 40 s approximately 5 min after initial exposure to light. At this time point oopsin is predominant and increases relative to rho during the 40 s duration of the light pulse.

Rights and permissions

Open Access This article is licensed under a Creative Commons Attribution 4.0 International License, which permits use, sharing, adaptation, distribution and reproduction in any medium or format, as long as you give appropriate credit to the original author(s) and the source, provide a link to the Creative Commons license, and indicate if changes were made. The

images or other third party material in this article are included in the article's Creative Commons license, unless indicated otherwise in a credit line to the material. If material is not included in the article's Creative Commons license and your intended use is not permitted by statutory regulation or exceeds the permitted use, you will need to obtain permission directly from the copyright holder. To view a copy of this license, visit <http://creativecommons.org/licenses/by/4.0/>.

Reprints and Permissions

About this article

Cite this article

Chen, S., Getter, T., Salom, D. *et al.* Capturing a rhodopsin receptor signalling cascade across a native membrane. *Nature* **604**, 384–390 (2022). <https://doi.org/10.1038/s41586-022-04547-x>

- Received: 26 August 2021
- Accepted: 14 February 2022
- Published: 06 April 2022
- Issue Date: 14 April 2022
- DOI: <https://doi.org/10.1038/s41586-022-04547-x>

Share this article

Anyone you share the following link with will be able to read this content:

[Get shareable link](#)

Sorry, a shareable link is not currently available for this article.

[Copy to clipboard](#)

This article was downloaded by **calibre** from <https://www.nature.com/articles/s41586-022-04547-x>

| [Section menu](#) | [Main menu](#) |

Amendments & Corrections

- [**Author Correction: A chickpea genetic variation map based on the sequencing of 3,366 genomes**](#) [25 March 2022]
Author Correction •
- [**Publisher Correction: A trispecific antibody targeting HER2 and T cells inhibits breast cancer growth via CD4 cells**](#) [24 March 2022]
Publisher Correction •
- [**Publisher Correction: Evolution of enhanced innate immune evasion by SARS-CoV-2**](#) [24 March 2022]
Publisher Correction •
- [**Publisher Correction: Mechanisms of inhibition and activation of extrasynaptic \$\alpha\beta\$ GABA_A receptors**](#) [24 March 2022]
Publisher Correction •

[Download PDF](#)

- Author Correction
- Open Access
- [Published: 25 March 2022](#)

Author Correction: A chickpea genetic variation map based on the sequencing of 3,366 genomes

- [Rajeev K. Varshney](#) ORCID: orcid.org/0000-0002-4562-9131^{1,2},
- [Manish Roorkiwal](#) ORCID: orcid.org/0000-0001-6595-281X¹,
- [Shuai Sun](#) ORCID: orcid.org/0000-0003-1092-3186^{3,4,5},
- [Prasad Bajaj](#) ORCID: orcid.org/0000-0002-3282-9441¹,
- [Annapurna Chitikineni](#)¹,
- [Mahendar Thudi](#) ORCID: orcid.org/0000-0003-2851-6837^{1,6},
- [Narendra P. Singh](#)⁷,
- [Xiao Du](#)^{3,4},
- [Hari D. Upadhyaya](#)^{8,9},
- [Aamir W. Khan](#) ORCID: orcid.org/0000-0001-9734-8123¹,
- [Yue Wang](#) ORCID: orcid.org/0000-0003-2103-4237^{3,4},
- [Vanika Garg](#) ORCID: orcid.org/0000-0001-6446-4603¹,
- [Guangyi Fan](#)^{3,4,10,11},
- [Wallace A. Cowling](#) ORCID: orcid.org/0000-0002-3101-7695¹²,
- [José Crossa](#)¹³,
- [Laurent Gentzbittel](#) ORCID: orcid.org/0000-0001-7851-0332¹⁴,
- [Kai Peter Voss-Fels](#) ORCID: orcid.org/0000-0003-0782-366X¹⁵,
- [Vinod Kumar Valluri](#)¹,
- [Pallavi Sinha](#)^{1,16},
- [Vikas K. Singh](#)^{1,16},

- [Cécile Ben](#)^{14,17},
- [Abhishek Rathore](#) ORCID: orcid.org/0000-0001-6887-4095¹,
- [Ramu Punna](#) ORCID: orcid.org/0000-0003-3998-568X¹⁸,
- [Muneendra K. Singh](#)¹,
- [Bunyamin Tar'an](#)¹⁹,
- [Chellapilla Bharadwaj](#)²⁰,
- [Mohammad Yasin](#)²¹,
- [Motisagar S. Pithia](#)²²,
- [Servejeet Singh](#)²³,
- [Khela Ram Soren](#)⁷,
- [Himabindu Kudapa](#) ORCID: orcid.org/0000-0003-0778-9959¹,
- [Diego Jarquín](#) ORCID: orcid.org/0000-0002-5098-2060²⁴,
- [Philippe Cubry](#)²⁵,
- [Lee T. Hickey](#) ORCID: orcid.org/0000-0001-6909-7101¹⁵,
- [Girish Prasad Dixit](#)⁷,
- [Anne-Céline Thuillet](#)²⁵,
- [Aladdin Hamwieh](#) ORCID: orcid.org/0000-0001-6060-5560²⁶,
- [Shiv Kumar](#)²⁷,
- [Amit A. Deokar](#)¹⁹,
- [Sushil K. Chaturvedi](#)²⁸,
- [Aleena Francis](#)²⁹,
- [Réka Howard](#)³⁰,
- [Debasis Chattopadhyay](#)²⁹,
- [David Edwards](#) ORCID: orcid.org/0000-0001-7599-6760¹²,
- [Eric Lyons](#)³¹,
- [Yves Vigouroux](#) ORCID: orcid.org/0000-0002-8361-6040²⁵,
- [Ben J. Hayes](#) ORCID: orcid.org/0000-0002-5606-3970¹⁵,
- [Eric von Wettberg](#) ORCID: orcid.org/0000-0002-2724-0317³²,
- [Swapan K. Datta](#)³³,
- [Huanming Yang](#)^{10,11,34,36},
- [Henry T. Nguyen](#) ORCID: orcid.org/0000-0002-7597-1800³⁵,
- [Jian Wang](#)^{11,36},
- [Kadambot H. M. Siddique](#) ORCID: orcid.org/0000-0001-6097-4235¹²,

- [Trilochan Mohapatra³⁷](#),
- [Jeffrey L. Bennetzen](#) ORCID: [orcid.org/0000-0003-1762-8307³⁸](https://orcid.org/0000-0003-1762-8307),
- [Xun Xu](#) ORCID: [orcid.org/0000-0002-5338-5173^{10,39}](https://orcid.org/0000-0002-5338-5173) &
- [Xin Liu](#) ORCID: [orcid.org/0000-0003-3256-2940^{10,11,40,41}](https://orcid.org/0000-0003-3256-2940)

[*Nature*](#) volume **604**, page E12 (2022)

- 671 Accesses
- 2 Altmetric
- [Metrics details](#)

Subjects

- [Agricultural genetics](#)
- [Natural variation in plants](#)
- [Plant breeding](#)
- [Structural variation](#)

The [Original Article](#) was published on 10 November 2021

Correction to: *Nature* <https://doi.org/10.1038/s41586-021-04066-1>
Published online 10 November 2021

In Extended Data Fig. 1 of this Article, the labels ‘Market class’ and ‘Biological status’ were inadvertently swapped. In the corresponding figure legend, “Track 1: Biological status; Track 2: Market class;” should have been “Track 1: Market class; Track 2: Biological status;”. The original Article has been corrected online

Author information

Affiliations

1. Center of Excellence in Genomics and Systems Biology, International Crops Research Institute for the Semi-Arid Tropics (ICRISAT), Hyderabad, India

Rajeev K. Varshney, Manish Roorkiwal, Prasad Bajaj, Annapurna Chitikineni, Mahendar Thudi, Aamir W. Khan, Vanika Garg, Vinod Kumar Valluri, Pallavi Sinha, Vikas K. Singh, Abhishek Rathore, Muneendra K. Singh & Himabindu Kudapa

2. State Agricultural Biotechnology Centre, Centre for Crop and Food Innovation, Murdoch University, Murdoch, Western Australia, Australia

Rajeev K. Varshney

3. BGI-Qingdao, BGI-Shenzhen, Qingdao, China

Shuai Sun, Xiao Du, Yue Wang & Guangyi Fan

4. China National GeneBank, BGI-Shenzhen, Shenzhen, China

Shuai Sun, Xiao Du, Yue Wang & Guangyi Fan

5. College of Life Sciences, University of Chinese Academy of Sciences, Beijing, China

Shuai Sun

6. Institute of Crop Germplasm Resources, Shandong Academy of Agricultural Sciences (SAAS), Jinan, China

Mahendar Thudi

7. ICAR–Indian Institute of Pulses Research, Kanpur, India

Narendra P. Singh, Khela Ram Soren & Girish Prasad Dixit

8. Genebank, ICRISAT, Hyderabad, India

Hari D. Upadhyaya

9. University of Georgia, Athens, GA, USA

Hari D. Upadhyaya

10. BGI-Shenzhen, Shenzhen, China

Guangyi Fan, Huanming Yang, Xun Xu & Xin Liu

11. State Key Laboratory of Agricultural Genomics, BGI-Shenzhen, Shenzhen, China

Guangyi Fan, Huanming Yang, Jian Wang & Xin Liu

12. The UWA Institute of Agriculture, and School of Agriculture and Environment, The University of Western Australia, Perth, Western Australia, Australia

Wallace A. Cowling, David Edwards & Kadambot H. M. Siddique

13. Biometrics and Statistics Unit, International Maize and Wheat Improvement Center (CIMMYT), Texcoco, Mexico

José Crossa

14. Digital Agriculture Laboratory, Skolkovo Institute of Science and Technology, Moscow, Russia

Laurent Gentzbittel & Cécile Ben

15. Queensland Alliance for Agriculture and Food Innovation, The University of Queensland, St Lucia, Queensland, Australia

Kai Peter Voss-Fels, Lee T. Hickey & Ben J. Hayes

16. International Rice Research Institute (IRRI), South-Asia Hub, ICRISAT, Hyderabad, India

Pallavi Sinha & Vikas K. Singh

17. Laboratoire Ecologie Fonctionnelle et Environnement, Université de Toulouse, CNRS, Toulouse, France

Cécile Ben

18. Institute for Genomic Diversity, Cornell University, Ithaca, NY, USA

Ramu Punna

19. Department of Plant Sciences, University of Saskatchewan, Saskatoon, Saskatchewan, Canada

Bunyamin Tar'an & Amit A. Deokar

20. ICAR–Indian Agricultural Research Institute (IARI), New Delhi, India

Chellapilla Bharadwaj

21. Rajmata Vijayaraje Scindia Krishi Vishwa Vidyalaya, Gwalior, India

Mohammad Yasin

22. Junagadh Agricultural University, Junagadh, India

Motisagar S. Pithia

23. Rajasthan Agricultural Research Institute (RARI), Durgapura, India

Servejeet Singh

24. Department of Agronomy and Horticulture, University of Nebraska–Lincoln, Lincoln, NE, USA

Diego Jarquín

25. DIADE (Diversity-Adaptation-Development of Plants), Université de Montpellier, Institut de Recherche pour le Développement (IRD),

Montpellier, France

Philippe Cubry, Anne-Céline Thuillet & Yves Vigouroux

26. International Centre for Agricultural Research in the Dry Areas (ICARDA), Cairo, Egypt

Aladdin Hamwieh

27. International Centre for Agricultural Research in the Dry Areas (ICARDA), Rabat, Morocco

Shiv Kumar

28. Rani Lakshmi Bai Central Agricultural University, Jhansi, India

Sushil K. Chaturvedi

29. National Institute of Plant Genome Research, New Delhi, India

Aleena Francis & Debasis Chattopadhyay

30. Department of Statistics, University of Nebraska–Lincoln, Lincoln, NE, USA

Réka Howard

31. School of Plant Sciences, University of Arizona, Tucson, AZ, USA

Eric Lyons

32. Department of Plant and Soil Science, University of Vermont, Burlington, VT, USA

Eric von Wettberg

33. University of Calcutta, Kolkata, India

Swapan K. Datta

34. Guangdong Provincial Academician Workstation of BGI Synthetic Genomics, BGI-Shenzhen, Shenzhen, China

Huanming Yang

35. Division of Plant Sciences, University of Missouri, Columbia, MO, USA

Henry T. Nguyen

36. James D. Watson Institute of Genome Science, Hangzhou, China

Huanming Yang & Jian Wang

37. Indian Council of Agricultural Research (ICAR), New Delhi, India

Trilochan Mohapatra

38. Department of Genetics, University of Georgia, Athens, USA

Jeffrey L. Bennetzen

39. Guangdong Provincial Key Laboratory of Genome Read and Write, BGI-Shenzhen, Shenzhen, China

Xun Xu

40. BGI-Beijing, BGI-Shenzhen, Beijing, China

Xin Liu

41. BGI-Fuyang, BGI-Shenzhen, Fuyang, China

Xin Liu

Corresponding authors

Correspondence to [Rajeev K. Varshney](#) or [Xin Liu](#).

Rights and permissions

Open Access This article is licensed under a Creative Commons Attribution 4.0 International License, which permits use, sharing, adaptation, distribution and reproduction in any medium or format, as long as you give appropriate credit to the original author(s) and the source, provide a link to the Creative Commons license, and indicate if changes were made. The images or other third party material in this article are included in the article's Creative Commons license, unless indicated otherwise in a credit line to the material. If material is not included in the article's Creative Commons license and your intended use is not permitted by statutory regulation or exceeds the permitted use, you will need to obtain permission directly from the copyright holder. To view a copy of this license, visit <http://creativecommons.org/licenses/by/4.0/>.

[Reprints and Permissions](#)

About this article

Cite this article

Varshney, R.K., Roorkiwal, M., Sun, S. *et al.* Author Correction: A chickpea genetic variation map based on the sequencing of 3,366 genomes. *Nature* **604**, E12 (2022). <https://doi.org/10.1038/s41586-022-04660-x>

- Published: 25 March 2022
- Issue Date: 14 April 2022
- DOI: <https://doi.org/10.1038/s41586-022-04660-x>

Share this article

Anyone you share the following link with will be able to read this content:

[Get shareable link](#)

Sorry, a shareable link is not currently available for this article.

[Copy to clipboard](#)

Provided by the Springer Nature SharedIt content-sharing initiative

This article was downloaded by **calibre** from <https://www.nature.com/articles/s41586-022-04660-x>

| [Section menu](#) | [Main menu](#) |

[Download PDF](#)

- Publisher Correction
- [Published: 24 March 2022](#)

Publisher Correction: A trispecific antibody targeting HER2 and T cells inhibits breast cancer growth via CD4 cells

- [Edward Seung](#)^{1,2 nA1},
- [Zhen Xing](#)^{1 nA1},
- [Lan Wu](#)^{1,2},
- [Ercole Rao](#)³,
- [Virna Cortez-Retamozo](#)¹,
- [Beatriz Ospina](#)¹,
- [Liqing Chen](#)¹,
- [Christian Beil](#)³,
- [Zhili Song](#)¹,
- [Bailin Zhang](#)¹,
- [Mikhail Levit](#)¹,
- [Gejing Deng](#)¹,
- [Andrew Hebert](#)¹,
- [Patrick Kirby](#)^{1 nAffS},
- [Aiqun Li](#)¹,
- [Emma-Jane Poulton](#)¹,
- [Rita Vicente](#)⁴,
- [Audrey Garrigou](#)⁴,
- [Peter Piepenhagen](#)¹,

- [Greg Ulinski¹](#),
- [Michele Sanicola-Nadel^{1 nAff6}](#),
- [Dinesh S. Bangari ORCID: orcid.org/0000-0002-9909-1146¹](#),
- [Huawei Qiu¹](#),
- [Lily Pao ORCID: orcid.org/0000-0002-7626-2782¹](#),
- [Dmitri Wiederschain^{1 nAff7}](#),
- [Ronnie Wei^{1,2}](#),
- [Zhi-yong Yang ORCID: orcid.org/0000-0002-9938-5929^{1,2}](#) &
- [Gary J. Nabel ORCID: orcid.org/0000-0003-0619-4419^{1,2}](#)

Nature volume **604**, page E13 (2022)

- 733 Accesses
- 1 Altmetric
- [Metrics details](#)

Subjects

- [Cancer](#)
- [Immunology](#)

The [Original Article](#) was published on 23 February 2022

Correction to: *Nature* <https://doi.org/10.1038/s41586-022-04439-0>
 Published online 23 February 2022

In the version of this article initially published, there were labeling errors in Fig. 1a. In the top-left, bright green “Anti-HER2” section, the top peptide node now labeled “VH-3” initially appeared as “VL-3.” In the top-middle blue “Anti-CD3” section, the lower node now labeled “VH-2” initially appeared as “VL-2.” In the top-right olive “Anti-CD28” section, the top node now labeled “VH-1” and the lower node now labeled “VL-1” initially

appeared as “VL-1” and “VL-3,” respectively. The changes have been made to the HTML and PDF versions of the article

Author information

Author notes

1. Patrick Kirby

Present address: Dragonfly Therapeutics, Waltham, MA, USA

2. Michele Sanicola-Nadel

Present address: GSK, Waltham, MA, USA

3. Dmitri Wiederschain

Present address: Jounce Therapeutics, Cambridge, MA, USA

4. These authors contributed equally: Edward Seung, Zhen Xing

Affiliations

1. Sanofi R&D, North America, Cambridge, MA, USA

Edward Seung, Zhen Xing, Lan Wu, Virna Cortez-Retamozo, Beatriz Ospina, Liqing Chen, Zhili Song, Bailin Zhang, Mikhail Levit, Gejing Deng, Andrew Hebert, Patrick Kirby, Aiqun Li, Emma-Jane Poulton, Peter Piepenhagen, Greg Ulinski, Michele Sanicola-Nadel, Dinesh S. Bangari, Huawei Qiu, Lily Pao, Dmitri Wiederschain, Ronnie Wei, Zhi-yong Yang & Gary J. Nabel

2. ModeX Therapeutics, Natick, MA, USA

Edward Seung, Lan Wu, Ronnie Wei, Zhi-yong Yang & Gary J. Nabel

3. Sanofi R&D, Frankfurt, Frankfurt am Main, Germany

Ercole Rao & Christian Beil

4. Sanofi R&D, Montpellier, Montpellier, France

Rita Vicente & Audrey Garrigou

Corresponding authors

Correspondence to [Lily Pao](#), [Zhi-yong Yang](#) or [Gary J. Nabel](#).

Rights and permissions

[Reprints and Permissions](#)

About this article

Cite this article

Seung, E., Xing, Z., Wu, L. *et al.* Publisher Correction: A trispecific antibody targeting HER2 and T cells inhibits breast cancer growth via CD4 cells. *Nature* **604**, E13 (2022). <https://doi.org/10.1038/s41586-022-04652-x>

- Published: 24 March 2022
- Issue Date: 14 April 2022
- DOI: <https://doi.org/10.1038/s41586-022-04652-x>

Share this article

Anyone you share the following link with will be able to read this content:

[Get shareable link](#)

Sorry, a shareable link is not currently available for this article.

[Copy to clipboard](#)

Provided by the Springer Nature SharedIt content-sharing initiative

This article was downloaded by **calibre** from <https://www.nature.com/articles/s41586-022-04652-x>

| [Section menu](#) | [Main menu](#) |

[Download PDF](#)

- Publisher Correction
- Open Access
- [Published: 24 March 2022](#)

Publisher Correction: Evolution of enhanced innate immune evasion by SARS-CoV-2

- [Lucy G. Thorne](#) [ORCID: orcid.org/0000-0001-7358-6047](#)¹ na1,
- [Mehdi Bouhaddou](#)^{2,3,4,5} na1,
- [Ann-Kathrin Reuschl](#)¹ na1,
- [Lorena Zuliani-Alvarez](#)^{2,3,4,5} na1,
- [Ben Polacco](#) [ORCID: orcid.org/0000-0003-1570-9234](#)^{2,3,4,5},
- [Adrian Pelin](#)^{2,3,4,5},
- [Jyoti Batra](#)^{2,3,4,5},
- [Matthew V. X. Whelan](#)¹,
- [Myra Hosmillo](#)⁶,
- [Andrea Fossati](#) [ORCID: orcid.org/0000-0001-5170-4903](#)^{2,3,4,5},
- [Roberta Ragazzini](#) [ORCID: orcid.org/0000-0003-2186-293X](#)⁷ nAff1,
- [Irwin Jungreis](#) [ORCID: orcid.org/0000-0002-3197-5367](#)^{8,9},
- [Manisha Ummadi](#)^{2,3,4,5},
- [Ajda Rojc](#)^{2,3,4,5},
- [Jane Turner](#)¹,
- [Marie L. Bischof](#)¹,
- [Kirsten Obernier](#) [ORCID: orcid.org/0000-0002-4025-1299](#)^{2,3,4,5},
- [Hannes Braberg](#) [ORCID: orcid.org/0000-0002-7070-2257](#)^{2,3,4,5},
- [Margaret Soucheray](#)^{2,3,4,5},
- [Alicia Richards](#)^{2,3,4,5},

- [Kuei-Ho Chen](#) ORCID: [orcid.org/0000-0001-6541-0578^{2,3,4,5}](https://orcid.org/0000-0001-6541-0578),
- [Bhavya Harjai](#)^{2,3,4,5},
- [Danish Memon](#) ORCID: [orcid.org/0000-0002-1365-0710¹⁰](https://orcid.org/0000-0002-1365-0710),
- [Joseph Hiatt](#)^{2,3,4,5},
- [Romel Rosales](#)^{11,12},
- [Briana L. McGovern](#) ORCID: [orcid.org/0000-0002-0492-9904^{11,12}](https://orcid.org/0000-0002-0492-9904),
- [Aminu Jahun](#) ORCID: [orcid.org/0000-0002-4585-1701⁶](https://orcid.org/0000-0002-4585-1701),
- [Jacqueline M. Fabius](#)^{2,3,4,5},
- [Kris White](#) ORCID: [orcid.org/0000-0003-0889-0506^{11,12}](https://orcid.org/0000-0003-0889-0506),
- [Ian G. Goodfellow](#) ORCID: [orcid.org/0000-0002-9483-510X⁶](https://orcid.org/0000-0002-9483-510X),
- [Yasu Takeuchi](#)^{1 nAff15},
- [Paola Bonfanti](#) ORCID: [orcid.org/0000-0001-9655-3766^{7 nAff1}](https://orcid.org/0000-0001-9655-3766),
- [Kevan Shokat](#) ORCID: [orcid.org/0000-0001-8590-7741^{2,3,4,5,13}](https://orcid.org/0000-0001-8590-7741),
- [Natalia Jura](#) ORCID: [orcid.org/0000-0001-5129-641X^{2,3,5,14,15}](https://orcid.org/0000-0001-5129-641X),
- [Klim Verba](#) ORCID: [orcid.org/0000-0002-2238-8590^{2,3,5}](https://orcid.org/0000-0002-2238-8590),
- [Mahdad Noursadeghi](#) ORCID: [orcid.org/0000-0002-4774-0853¹](https://orcid.org/0000-0002-4774-0853),
- [Pedro Beltrao](#)^{2,10},
- [Manolis Kellis](#) ORCID: [orcid.org/0000-0001-7113-9630^{8,9}](https://orcid.org/0000-0001-7113-9630),
- [Danielle L. Swaney](#) ORCID: [orcid.org/0000-0001-6119-6084^{2,3,4,5}](https://orcid.org/0000-0001-6119-6084),
- [Adolfo García-Sastre](#) ORCID: [orcid.org/0000-0002-6551-1827^{11,12,16,17,18}](https://orcid.org/0000-0002-6551-1827),
- [Clare Jolly](#) ORCID: [orcid.org/0000-0002-4603-2281¹](https://orcid.org/0000-0002-4603-2281),
- [Greg J. Towers](#) ORCID: [orcid.org/0000-0002-7707-0264¹](https://orcid.org/0000-0002-7707-0264) &
- [Nevan J. Krogan](#) ORCID: [orcid.org/0000-0003-4902-337X^{2,3,4,5}](https://orcid.org/0000-0003-4902-337X)

Nature volume **604**, page E14 (2022)

- 489 Accesses
- 1 Altmetric
- [Metrics details](#)

Subjects

- [SARS-CoV-2](#)
- [Systems biology](#)

The [Original Article](#) was published on 23 December 2021

Correction to: *Nature* <https://doi.org/10.1038/s41586-021-04352-y>
Published online 23 December 2021

In the version of this article initially published, there were labeling errors in Figs. 2 and 3. In Fig. 2c, the labels “10 h” and “24 h” were omitted from atop the left and right-hand lanes of the heatmap, respectively. In Fig. 3i, the y-axis label, now reading “Alpha sgRNA reads”, initially appeared as “Alpha RNA reads”. The errors have been corrected in the HTML and PDF versions of the article

Author information

Author notes

1. Roberta Ragazzini & Paola Bonfanti

Present address: Division of Infection and Immunity, University College London, London, UK

2. Yasu Takeuchi

Present address: Cardiovascular Research Institute, University of California San Francisco, San Francisco, CA, USA

3. These authors contributed equally: Lucy G. Thorne, Mehdi Bouhaddou, Ann-Kathrin Reuschl, Lorena Zuliani-Alvarez

Affiliations

1. Division of Infection and Immunity, University College London, London, UK

Lucy G. Thorne, Ann-Kathrin Reuschl, Matthew V. X. Whelan, Jane Turner, Marie L. Bischof, Yasu Takeuchi, Mahdad Noursadeghi, Clare Jolly & Greg J. Towers

2. QBI Coronavirus Research Group (QCRG), University of California San Francisco, San Francisco, CA, USA

Mehdi Bouhaddou, Lorena Zuliani-Alvarez, Ben Polacco, Adrian Pelin, Jyoti Batra, Andrea Fossati, Manisha Ummadi, Ajda Rojc, Kirsten Obernier, Hannes Braberg, Margaret Soucheray, Alicia Richards, Kuei-Ho Chen, Bhavya Harjai, Joseph Hiatt, Jacqueline M. Fabius, Kevan Shokat, Natalia Jura, Klim Verba, Pedro Beltrao, Danielle L. Swaney & Nevan J. Krogan

3. Quantitative Biosciences Institute (QBI), University of California San Francisco, San Francisco, CA, USA

Mehdi Bouhaddou, Lorena Zuliani-Alvarez, Ben Polacco, Adrian Pelin, Jyoti Batra, Andrea Fossati, Manisha Ummadi, Ajda Rojc, Kirsten Obernier, Hannes Braberg, Margaret Soucheray, Alicia Richards, Kuei-Ho Chen, Bhavya Harjai, Joseph Hiatt, Jacqueline M. Fabius, Kevan Shokat, Natalia Jura, Klim Verba, Danielle L. Swaney & Nevan J. Krogan

4. J. David Gladstone Institutes, San Francisco, CA, USA

Mehdi Bouhaddou, Lorena Zuliani-Alvarez, Ben Polacco, Adrian Pelin, Jyoti Batra, Andrea Fossati, Manisha Ummadi, Ajda Rojc, Kirsten Obernier, Hannes Braberg, Margaret Soucheray, Alicia Richards, Kuei-Ho Chen, Bhavya Harjai, Joseph Hiatt, Jacqueline M. Fabius, Kevan Shokat, Danielle L. Swaney & Nevan J. Krogan

5. Department of Cellular and Molecular Pharmacology, University of California San Francisco, San Francisco, CA, USA

Mehdi Bouhaddou, Lorena Zuliani-Alvarez, Ben Polacco, Adrian Pelin, Jyoti Batra, Andrea Fossati, Manisha Ummadi, Ajda Rojc, Kirsten Obernier, Hannes Braberg, Margaret Soucheray, Alicia

Richards, Kuei-Ho Chen, Bhavya Harjai, Joseph Hiatt, Jacqueline M. Fabius, Kevan Shokat, Natalia Jura, Klim Verba, Danielle L. Swaney & Nevan J. Krogan

6. Division of Virology, Department of Pathology, Addenbrooke's Hospital, University of Cambridge, Cambridge, UK
Myra Hosmillo, Aminu Jahun & Ian G. Goodfellow
7. Epithelial Stem Cell Biology and Regenerative Medicine Laboratory, The Francis Crick Institute, London, UK
Roberta Ragazzini & Paola Bonfanti
8. MIT Computer Science and Artificial Intelligence Laboratory, MIT, Cambridge, MA, USA
Irwin Jungreis & Manolis Kellis
9. Broad Institute of MIT and Harvard, Cambridge, MA, USA
Irwin Jungreis & Manolis Kellis
10. European Molecular Biology Laboratory (EMBL), European Bioinformatics Institute, Wellcome Genome Campus, Hinxton, UK
Danish Memon & Pedro Beltrao
11. Department of Microbiology, Icahn School of Medicine at Mount Sinai, New York, NY, USA
Romel Rosales, Briana L. McGovern, Kris White & Adolfo García-Sastre
12. Global Health and Emerging Pathogens Institute, Icahn School of Medicine at Mount Sinai, New York, NY, USA
Romel Rosales, Briana L. McGovern, Kris White & Adolfo García-Sastre

13. Howard Hughes Medical Institute, San Francisco, CA, USA

Kevan Shokat

14. Division of Advanced Therapies, National Institute for Biological Standards and Control, South Mimms, UK

Natalia Jura

15. Cardiovascular Research Institute, University of California San Francisco, San Francisco, CA, USA

Natalia Jura

16. The Tisch Cancer Institute, Icahn School of Medicine at Mount Sinai, New York, NY, USA

Adolfo García-Sastre

17. Department of Medicine, Division of Infectious Diseases, Icahn School of Medicine at Mount Sinai, New York, NY, USA

Adolfo García-Sastre

18. Department of Pathology, Molecular and Cell-Based Medicine, Icahn School of Medicine at Mount Sinai, New York, NY, USA

Adolfo García-Sastre

Corresponding authors

Correspondence to [Clare Jolly](#), [Greg J. Towers](#) or [Nevan J. Krogan](#).

Rights and permissions

Open Access This article is licensed under a Creative Commons Attribution 4.0 International License, which permits use, sharing, adaptation, distribution and reproduction in any medium or format, as long

as you give appropriate credit to the original author(s) and the source, provide a link to the Creative Commons license, and indicate if changes were made. The images or other third party material in this article are included in the article's Creative Commons license, unless indicated otherwise in a credit line to the material. If material is not included in the article's Creative Commons license and your intended use is not permitted by statutory regulation or exceeds the permitted use, you will need to obtain permission directly from the copyright holder. To view a copy of this license, visit <http://creativecommons.org/licenses/by/4.0/>.

[Reprints and Permissions](#)

About this article

Cite this article

Thorne, L.G., Bouhaddou, M., Reuschl, AK. *et al.* Publisher Correction: Evolution of enhanced innate immune evasion by SARS-CoV-2. *Nature* **604**, E14 (2022). <https://doi.org/10.1038/s41586-022-04653-w>

- Published: 24 March 2022
- Issue Date: 14 April 2022
- DOI: <https://doi.org/10.1038/s41586-022-04653-w>

Share this article

Anyone you share the following link with will be able to read this content:

[Get shareable link](#)

Sorry, a shareable link is not currently available for this article.

[Copy to clipboard](#)

Provided by the Springer Nature SharedIt content-sharing initiative

This article was downloaded by **calibre** from <https://www.nature.com/articles/s41586-022-04653-w>

| [Section menu](#) | [Main menu](#) |

[Download PDF](#)

- Publisher Correction
- Open Access
- [Published: 24 March 2022](#)

Publisher Correction: Mechanisms of inhibition and activation of extrasynaptic $\alpha\beta$ GABA_A receptors

- [Vikram Babu Kasaragod](#)^{1,2},
- [Martin Mortensen](#) [ORCID: orcid.org/0000-0002-5873-7107](#)³,
- [Steven W. Hardwick](#) [ORCID: orcid.org/0000-0001-9246-1864](#)⁴,
- [Ayla A. Wahid](#) [ORCID: orcid.org/0000-0001-8128-9632](#)¹,
- [Valentina Dorovskikh](#)³,
- [Dimitri Y. Chirgadze](#) [ORCID: orcid.org/0000-0001-9942-0993](#)⁴,
- [Trevor G. Smart](#) [ORCID: orcid.org/0000-0002-9089-5375](#)³ &
- [Paul S. Miller](#) [ORCID: orcid.org/0000-0002-6512-9441](#)¹

[Nature](#) volume 604, page E15 (2022)

- 421 Accesses
- 2 Altmetric
- [Metrics details](#)

Subjects

- [Cryoelectron microscopy](#)
- [Ion channels in the nervous system](#)
- [Molecular neuroscience](#)

The [Original Article](#) was published on 09 February 2022

Correction to: *Nature* <https://doi.org/10.1038/s41586-022-04402-z>

Published online 9 February 2022

In the version of this article initially published, the first sentence of the Author contributions section was truncated. The section has been amended to begin “V.B.K. performed protein purification, atomic model building and structural interpretation.” The error has been corrected in the HTML and PDF versions of the article.

Author information

Affiliations

1. Department of Pharmacology, University of Cambridge, Cambridge, UK

Vikram Babu Kasaragod, Ayla A. Wahid & Paul S. Miller

2. MRC Laboratory of Molecular Biology, Cambridge, UK

Vikram Babu Kasaragod

3. Department of Neuroscience, Physiology and Pharmacology, University College London, London, UK

Martin Mortensen, Valentina Dorovskykh & Trevor G. Smart

4. Cryo-EM Facility, Department of Biochemistry, University of Cambridge, Cambridge, UK

Steven W. Hardwick & Dimitri Y. Chirgadze

Corresponding authors

Correspondence to [Trevor G. Smart](#) or [Paul S. Miller](#).

Rights and permissions

Open Access This article is licensed under a Creative Commons Attribution 4.0 International License, which permits use, sharing, adaptation, distribution and reproduction in any medium or format, as long as you give appropriate credit to the original author(s) and the source, provide a link to the Creative Commons license, and indicate if changes were made. The images or other third party material in this article are included in the article's Creative Commons license, unless indicated otherwise in a credit line to the material. If material is not included in the article's Creative Commons license and your intended use is not permitted by statutory regulation or exceeds the permitted use, you will need to obtain permission directly from the copyright holder. To view a copy of this license, visit <http://creativecommons.org/licenses/by/4.0/>.

[Reprints and Permissions](#)

About this article

Cite this article

Kasaragod, V.B., Mortensen, M., Hardwick, S.W. *et al.* Publisher Correction: Mechanisms of inhibition and activation of extrasynaptic $\alpha\beta$ GABA_A receptors. *Nature* **604**, E15 (2022). <https://doi.org/10.1038/s41586-022-04663-8>

- Published: 24 March 2022
- Issue Date: 14 April 2022
- DOI: <https://doi.org/10.1038/s41586-022-04663-8>

Share this article

Anyone you share the following link with will be able to read this content:

[Get shareable link](#)

Sorry, a shareable link is not currently available for this article.

[Copy to clipboard](#)

Provided by the Springer Nature SharedIt content-sharing initiative

This article was downloaded by **calibre** from <https://www.nature.com/articles/s41586-022-04663-8>

| [Section menu](#) | [Main menu](#) |